

Stony Brook University



OFFICIAL COPY

The official electronic file of this thesis or dissertation is maintained by the University Libraries on behalf of The Graduate School at Stony Brook University.

© All Rights Reserved by Author.

Multifunctional, chitosan-based nano therapeutics: design and application for two- and three-dimensional cell culture systems

A Dissertation Presented

by

Giulia Suarato

to

The Graduate School

in Partial Fulfillment of the

Requirements

for the Degree of

Doctor of Philosophy

in

Materials Science and Engineering

Stony Brook University

August 2016

Stony Brook University

The Graduate School

Giulia Suarato

We, the dissertation committee for the above candidate for the
Doctor of Philosophy degree, hereby recommend
acceptance of this dissertation.

**Dr. Yizhi Meng – Dissertation Advisor
Materials Science and Engineering**

**Dr. Dilip Gersappe – Chairperson of Defense
Materials Science and Engineering**

**Dr. Mircea Cotlet – Internal member
Materials Science and Engineering**

**Dr. Wei Yin – Outside member
Biomedical Engineering**

**Dr. Maya Shelly – Outside member
Neurobiology and Behavior**

This dissertation is accepted by the Graduate School

Nancy Goroff
Interim Dean of the Graduate School

Abstract of the Dissertation

Multifunctional, chitosan-based nano therapeutics: design and application for two- and three-dimensional cell culture systems

by

Giulia Suarato

Doctor of Philosophy

in

Materials Science and Engineering

Stony Brook University

2016

There is a constant demand for sensitive and effective anti-cancer drug delivery systems, capable of detecting early-stage pathological conditions and increasing patient survival. Recently, chitosan-based drug delivery nanocomplexes have been shown to smartly respond to the distinctive features of the tumor microenvironment, a complex network of extracellular molecules, stromal and endothelial cells, which supports the tumor formation and its metastatic invasion. Due to biocompatibility, easy chemical tailorability, and pH-responsiveness, chitosan has emerged as a promising candidate for the formulation of supramolecular multifunctional materials. The present study focuses on the design, fabrication and characterization of fluorescently labelled, hydrophobically modified glycol chitosan nanoparticles (HGC NPs), suitably tailored for the delivery of anti-neoplastic compounds to various tumor models.

In the first part of this thesis, doxorubicin-loaded HGC NPs have been delivered to a bone cancer model, both in monolayer and in 3D spheroid configuration, to assess for differences in the delivery profiles and in the therapeutic efficacy. Compared to the free drug, nanocomplexes showed rapid uptake and a more homogeneous distribution in 3D spheroids, a powerful cellular tool which recapitulates some of the *in vivo* tumor microenvironment features.

In a second part of this thesis work, with the purpose of designing an active targeting tumor-homing nano-therapeutic system, HGC NPs have been linked, via avidin-biotin interaction, with a IVS4 peptide, a small molecule with inhibitory activity on MMP-14 – mediated functions. An extensive study conducted on triple negative breast cancer cells in monolayer revealed the MMP-14 – IVS4-HGC association at the cancer cell membrane, the preferential uptake, and the consequent impairment of protease-associated migratory ability.

As an additional application of our engineered construct, HGC micelles have been decorated with liver kinase B1 (LKB1), a critical kinase involved in neuronal cell polarization, with the aim of regulating axon development. Our preliminary data indicated that, when treated with HGC-LKB1 NPs, primary rat embryo hippocampal neurons *in vitro* presented a multiple axon phenotype, validating the potential use of our multifunctional system as local protein delivery agent. In addition, we successfully performed for the first time *in utero* electroporation delivery of the chitosan nano-micelles, demonstrating the *in vivo* uptake potential of our system.

Dedication Page

Ho parlato in sogno con te, Afrodite

Saffo, *Frammenti*

To my parents, for their unconditional support and love.

Table of Contents

Chapter 1:

Design and characterization of chitosan-based nanotherapeutics	1
1.1 Nanomedicine in Cancer Therapy	1
1.2 The cancer microenvironment and its interaction with nanotherapeutics	2
1.3 Passive and Active Targeting	4
1.4 Mechanisms of cellular internalization	7
1.5 Model of Endosomal Escape	9
1.6 Tumor Microenvironment in Multi-Drug Resistant (MDR) Cancers	11
1.7 Role of pH in MDR Development	12
1.8 Polymeric micelles as drug delivery agents	13
1.9 Micellar formulations: advantages and strategies for improvement	16
1.10 Stimuli-responsive micelles:	
pH-induced mechanisms for nanocarrier destabilization	17
1.11 Polysaccharide-based micelles	19
1.12 Chitosan as a biomaterial for cancer therapy	20
1.13 pH-responsive amphiphilic chitosan derivatives.....	22
1.14 Chitosan-based micelles as probes to visualize the tumor microenvironment.....	26
1.15 Micelle characterization techniques	28
1.16 Micelle visualization techniques	30
1.17 Future perspectives	31

Chapter 2:

Hydrophobically modified glycol-chitosan micelles as drug delivery agents: application to a two-dimensional bone cancer model	33
2.1 Introduction	33
2.2 Methods	36
2.3 Results and Discussion	49
2.4 Conclusions and Future Perspectives.....	85

Chapter 3:

Multifunctional, chitosan-based micelles to target breast cancer cell invasiveness	87
3.1 Introduction	87
3.2 Methods	96
3.3 Results and Discussion	106
3.4 Conclusions and Future Perspectives.....	139

Chapter 4:

Hydrophobically modified glycol-chitosan micelles as drug delivery agents: application to a three-dimensional bone cancer model.....141

4.1 Introduction141

4.2 Methods146

4.3 Results and Discussion153

4.4 Conclusions180

Chapter 5:

Micellar nanocomplexes for local delivery of LKB1 to dictate axon development in a neuronal culture *in vitro*182

5.1 Introduction182

5.2 Methods188

5.3 Results and Discussion197

5.4 Conclusions220

Chapter 6:

Conclusions and Future Outlook.....222

References.....228

List of Figures/Tables/Illustrations

Figure 1.1 Tumor microenvironment: the complex architecture of the region surrounding the cancer mass is characterized by unique features, which can impair or determine the success of a drug delivery vehicle. (Canvas Draw 1.0.1)

Figure 1.2 Passive and active targeting at the tumor microenvironment: the leaky and highly disorganized endothelium structure of the tumor microenvironment favors the nanoparticles accumulation in the tumor tissue (the so-called “enhanced permeability and retention effect”). The targeting efficiency can be improved by designing engineered multifunctional nanotherapeutics, able to actively recognize cancer cells. (Inkscape 0.48.42)

Figure 1.3 Endocytosis mechanisms and nanoparticle intracellular fate: nanotherapeutics can be internalized by cancer cells through multiple endocytic pathways, depending on the physicochemical and morphological features of the artificial carrier as well as on the cell type. Those pathways determine the intracellular fate of the internalized nanocarriers, which can be either degraded or released active in the cytosol. (Inkscape 0.48.4)

Figure 1.4 Hypothetical mechanisms of endosomal escape: in the proton-sponge model (a), cationic polymers presenting protonable functional groups are able to buffer the pH inside intracellular vesicles such as endosomes and lysosomes. The accumulation of H⁺ ions favors an influx of counterions that ultimately leads to osmotic swelling and vesicle membrane rupture. In the electrostatic destabilization model (b), the cationic polymer chains interact with the negatively charged endosomal membrane, causing the polymer to swell. The consequent endosomal rupture allows the delivery of the active agents into the cytosol. (Inkscape 0.48.4)

Figure 1.5 Micelle formation: in water-based environment, amphiphilic molecules are able to self-assemble in highly organized supramolecular structures, and act as reservoirs for anticancer compounds. The self-assembly process is energetically favored above a threshold concentration value, the so-called critical micelle concentration (CMC). (AutoCAD 2014)

Table 1.1 Examples of acid-labile chemical bonds and their degradation products.

Figure 1.6 Chemical structure of chitosan (Accelrys Draw 4)

Table 1.2 pH-responsive chitosan (CS) derivative micelles

Figure 2.1 Schematic depicting the synthesis steps involved in the formulation of the Cy5.5-labelled, hydrophobically modified glycol chitosan polymer, and subsequent self-assembly nanoparticle preparation by means of a probe-type sonicator. *Figure 2.1 Synthesis process of HGC conjugate*

Figure 2.2 Synthesis process and chemical structure of the HGC conjugate, and of its fluorescently labelled derivative.

Figure 2.3 Schematic depicting the doxorubicin complexation with the HGC polymer.

Figure 2.4 Schematic depicting the self-assembly process of amphiphilic polymeric chain: (a) building blocks of the system, (b) resulting polymer chain, and (c) micellar structure with the hydrophobic core containing the 5- β -cholanic acid pendants and the hydrophilic shell presenting the glycol residues.

Figure 2.5 TEM micrographs of HGC_(0.185) self-assembled complexes depicting ellipse-shaped nanoparticles with faceted contours. The average hydrodynamic diameter measured by DLS is 288.6 ± 21.8 nm and the average zeta potential is $+13.2 \pm 0.2$ mV. Scale bar 200 μ m.

Figure 2.6 IR spectra: overlay in the region 4000-2500 cm^{-1}

Figure 2.7 IR spectra: overlay in the region 2000-700 cm^{-1}

Table 2.1 IR frequencies of the representative functional groups expressed in cm^{-1}

Table 2.2 Area associated with the IR frequencies of the representative groups

Figure 2.8 Comparison of the zeta potential titration curve (zeta potential vs pH) for (a) the glycol chitosan, HGC_(0.0115) and HGC_(0.185) polymeric systems and the nanoparticulate systems: (b) HGC_(0.0115) polymer and nanoparticles, (c) HGC_(0.185) polymer and nanoparticles, (d) HGC_(0.0115) and HGC_(0.185) nanoparticles. Error bars represent s.e. of 9 measurements.

Figure 2.9 Glycol chitosan polymer suspension: zeta potential titration curve and derivation of the isoelectric point (pI) for the system.

Table 2.3 Physical properties of the chitosan-derivative polymers and nanoparticles

Table 2.4 Comparison between the Doxorubicin-polymer systems

Figure 2.10 TEM micrographs of self-assembled (a) Doxorubicin-HGC_(0.0115) and (b) Doxorubicin-HGC_(0.185) nanocomplexes. Scale bar 200 μ m.

Figure 2.11 Release kinetics of doxorubicin from Doxorubicin-HGC_(0.185) NPs in PBS (pH 7.4) and $\text{KH}_2\text{PO}_4 - \text{Na}_2\text{HPO}_4$ buffer (pH 5.5).

Figure 2.12 Effect of the administration time and NP concentration on the uptake of Cy5.5-HGC_(0.0115) NP into MG-63 cells: 500 $\mu\text{g}/\text{ml}$ (a-d) and 1000 $\mu\text{g}/\text{ml}$ (e-h) delivered for 15 minutes (a,e), 30 minutes (b,f), 1 hour (c, g) and 3 hours (d, h). Scale bar 50 μ m.

Figure 2.13 Effect of the administration time and NP concentration on the uptake of Cy5.5-HGC_(0.185) NP into MG-63 cells: 500 $\mu\text{g}/\text{ml}$ (a-d) and 1000 $\mu\text{g}/\text{ml}$ (e-h) delivered for 15 minutes (a,e), 30 minutes (b,f), 1 hour (c, g) and 3 hours (d, h). Scale bar 50 μ m.

Figure 2.14 Figure 2.12 Intracellular fate of the nanocomplexes: HGC_(0.0115) NPs (a-c) and HGC_(0.185) NPs (d-f) delivered for 1 hour at a concentration of 500 $\mu\text{g}/\text{ml}$: LysoTracker Green (a, d), Cy5.5-HGC micelles (b, e) and merge images (c, f). Scale bar 100 μ m.

Figure 2.15 Morphological analysis of MG-63 cells: actin staining (top panel), fibronectin staining (middle panel) and merged channel (lower panel). Control, serum starved cells (a,d, g), cells treated with 500 $\mu\text{g}/\text{ml}$ (b, e, h) and 1000 $\mu\text{g}/\text{ml}$ (c, f, i) of HGC_(0.185) NPs for 3 hours. The elongated spindle-like shape is clearly identifiable in the isolated cells. Thin cell membrane protrusion (filopodia) are visible (white arrows), especially in the serum starved-cells. No significant disruption of the actin architecture is visible after the NP treatment. Scale bar 100 μ m.

Figure 2.16 Displacement from the origin of MG-63 cells treated with HGC_(0.185) NPs at various time and concentration NPs (a-g), and their corresponding average cell speeds (h). A Student's *t*-test was conducted considering a *p* value < 0.01 (**), comparing each treatment condition with the untreated control sample.

Figure 2.17 Fluorescent microscope images of MG-63 cells treated with free doxorubicin at concentrations of 1 μ M, 3 μ M and 10 μ M, for different delivery time. The grey scale images show the doxorubicin channel (observed under the PI filter), while in the colored images the overlay of actin fiber (FITC), nuclei (DAPI) and doxorubicin (PI) is reported. Scale bar 100 μ m.

Figure 2.18 Confocal micrographs of MG-63 cells treated for 1 hour (1-c) and 24 hours (d-f) with free doxorubicin at concentrations of 1 μ M (a,d), 3 μ M (b,e) and 10 μ M (c, f). Scale bar 75 μ m.

Figure 2.19 Confocal micrographs of MG-63 cells treated for 24 hours (a-c), 48 hours (d-f) and 72 hours (g-i) with doxorubicin-HGC_(0.185) NPs at concentrations of 24.3 μ g/ml (left panel, a-d-g), 81.1 μ g/ml (middle panel, b-e-h) and 243.4 μ g/ml (right panel, c-f-i). Scale bar 75 μ m, and 50 μ m for image (e).

Figure 2.20 Confocal micrographs of MG-63 cells treated for 24 hours with Doxo-HGC_(0.185) NPs at concentrations of 24.3 μ g/ml (a-c), 81.1 μ g/ml (d-f). Doxorubicin is visualized under the TRITC channel (red), while the lysosomal vesicles are stained in green. The right panel depicts the overlays. Scale bar 75 μ m.

Figure 2.21 Cell viability of MG-63 cell monolayers treated with HGC_(0.185) NPs at different concentrations, up to 72 hours. The results presented are the average of three independent experiments and a Student's *t*-test was performed considering *p* < 0.05 (*). Data comparison and statistics were conducted between each HGC_(0.185) nanoparticle concentration and the corresponding control, serum starved sample at the same time point.

Figure 2.22 Cell viability of MG-63 cell monolayers treated up to 72 hours with free doxorubicin at different concentration, up to 72 hours. Data represent the average of three independent experiments and a Student's *t*-test was performed considering *p* < 0.05 (*). Data comparison and statistics were conducted between each free drug concentration and the corresponding control, serum starved sample at the same time point.

Figure 2.23 Viability of MG-63 cell monolayer treated up to 72 hours with doxorubicin-HGC_(0.185) NPs at different concentrations, up to 72 hours. The results presented are the average of three independent experiments and a Student's *t*-test was performed considering *p* < 0.05 (*). Data comparison and statistics were conducted between each doxorubicin-HGC_(0.185) concentration and the corresponding control, serum starved sample at the same time point.

Figure 2.24 Comparison of the viability of MG-63 cell monolayer treated for 24 hours (a), 48 hours (b) and 72 hours (c) with either free doxorubicin (solid markers) or empty HGC_(0.185) nano-vehicles (hollow markers).

Figure 2.25 Comparison of the viability of MG-63 cell monolayer treated for 24 hours (a), 48 hours (b) and 72 hours (c) with either empty HGC_(0.185) nano-vehicles (hollow markers) or doxorubicin-loaded HGC_(0.185) nanocomplexes (solid markers).

Figure 2.26 Comparison of the viability of MG-63 cell monolayer treated for 24 hours (a), 48 hours (b) and 72 hours (c) with either free doxorubicin (solid markers), empty HGC_(0.185) nanovehicles (hollow markers), or doxorubicin-loaded HGC_(0.185) nanocomplexes (bi-color markers).

Figure 3.1 Schematic of the cell-matrix interaction: (a) a cell surrounded by ECM; (b) cell signaling at invadopodia, with MMP-14 associated ECM degradation and cell migration processes; (c) basal lamina and ECM components.

Figure 3.2 General structures of matrix metalloproteinases' subgroups: (a) minimal domain of MMP-7, -26; single-hemopexin (PEX) domain of MMP-1, -2, -8, -9, -13, -3, -10, -11, -12, -19, -20, -22, -28; (c) transmembrane MMP-14, -15; (d) glycoposphatidylinositol GPI-anchored MMP-17, -25; (e) Cys/Pro-Rich/IgG-like MMP-23. In panel (f) the homodimerization of MMP-14 allows the activation of the signaling cascade which leads to cell migration, invasion of the ECM and metastasis formation. The binding of the IVS4 peptide at the PEX domain interferes with the homodimerization process, preventing MMP-14 associated cellular functions.

Figure 3.3 Hypothetical mechanism of uptake, internalization, and action of the IVS4-decorated HGC nanomicelles, interacting with a cancer cell expressing MMP-14 at its surface. (1) Micelle interaction with the MMP14, *via* PEX domain, over-expressed at the membrane of invasive cancer cells; (2) internalization process and trafficking, involving association with endosomes and intracellular vesicles; (3) endosome escape and cytotoxic drug release in the cytosol, which can lead to effective cell death (4).

Figure 3.4 Flow diagram depicting the plating, treatment and post processing of the internalization mechanism experiment. MDA-MB-231 cells were treated with 2.5 $\mu\text{g/ml}$ of Cy3-HGC-IVS4 NPs and with the primary antibody for MMP-14. The first incubation was carried out at 4 $^{\circ}\text{C}$, to slow down the internalization process and endocytic recycling.

Figure 3.5 Cell migration assay: 2D collagen dots are plated in 96 well plates and treated with various concentration of nanoparticles (NPs) for 8 hours. Samples are fixed in 8% formaldehyde containing 2.5 $\mu\text{g/ml}$ of DAPI, to highlight the cell nuclei. Fluorescence image acquisition of zoomed area allows the identification of the cells migrating and escaping from the bulk mass. Cell counting is performed via ImageJ software, with a ITCN plugin.

Figure 3.6 Synthesis of peptide decorated-HGC: (1) glycol chitosan is biotinylated in water with sulfo-NHS-LC-biotin to form BGC; (2) the first biotin-avidin bond is allowed to form in water, by mixing for 2 hours the dialyzed and lyophilized BCG product with avidin; (3) the resulting material is hydrophobically modified *via* reaction with 5- β -cholanic acid in methanol, in the presence of NHS and EDC as catalyzers; (4) the biotinylated peptide is added, together with the fluorophore, to complete the functionalization of the system.

Table 3.1 Average diameter and average surface charge measurements of nanomicelles

Figure 3.7 TEM micrographies of HGC micelles (a,b), HGC-IVS4 micelles (c, d) and HGC-control peptide micelles (e,f).

Figure 3.8 Confocal images of MCF-10A cells (a, b, c, g, h, i) and MDA-MB-231 cells (d, e, f, l, m, n) treated for either 8 hours (a-f) or 24 hours (g-n) with 2.5 $\mu\text{g}/\text{ml}$ of Cy3-HGC NPs (a, d, g, l), Cy3-HGC-control peptide NPs (b, e, h, m) and Cy3-HGC-IVS4 NPs (c, f, i, n). Images are representative of 3 independent uptake experiment. Scale bar 30 μm .

Figure 3.9 Confocal images of COS-pQ cells (a, b, c, g, h, i) and COS-MMP14 cells (d, e, f, l, m, n) treated for either 8 hours (a-f) or 24 hours (g-n) with 1 $\mu\text{g}/\text{ml}$ of Cy3-HGC NPs (a, d, g, l), Cy3-HGC-control peptide NPs (b, e, h, m) and Cy3-HGC-IVS4 NPs (c, f, i, n). Images are representative of 3 independent uptake experiment. Scale bar 30 μm .

Figure 3.10 Cell viability of MDA-MB-231 cells treated with different nanoparticles (NPs) continuously for up to 3 days. Error bars represent s.e. of 3 independent experiments. Student's *t*-tests were performed between the treated samples and the control, untreated sample, at each time point, considering a *p* value < 0.01 (**).

Figure 3.11 Cell viability of MCF-10A cells treated with different nanoparticles (NPs) continuously for up to 3 days. Error bars represent s.e. of 3 independent experiments. Student's *t*-tests were performed between the treated samples and the control, untreated sample, at each time point, considering a *p* value < 0.05 (*).

Figure 3.12 Cell viability of COS-MMP14 cells treated with different nanoparticles (NPs) continuously for up to 3 days. Error bars represent s.e. of 3 independent experiments. Student's *t*-tests were performed between the treated samples and the control, untreated sample, at each time point, considering a *p* value < 0.01 (**).

Figure 3.13 Cell viability of COS-pQ cells treated with different nanoparticles (NPs) continuously for up to 3 days. Error bars represent s.e. of 3 independent experiments. Student's *t*-tests were performed between the treated samples and the control, untreated sample, at each time point, considering a *p* value < 0.01 (**).

Figure 3.14 Cell viability of cells treated with HGC-Biotin nanoparticles (NPs) continuously for up to 3 days. Error bars represent s.e. of 3 independent experiments. Student's *t*-tests were performed between the treated samples and the control, untreated sample, at each time point, considering a *p* value < 0.01 (**).

Figure 3.15 Propidium iodide staining (red channel) and DAPI staining (blue channel) of COS-pQ cells untreated (a) or treated with 10 $\mu\text{g}/\text{ml}$ (b) or 50 $\mu\text{g}/\text{ml}$ (c) of HGC-Biotin NPs. (d) represent the control sample treated with staurosporine.

Figure 3.16 2D dot migration assay. Upper panel: fluorescence microscope representative images depicting MDA-MB-231 cells untreated (a) or treated with 0.1 $\mu\text{g}/\text{ml}$ of HGC-control peptide (b) or with 0.1 $\mu\text{g}/\text{ml}$ of HGC-IVS4 (c). COS-MMP14 cells were either untreated (d) or treated with 2.5 $\mu\text{g}/\text{ml}$ of HGC-control peptide (e) or with 2.5 $\mu\text{g}/\text{ml}$ of HGC-IVS4 (f). The fold changes in cell migration are reported for both cell lines (g, h). Student's *t*-tests between samples treated with control NPs and with IVS4-NPs were performed, considering *p* values < 0.05 (*) or *p* < 0.01 (**).

Figure 3.17 Super resolution microscope imaging of MDA-MB-231 cells stained for MMP-14 and treated with Cy3-HGC-IVS4 NPs for different time points (0, 2, 5, 10 and 30 minutes). The

green channel shows the MMP14 membrane or intracellular distribution, the red channel depicts the peptide-decorate NPs, while the blue channel shows the cell nuclei. Scale bar 5 μm .

Figure 3.18 Super resolution microscope imaging of MDA-MB-231 cells stained for MMP-14 and treated with Cy3-HGC-IVS4 NPs 30 minutes. The various focus planes allow the visualization of the different intracellular distribution of the matrix metalloproteinase with respect of the peptide-decorate NPs. Separate channels showing MMP14 staining (green), nuclear staining (blue) and Cy3-HGC-IVS4 NPs (red) are presented. Scale bar 5 μm .

Figure 3.18 Super resolution microscope imaging of MDA-MB-231 cells stained for MMP-14 and treated with Cy3-HGC-IVS4 NPs for 30 minutes. The 3D volume reconstruction allows the visualization of the co-localized signals pertaining to the MMP14 (green) and the Cy3-HGC-IVS4 NPs (red).

Figure 3.20 Super resolution microscope imaging of MDA-MB-231 cells stained for early endosome (EEA1 antibody, green channel) and treated with Cy3-HGC-IVS4 NPs (red channel) different time points. The blue channel depicts the cell nuclei. Scale bar 5 μm .

Figure 3.21 Super resolution microscope imaging of MDA-MB-231 cells stained for early endosome (EEA1 antibody, green channel) and treated with Cy3-HGC-IVS4 NPs (red channel) for 8 hours. The blue channel depicts the cell nuclei. The 3D volume reconstruction allows the visualization of the Cy3-HGC-IVS4 NPs enveloped in the endosomal vesicles (white arrows).

Figure 3.22 Super resolution microscope imaging of MDA-MB-231 cells stained for lysosomes (LAMP1, green channel) treated with Cy3-HGC-IVS4 NPs for different time points. The blue channel depicts the cell nuclei. Scale bar 5 μm .

Figure 3.23 Super resolution microscope imaging of MDA-MB-231 cells stained for lysosomes (LAMP1, green channel) and treated with Cy3-HGC-IVS4 NPs 18 hours. The images acquired at different planes of focus allows the visualization of the vesicle intracellular distribution, with respect of the up-taken nanoparticles. The blue channel depicts the cell nuclei. Scale bar 5 μm .

Figure 3.24 Super resolution microscope imaging of MDA-MB-231 cells stained for lysosomes (LAMP1, green channel) and treated with Cy3-HGC-IVS4 NPs 24 hours. The images acquired at different planes of focus allows the visualization of the vesicle intracellular distribution, with respect of the up-taken nanoparticles. The blue channel depicts the cell nuclei. Scale bar 5 μm .

Figure 3.25 Super resolution microscope imaging of MDA-MB-231 cells stained for a Golgi membrane protein (anti-giantin, green channel) treated with Cy3-HGC-IVS4 NPs for different time points. The blue channel depicts the cell nuclei. Scale bar 5 μm .

Figure 3.26 Super resolution microscope image of MDA-MB0231 cell stained for a Golgi membrane protein (anti-giantin, green channel) treated with Cy3-HGC-IVS4 NPs for 18 hours (red channel). The blue channel depicts the cell nuclei. Scale bar 5 μm .

Figure 3.27 Super resolution microscope image of MDA-MB0231 cell stained for a Golgi membrane protein (anti-giantin, green channel) treated with Cy3-HGC-IVS4 NPs for 24 hours (red channel). The blue channel depicts the cell nuclei. Scale bar 5 μm .

Figure 3.28 Super resolution microscope imaging of MDA-MB-231 cells stained for a Golgi membrane protein (anti-giantin, green channel) and treated with Cy3-HGC-IVS4 NPs (red channel) for 24 hours. The blue channel depicts the cell nuclei. The 3D volume reconstruction allows the visualization of the Cy3-HGC-IVS4 NPs in the close proximity of the Golgi walls.

Figure 3.29 Cell viability of MDA-MB-231 cells treated with free Ansamitocin P-3 and with empty and drug-loaded NPs continuously for up to 9 days. Error bars represent s.e. of 3 independent experiments. Student's *t*-tests were performed between the treated samples and the control, untreated sample, at each time point, considering *p* values < 0.05 (*) or < 0.01 (**).

Figure 3.30 Cell viability of MCF-10A cells treated with free Ansamitocin P-3 and with empty and drug-loaded NPs continuously for up to 9 days. Error bars represent s.e. of 3 independent experiments. Student's *t*-tests were performed between the treated samples and the control, untreated sample, at each time point, considering *p* values < 0.05 (*) or < 0.01 (**).

Figure 4.1 Schematic depicting the plating liquid overlay plating protocol for the fabrication of 3D tumor spheroids.

Figure 4.2 Schematic depicting the processing protocol (fixing, staining and mounting) for the imaging sample preparation of 3D tumor spheroids.

Figure 4.3 3D Spheroids of MG-63 cells plated at different starting cell densities: (a) average spheroid volumes over culture time, (b) change in spheroid volume over culture time, (c) phase contrast images of spheroids at day 3 (upper panel) and day 9 (lower panel) of culture. The dotted lines defined the cells not included in the bulk mass (“*sunny-side-up*” configuration). Scale bar 500 μm .

Figure 4.4 Live-dead staining of MG-63 spheroids plated at 25000 cells/well (top row) and at 50000 cells/well (bottom row). The fluorescein molecules (FDA, green channel) stain for the live population of cells, while the propidium iodide (PI, red channel) highlights the necrotic core. Scale bar 500 μm .

Figure 4.5 Live-dead staining of MG-63 spheroids plated at 25000 cells/well (top row) and at 50000 cells/well (bottom row) and incubated for different time points. The fluorescein molecules (FDA, green channel) stain for the live population of cells, while the propidium iodide (PI, red channel) highlights the evolution of the necrotic core. Scale bar 500 μm .

Figure 4.6 Average volume of MG-63 3D spheroids and of the corresponding necrotic cores, with respect to the culture conditions. Error bars represent s.e. of 12 spheroids (a). Ratio between the volume of the necrotic core and the volume of the spheroids, with respect to the culture conditions (b).

Figure 4.7 Confocal micrographs of mature MG-63 spheroids stained with Alexa Fluor 488 phalloidin to highlight the actin structure. The three-dimensional arrangement of the cytoskeleton and the compact network of cancer cells is visible from the high magnification images (63X). Scale bar 50 μm .

Figure 4.8 Normalized spheroid volume versus treatment time for spheroids treated with (a) free doxorubicin, (b) HGC_(0.185) NPs and (c) doxorubicin-loaded HGC_(0.815) NPs

Figure 4.9 Average spheroid volume versus treatment concentration for spheroids treated with (a) free doxorubicin, (b) HGC_(0.185) NPs and (c) doxorubicin-loaded HGC_(0.185) NPs. The double x axis in (c) allows the comparison between the concentration of the free drug and the nanoparticles.

Figure 4.10 Confocal micrographs of MG-63 3D spheroids treated with free doxorubicin at concentrations of 10 μ M (a-e), 30 μ M (d-l), 100 μ M (m-q) for different time points. Images were acquired with a 10X dry lens, at a scan speed of 10Hz and with a resolution of 1024x1024 pixels. Scale bar 100 μ m.

Figure 4.11 Confocal micrographs of MG-63 3D spheroids treated with Cy5.5-HGC_(0.185) NPs at concentrations of 75.3 μ g/ml (a-e), 226 μ g/ml (d-l), 753 μ g/ml (m-q) for different time points. White arrows highlight the presence of voids in the spheroid structure, a possible result of air bubble entrapment during plating. Images were acquired with a 10X dry lens, at a scan speed of 10Hz and with a resolution of 1024x1024 pixels. Scale bar 75 μ m for e, i, o, q and 100 μ m for the other spheroids.

Figure 4.12 High magnification (63X) confocal micrographs of MG-63 spheroids treated with Cy5.5-HGC_(0.185) NPs at a concentration of 226 μ g/ml for 1 hour (a-c) and at a concentration of 753 μ g/ml for 1 hour (d-f) or 24 hours (g-i), The high magnification allows the visualization of clusters of NPs within the 3D cancer cell network. Scale bar 25 μ m for a-f and 10 μ m for g, h, i.

Figure 4.13 Confocal micrographs of MG-63 3D spheroids treated with doxorubicin-loaded HGC_(0.185) NPs at concentrations of 81.1 μ g/ml (a-e), 234 μ g/ml (d-l), 811 μ g/ml (m-q) for different time points. Images were acquired with a 10X dry lens, at a scan speed of 10Hz and with a resolution of 1024x1024 pixels. Scale bar 100 μ m.

Figure 4.14 Penetration analysis protocol: intensity profiles

Figure 4.15 Penetration analysis protocol: data processing

Figure 4.16 Penetration profile analysis of free doxorubicin in MG-63 3D spheroids treated for different time points. The plots were obtained from the mid cross section of the spheroids: four plot profiles, separated of 45 degrees, were drawn and analyzed in ImageJ. The average fluorescent signal was then calculated.

Figure 4.17 Comparison of the penetration profiles of free doxorubicin delivered to MG-63 3D spheroids at different concentrations. The plots were obtained from the mid cross section of the spheroids: four plot profiles, separated of 45 degrees, were drawn and analyzed in ImageJ. The average fluorescent signal was then calculated.

Figure 4.18 Penetration profile analysis of Cy5.5-HGC_(0.185) NPs in MG-63 3D spheroids treated for different time points. The plots were obtained from the mid cross section of the spheroids: four plot profiles, separated of 45 degrees, were drawn and analyzed in ImageJ. The average fluorescent signal was then calculated.

Figure 4.19 Comparison of the penetration profiles of Cy5.5-HGC(0.185) NPs delivered to MG-63 3D spheroids at different concentrations. The plots were obtained from the mid cross section of the spheroids: four plot profiles, separated of 45 degrees, were drawn and analyzed in ImageJ. The average fluorescent signal was then calculated.

Table 4.1 Penetration profile parameters for the free doxorubicin treated spheroids

Figure 5.1 Model for local LKB1 activity in undifferentiated neurite of cultured hippocampal neurons: localized activation of LKB1, mediated by its interaction with co-factor STRAD, initiates axon development *via* local SAD and Tau phosphorylation. The resulting microtubule polymerization directs axon formation at the tip of the neurite.

Figure 5.2 Fabrication process of the SPIONs-loaded Cy5.5-HGC-B4F micellar complexes

Figure 5.3 Schematic depicting the *in utero* electroporation procedure. First, the uterus of the pregnant rat mother is exposed by laparotomy. Subsequently, the injection into the lateral ventricles of plasmid DNA and chitosan nanocomplexes is carried out by means of a sharp tip. Electroporation (30-50 V) is performed with two electrodes, to temporarily disrupt the cell membrane and favor the passage of the macromolecules through the pores. The embryos are placed back in the abdominal cavity.

Figure 5.4 Synthesis of HGC-LKB1: (1) glycol chitosan is biotinylated in water with sulfo-NHS-LC-biotin to form BGC; (2) the first biotin-avidin bond is allowed to form in water, by mixing for 2 hours the dialyzed and lyophilized BCG product with avidin; (3) the resulting material is hydrophobically modified *via* reaction with 5- β -cholanic acid in methanol, in the presence of NHS and EDC as catalyzers; (4) a water-based solution of biotinylated-LKB1 is added drop-wise to the avidinate-biotinylated HGC suspension and let stir for 2 hours, to assist the formation of the second biotin-avidin bond. The final product is collected after centrifugation. The inset reports a representative DLS measurement and a TEM micrography.

Figure 5.5 Immunoblotting of several molecules of interest, involved in the signaling cascade for axon development. HeLa cells, not expressing endogenous LKB1, have been transfected with different combinations of cDNA for LKB1, STRAD (LKB1 co-factor) and SAD-A and Tau (LKB1 downstream effectors). Consequently, the lysates of the different cell samples have been treated for 2 hours with either plain chitosan nanoparticles or with LKB1-chitosan nanocomplexes. Only HeLa cells transfected with cDNAs for Tau/SAD-A/STRAD and treated with LKB1-chitosan nanocomplexes have shown the presence of phosphorylated Tau at the Ser262 site (red lane), indicating the preserved functionality of the polymer-linked kinase. β -actin represents a control for the lysate volume.

Figure 5.6 Confocal micrographs overlays of Cy5.5 and DIC channels depicting primary E19 rat hippocampal neurons treated with Cy5.5-HGC nanoparticles for different time points. The overlay facilitates the visualization of the nanoparticle intracellular distribution. White circles highlight Cy5.5-HGC NPs internalized at the tip of growing processes at shorter time points, while black arrows are indicating nanocomplexes up-taken within the neurite length at longer time points. Scale bars 30 μ m.

Figure 5.7 Confocal micrographs depicting primary E19 rat hippocampal neurons treated with DAPI-glucuronic acid coated SPIONs for different time points: 18 hours (a); 24 hours (b); 48 hours (c). Arrows are indicating the prevalent accumulation of the MNPs into the cell soma of the neurons. Zoomed image in (d) allows the resolution of the NP clusters within the cell soma. Scale bar 30 μm .

Figure 5.8 Confocal microscopy images of primary hippocampal neurons (E19) treated for 30 hours with SPIONs-loaded-Cy5.5-HGC-B4F nanocomplexes. In the upper panel (a, b, c and d), the separate channels used for the acquisition are shown. In the lower panel (e, f, g), a sequence of images with merged channels are presented. The intracellular distribution of the nanocomplexes at the tip of growing processes is highlighted (white arrows). Scale bar 10 μm .

Figure 5.9 Confocal microscopy images of primary hippocampal neurons (E19) treated for 30 hours with SPIONs-loaded-Cy5.5-HGC-B4F nanocomplexes. In the upper panel (a, b, c and d), the separate channels used for the acquisition are shown. In the middle panel (e, f, g), the overlays of the separate fluorescence channels with the DIC allow the visualization of the nanocomplexes distribution within the cells. The bottom panel (h, I, l) presents different combinations of fluorescence channel overlays, to highlight the co-localization of the nanocomplexes' components. Scale bars 10 μm .

Table 5.1 Morphological parameters obtained via neuronal cell tracing for the Cy5.5-HGC NP treated samples and their respective controls.

Table 5.2 Morphological parameters obtained via neuronal cell tracing for the SPIONs-loaded-Cy5.5-HGC-B4F NP treated samples and their respective controls.

Figure 5.10 Composite tracing of neurites from a random sampling of 10 neurons from each treatment to demonstrate variance in neurite length and number. Scale bar 30 μm .

Figure 5.11 Bar graphs representing the variations of the neuronal morphological parameters for the Cy5.5-HGC NP treated samples (a), the SPIONs loaded-HGC-B4F NP treated samples (b). The average number of neuritic processes per cell is reported in (c). Error bars represent the s.e.. A Student's *t*-test between each treated sample and the corresponding control were performed, considering a *p* value < 0.01 (**).

Figure 5.12 Tracing of a representative pool of primary hippocampal neurons treated with Cy5.5-HGC NPs or with Cy5.5-HGC-LKB1 NPs. Axons were traced in red, while dendrites were traced in green. Blue arrows identify the multiple axon cells.

Figure 5.13 Confocal images of primary hippocampal neurons treated for 72 hours with Cy5.5-HGC NPs (a-c) or with Cy5.5-HGC-LKB1 NPs (e-g and i-m). The green channel depicts the Tuj staining (general neuronal marker) while the red channel shows the Smi-312 staining (specific for the axon). Overlaid images are reported in (c), (g) and (m) with scale bar of 50 μm . In (d), (h) and (n) the corresponding neuronal tracing are reported, showing in green the dendritic processes and in red the axons.

Figure 5.14 Confocal images of primary hippocampal neurons treated for 72 hours with Cy5.5-HGC-LKB1 NPs. The image is the overlay of green channel (Tuj), red channel (Smi) and magenta channel (Cy5.5) with a scale bar of 50 μm . The inserts are reporting the overlay and the separate

channels of the cropped soma of the multiple axon neurons, to better visualize the localization of the HGC-LKB1 NPs within them.

Figure 5.15 (a, b) Confocal microscopy overlay tiling of a E18 rat embryo brain slice, depicting left and right ventricles and cortical plate (scale bar 250 μm). (c) depicts the Cy5.5 signal pertaining to the chitosan nanomicelles, injected *via in utero* electroporation at E16.5. The inserts (d-f) show neurons migrating towards the cortical plate, presenting Cy5.5-chitosan nanomicelles internalized in the cell cytoplasm.

Figure 5.16 (a) Confocal microscopy tiling of a E18 rat embryo brain slice, depicting the ventricle, where the Cy5.5-chitosan micelles have been injected at E16.5 *via in utero* electroporation. Inserts (b) and (c) highlights the presence of some nanocomplexes in the blood vessels of the brain (yellow arrows), while insert (d) show the presence of Cy5.5-chitosan nanocomplexes internalized by neurons migrating toward the cortical plate.

Figure 5.17 Confocal images of E18 cortical progenitors injected *in utero* at E16.5 with Cy5.5-HGC nanomicelles at a concentration of 0.025 mg/ml (c). The blue signal in (a) represents the counterstain with DAPI. In (b) and (c) inserts radially migrating neurons are visualized.

List of Abbreviations

ECM – extracellular matrix
MDR – multi drug resistance
RGD – arginine-glycine-aspartic peptide
DNA –deoxyribonucleic acid
RNA – ribonucleic acid
ATP – adenosine triphosphate
GTPase – guanosine triphosphate hydrolase
EPR – enhanced permeability and retention
IFP – interstitial fluid pressure
EGFR – epidermal growth factor receptor
PEX – hemopexin domain
MMP-14 – matrix metalloproteinase-14
MMP-2 – matrix metalloproteinase-2
CME – clathrin-mediated endocytosis
PEI – poly(ethyleneimine)
PCL – poly- ϵ -caprolactone
PLLA – poly-L-lactic acid
CMC – critical micelle concentration
MMPs – matrix metalloproteinases
CS – chitosan
CA – cholanic acid
DS – degree of substitution
GC – glycol chitosan
HGC – hydrophobically modified glycol chitosan
B-GC – biotinylated glycol chitosan
AB-GC – avidinated, biotinylated glycol chitosan
EDC – 1-Ethyl-3-[3-dimethylaminopropyl]carbodiimide hydrochloride
NHS – N-hydroxysuccinimide ester
DMSO – dimethyl sulfoxide
TEA – triethylamine
ATP – adenosine triphosphate
HABA – 4'-hydroxyazobenzene-2-carboxylic acid
PBS – phosphate buffer saline
DMEM – Dulbecco's Modified Eagle Medium
FBS – fetal bovine serum
P/S – pen/strep
BSA – bovine serum albumin
MTS – [3-(4,5-dimethylthiazol-2-yl)-5-(3-carboxymethoxyphenyl)- 2-(4-sulfophenyl)-2H-tetrazolium salt
DAPI – 4'-6-diamino-2-phenylimidazole
TRITC – tetramethylrhodamine dye
FITC – fluorescein isothiocyanate
PI – propidium iodide
FDA – fluorescein diacetate

Cy3 – cyanine 3
Cy5.5 – cyanine 5.5
DIC – differential interference contrast
HCl – hydrochloric acid
NaOH – sodium hydroxide
MWCO – molecular weight cut off
MRI – magnetic resonance imaging
CT – computed tomography
SPECT– single-photon emission computed tomography
PET – positron electron tomography
NIRF – near infra-red
IR – infrared
DLS – dynamic light scattering
TEM – transmission electron microscopy
SEM– scanning electron microscopy
SPIONs – super paramagnetic iron oxide nanoparticles
MNPs – magnetic nanoparticles
pKa – logarithm of the acid dissociation constant
pI – isoelectric point
B4F – biotinylated fluorescein
LKB1 – ser/thr protein kinase Liver Kinase B1
SAD-A / SAD-B – Synapses of the Smid Defective
STRAD- α - Ste20-related adapter pseudokinase
Tau – microtubule stabilizing protein
Tuj-1 – neuron-specific class II β -tubulin
Smi-321– anti-neurofilament antibody
MO25 α – mouse protein 25
PMSE – Polyhydramnios Megalencephaly and Symptomatic Epilepsy
MA – multiple axon
VZ – ventricular zone
SVZ – subventricular zone
IV – intermediate zone
CP – cortical plate
E16.5, E18, E19 – days of the embryonic stage
TICs – tumor initiating cells
CAM – chorioallantoic membrane

Acknowledgments

I would like to thank Prof. Yizhi Meng, for accepting me in her lab, and for giving me her support and precious guidance, both scientifically and personally, during those years of my doctoral studies. The development of my research work was also possible thanks to the presence of my lab mates, Dr. Kate Dorst, Weiyi Li and Derek Rammelkamp, with whom I had stimulating scientific discussions and with whom I worked closely in the past years.

I would like to thank Prof. Maya Shelly, from the Department of Neurobiology and Behavior at Stony Brook, for her guidance both in the laboratory work and in the data analysis, and for her precious assistance during the completion of the neurobiology project presented in this thesis work. Moreover, I am deeply thankful to Prof. Shelly's group, Dr. Seong-il Lee, Dr. Tanvir Kahn and Sneha Rao, for their continuous support and for patiently teaching me their expertise in neuronal culture over those years.

My sincere thanks to Prof. Jian Cao, from the Department of Medicine at Stony Brook, for his valuable guidance and relevant advice in the development of the breast cancer project presented in this thesis work. In addition, I would like to thank Jillian Cathcart, from the Department of Pharmacological Sciences, for working hands-on with me in the project, for our interesting scientific discussions and for teaching me new laboratory techniques.

I would like to thank Dr. Mircea Cotlet and Dr. Dmytro Nykypanchuk, from the Soft and Bio Nanomaterials group of the Center for Functional Nanomaterials at Brookhaven National Laboratory (supported by the U.S. Department of Energy, Office of Basic Energy Sciences, under Contract No. DE-SC0012704), for training me on several nanoparticle characterization techniques and microscopy techniques.

Moreover, I would like to thank Shelagh Zegers, from the Department of Marine Science at Stony Brook, for her precious help with the lyophilization of the synthesized compounds, and Dr. Michele Caruso, from the Medicinal Chemistry Department at Nerviano Medical Sciences (Milano, Italy), for the kind donation of the Doxorubicin used in this thesis work.

Lastly, I would like to thank Gustavo Monteiro for our interesting discussions about the nanoparticle penetration profile into the 3D spheroids tumor models.

Publications

Peer Reviewed Journal Publications and Book Chapter

J. Cathcart, **G. Suarato**, W. Li, Y. Meng, J. Cao; Tumor-homing peptide to target cancer cell invasiveness (in preparation)

G. Suarato, Y. Meng, M. Shelly; Micellar nanocomplexes for biomagnetic delivery of intracellular proteins to dictate axon formation during neuronal development (under review in *Biomaterials*)

G. Suarato, W. Li, Y. Meng; The role of pH-responsiveness in the design of chitosan-based nanotherapeutics: a review, *Biointerphases*, 11, 04B201 (2016)

M. Shelly, S. Lee, **G. Suarato**, Y. Meng, S. Pautot; Photolithography-based substrate microfabrication for patterning semaphorin 3A to study neuronal development, *Methods in Molecular Biology*, Humana Press (in press)

A. Chin, **G. Suarato**, Y. Meng; Evaluation of physico-chemical characteristics of hydrophobically modified glycol chitosan nanoparticles and their biocompatibility in murine osteosarcoma and osteoblast-like cells, *Journal of Nanotechnology and Smart Materials*, 1 (2014)

Conference Presentations

G. Suarato, J. Cathcart, W. Li, J. Cao, Y. Meng, Targeting cancer cell invasiveness using homing peptide-nanocomplexes (oral presentation), American Physical Society Meeting, 14 – 18 March 2016, Baltimore, Maryland, USA

G. Suarato, A. Chin, Y. Meng, Hydrophobically modified glycol chitosan nanoparticles: enzymatic stability, pH responsiveness, biocompatibility and uptake (oral presentation), Biomedical Engineering Society Meeting, 22 – 25 October 2014, San Antonio, Texas, USA

G. Suarato, Y. Meng, Effect of the hydrophobic modification on the physico-chemical properties of self-assembled glycol chitosan nanoparticles for tumor-specific drug delivery (poster), Materials Research Society Meeting, 21 – 25 April 2014, San Francisco, California, USA

G. Suarato, A. Chin, Y. Meng, NIR fluorescent chitosan-based nanoparticles for tracking and delivery of cancer therapeutic molecules in living systems (poster), American Physical Society Meeting, 18 – 22 March 2013, Baltimore, Maryland, USA

G. Suarato, A.K. Bherwani, C.C. Chang, A. Akhavan, M. Simon, M. Rafailovich, Role of surface chemistry and morphology in dental pulp stem cell differentiation (poster, SciMix selection), American Chemical Society, 25 – 29 March 2012, San Diego, California, USA

G. Suarato, A.K. Bherwani, C.C. Chang, M. Rafailovich, M. Simon, Dental pulp stem cell differentiation on poly-4-vinyl-pyridine surfaces (oral presentation), American Physical Society Meeting, 27 February – 2 March 2012, Boston, Massachusetts, USA

A.K. Bherwani, **G. Suarato**, S. Qin, C.C. Chang, A. Akhavan, J. Spiegel, V. Jurukovski, M. Rafailovich, M. Simon, Spontaneous differentiation of dental pulp stem cells on dental polymers (oral presentation), American Physical Society Meeting, 27 February – 2 March 2012, Boston, Massachusetts, USA

G. Suarato, S. Qin, C.C. Chang, A. Akhavan, J. Spiegel, V. Jurukovski, M. Rafailovich, M. Simon, Induction of dental pulp stem cell differentiation by non-degradable polymers (poster), Materials Research Society Meeting, 27 November – 2 December 2011, Boston, Massachusetts, USA

Chapter 1:

Design and characterization of chitosan-based nanotherapeutics

1.1 Nanomedicine in cancer therapy

Excerpt reprinted with permission from Suarato *et al.*, *Biointerphases*, 11 (2016), AIP Publishing LLC, Copyright (2016)

Cancer is the abnormal, uncontrolled cell proliferation enabled by the interplay between genetic instabilities, mutations and environmental factors.¹ In the past decade, several hallmarks of cancer cells have been defined, such as resistance to cell death, evasion of growth suppression, and ability to induce angiogenesis and invade other tissues. More recently, analytical genome technologies have aided in the identification of such characteristics as the ability to reprogram cellular metabolism in order to supply the energy demand for cell growth, as well as the capability to elude the immune destruction pathways², all of which have helped to gain a deeper understanding of the factors involved in disease etiology and progression.

To date, cancer is the second leading cause of morbidity and mortality in the United States. The total estimated deaths from colon cancer, lung cancer and breast cancer in 2014 were reported to be 50,310, 159,260 and 40,430, respectively.³ While the incidence of the disease within the population appears to remain constant, the survival rate of patients has increased from 49% in the 1970s to 68% in the 2010s, which can be partly credited to advancements in cancer diagnostics and treatment. Although long-term survival of cancer patients has improved considerably, advanced stage malignancies still result in death within only five years of diagnosis.⁴ For many cancer patients, poor selectivity as well as limited safety and efficacy of conventional chemotherapeutic approaches are a widespread problem.⁵ In the past decade, along with chemotherapy, surgery and radiation therapy, advances made in the field of nanotechnology have overcome some of these limitations and have led to new strategies that contribute greatly to the overall increase in patient survival.

Chemotherapy treatment for cancer typically involves the simultaneous administration of several synthetic drugs. For example, doxorubicin, an antibiotics drug, has been used in combination with cyclophosphamide, an alkylating drug, in the treatment of breast cancer.⁶ Although effective in killing rapidly dividing cells and decreasing the risk of recurrence after

surgery, chemotherapy can lead to the insurgence of severe side effects. In fact, most of the chemotherapeutic agents are non-specific and are considerably toxic to normally dividing cells. In some cases, cardiotoxicity, kidney damage and immunosuppression can result, leading to therapy failure and death. Moreover, the phenomenon of multidrug resistance (MDR), whose mechanisms are not yet fully understood, may further limit the success of the chemotherapy treatment.⁷ One strategy to increase drug selectivity toward cancer cells and to overcome resistance is to deliver antitumor compounds using nanoparticulate carriers.⁸ This approach, which applies nanotechnological principles to the design of novel therapeutics, is a subset of the rapidly expanding scientific field known as nanomedicine.⁹⁻¹⁴ The Medical Standing Committee of the European Science Foundation first defined the term “nanomedicine” in 2004¹⁵ as a nanometer-sized system, consisting of at least one active component, able to interact with the biological environment at a cellular level and to perform diagnosis, treatment or prevention of a disease. The National Institutes of Health further built upon these concepts to emphasize, in particular, the understanding and control of new material properties at the atomic and molecular level.¹⁶ In addition to the design of smart targeted drug release systems, areas of focus under nanomedicine also include the development of new miniaturized diagnostics systems (i.e. lab-on-a-chip platforms, nanosensors, nanoparticles for imaging) and the improvement of new pharmaceutical formulations.^{13, 17}

When developing a nanotherapeutic, characteristics such as biodegradability, genotoxicity, cytotoxicity, multifunctionality and amphiphilicity need to be carefully considered. The possible challenges that a nanovehicle may encounter en route from the administration site to the pathological site, or from the tumor microenvironment to the intracellular domain, can critically affect the therapeutic efficiency of the cargo.

1.2 The cancer microenvironment and its interaction with nanotherapeutics

Excerpt reprinted with permission from Suarato *et al.*, *Biointerphases*, 11 (2016), AIP Publishing LLC, Copyright (2016)

The majority of solid tumors is constituted by an ensemble of distinct cell types and subtypes that contribute overall to tumor growth: cancer stem cells, invasive cancer cells, stromal cells, fibroblasts, endothelial cells, and tumor-promoting immune cells. The region surrounding the cancer mass is defined as “tumor microenvironment,” a complex network of extracellular

matrix molecules, stromal and endothelial cells, which evolves during tumor progression and actively supports its invasion and metastatic transformation.² It is through this intricate, heterogeneous architecture that a cancer nanotherapeutic has to navigate in order to successfully exploit its function.

The delivery of a nanotherapeutic agent from the site of injection to the site of action involves multiple kinetics steps: a) transport in the blood stream; b) extravasation from the tumor vasculature into the tumor interstitium; c) binding to the cell membrane; d) intracellular trafficking. Physiological factors such as tumor blood vasculature conditions, lymphatic drainage and tumor interstitial fluid pressure (IFP), as well as physicochemical and morphological features of the nanocarriers, collectively determine the success of the delivery device.⁸

Transport of the nanoparticles across the blood vessel walls is usually driven by two different modalities: diffusion and convection through capillary pores. While diffusion is based on the presence of concentration gradients, transport through capillary pores is a more complex phenomenon that involves pressure gradients across blood vessels and is strictly related to the morphological and structural features of the tumor vasculature. Discontinuity in the endothelium of tumor blood vessel due to junction gaps (100 nm to 700 nm in size) causes leakiness, which favors nanoparticle extravasation.¹⁸ On the other hand, the defective vasculature also elevates the IFP, hampering the overall fluid transport and, consequently, limiting drug nanocarrier circulation. In the tumor tissue, the architecture of the blood vessels is highly heterogeneous: small veins and venules are located in the interior part of the tumor mass, while few arteries are present in the periphery. As a result, blood flow is higher in the periphery and lower in the center. Moreover, regions with no vasculature or perfused by small capillaries are also present. All these heterogeneities lead to the formation of hypoxic and necrotic regions within the tumor mass, which ultimately affect the uniformity of the drug nanocarrier distribution. Another distinctive characteristic of the tumor microenvironment is the lack of a functional lymphatic drainage, which can lead to the reduction of nanoparticle clearance from the tumor site. At the same time, the IFP is increased as a result of stagnant blood fluid build-up, further limiting the overall transvascular transport.¹⁸

The tumor microenvironment (Figure 1.1) thus plays a paradoxical role in the success of a cancer nanotherapeutic. While nanoparticle extravasation from the blood vessels and retention at the tumor site is favored by the leaky vasculature and the impaired lymphatic system, the

heterogeneous vascularization and the presence of necrotic regions constitute multiple barriers to the transport within the solid tumor.

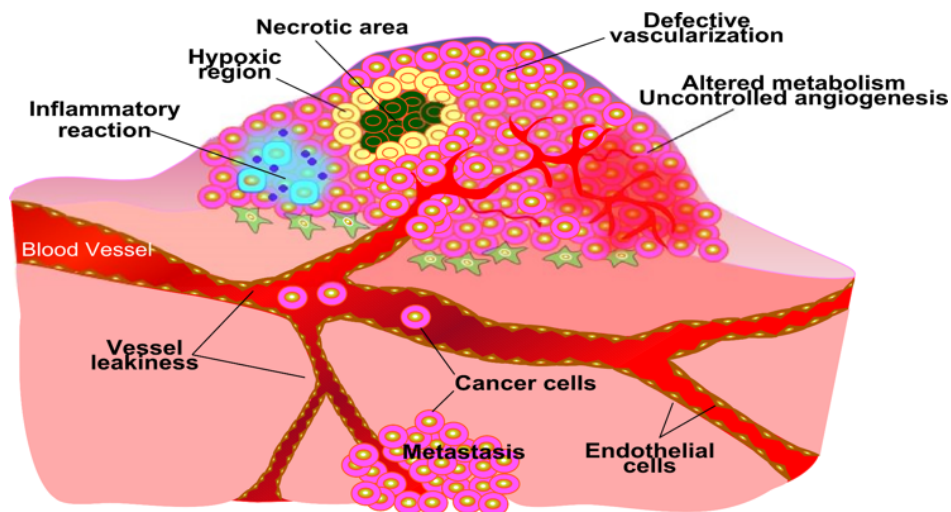


Figure 2.1 Tumor microenvironment: the complex architecture of the region surrounding the cancer mass is characterized by unique features, which can impair or determine the success of a drug delivery vehicle. (Canvas Draw 1.0.1)

1.3 Passive and active targeting

Excerpt reprinted with permission from Suarato *et al.*, *Biointerphases*, 11 (2016), AIP Publishing LLC, Copyright (2016)

The size and surface characteristics of the nanocarriers play a fundamental role in their effective delivery. Optimization of these factors can prevent nanoparticle uptake by macrophages and clearance in the liver and spleen by the reticulo-endothelial system (RES), allowing the selective extravasation in the pathological site. Sinusoid in spleen and fenestra in liver have diameters ranging from 150 nm to 200 nm, and the porosity of the endothelial layer of the defective tumor vasculature can vary from 100 nm to 700 nm. A nanoparticle size of 200 nm with a hydrophilic coating is considered optimal for an anti-cancer drug carrier to be administered intravenously.¹⁹ These features help to prevent the adsorption of opsonins (proteins involved in macrophage recognition and immune response activation), thus prolonging the blood circulation of the nanoparticles and favoring the tumor tissue targeting. Recently, the shape and the rigidity of the nanovectors have also been considered key factors for the success of the delivery device.¹⁹

The accumulation and retention of nanoparticles in the tumor microenvironment is a phenomenon known as the “enhanced permeability and retention (EPR)” effect (Figure 1.2). The role of the tumor vasculature in cancer treatment was initially proposed in the late 1970s by Maeda et al., who developed the first nanosized polymeric anti-cancer agent that was able to selectively target tumor tissues. The term EPR effect was then coined in 1986 by Matsumura and Maeda^{20, 21} to describe the accumulation of Evans blue dye linked with albumin in the tumor tissue after intravenous injection.²²

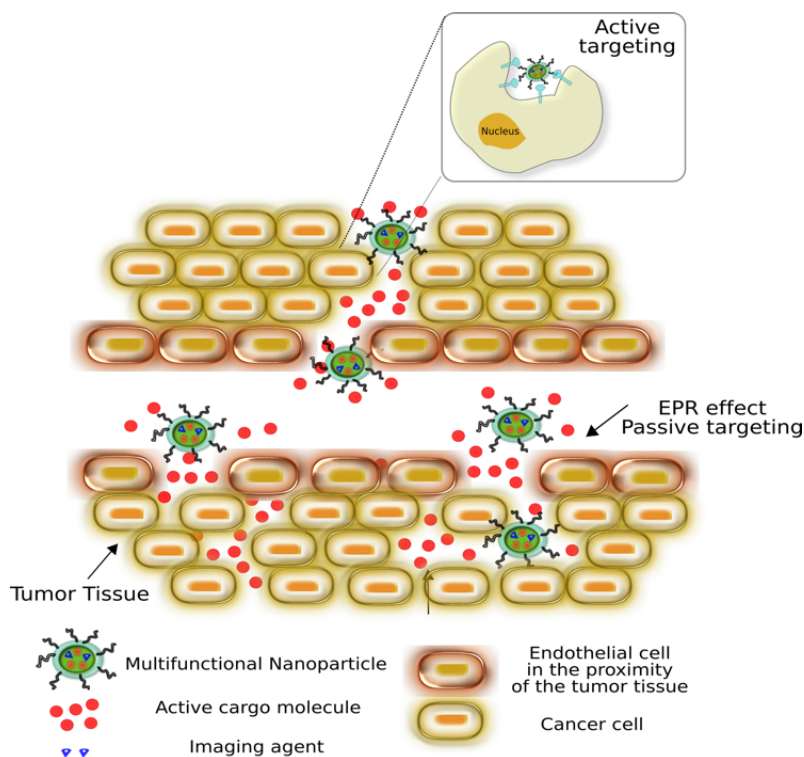


Figure 1.2 Passive and active targeting at the tumor microenvironment: the leaky and highly disorganized endothelium structure of the tumor microenvironment favors the nanoparticles accumulation in the tumor tissue (the so-called “enhanced permeability and retention effect”). The targeting efficiency can be improved by designing engineered multifunctional nanotherapeutics, able to actively recognize cancer cells. (Inkscape 0.48.42)

Broadly speaking, the EPR effect is responsible for the passive targeting of the nanotherapeutics with $M_w > 50$ kDa. Due to the porosity of the defective tumor endothelium, nanoparticles smaller than 200 nm can be transported and dispersed in the interstitium, whereas larger delivery vectors (up to 700 nm) remain localized in the peri-vascular space. Moreover, the endothelial cells constituting the vessels present a negatively charged membrane, which can more

favorably attract cationic nanoparticles through electrostatic interactions. In addition, the metabolic rate of rapidly growing cancer cells is relatively high, which requires a continuous supply of oxygen and nutrients. The necessary metabolic processes, needed to sustain enough energy for survival and proliferation, result in a more acidic environment.¹⁸ In order to enhance the delivery efficiency of nanotherapeutics, engineered stimuli-responsive systems that take advantage of such tumor characteristics as low pH have gathered increasing interest in recent years, thus paving the way for targeted drug delivery.

Targeted therapy is a novel cancer therapeutic approach that successfully combines chemotherapy with nanotechnology. Unlike standard chemotherapy, targeted therapy is based on the precise delivery of the active drug at the tumor site by means of artificial functional platforms.²³ In order to enhance nanoparticle selectivity, several approaches have been utilized, mostly involving the functionalization of the carrier with ligands or antibodies that are specifically recognized by receptors on the cancer cell membrane.²⁴ One of the most common strategies is the use of folate-drug conjugates, which bind to the folate receptor and are internalized into the cells via receptor-mediated mechanisms. Other ligands such as albumin, cholesterol, transferrin, and specific receptors for Her2/neu and epidermal growth factors have also been used in cancer drug delivery systems. For example, cyclic arginine-glycine-aspartic (RGD) peptide was conjugated onto the poly (ethylene glycol)-b-poly (2-(diisopropyl amino) ethylmethacrylate) copolymer to image the angiogenic tumor endothelial cells through binding with $\alpha v\beta 3$ integrins.²⁵ Commercial anticancer compounds, such as Tarceva® (erlotinib) and Iressa® (gefitinib), act by specifically targeting the overactive epidermal growth factor receptor (EGFR) tyrosine kinase expressed at the tumor cell surface.²⁶ Alternatively, nanoparticles functionalized with trans-activating-transcriptional peptide (TaT) are able to interact with lipid rafts in a receptor-independent manner.²⁷ Once selectively taken up by the cancer cells and invaginated into their intracellular vesicles, these functional nanocarriers should ideally possess the necessary physicochemical properties to escape from the intracellular compartments (e.g. endosomes and lysosomes) and reach the cytosol to release the active drug. In addition, receptor-targeting nanovehicles can also inhibit the ability of cancer cells to counteract the antitumor compounds' effects.²⁸ In fact, by being internalized through endosomes, the nanovehicle may avoid recognition by the P-glycoprotein efflux pump, one of the mediators of the MDR mechanism. As a result, the anti-cancer compound

can be efficiently delivered and released in its active form. The possible mechanisms of cellular internalization that an engineered nanoparticle can undergo are discussed below.

1.4 Mechanisms of cellular internalization

Excerpt reprinted with permission from Suarato *et al.*, *Biointerphases*, 11 (2016), AIP Publishing LLC, Copyright (2016)

The potential challenges associated with the use of nanomedicine constructs for drug and gene delivery are numerous. The physicochemical characteristics and morphological features of the nanocarriers are essential design criteria and should be tailored accordingly. The stability of the nanovector is paramount for the cargo molecule to be protected during travel to the pathological site and the subsequent cellular internalization. Once at the tumor site, there are additional hurdles for the nanoparticles to overcome, such as penetration of the plasma membrane, endosomal escape and cytoplasm trafficking (Figure 1.3). thus paving the way for targeted drug delivery.

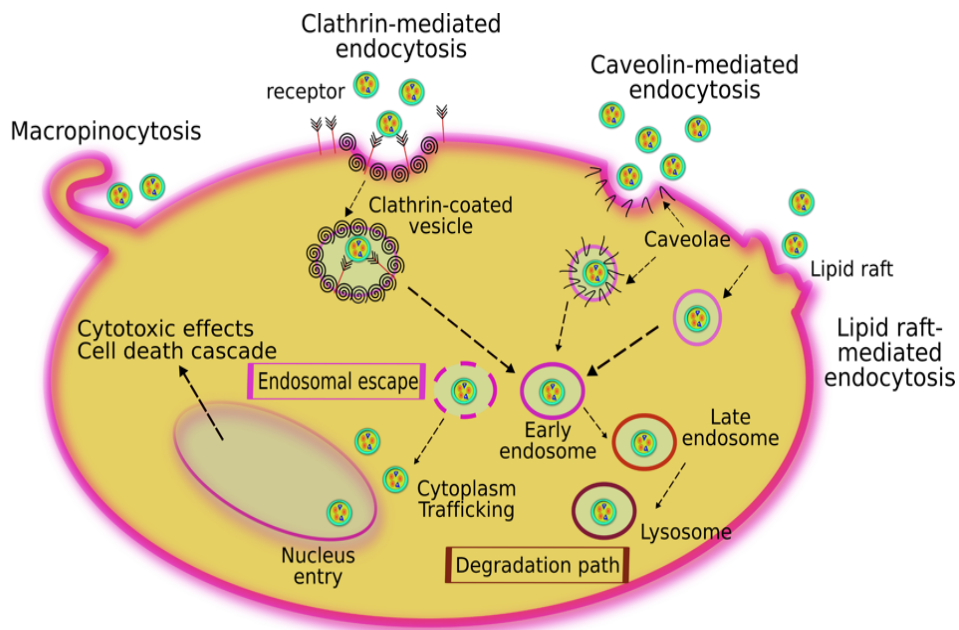


Figure 1.3 Endocytosis mechanisms and nanoparticle intracellular fate: nanotherapeutics can be internalized by cancer cells through multiple endocytic pathways, depending on the physicochemical and morphological features of the artificial carrier as well as on the cell type. Those pathways determine the intracellular fate of the internalized nanocarriers, which can be either degraded or released active in the cytosol. (Inkscape 0.48.4)

Depending on the physicochemical and morphological features of the nanocarrier and the cell type, there are several possible endocytic pathways: phagocytosis, macropinocytosis, clathrin- and caveolae-mediated endocytosis, and lipid raft mediated endocytosis¹⁹ (Figure 1.3). **Phagocytosis** is restricted to specialized immune cells (macrophages, monocytes, neutrophils) whose function is to clear pathogens, dead cells and arterial deposits of fat. This process is regulated by the presence of specific cell-surface receptors and involves Rho-family GTPase signaling cascade.²⁹ As an example, tagging of the foreign nanoparticles by opsonin molecules is required for macrophage recognition and subsequent cargo-shaped invagination formation. Phagocytosis plays a crucial role in digesting apoptotic cells and clearing sites of inflammation during immune response activation. **Macropinocytosis** involves Rho-family GTPase signaling cascade and the actin-driven formation of membrane protrusions.³⁰ These membrane ruffled extensions usually form around a portion of extracellular fluid and subsequently collapse and fuse with the plasma membrane to form macropinosomes of dimensions $> 1 \mu\text{m}$ (Figure 1.3). This fluid internalization process seems to be cholesterol dependent: the accumulation of lipids in specific, activated areas of the plasma membrane may cause molecular re-organization at these sites, which may account for dramatic morphological changes.³¹ Although macropinocytosis seems to play a role in regulating different signaling pathways and in directing cell migration, a deeper understanding of the membrane ruffling and the fusion process still needs to be achieved.²⁹ **Clathrin-mediated endocytosis (CME)** is a crucial mechanism in charge of nutrient uptake and intracellular communication. The CME pathway encompasses either receptor-dependent or independent (non-specific adsorption) mechanisms and the endocytosed material is transferred to lysosomes, which are membrane-bound organelles containing acid hydrolases that maintain the luminal environment at a pH of 4.5-5.0 and are responsible for the digestion of the intracellular material. Clathrin, a cytosolic coat protein, presents a three-legged structure called triskelin. During CME, clathrin assembles at the cell membrane in a basket-like structure to form vacuoles and pits (Figure 1.3). The GTPase dynamin is involved in the fusion of the pits and in the formation of the clathrin-coated vesicles (100-120 nm),^{29, 31} which deliver the cargo to early endosomes that mature in lysosomes for degradation. In **caveolae-mediated endocytosis**, flask-shaped membrane invaginations with dimensions of 50-80 nm, or caveolae, are involved.¹⁹ Caveolae formation is assisted by cholesterol molecules, sphingolipids and caveolin, a dimeric protein that self-assembles to form a coat on the surface of the vesicles.²⁹ Consequently, these vesicles are pinched

off of the membrane by GTPase dynamin to form cytosolic caveolar compartments (Figure 1.3), which appear to be free from the digestive enzymes contained in late endosomes and lysosomes. Therefore, owing to the possibility of escaping endosomal digestion and bypassing lysosomal degradation, the use of this pathway for drug delivery application is receiving increasing attention.¹⁹ **Lipid-based rafts** of 40-50 nm provide a physical basis for protein sorting, but the mechanism remains poorly understood.^{29, 32}

The contribution of these pathways in the cellular uptake of synthetic, non-viral nanovectors is not fully clear, and better understanding of intracellular trafficking of nanoparticles would greatly improve the success of the delivery.³³

1.5 Model of endosomal escape

Excerpt reprinted with permission from Suarato *et al.*, *Biointerphases*, 11 (2016), AIP Publishing LLC, Copyright (2016)

When the nanocarrier enters the cells via the endocytosis pathway, endosome internalization represents the main barrier for an efficient delivery. The endomembrane trafficking is constituted by a complex platform of interconnected intra- and extra-cellular trafficking events. The cargo molecule can undergo enzymatic degradation before exerting its function. In this case, endosomal escape of the nanovector and/or the active compound is necessary. Cationic polymer-based carriers have shown the ability to escape the endocytic vesicles, and two mechanisms have been hypothesized: 1) proton-sponge effect, and 2) electrostatic destabilization model. In the proton-sponge model, excess number of ionizable amine groups on the polymer backbone buffers the pH and forces ATPase to pump additional protons in order to acidify the endosome (Figure 1.4a). The accumulation of protons results in an influx of counterions, which causes osmotic swelling and subsequent rupture of the endosomal membrane. The cargo is then released and escapes lysosomal degradation.^{27, 34} Supporting this hypothesis are the observations of endosome swelling in the presence of buffering poly(ethyleneimine) (PEI) and poly(amido amine) dendrimers.^{27, 35} The second possible mechanism (Figure 1.4b) hypothesizes that the negatively charged endosomal membrane interacts with the cationic nanocarrier polymer and the disruption arising from this electrostatic interaction leads to polymer swelling and the eventual release of the cargo from the endosome.³⁴ In their study, Ko and coworkers³⁶ developed a degradable cationic polymer/DNA complex as an efficient non-viral transfecting system. The presence of an acid-

labile ketal linkage favored the hydrolysis of the polymer chains, leading to the generation of free amine groups and the swelling of the complex, which ultimately caused endosomal membrane destabilization and rupture.³⁶

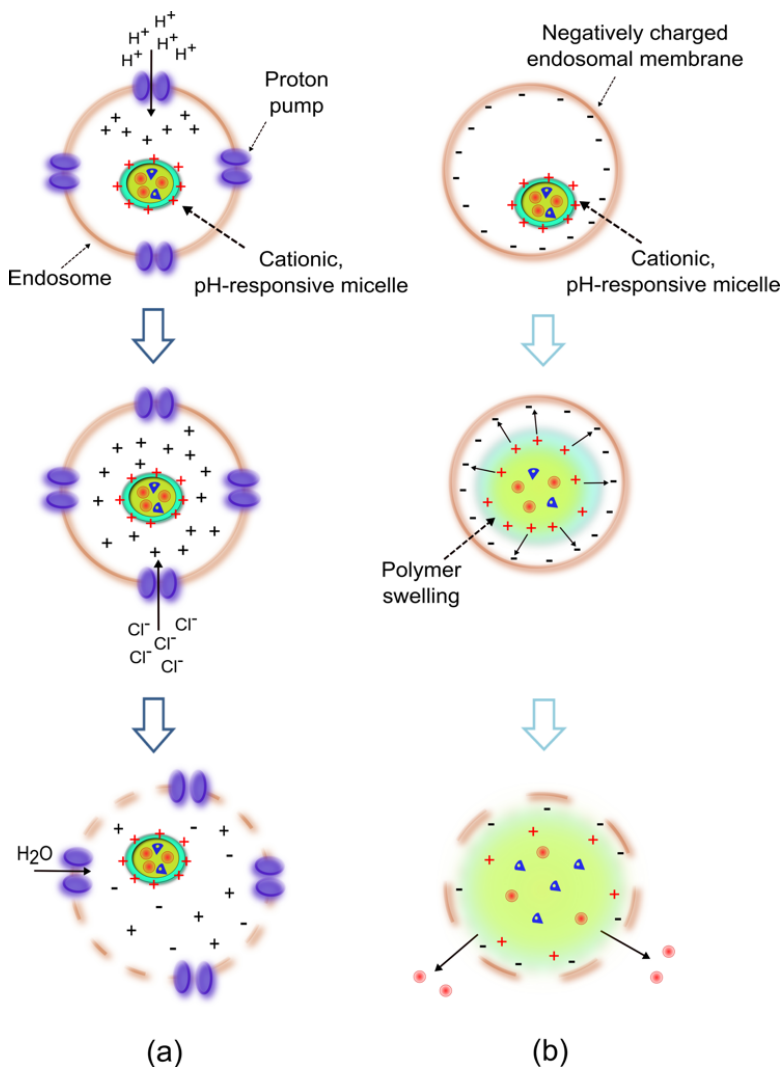


Figure 1.4 Hypothetical mechanisms of endosomal escape: in the proton-sponge model (a), cationic polymers presenting protonable functional groups are able to buffer the pH inside intracellular vesicles such as endosomes and lysosomes. The accumulation of H^+ ions favors an influx of counterions that ultimately leads to osmotic swelling and vesicle membrane rupture. In the electrostatic destabilization model (b), the cationic polymer chains interact with the negatively charged endosomal membrane, causing the polymer to swell. The consequent endosomal rupture allows the delivery of the active agents into the cytosol. (Inkscape 0.48.4)

1.6 Tumor microenvironment in multi-drug resistant (MDR) cancers

Excerpt reprinted with permission from Suarato *et al.*, *Biointerphases*, 11 (2016), AIP Publishing LLC, Copyright (2016)

Anti-cancer drug resistance constitutes a major obstacle in the treatment of tumor malignancies and it is considered one of the main causes of chemotherapy failure. The resilience against chemotherapy agents that differ in structure and function is defined as multi-drug resistance (MDR). Although this complex phenomenon is not fully understood, two main classes of mechanisms have been proposed and are currently investigated: mechanisms predominantly mediated by ATP-driven extrusion transporters of the ATP-binding cassette (ABC) superfamily (also designated as drug efflux pumps), and mechanisms that are independent of drug efflux pumps.^{37, 38}

Examples of ABC superfamily transporters, which show broad substrate specificity, include P-glycoprotein (P-gp, also known as ABCB1), multi-drug resistance proteins (MRPs/ABCC), breast cancer resistance protein (BCRP, also defined as ABCC2) and mitoxantrone resistance protein (MXR1/BCRP/ABCG2). MDR cancer cells, characterized by over-expression of the abovementioned efflux proteins at their membrane, can prevent the intracellular accumulation of the active small drug (i.e. paclitaxel, docetaxel, doxorubicin). As a result, a higher treatment dose is needed, with potentially harmful side effects for the patient. Engineered nanoformulations that accumulate in the tumor tissue and only release the chemotherapeutic molecules after being internalized in the cancer cell, thus preventing recognition of the drug from the transporters, constitute a possible strategy to overcome extrusion pump-based MDR. With this approach, the intracellular drug concentration is increased and a more effective cytotoxicity is achieved.^{28, 38-43}

Other cellular factors involved in the development of the drug resistance phenomenon reside in increased drug metabolism, efficient DNA repair and defective apoptotic machinery.³⁷ **Anti-apoptotic** cellular defense cascades are activated through up-regulation of Bcl-2 (pro-survival regulator) and nuclear factor kappa B (NF- κ B). Novel anti-cancer therapies are focused on targeting cell death pathways, as well as DNA repair mechanisms.⁴⁴⁻⁴⁷ Yoon et al. designed multifunctional chitosan-based nanoparticles for the sequential delivery of doxorubicin (apoptosis-inducing drug) and Bcl-2 si-RNA (suppressor of anti-apoptotic defense mechanism) to PC-3 tumor-bearing athymic nude mice.⁴⁴ The enhanced anti-cancer effect of the combined treatment

was visible in the tumor shrinkage (9.4-fold decrease at 51 days post-treatment) and histology (necrotic area observed around tumor vessels).

1.7 Role of pH in MDR development

Excerpt reprinted with permission from Suarato *et al.*, *Biointerphases*, 11 (2016), AIP Publishing LLC, Copyright (2016)

The ability of cancer cells to resist a vast range of anti-cancer therapies is indicative of the dynamic nature of the tumor tissue. Recently, attention has been focused on the role of the tumor microenvironment physiology in the cancer MDR etiology. Typical features of 3D solid tumor are: high interstitial fluid pressure (due to leaky vasculature and irregular blood flow), hypoxia (limited diffusion of O₂), and low extracellular pH.^{18,48} The interstitial fluid pressure rises to 100 mmHg, while the lymphatic drainage is impaired and the blood vessel network is unorganized. This leads to heterogeneous drug distribution, resulting in a partial diffusion of the active compound to the tumor cells located far from the blood vessels. Hypoxic and necrotic areas are present in the inner core of the tumor mass, which further limit drug penetration and pose an additional obstacle to treatment.

Drug resistance is also characterized by the presence of a pH gradient across the cell membrane. Ion pumps, such as vacuolar-type H⁺ ATPase exchangers, Na⁺/H⁺ exchangers and Na⁺-dependent Cl⁻/bicarbonate exchangers, promote the efflux of H⁺ ions, favoring the acidification of the outer milieu and the alkalinization of the intracellular compartment. Therefore, the permeability of an active compound across the membrane would be dependent on its state of ionization, as the uncharged species is permeable, while the charged form remains confined outside the cell.⁴⁹ In addition, hypoxia and acidic extracellular pH increase the production of metabolic acids, up-regulate anti-apoptotic pathways and activate proteases (such as cathepsin B, MMP-2 and MMP-9), thus supporting cancer cell invasion and metastasis.

The properties and structure of the lipid bilayer play a critical role in drug bioavailability. As such, the biomechanical interactions resulting from the steric hindrance of the anti-cancer molecule and the cell membrane surface tension can determine the actual transport of the drug across the membrane leaflets. In their work, Daniel *et al.*⁵⁰ present an extensive theory on the role of proton dynamics and the effect of the membrane fluid mosaic model in the maintenance of MDR. Properties that are of particular interest in MDR are membrane fluidity and lateral mobility.

Depending on the lipid density, the level of saturation of the hydrophobic tails, and the presence of rigid molecules (such as cholesterol and sphingolipids), stiff “lipid rafts” may form. Therefore, a rigid and densely packed membrane would act as a mechanical barrier for high molecular weight drugs. On the other hand, low molecular weight compounds, with small cross-sectional area and lower steric hindrance, would be less affected by the cell membrane fluidity and be able to penetrate easily. Moreover, the residence time of the active drug within the lipid leaflets may be crucial: if longer, the interactions with efflux pumps may be favored, resulting in molecule recognition and expulsion. The up-regulation of proton pumps in drug resistant cells leads to the establishment of a negative pH gradient in the cytosol. In the inner leaflet, mainly composed of negatively charged phosphatidylserine, increased charge repulsions contribute to stiffen the membrane and to counteract the chemotherapeutic agent internalization. Under these considerations, targeting the pH of tumor cells would give new insights into the MDR phenomenon and open potential frontiers in cancer treatment.

1.8 Polymeric micelles as drug delivery agents

Excerpt reprinted with permission from Suarato *et al.*, *Biointerphases*, 11 (2016), AIP Publishing LLC, Copyright (2016)

With the establishment of nanomedicine, several synthetic platforms have been developed and studied as targeting agents in conjunction with chemotherapy. Specifically, polymeric nanoparticles, polymeric micelles, liposomes, viral-based systems, carbon nanotubes, dendrimers and inorganic nanoparticles (e.g. gold, silica, iron oxide nanoparticles) are of medical importance.^{28, 51-57} By optimizing size, architecture and surface features, nanotherapeutics have improved the biodistribution and have increased the drug circulation time in the blood stream, thus overcoming the limitations of conventional drug delivery methods. Moreover, nanocarriers enhance the solubility of the active component, thereby adding protection during delivery and promoting the transportation across biological barriers (plasma membrane, blood-brain-barrier, lung and gastro-intestinal tract).²⁶ Recently, polymeric micelles have attracted the attention of the scientific community due to their versatile nature. When exposed to an aqueous environment, amphiphilic polymer chains are able to self-assemble into a well-defined and stable core-shell structure. The self-assembly is energetically favored above a threshold concentration value, the critical micelle concentration (CMC) (Figure 1.5).

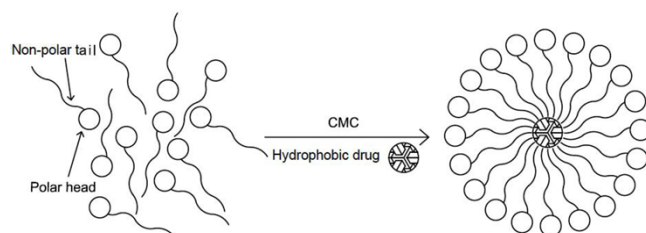


Figure 1.5 Micelle formation: in water-based environment, amphiphilic molecules are able to self-assemble in highly organized supramolecular structures, and act as reservoirs for anticancer compounds. The self-assembly process is energetically favored above a threshold concentration value, the so-called critical micelle concentration (CMC). (AutoCAD 2014)

In regular micelles, the hydrophobic core-hydrophilic shell structure can be achieved in hydrophilic solvent, when the polymer polar moieties are surrounded by the solvent molecules, while the non-polar segments migrate away from the solvent. In contrast, when exposed to a hydrophobic environment, reverse micelles can be obtained, presenting a hydrophilic core and the hydrophobic outer layer facing towards the solvent.¹¹ In regular micelles, the core region can act as a reservoir for a plethora of hydrophobic anti-cancer drugs, thereby enhancing their poor solubility in water. The external shell prevents the degradation of the cargo molecules and facilitates their circulation in water-based media, such as blood, mucus and saliva. On the other hand, reverse micelles are good candidates for delivering hydrophilic drugs and proteins in oily injections. Owing to their easy chemical tailoring, a broad range of multifunctional polymer micelles that incorporate various ligands and imaging agents have also been developed.⁵⁸⁻⁶¹

Anticancer drugs such as doxorubicin, paclitaxel and camptothecin present limited water solubility. To alleviate the solubility problem, these compounds can be chemically conjugated to biodegradable polymers¹⁰ or encapsulated into the hydrophobic core of polymeric and lipid micelles, while the hydrophilic shell prevents the core from interacting with the environment and helps to preserve the intactness of the cargo molecules.⁶¹⁻⁶⁴ For example, Pan and coworkers⁶¹ developed self-assembled chitosan-derivative micelles for the encapsulation of paclitaxel. The system, presenting both hydroxypropyl and cholic acid substitutions at the primary amine of the D-glucosamine units, exhibited an amphiphilic behavior that contributed to a drug loading efficiency up to 88.6% in micelles of 338 nm in diameter.

More complex diblock, triblock or grafted micellar structures can be formed when polymer molecules constituted of multiple and diverse blocks are used. Increasing the length of the hydrophobic portion can decrease the CMC, hence increasing the stability of the self-assembled system. As an additional effect, the presence of strong hydrophobic interactions in the core of the micelles may favor a prolonged release of the cargo.^{11, 65, 66} In this regard, the use of lipid-like molecules such as fatty acyl chains for the hydrophobic segment of the copolymer constitutes a useful approach. In their work, Li *et al.*⁶⁷ designed a series of grafted copolymers of N-octyl-N-(2-carboxybenzoyl) chitosan derivatives. The different polymers, obtained by varying the reaction time of the starting materials, were extensively characterized in terms of their structures and properties, to validate the grafting of the functional residues on the chitosan backbone. Vibrational spectroscopy data suggested the presence of long alkyl groups on the nitrogen at the C2 position of the D-glucosamine unit of the chitosan chains. X-ray diffraction patterns revealed the effect of the introduction of octyl and carboxylbenzoyl groups on the ability of the starting material to form hydrogen bonds and semi-crystalline structures. The synthetic amphiphilic polymers were able to form micelles with CMC ranging from 0.07 to 0.32 mg/ml, depending on the degree of substitution of the octyl group. Moreover, the nanovehicles revealed high stability under neutral conditions and showed affinity for paclitaxel, whose entrapment efficiency ranged from 51.4 to 61.4 %. In a similar work, Xiangyang *et al.*⁶⁸ synthesized doxorubicin-loaded N-succinyl,N'-octyl chitosan micelles, varying the degree of substitution of the octyl and the succinyl moieties. The pyrene intensity characterization study revealed the ability of the polymers to form micelles with CMC ranging from 2.4 to 5.9 µg/ml. The drug release was inversely dependent on the octyl chain content, suggesting the key role of the polymer chain-drug interactions in the delivery process. In fact, a higher amount of octyl residues would lead to a more hydrophobic micellar core, which, subsequently, would prevent the diffusion of the hydrophobic drug towards the shell and its release into the media.

1.9 Micellar formulations: advantages and strategies for improvement

Excerpt reprinted with permission from Suarato *et al.*, *Biointerphases*, 11 (2016), AIP Publishing LLC, Copyright (2016)

The facile chemical tailoring of the polymeric micelles allows the fabrication of self-assembled structures of various types and different surface properties. Depending on the characteristics of the molecular building blocks, precise range of sizes can be obtained. This parameter plays a critical role in determining the nanocarrier route of entry into the cell. On one hand, liposomes and polymeric nanoparticles have dimensions that can often reach the micrometer scale, limiting the EPR effect. On the other hand, small inorganic nanoparticles can be endocytosed in caveolae or clathrin vesicles.³³ Unlike these delivery systems, most of the polymeric micelles present diameters of a few hundred nanometers, which would favor the vessel extravasation and, at the same time, avoid the uptake through intracellular degradation paths. Moreover, micelles are typically more stable than liposomes under *in vivo*-like conditions, and, when internalized, their degradation products enter metabolic pathways without releasing ions or synthesis adjuvant elements, which might carry a cytotoxic potential.¹¹ The micelle fabrication process is relatively fast and simple, and is generally carried out in a water-based environment, unlike the synthesis of dendrimers, whose regular patterns are the result of a long sequence of reaction steps. Lastly, the extended surface area and the core-shell structure allow multiple functionalizations and a higher packing of the payload compared to polymeric bulk nanoparticles.¹¹ Taken together, these features contribute to make polymeric micelles uniquely interesting tools for the design of drug delivery platforms. One should note, however, that due to the tendency to disassembly beyond the CMC, the fabrication of long-circulating polymeric micelles that are able to continuously sustain the cargo release, is still a challenge. Stabilization strategies to delay the micelle degradation are based on the selection of polymeric components with a slow biodegradation rate; on the cross-linking of the shell (to prevent a burst release); and on the cross-linking of the core (to trap the drug in a matrix-like environment, thereby controlling the diffusion rate).¹¹ In addition, the use of low critical solution temperature hydrogels for the micelle core has also been proposed, in which the hydrogel portion would remain swollen (open state) at room temperature, allowing drug penetration, and would subsequently collapse (closed state) at physiological temperature. Thus, the active drug would remain locked in the micellar core network, leading to a more sustained release.^{11, 69}

1.10 Stimuli-responsive micelles: pH-induced mechanisms for nanocarrier destabilization

Excerpt reprinted with permission from Suarato *et al.*, *Biointerphases*, 11 (2016), AIP Publishing LLC, Copyright (2016)

In the past decade, the rapid development of highly functionalized, stimuli-responsive platforms has helped physicians to confront the challenges associated with cancer diagnosis and treatment. In fact, there is a constant demand for sensitive and efficient systems that are capable of detecting early-stage pathological conditions in patients, particularly when administered at low concentrations to reduce potential side-effects.²⁵ The design of engineered nanotherapeutics needs to take into consideration the simple route of administration and targeted delivery at the biological compartment of interest. Moreover, these nanocarriers must be able to respond and adapt to the surrounding pathological environment in order to release the payload only when needed.¹⁰

The tailorable chemistry of polymeric micelles allows them to be easily modified by conjugation of sensitive moieties. Therefore, these systems are considered good candidates for the design of stimuli-responsive nanotherapeutics that can be triggered by physical, chemical and biological cues. In addition, the assembly of stimuli-responsive molecules in micellar structures enhances the “smart” performance, as the inner core of the micelle can protect active drugs and imaging agents. Once at the desired site of action, the stimulus triggers dramatic transformations in the micelle properties (such as secondary structure alterations, bond-breakage, change in solubility and supramolecular assembly).⁷⁰


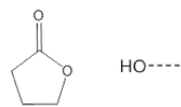
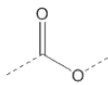
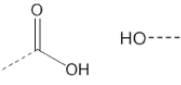
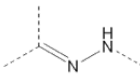
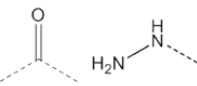
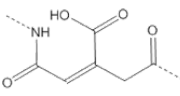
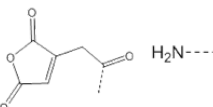
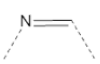
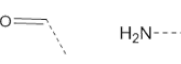
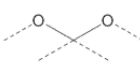
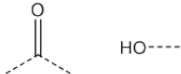
Due to the intense metabolic activity of cancer cells under both aerobic and anaerobic conditions, the tumor microenvironment is highly acidic compared to normal tissue. Tumors exhibit pH values between 5.7 and 7.8, while normal tissues typically have a pH of about 7.4.⁷¹ As such, pH-responsive platforms have shown improved efficiency in cancer treatment.⁷⁰ These nanocarriers are designed to store and protect the cargo molecule at physiological pH, and release it when the pH trigger point is reached at the therapeutic site of interest. Several pH-responsive drug release approaches have been investigated, primarily based on the chemical tailoring of the polymer micelle components.

One strategy for developing stimuli-responsive polymeric theranostics is to introduce chemical groups capable of accepting or donating protons and, as a consequence, driving pH-dependent changes in the micellar systems. Polyelectrolytes presenting “ionizable” groups (i.e. amines, phosphoric acids, carboxylic acids) in the main backbone or in the side chains can

dramatically modify their conformation in response to a change in pH of the aqueous medium. Examples of such conformational changes are dissociation, destabilization (swelling), and variation of the partition coefficient between the active drug and the nanovehicle.^{70, 72, 73} Anionic polyelectrolytes usually present carboxylic acid groups or sulfonamide groups and can undergo pH-triggered polarity change and charge reversal. On the other hand, cationic polyelectrolytes containing pyridine groups, imidazole groups and secondary or tertiary amine groups are more prone to pH-dependent phase transitions.

Another approach is based on the introduction of acid-labile chemical bonds, either in the basic components of the nanovehicles or covalently introduced between the drug and the polymer micellar structure. Common acid-labile chemical bonds used for this purpose are acetal, hydrazine, imine and cis-aconityl bonds (Table 1.1). These functional groups are stable at physiological pH, but hydrolyze and degrade in acidic environments. If present within the polymer structure, the hydrolysis of the acid sensitive bonds leads to the disintegration of the micelle and the release of the cargo molecule.

Table 3.1 Examples of acid-labile chemical bonds and their degradation products.

	Acid-labile chemical bond	Degradation Products
Orthoester		
Ester		
Hydrazone		
Cis-aconityl		
Imine		
Acetal		

In the acetal group, one carbon atom is linked through single bonds to two oxygen atoms. Under acidic conditions, the oxygen atom is protonated and activates the carbon atom. Water molecules can then attack the acetal linker, leading to the formation of aldehyde and alcohol as degradation products. The hydrazone (containing carbon-nitrogen double bond) and the *cis*-aconityl linkers (presenting a carboxylic acid group in *cis* position with the hydrolytic bond) have been widely used to couple anticancer molecules to polymeric micelles.⁷⁴⁻⁷⁸

Taking advantage of the tumor microenvironment's acidic pH has proven to be a promising strategy to target cancer cells. When designing a pH-responsive platform for cancer theranostic, the physicochemical properties of the micellar components play a fundamental role. Moreover, the targeting efficiency can be further improved by combining other stimuli-responsive features^{79, 80} or by introducing specific ligands for cancer cell surface receptors.^{62, 81-83}

1.11 Polysaccharide-based micelles

Excerpt reprinted with permission from Suarato *et al.*, *Biointerphases*, 11 (2016), AIP Publishing LLC, Copyright (2016)

Natural polysaccharides, such as starch, alginate,⁸⁴ pullulan⁸⁵ and chitosan, have been widely exploited within the last two decades as potential micelle systems due to their excellent biocompatibility, biodegradability and abundance. Moreover, the presence of existing functional groups on the polymer chains favors the chemical modification of these polysaccharides with hydrophobic moieties (i.e. linoleic acid, stearic acid and cholanic acid), leading to flexible derivatives that are able to self-assemble in micellar structures and transport several substituents with multiple functionalities. For example, lipid-functionalized dextran-based micelles were utilized for the delivery of doxorubicin by Kobayashi *et al.*⁴⁰ In this study, doxorubicin-loaded micelles showed 5- to 10-fold anti-proliferative activity against osteosarcoma KHPS and ovarian SKOV-3 cancer cells, when compared to the free drug. In addition, doxorubicin-encapsulating micelles exhibited higher cytotoxic activity at lower concentrations for both drug-sensitive and drug-resistant cancer cells. Amongst those versatile natural polysaccharides, chitosan has gained the attention of the research community as the building block for effective cancer drug delivery systems. Its appeal mainly resides in its pH-responsiveness, which provides high potential when tumor microenvironment and pH gradients are involved. The following sections will provide a

detailed overview of the general physicochemical properties of chitosan and its derivatives, as well as their applications as powerful stimuli-responsive tools in cancer drug delivery platforms.

1.12 Chitosan as a biomaterial for cancer therapy

Excerpt reprinted with permission from Suarato *et al.*, *Biointerphases*, 11 (2016), AIP Publishing LLC, Copyright (2016)

Chitosan is a natural biodegradable linear copolymer containing β -(1-4)-linked D-glucosamine and N-acetyl-D-glucosamine randomly distributed. Chitosan is obtained from deacetylation of natural chitin, the major component of exoskeletons in crustaceans, by hydrolysis under alkali conditions at high temperature (Figure 1.6).⁸⁶ Thanks to its natural origins, biocompatibility and biodegradability, this material has been widely used as a pharmaceutical adjuvant and presents potential applications as drug carrier. Chitosan is subjected to enzymatic hydrolysis by chitinases and chitosanases, secreted by intestinal microorganisms and non-specific enzymes such as lysozymes.⁸⁶ Physical and chemical properties of chitosan depend on its molecular weight and degree of deacetylation, as well as from the presence of substitutional moieties. By tailoring these features, the capabilities of this biopolymer as a controlled delivery system can be greatly enhanced.

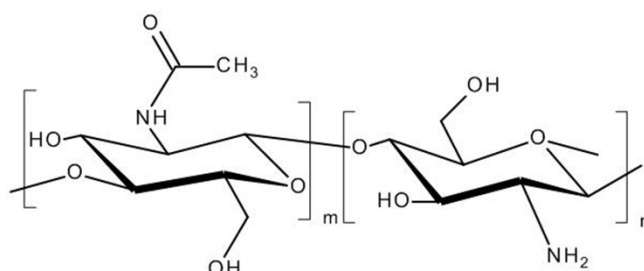


Figure 1.6 Chemical structure of chitosan (Accelrys Draw 4)

The degree of deacetylation is related to the number of protonable amine groups at the C2 position of the glucosamine residues in the chitosan chain. Thus, the degree of acetylation affects chitosan solubility, hydrophilicity and electrostatic interactions with polyanions. At $\text{pH} < 6.5$, the amine groups are protonated (polycationic behavior): the polymer is soluble in most organic acids. On the other hand, at $\text{pH} > 6.5$ the amine groups are deprotonated and can undergo interpolymer associations, resulting in the precipitation of chitosan into networks or fibers.⁸⁷ All of the above mentioned factors should be taken into account when designing a chitosan-based platform for targeted drug delivery.

The polycationic nature of chitosan makes it a suitable material for electrostatic interactions with negatively charged molecules (such as nucleic acids and proteins), therefore facilitating adsorption at the cell membrane and subsequent cellular uptake. Moreover, the presence of amine groups renders chitosan highly responsive to external stimuli such as variations in temperature and pH.^{79, 80, 88, 89} Other biorelevant properties — such as adhesivity, biodegradability, antibacterial activity, antitumor effect, enhanced permeability and retention (EPR) effect, and buffering effect — contribute to an increased interest toward the use of chitosan as a biomedical material. The amino groups within the molecule can be combined with the highly hydrated glycoproteins present in the mucus leading to hydrogen bonds and adhesive effect. This would prolong the adsorption of chitosan molecules to mucus-coated membranes (gastrointestinal tract, oral and nasal tracts), increasing the retention time of the chitosan-based delivery systems at the site of interest and improving the drug bioavailability. Furthermore, chitosan is an adsorption promoter and is believed to aid in drug transport across the mucous membrane by opening tight junctions between cells.^{73, 87, 88, 90}

The molecular weight of the polymeric chain greatly affects the size and morphology of the chitosan-based systems and plays a central role in their uptake and toxicity. In general, depending on the size, shape and surface functionalization of the chitosan-based carriers, a certain *in vivo* biodistribution can be achieved. The targeting abilities can be enhanced by modifying the polymer structure with ligands to increase cell recognition through receptor-mediated endocytosis.⁸⁸

Another interesting feature that promotes chitosan as a promising material for effective drug delivery is the “proton-sponge effect” or “buffering effect”,²⁷ which has been proposed to explain the ability of chitosan to partially escape endosomal degradation (Figure 3a). In fact, when internalized by acidic vesicles, chitosan appears to act as a “proton-sponge” and, depending on the degree of acetylation and the availability of free amine groups, it attracts H⁺ ions from the cytosol. As a result, this buffering behavior causes osmotic swelling and the rupture of the acidic compartment, leading to the release of the chitosan vector and its active cargo molecule into the cytosol.

Poor solubility in water and non-acidic solutions constitutes the main drawback for the application of chitosan in the biomedical field. To overcome this limitation and to improve broad pH range stability and adhesivity of chitosan,^{91, 92} several chemical modifications of the chitosan

chain have been investigated, either by grafting small molecules on the main backbone, by carboxymethylation of the hydroxyl group or by quaternization of the free amine group.⁷³

1.13 pH-responsive amphiphilic chitosan derivatives

Excerpt reprinted with permission from Suarato *et al.*, *Biointerphases*, 11 (2016), AIP Publishing LLC, Copyright (2016)

The presence of secondary and tertiary amine groups not only enhances the adsorption of chitosan derivatives at the cancer cell membrane, but also favors their pH-sensitivity. These materials have wide applicability in cancer treatment, due to the physiological characteristics of the tumor milieu, where cytosolic pH decreases significantly. Table 1.2 summarizes some of the recent work published in the literature on chitosan-based, pH-responsive micellar systems as cancer nanotherapeutic strategies.

Table 1.2 pH-responsive chitosan (CS) derivative micelles

Micellar System	Drug/molecule loaded	Proposed pH-sensitivity mechanism	Cancer model	Ref
P(N-isopropyl-acrylamide)-g-CS	Lilic	pH and thermo, reversed core-shell structure	-	[93]
PHCS-PNIPAA _n & P(AA-co-tBA)	Prednisone acetate	pH and thermo	-	[94]
6- <i>O</i> -dodecyl chitosan carbamate	Complex with pDNA	Carbamate linkage breaks at pH 4.6	A549 cells	[95]
N-octyl-N(2-carboxyl benzoyl) CS	Paclitaxel	Hydrolysis at pH 5.0	MCF-7, KB cells	[67, 96]
Pluronic F127-CS	Doxorubicin +Paclitaxel	Micelle disassembly	-	[72]
N-(2,3-dihydroxypropyl)-CS-cholic acid	Paclitaxel	Decreasing micelle core density	MCF-7 cells	[97, 98]
Quaternary ammonium palmitoyl glycol chitosan	Propofol +Prednisolone	-	In vivo pharmacodynamics activity	[99]
Deoxycholic acid+folic acid hydroxypropyl CS	Doxorubicin	Amido linkage	HeLa, HBE cells	[100]
NIPAA _n /CS	Camptothecin	pH and thermo response	SW480 cells	[64]
Stearic acid-g-CS oligosaccharide	Doxorubicin	-	MCF-7, MCF-7/Adr, QGY cells	[101]

<i>O</i> -carboxymethyl CS- cholic acid+glycyrrhetic acid	Rhodamine B	-	HepG2, HeLa, MCF-7 cells	[102]
PEG-arachidyl CS	Doxorubicin	Sheath effect	K562 cells + in vivo pharmacokinetics	[103]
Deoxycholic acid- <i>O</i> - carboxylethylated- CS+folic acid	Paclitaxel	-	MCF-10A cells	[81, 82]
Carboxymethyl CS- quercetin	Paclitaxel	Bypassing of the P-gp pumps	HepG2 + in vivo pharmacokinetics	[43]
Folic acid-PEG-CS- PAMAM	Plasmid DNA	Lysosomal escape	HepG2, KB cells	[83]
Galactosylated CS+hyaluronate	Doxorubicin	Surface charge reversal	HepG2 cells	[62]
Cholesterol-modified CS	Epirubicin, Doxorubicin	-	HeLa, HepG2 cells	[104, 105]
Deoxycholic acid carboxymethyl CS	Doxorubicin	pH-dependent micelle aggregation and deformation	MCF-7 cells	[106]
2,3-dimethylmaleic anhydride- <i>g</i> -glycol CS	Model protein	Charge switching	-	[89]
<i>N</i> -succinyl-palmitoyl- CS	Paclitaxel	-	A549 cells + in vivo orthotopic and subcutaneous lung tumor	[63]
Lactobionic-acid-CS- stearic acid	Doxorubicin	-	HepG2, BEL-7402 cells + in vivo study	[62]
<i>N</i> -naphthyl- <i>N</i> , <i>O</i> - succinyl CS	Meloxicam	Succinic acid ionized at pH < pKa (= 4.21)	Caco-2 cells	[107]
<i>O</i> -carboxymethyl CS- polyethyleneimine	Doxorubicin + genes	Hydrazone bond	HepG2, A549 cells	[78]
octreotide-PEG- monostearate <i>N</i> -octyl- <i>N</i> -succinyl- <i>O</i> - carboxymethyl CS	Doxorubicin	Micelle destabilization for protonation of -COO ⁻	SMMC-7721, CHO cells +in vivo pharmacokinetics	[108]

One of the approaches explored to obtain amphiphilic derivatives is the conjugation with cholesterol-like molecules. A cholesterol modified chitosan conjugate with succinyl linkages has been synthesized by Wang et al. as a suitable carrier for epirubicin, a hydrophobic anti-cancer drug from the class of anthracyclines.¹⁰⁴ Jin and co-workers proposed the use of amphiphilic deoxycholic acid modified carboxymethyl chitosan (DOCA-DCMC) self-assembled nanoparticles as pH-responsive delivery agents.¹⁰⁶ The DCMC micelle loaded with doxorubicin (encapsulation efficiency ranging from 50 to 79 wt.%) showed high stability at physiological pH (diameter \approx 200

nm), while at lower pH the protonation of the amine and carboxymethyl groups caused deformation (diameter > 600 nm) and loosening of the core. As a result of the more permeable inner compartment, drug release was accelerated. In addition, release was observed to be inversely proportional to the degree of substitution of DOCA, indicating an increased hydrophobic interaction between the nanoparticle core and the drug (Figure 9a). Moreover, doxorubicin loaded DOCA-DCMC micelles showed a time-dependent accumulation in MCF-7 cells and MCF-7/Adr breast cancer cells and a 4-fold cytotoxicity against the drug-resistant strain, when compared to free anthracycline.

Similar pH-sensitive chitosan derivative systems have demonstrated stimuli-responsiveness via the addition of hydrophobic^{61, 105, 109-113} or protonable moieties.^{85, 108, 114-119} For example, Hsiao *et al.*⁵⁸ improved the pH-responsiveness of amphiphilic carboxymethyl-hexanoyl chitosan micelles by poly(acrylic acid) (PAA) incorporation. With a PAA degree of substitution of 47.2% the hybrid system showed a more significant response to the pH change in terms of particle size, volume and surface charge, as well as encapsulation efficiency and release profile. Zhao and coworkers⁶² engineered a pH-responsive surface charge-reversible polyelectrolyte based on the co-precipitation of galactosylated chitosan and hyaluronate. While the galactose moiety conferred the targeting ability (due to the affinity to the galactose receptors overexpressed on the cell membrane of hepatocytes), the pH-dependence allowed an efficient release.

The complex nanoparticles presented positive charges on the chitosan backbone and negative charges on the hyaluronic acid molecules. The nanoparticles were able to retain spherical morphology at neutral conditions, to favor blood circulation. However, in slightly acidic environment (pH 6.2 to 6.0), the surface charge of the polyelectrolyte changed from -3.47 mV to +5.71 mV as a result of the protonation of chitosan, leading to a consequent expansion of the structure.

One of the key features of the pH-responsive nanotherapeutics is their ability to escape the degradation pathways and release the active cargo molecules in the cytosol via the “proton sponge effect.” In this regard, an interesting work was recently published by Wang *et al.*⁸³, who proposed a non-viral gene delivery system for cancer cell targeting. Here, PAMAM (polyamidoamine) was complexed with pDNA and HMGB1 (high motility group box 1) as nuclear localization signal, to form PHD complexes (consisting of PAMAM/HMGB1/pDNA). In a second step of the design, the system was complexed with carboxylated chitosan modified with folic acid and polyethylene

glycol, to form FPCPHD complexes (consisting of PHDs and PEG-tethered carboxylated chitosan modified with folic acid). Intracellular trafficking analysis with epithelial carcinoma KB cells revealed the ability of the FPCPHD complexes to escape endosome and lysosome digestion and to effectively penetrate the cell nuclei within 3 hours post treatment. At early-stage of endocytosis, the intracellular vesicles appeared as punctate signals clustered around the nuclei. Over time, the buffering effect exerted by the entrapped FPCPHD micelles caused vesicle rupture. After 4 hours of delivery, the pH-responsive, multifunctional gene delivery system translocated into the nuclei.

In the past decade several studies have been published on chitosan derivative systems bearing an ethylene glycol residue and modified with a cholesterol-like molecule, the 5- β -cholanic acid.^{60, 120-127} Glycol chitosan is soluble in water, a characteristic that makes the quaternization of the primary free amine an easy, fast and water-based process. Glycol chitosan can be covalently linked with 5- β -cholanic acid to obtain an amphiphilic molecule that self-assembles in an aqueous environment. These hydrophobically modified glycol chitosan nanoparticles have been investigated as carriers for paclitaxel,¹²⁸ RGD peptide¹²³ and doxorubicin,¹²⁹ and were delivered to cancer cells to study their uptake mechanisms.^{125, 130} Moreover, in order to combine the delivery of a certain active agent with its real-time tracking inside a living system, numerous studies have reported the loading of the glycol chitosan nanoparticles with probes for magnetic resonance imaging (MRI),¹²⁶ photosensitizers or near-infrared fluorescent dyes.^{131, 132} For example, Huo et al. designed N-octyl-*O*-glycol chitosan (OGC) by introducing hydrophobic alkyl chains to the glycol chitosan main backbone. As a carrier for paclitaxel, OGC showed high drug loading capacity (32 wt.%) and cytotoxicity against human hepatoma HepG2 cells.¹³³

Glycol chitosan grafted with 2,3-dimethylmaleic anhydride (GC-DMA) was used to prepare a charge-switchable nanocarrier.⁸⁹ At physiological pH, the negatively charged DMA stabilizes a positive protein molecule (model drug) in the inner compartment of the micelle. In the event of a drop in pH, the anhydride substituent dissociates from the main backbone, leaving a positive residual charge on the amine groups. The micelle expands due to the positive charge repulsion and the protein drug is released. Similar approaches based on the use of different biodegradable amphiphilic polymers, modified to enhance their response to the tumor microenvironment characteristics and/or the intracellular vesicle conditions, have also been investigated and have shown successful applicability.¹³⁴⁻¹³⁷

1.14 Chitosan-based micelles as probes to visualize the tumor microenvironment

Excerpt reprinted with permission from Suarato *et al.*, *Biointerphases*, 11 (2016), AIP Publishing LLC, Copyright (2016)

One of the greatest challenges in cancer diagnosis is the development of sensitive tumor imaging techniques to detect the pathology during its earliest stage. In the past decade, several techniques (i.e. magnetic resonance, positron emission tomography, computed tomography, ultrasound, fluorescent optical imaging and single-photon emission computed tomography) have been implemented to gain insight into the anatomical and pathological state of tumor masses in patients. More interestingly, with the aim of improving sensitivity, tissue-penetration and specificity, these imaging modalities have been combined with the administration of nanoprobe for cancer theranostics.¹³⁸⁻¹⁴⁰ The main advantages of multifunctional nanoprobe reside in their ultrasensitive detection ability (at pico- and nano-molar concentrations) and the potential to achieve high biological specificity. Thus, tumor masses can be differentiated more easily from the normal tissue, thereby minimizing background signal. To date, many imaging agents target cancer cell membrane specific biomarkers, such as Her2/neu, EGFR and folate receptors.^{141, 142} However, these cancer specific binding sites are expressed only in a subset of patients, thus limiting the applicability of these systems. In addition, smart nanoprobe capable of switching from an OFF (invisible) state to an ON (detectable) state when in the proximity of the tumor microenvironment, seem to have broader applicability. Within this approach, the identification of cancerous tissue would be possible independently from its histology or patient-to-patient variation.²⁵ The physicochemical properties of polymeric micelles, in combination with the EPR effect, favor the concentration of the markers at the pathological site of interest. The resulting increase in contrast resolution aids in the detection of traditionally inaccessible cancerous masses, as well as the visualization of their architecture.^{8, 26}

Several studies have documented the use of pH-sensitive nanoprobe for the detection of cancer associated acidosis (pH ranging from 6.4 to 6.8). In order to achieve the desired activation (ON state) within the acidic microenvironment, these nanoparticles do not fluoresce at physiological pH but emit strong signal at lower pH. The acid dissociation constant (pKa) is tunable ($\Delta\text{pH}_{\text{ON/OFF}} < 0.25$) to maximize the contrast between normal and tumor tissue. Moreover, the nanoprobe should carry a fluorophore (usually excited at longer wavelengths), and a tumor targeting unit to assist with the internalization of the delivery system and the amplification

of the signal in the acidic cellular compartments. Nwe and coworkers¹⁴³ designed a pH-responsive MRI contrast agent based on Gd-labelled glycol chitosan (GC-NH₂-GdDOTA). At physiological pH the micelles exhibited near-neutral charge, preventing blood protein association. At lower pH the protonation of the amine groups drove the electrostatic interactions with the negatively charged cancer cell membrane, enhancing the micelle adsorption and retention at the site of interest. As a result, the acquisition of diagnostic information was favored.

Recently, the design of engineered, multifunctional nanocarriers has helped establish multimodality imaging approaches, aimed to overcome true-negative or false-positive diagnosis results and to optimize the effective intervention.^{138, 144} In fact, by incorporating the strengths of several imaging modalities into one nanoprobe system, a highly accurate detection of the disease becomes feasible. One of the most extensively studied multimodal imaging platforms is the dual labeling of near-infrared fluorescent (NIRF) dye and magnetic resonance (MR) contrast agents.^{59, 60, 111, 124, 145} Using this approach, NIRF optical imaging allows rapid scanning and identification of the pathological areas, while the high spatial resolution and deep tissue penetration of the MR contrast agents help to precisely visualize the tumor masses. Cy5.5-labeled glycol chitosan modified with cholanic acid (GC-CA) was conjugated with DOTA (1,4,7,10-tetraazacyclododecane-1,4,7,10-tetracetic acid) to chelate gadolinium (Gd(III)).¹²⁴ The self-assembled Cy5.5-GC-CA nanoparticles, encapsulating up to 6.28 wt% of Gd(III), were administrated to squamous cell carcinoma (SCC7) tumor bearing mice. The tendency of the nanoprobe to accumulate at the pathological site was highlighted by the NIRF imaging at 1 day post injection. Following a similar rationale, Key *et al.*⁶⁰ prepared superparamagnetic iron oxide nanoparticle (SPION) encapsulated Cy5.5-GC-CA nanoparticles, with 6.64 wt% of Fe and particle size ranging from 250 nm to 300 nm. The real-time *in vivo* imaging revealed the nanoparticle biodistribution and tumor targeting in live mice bearing SCC7 cancer cells.

Positron electron tomography (PET) and single-photon emission computed tomography (SPECT) are FDA approved nuclear medicine imaging modalities based on the recording of γ -rays from a patient's body.¹³⁸ Various positron-emitting isotopes can be used to highlight metabolically active hotspots, such as growing cancerous masses. The high sensitivity of SPECT and PET can be synergistically coupled to the precise spatial resolution of MRI and computed tomography (CT), to achieve imaging accuracy as well as specific information on the biological constituents of the tumor microenvironment^{144, 146-149} In their work, Lee *et al.*¹⁴⁹ developed a radiolabeled glycol

chitosan nanoparticulate probe for PET/optical activable imaging. The multifunctional system was obtained via aqueous-based orthogonal click reaction and the resulting probe consisted of a glycol chitosan shell decorated with a Cy5.5-MMP-sensitive peptide, a ^{64}Cu radiolabeled DOTA complex and a dark quencher. When in proximity of active MMP-2 and MMP-13 (usually overexpressed at the cancer microenvironment), the MMP-sensitive peptides on the outer shell were cleaved and the Cy5.5 molecules released, leading to a bright fluorescent signal. Driven by a similar purpose, Polyák and co-workers^{146, 147} investigated the in vivo application of a chitosan-based $^{99\text{m}}\text{Tc}$ -poly- γ -glutamic acid - folic acid self-assembled nanoparticle as SPECT/CT imaging agent with potential clinical use. Although still under development, the design and the applicability studies of multifunctional imaging nanoparticles is nowadays receiving great attention by the medical and scientific communities. In fact, by carefully combining imaging modalities and targeting ability, precise detection and resolution of tumor masses and micro-metastases can be achieved. In this way, fluorescence-guided surgery can be performed to enhance the success of the anti-neoplastic treatment.

1.15 Micelle characterization techniques

Dynamic Light Scattering

Physicochemical properties and morphological features of nanoparticulate systems can be assessed with several characterization techniques. The hydrodynamic volume of nanoparticles in suspension in a water-based media is usually obtained *via* Dynamic Light Scattering (DLS). This fast and automatized method allows routine, non destructive measurements. The main principle behind DLS (also known Photon Correlation Spectroscopy) is the scattering of light due to small particles in Brownian motion. A monochromatic light beam (usually a red laser in the range of 633-675 nm) passes through a suspension containing particles in motion. Upon hitting, the electric field of the light induces an oscillation in the polarization of the molecules / atoms constituting the nanoparticles. As a result, the impinging light changes its wavelength: the frequency shift, the light polarization and the intensity of the scattered light are related to the size, the shape and the molecular constituents of the scattering particles. By means of statistical mechanics, diffusion theory and the concept of autocorrelation function, the “sphere size” distribution of the nanoparticles in motion can be derived. This sensitive technique allows the analysis of broadly

distributed samples (in terms of aggregates' size and molecular weight) and can be used to detect very diluted systems.¹⁵⁰

Zeta Potential

Nanoparticles in suspension may aggregate with time, precipitate in clusters or remain stably solvated by the surrounding media. An index of nanoparticle stability in suspension is given by the value of the Zeta Potential.¹⁵¹ At the interface between a nanoparticle and its surrounding medium, ions and counter-ions are formed and in continuous relative movement. The liquid layer surrounding the particle is composed of an inner region (the Stern layer), with strongly bound ions which follow the nanoparticle in its movement, and an outer region (the diffuse layer), with loosely attached ions which do not travel in association with the particle. The boundary between the Stern layer and the diffuse layer is known as slipping plane and its potential is called Zeta Potential. More specifically, the technique provides a value of the surface charge that a nanoparticle carries in suspension. This parameter can indicate the nanotherapeutics ability to adsorb to cell membranes or to mucosae layers. This property, closely related to the chemistry of the material and the structure of the nanoparticulate systems, is greatly affected by the pH of the suspension media. Considering the characteristics of the tumor microenvironment and the variation in the pH that nanotherapeutics encounter during their journey from the circulating system, to the tumor site, to the intracellular vesicles, assessing the nanoparticle Zeta Potential with respect of the pH is crucial to elucidate its behavior and its possible therapeutic efficacy.

Electron Microscopy

Information on the morphology and surface texture of nanoparticles can be obtained by means of a scanning electron microscope (SEM). Thanks to the use of an electron beam, ejected from a tungsten filament and focused through magnetic lenses, this microscopy technique is able to couple high resolution (up to 500,000 times) with large depth of field. When a beam of electrons impinges on a specimen, they can be reflected from the specimen or absorbed and scattered within the specimen. As a result of this interaction, two types of electrons can be generated: the secondary electrons and the back-scattered electrons. Secondary electrons are emitted from the valence bands of the atoms constituting the sample and, due to their relatively low energy, they can be detected to gain information on the topographical features of the sample's surface. On the other hand,

backscattered electrons carry higher energy and contain information about the chemical composition of the sample. Moreover, SEM is capable of performing elemental analysis and in situ XRD diffraction. In addition, the technique allows imaging of biological samples, upon proper specimen preparation (i.e. fixation, dehydration, sputter coating).

The transmission electron microscopy (TEM) can be considered a complementary imaging technique. Also in this case, high resolution in the order of a few Angstroms is obtained by means of an electron source, thermally emitted from a tungsten filament and focused with electromagnetic lenses. The image is the result of the interaction between the sample and the electrons transmitted through it. In fact, while some electrons are scattered from the sample, some others are absorbed by the material, travel through its thickness and reach a phosphor screen, where they constitute a “shadow image” of the sample. The image contrast (darker or lighter areas) is due to the different thickness, composition and density of the specimen. Careful sample preparation and precise experiment set ups are needed for the acquisition of high resolution and high quality images. Usually, for the analysis of nanoparticles in suspension, a few drops are placed on a copper or gold grid, consisting of a ring of 3 mm in diameter and a mesh size up to 100 μm . Consequently, the grid is let air dry, to allow the nanoparticles’ entrapment in the mesh. Measures of the nanoparticle size (in the dry state) and observation of their morphology and differential density composition can be obtained with this technique. Moreover, nanoparticles internalized in biological samples can be imaged to assess their distribution within intracellular compartments. In this case, resin embedding and sectioning of the sample is needed, in order to work with thin slices, which allow an effective electron transmission.

1.16 Micelle visualization techniques

Confocal Microscopy

Thanks to their versatile chemical structure, polymeric nanomicelles can be easily linked to a fluorescent moiety to favor their visualization, once internalized into cells or uptaken by tissues. At a clinical level, near infrared dyes can be used, to help the observation of the nanoparticle biodistribution by means of a low energy light source (near-IR). Inorganic materials, such as Fe_2O_3 or Gd ions, can be included in the micelle synthesis process, to aid the visualization of the tumor microenvironment with Magnetic Resonance Imaging.

At a laboratory level, confocal microscopy constitutes a powerful tool to obtain crucial info on the intracellular or intra-tissue distribution of fluorescently labelled nano-therapeutics. Good contrast is achieved by collecting only the light coming from the focal plane and excluding the contribution of the out-of-focus light. Compared to wide-field, standard fluorescence microscopy, fine details can be appreciated (down to a few nanometers) and a 3D reconstruction of a volume of specimen (about 250-300 nm thick) can be obtained by assembling a series of slices taken along the z axis (the so-called z -stack scanning mode). A laser is scanned across a fluorescently labelled sample by scanning mirrors. The sample is excited by the laser and fluoresces, and the emitted light passes through a pinhole. The signal is then detected by a photomultiplier tube. A point-to-point illumination is performed, and the computer software builds up the image one pixel at a time. This versatile microscopy technique allows imaging of living samples, when coupled with properly designed stages and upon fluorescence labelling of the cell components of interest.

Structure Illumination Microscopy

A further improvement of the image resolution can be achieved with the structured illumination microscopy (SIM). This technique is based on the analysis of the moiré pattern produced when a sample is illuminated with a high-frequency laser interference. More precisely, nine images are captured with a structured illumination shifted in phase. This acquisition process is repeated for three angles. The total 27 images are processed to obtain a super-resolution image. With a 100X objective and a multi-laser capability, multi-color imaging with a lateral resolution of 115 nm can be obtained. In addition, the 3D reconstruction of a sequence of slices acquired along the z axis (0.123 μm in thickness) allows the detailed observation of intracellular structures and their respective association / co-localization with internalized nanoparticles. The use of this powerful tool can greatly enhance the ability to address biological questions.

1.17 Future perspectives

Excerpt reprinted with permission from Suarato et al., *Biointerphases*, 11 (2016), AIP Publishing LLC, Copyright (2016)

Targeted drug delivery is an increasingly promising strategy to overcome limitations and complications associated with the classical chemotherapy approach. In the past years, the cancer biology community has indicated the critical role of the tumor microenvironment in the cancer

progression, highlighting lack of oxygen, unorganized vasculature and milieu acidification as key features.² As a result, smart materials capable of actively triggering a response when in the proximity of cancer cells have been extensively researched. Polymeric micelles are versatile and scalable technology platforms,¹⁵² and as such, several polymer micelle-based anticancer drug delivery systems have undergone preclinical evaluation.¹⁵³ In particular, NIR-labeled chitosan nanoparticles have demonstrated anti-tumor potential in a mouse animal model.¹⁵⁴ Due to their biocompatibility, tailorable chemistry and the presence of pH-sensitive functional groups, polysaccharides such as chitosan and their derivatives continue to be explored for their biomedical potential.

In addition, rapidly growing advances in the field of cancer nanotherapeutics have recently highlighted the importance of integrated multifunctional drug delivery systems capable of performing highly specific diagnostic and therapeutic tasks.³⁷ Chitosan has been successfully modified as MRI-NIRF and NIRF-CT multimodality nanoparticles and has demonstrated to be a versatile nanomaterial for cancer imaging.¹³⁸ A strategic design of the nanocarrier material, coupled with cancer cell target selectivity, tumor microenvironment stimuli-responsiveness and multimodal imaging capability, can indeed elevate the safety and efficacy of antitumor compounds. Further elucidation of chitosan's effectiveness as a polymeric micellar delivery system in relevant animal models is of utmost importance prior to any consideration for bench-to-bedside translation. These interdisciplinary approaches can ultimately enrich our fundamental knowledge of the neoplastic diseases as well as aid in developing strategies towards their eradication.

Chapter 2:

Hydrophobically modified glycol-chitosan micelles as drug delivery agents: application to a two-dimensional bone cancer model

2.1 Introduction

Osteosarcoma (OS) is a malignant mesenchymal tumor which constitutes the most common primary cancer in bone tissue. With an incidence of 4.8 million patients per year¹⁵⁵, this tumor is characterized by an aggressive growth, and it mostly affects adolescents and young adults, with peaks at age 16 for males and age 12 for females. In the majority of the cases, osteosarcoma generates from the metaphysis of long bones, the portion of a bone adjacent to the growth plate. The tumor is predominantly found in areas such as arms, legs, knees and shoulders, suggesting a role for rapid bone growth in the pathogenesis of OS. Important hallmarks of osteosarcoma are high invasion ability, early metastasis formation and high metastatic rate. During the last decades, developments in diagnosis strategies and clinical medicine have improved the success of the treatments of this solid tumor, reaching 65-76% of 5-year survival for patients with localized OS of the extremities.¹⁵⁶⁻¹⁵⁸ However, due to the high propensity of this tumor to invade lungs and other tissues, the outcome for patients with metastatic lesions shows a mortality incidence of more than 40 % and, in case of a relapse, the overall survival is less than 20%.¹⁵⁸ Among the causes that contribute to OS there are: rapid bone growth at the metaphysis area, environmental factors, such as radiation, and genetic predisposition due to syndromes or gene mutations.

Depending on the tumor stage and the patient's age, different therapeutic approaches are proposed. The current treatment options include surgery, chemotherapy and radiotherapy. In case of solid tumors accessible via surgical incision, low traumatic limb-salvage surgery remains the main therapeutic strategy. This procedure consists in the resection of the tumor followed by the reconstruction of the skeletal system and the surrounding soft tissue to restore the motor functionality.¹⁵⁹ Disadvantages associated with this practice might be related to complications, such as infections, osteoarthritis and difficulties in the rehabilitation. In addition, due to inadequate surgical margins, osteosarcoma cells can remain latent, leading to an aggressive tumor relapse. Therefore, adjuvant therapies pre- and post-surgery are required to limit tumor burden.

Currently, chemotherapy represents the most common treatment. Although effective, this approach is based on the use of cytotoxic drugs that usually attack cancerous cells as well as healthy cells, leading to various side effects (i.e. fatigue, nausea, vomiting, alopecia). Up to date, the available chemotherapeutic agents are cisplatin (platinum-containing compound), doxorubicin (anthracycline antibiotic), ifosfamide (alkylating agent) and methotrexate (anti-metabolite). All these compounds are associated with different levels of cytotoxicity to many tissues and organs (bladder, heart, intestine, skin, kidneys). On top of that, cancer cell resistance to chemotherapy is still a burden for the successful treatment of solid cancer.¹⁶⁰ Therefore, special consideration, in terms of doses and administration routes, is needed when dealing with young patients affected by osteosarcoma.

As an alternative approach, radiotherapy is often used in patients who refuse surgery or require palliation. Although performed as adjuvant method, radiotherapy might cause several side effects, such as erythema, epilation, fibrosis and radiation-induced neoplasia. In the past years, hormonal therapy, gene therapy and immunotherapy, as well as the use of novel therapeutic agents have been considered as valid alternatives.¹⁶¹⁻¹⁶³ Ando *et al.* proposed the use of liposomal muramyl tripeptide phosphatidyl ethanolamine as a delivery agent of an immune modulator, an adjuvant to chemotherapy, to improve the overall survival in patients with pulmonary metastases.¹⁶⁴ In 2005, the European American Osteosarcoma Study Group (EURAMOS) launched the first cooperative randomized clinical trial for localized OS (EURAMOS-I-COG, AOST0331) to study the addition of interferon and ifosfamide to standard chemotherapy agents¹⁶⁵. Phase II clinical trials on the toxicity profile of other adjuvants to chemotherapy (zoledronate, AOST06P1 and trastuzumab, AOST0121) are currently ongoing.

Considering the current status of the therapeutic strategies available for solid tumors such as OS, it is clear how important is the effectiveness of the chosen approach. Doses, drug formulation and routes of administrations can be finely tuned in order to minimize the side effects and obtain the desired outcome. Gene therapy constitutes a valid solution to deliver short nucleic acids in a more targeted manner, but the viral vector systems used for the delivery are not easily controllable. As a consequence, interest for non-viral vectors has recently increased, thanks to the many positive features that these systems present. In fact, liposomal complexes and polymeric and metallic nanoparticles can be synthesized according to their tailorable and chemical properties and selectively applied *in vivo* with minimal risk for the host.

Polymeric amphiphilics have recently attracted the attention of the research community as nano therapeutic agents, thanks to their unique physicochemical characteristics and their ability to form self-assembly structures. The study presented in this chapter focuses on the development of hydrophobically modified glycol chitosan (HGC), and on the analysis of how the physicochemical properties of this amphiphilic chitosan derivative contribute to the interaction of the biomaterial with human osteosarcoma cancer cells in a monolayer configuration. Glycol chitosan is a water soluble chitosan-derivative that can be easily modified to present an amphiphilic chemical structure. The HGC conjugates can self-organize in nanoparticulate systems, with a hydrophobic core, which acts as reservoir for an active agent compound, and a hydrophilic shell, that helps the solubility and favors the bio-distribution. Moreover, the peculiar chemistry of this system (with a positive residual charge at the surface, due to the free amino groups) and its deformability are responsible for the cell membrane adsorption and the cellular internalization of the nanoparticles (NPs). In addition, a recent study published by Yin *et al.*¹⁶⁶ in collaboration with our group assessed the hemo-compatibility of the HGC micellar systems, which did not cause hemolysis, nor affect platelet thrombogenicity and did not impair endothelial cell growth nor metabolic activity *in vitro*.

By tailoring the chemistry, a certain size and morphology can be obtained, resulting in a greater control of the route of entry in the cell. Macropinocytosis can become the preferred uptake mode of HGC NPs with the appropriate size, and lysosomal degradation can be avoided. In addition, the presence of free amine groups on the glycol chitosan chains might constitute the key factor for the success of the HGC complexes as drug delivery nanovectors. In fact, in case of endosomal capture, the amine groups can buffer the intra-vesicle acidic pH, leading to vesicle membrane swelling and rupture (the so-called “proton sponge effect”).^{19, 27} HGC NPs can be further functionalized with a near-infrared dye to allow non-invasive fluorescence optical tracking and imaging *in vivo*.

Considering the above mentioned physicochemical characteristics of the material system under study, we formulated the following hypotheses.

- Hypothesis (a): the extent of the hydrophobic substitution can modulate the behavior of the macromolecules in a water-based environment, affecting the self-assembly process and, thereby, the morphology and the physicochemical features of the resulting system.
- Hypothesis (b): the amphiphilic behavior of our micelles would allow an efficient drug

encapsulation, depending on the degree of hydrophobic modification introduced with the synthesis. Moreover, the pH-responsiveness of the chitosan-derivative nano-vehicles would allow a sustained release of the drug molecules in an acidic environment.

- Hypothesis (c): the cellular uptake mechanism and the intracellular fate of the nano therapeutics are dependent on the physicochemical and morphological features of the engineered systems. Moreover, micelle concentration and treatment duration are expected to play a crucial role in the uptake and internalization process.

In order to test our hypothesis, various chemical synthesis schemes and characterization methods have been implemented, and will be presented in details in the following sections of the Chapter. In addition, our nano therapeutic systems have been delivered to MG-63 cells in monolayers, as model for the human osteosarcoma. Cellular uptake experiments, cytomorphology and functional assays, and cytotoxicity analysis have been carried out in order to assess the suitability of the HGC micelles as drug delivery nano-carriers.

2.2 Methods

Synthesis of glycol chitosan-5 β -cholanolic acid conjugates

The hydrophobic modification of glycol chitosan (GC) with 5- β -cholanolic acid is carried out partially following the procedure presented by Kwon *et al.*¹²⁰ Briefly, GC (500 mg) is dissolved in HPLC water (60 ml). In a separate beaker, 5- β -cholanolic acid (150 mg), NHS (N-hydroxysuccinimide, 72 mg) and EDC (1-Ethyl-3-[3-dimethylaminopropyl]carbodiimide hydrochloride, 120 mg) were dissolved in methanol (60 ml) and subsequently added to the GC solution. The amount of reagents used in this first set of synthesis were based on a mol/mol feed ratio of 0.185 (moles of 5- β -cholanolic acid over moles of amino sugar residues present in the glycol chitosan chain). In order to vary the amount of hydrophobic modification introduced into the system, a mol/mol feed ratio of 0.0115 was also used in a second set of conjugation experiment (were 8.93 mg of 5- β -cholanolic acid, 4.27 mg of NHS, and 7.1 mg of EDC were used). The crosslinking agent EDC reacted with the carboxylic acid groups of the 5- β -cholanolic acid molecule to form an active intermediate (O-Acylsourester). As a result of a nucleophilic attack at the C = O from the primary amine of the glucosamine residue in the GC chain, a covalent amide bond was

formed and isourea was released as by-product. When NHS is present in the mixture a more stable intermediate can be formed at physiological pH. EDC coupled the carboxylic acid group of the cholesterol moiety to give an amine-reactive-NHS ester. The new stable intermediate was ready to react with primary amines to efficiently form amide bonds. After three days of dialysis to eliminate the unreacted cholesterol molecules and the by-products of the reactions (for 1 day against a water/methanol mixture (1/4, v/v) and for 1 day against pure water), the resulting system was centrifuged for 30 minutes at 2790 rpm, lyophilized for 3 days to obtain the GC-5- β -cholanolic acid conjugate (HGC), and then finely ground into powder. Subsequently, the HGC was labeled with a cyanine dye that emits in the near-infrared range (Cy5.5-NHS, ex = 673 nm, em = 707 nm). One mg of activated NHS-ester of the cyanine dye was dissolved in 250 μ l of DMSO. In a separate beaker HGC (100 mg) was dissolved in DMSO (40 ml) and the Cy5.5 solution was added drop wise. The resulting system was kept in the dark for 6 hours at room temperature under constant stirring. The N-hydroxysuccinimide ester reacted with the free amine on the HGC chain to form an amide bond. After dialysis, freeze-drying and grinding, an intense blue powder was obtained. The polymer synthesis process and the resulting chemical structures of the products are reported in Figure 2.1 and Figure 2.2, respectively.

Nanoparticle preparation

The HGC conjugate was suspended in HPLC water and vortexed. The suspension was then ultra-sonicated for 6 minutes with a probe-type sonifier (Soniprep 150, MSE, UK) equipped with an exponential probe (Figure 2.1). To prevent the increase in the temperature the particle suspension was kept in an ice bath. The self-assembled HGC nanoparticles were passed through syringe filters (pore sizes 0.8 and 0.2 μ m, Pall Corporation) as a sterilization method for the following characterization and cell culture delivery.

Nanoparticle physicochemical characterization

To assess the success of the conjugation, both the HGC conjugates and the starting materials were analyzed through Attenuated Total Reflectance *via* a Nicolet iS50-FT-IR spectrometer (Thermo Scientific). Spectra were collected from 659.9 to 4000.18 cm^{-1} with 16 scans per sample. The size distribution and the surface charge of HGC nanocomplexes suspension were determined at 25 $^{\circ}\text{C}$ by Dynamic Light Scattering (DLS, Zetasizer Nano, Malvern Instruments Ltd.,

Westborough, MA). Additional measurements were performed with a NanoBrook ZetaPlus Zeta Potential Analyzer (Brookhaven Instruments Corporation, NY).

In order to assess the pH responsiveness of the synthesized polymers as well as the behavior of the fabricated micellar systems, zeta potential measurements over a wide pH range (2.5-13.0) have been acquired. Briefly, the polymers presenting three different degrees of hydrophobic substitution were dissolved in HPLC water. The pH values of the suspensions were adjusted by adding either NaOH 0.1M or HCl 0.1M. Zeta potential measurements of the polymer suspensions were acquired. Subsequently, the suspensions were probe-type sonicated according to the protocol previously reported. The freshly prepared self-assembled nanoparticle suspensions were characterized in terms of surface charge and size. Zeta potential titration curves for the glycol chitosan polymer, the HGC_(0.0115) conjugated polymer and micellar system, and the HGC_(0.185) conjugated polymer and micellar system have been obtained. The isoelectric points (pI) of each system were calculated by fitting the curves with a first order exponential equation. In addition, the pKa (the acid-base dissociation reaction constant) values were estimated as the mid point between the calculated pI and the lowest pH used in the titration experiment.

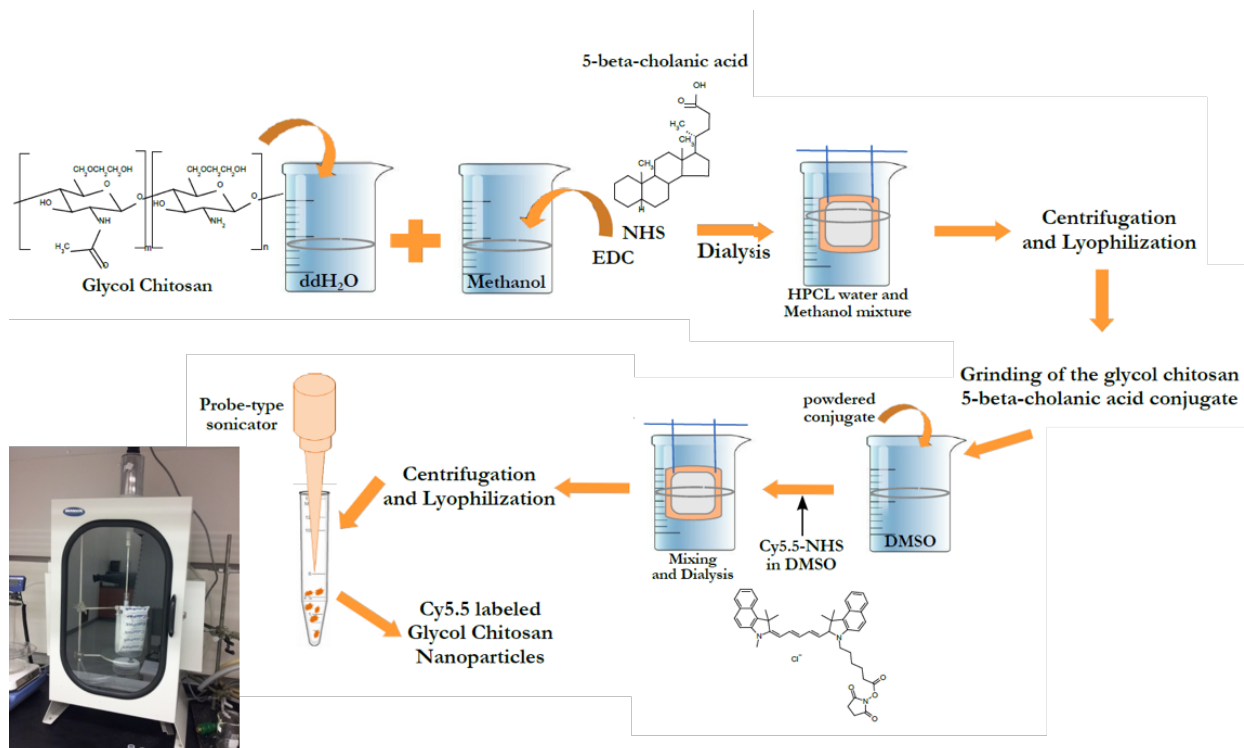


Figure 2.1 Schematic depicting the synthesis steps involved in the formulation of the Cy5.5-labelled, hydrophobically modified glycol chitosan polymer, and subsequent self-assembly nanoparticle preparation by means of a probe-type sonicator.

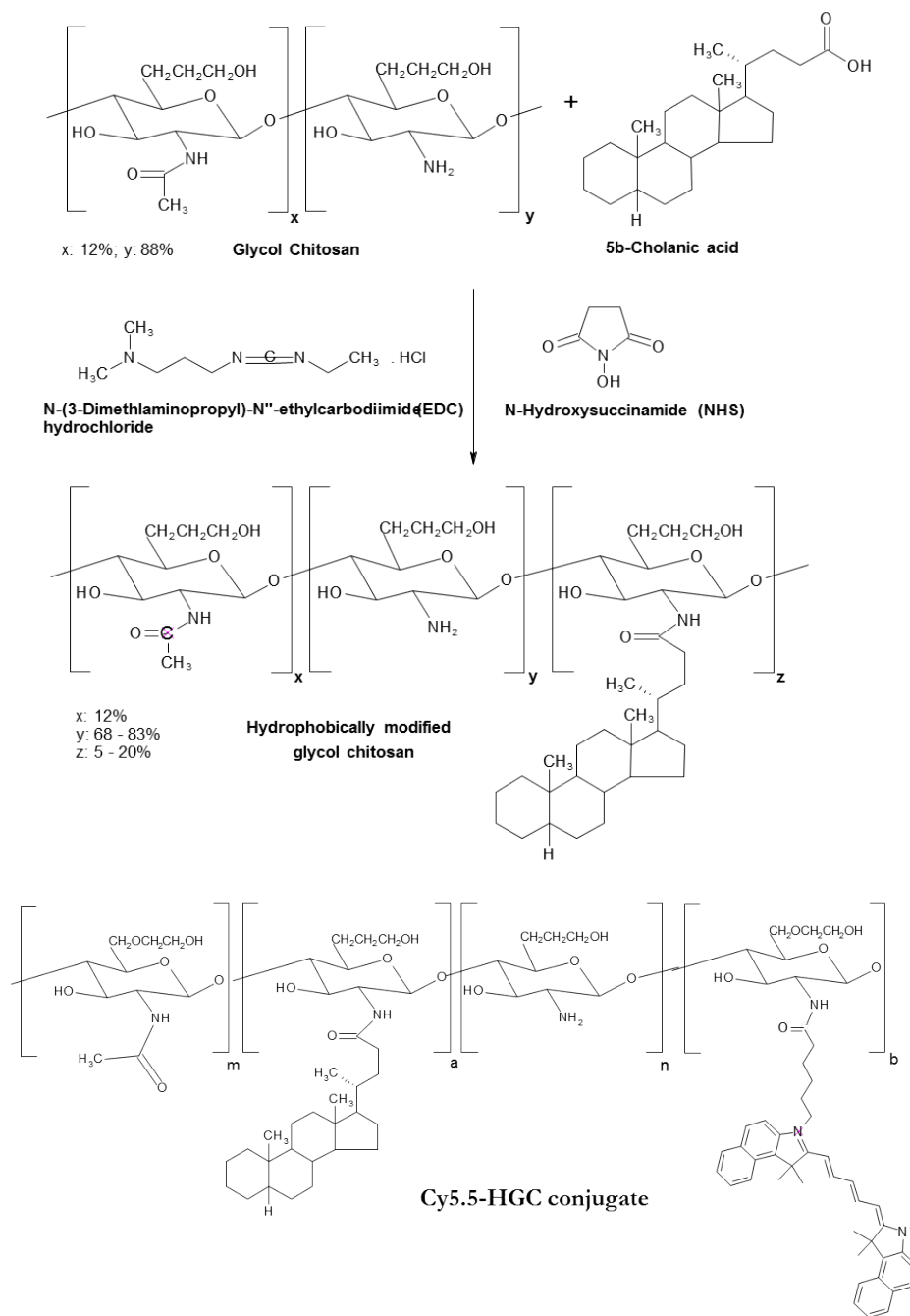


Figure 3.2 Synthesis process and chemical structure of the HGC conjugate, and of its fluorescently labelled derivative.

Morphological analysis of the self-assembled nanoparticles

The morphology was obtained by placing few drops of HGC nanoparticle suspension on Lacey Carbon Film on 300 mesh copper grids and the extra solution is blotted with filter paper and air dried. The grids are observed under the Transmission Electron Microscope (JEM-1400LaB6, 120keV TEM, JEOL) with an accelerating voltage of 60kV. The characterization of the HGC vehicles was carried out at the Center for Functional Nanomaterials at Brookhaven National Laboratory.

Drug loading onto HGC nanocomplexes

The hydrophobic core of the self-assembled HGC nanocomplexes can act as reservoir for hydrophobic molecule such as anticancer drug. In order to obtain a hydrophobic drug -amphiphilic polymer complex the following steps were carried out. In a round bottom flask, HGC powder (70 mg) was dissolved in dimethyl sulfoxide (DMSO, 20 ml). In an eppendorf tube, a solution of the hydrophobic drug, doxorubicin, in DMSO (3.5 mg/ml) was prepared, and a drop of trimethylamine (TEA) was introduced to favor the complexation reaction. Doxorubicin was kindly donated by Dr. Michele Caruso, from the Medicinal Chemistry of Nerviano Medical Sciences (Nerviano, Milano, Italy). The drug solution is added drop-wise and the mixture is kept under stirring for 5 hours, in the dark at room temperature. To favor the formation of self-assembled drug-polymer complexes, HPLC water (50 ml) was added to the mixture and the system was kept under stirring overnight. During this step the formation of a precipitate was observed, indicating the partial self-assembly of the amphiphilic polymer chains: when the phase separation occurred, the complexation of the hydrophobic drug within the hydrophobic segment of the polymer molecules was favored (Figure 2.3, step 1). To eliminate the drug molecule loosely complexed with the HGC polymeric chains, the suspension was loaded into dialysis cassettes (3.5 kDa molecular weight cut off) and dialyzed against HPLC water for 24 hours (Figure 2.3, step 2). The purified systems was centrifuged for 30 minutes at ~ 3000 rpm and lyophilized for 3 days to obtain the drug-HGC complex, and then finally ground into powder (Figure 2.3, steps 3, 4, and 5). The drug-loaded HGC self-assembled nanocomplexes were prepared as previously described. Doxo-HGC_(0.0115) and doxo-HGC_(0.185) NPs were characterized in terms of size and surface charge by Dynamic Light Scattering (DLS, Zetasizer Nano, Malvern Instruments Ltd., Westborough, MA) and their morphology was observed under the Transmission Electron Microscope (JEM-1400LaB6, 120keV TEM, JEOL).

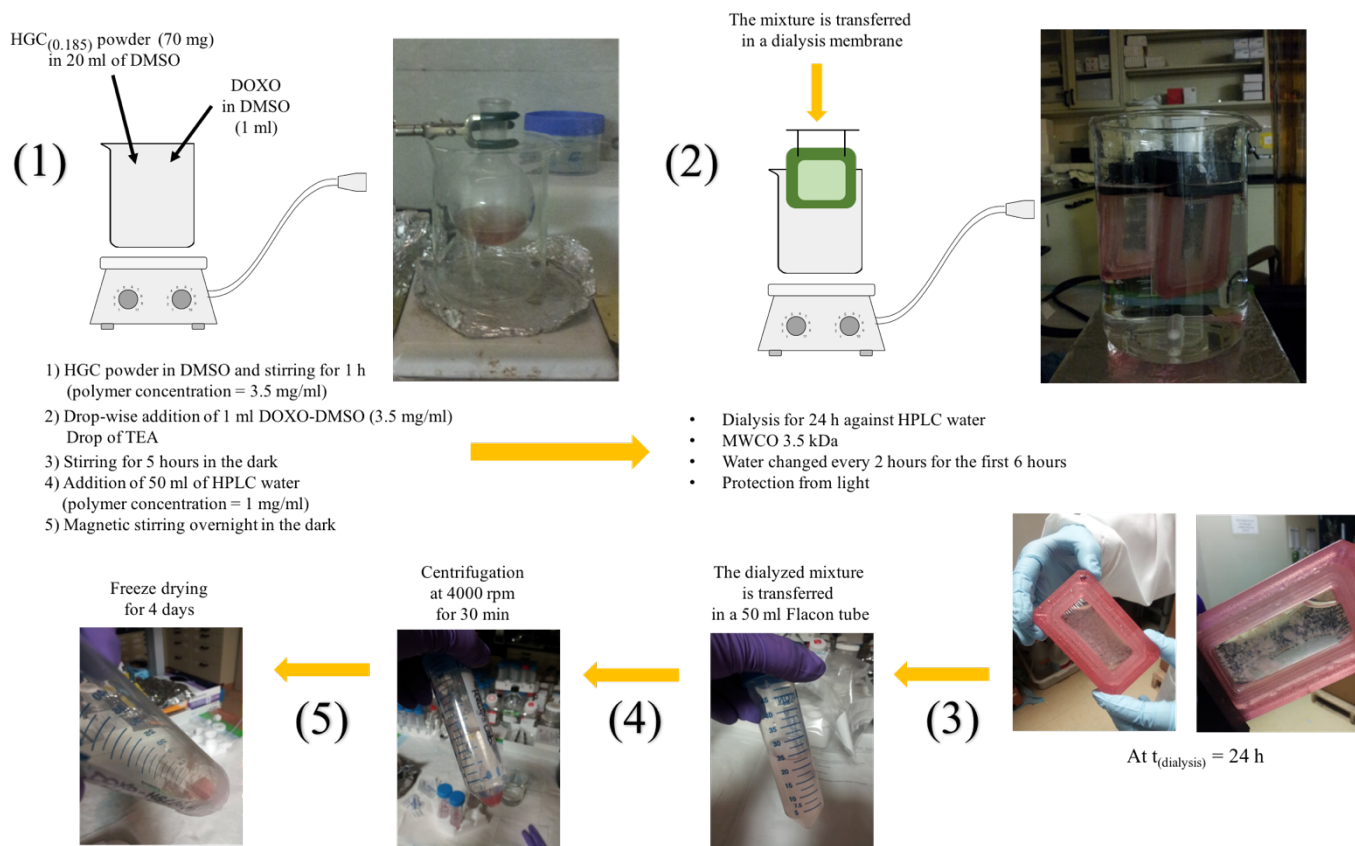


Figure 2.3 Schematic depicting the doxorubicin complexation with the HGC polymer.

Assessment of the loading content

To quantify the amount of physically encapsulated drug within the amphiphilic nanocomplexes. 2 mg of the freeze-dried doxo-HGC powder were dissolved in 2 ml of 0.1 M HCl. The presence of the mineral acid would favor the hydrolysis of the glycol chitosan derivative micelles and help the release of the complexed drug molecules. The resulting disrupted system was diluted in 8 ml of DMSO and aliquots of the solution were pipetted into 96 well-plate for the fluorescence emission readings at 580 nm (Tecan Infinite[®] 200 PRO, Switzerland). The readings were compared with a standard curve of doxorubicin in DMSO:HCl 0.1 M (10:2, v/v) previously obtained. Moreover, an equivalent amount of HGC conjugate (2 mg) was dissolved in 10 ml of the solvent mixture as blank. The evaluation of the loading content was performed considering the following equation:

$$LC\% = \frac{W_{Doxo \text{ in micelles}}}{W_{loaded \text{ micelles}}} \times 100$$

The evaluation of the encapsulation efficiency was performed considering the following equation:

$$EE\% = \frac{W_{Doxo \text{ in micelles}}}{W_{feed \text{ Doxo}}}$$

Release kinetics

The release experiment was carried out *in vitro*. Doxorubicin-loaded HGC_(0.185) freeze-dried powder were re-suspended in 4 ml of phosphate-buffered saline (PBS, pH 7.4) at a concentration of 1 mg/ml. The suspension was placed in a dialysis tubing (MWCO 10,000 Da) and the extremities were tied with clips. The sealed tube was immersed in a beaker containing 40 ml of PBS at pH 7.4 and the system was kept under gentle shaking, at room temperature, in the dark. At predetermined time intervals, 3 ml were taken from the beaker for evaluation and were replaced with fresh buffer, to maintain the sink conditions. To observe the effect of the pH on the release behavior of the micellar system, a parallel experiment was performed re-suspending the doxorubicin-loaded HGC_(0.185) freeze dried powder in 6 ml of KH₂PO₄ – Na₂HPO₄ buffer (pH 5.5) at a concentration of 1 mg/ml. For the detection of the released doxorubicin, a fluorescence plate

reader was used (Tecan Infinite 200 PRO, Switzerland) considering 485 nm as excitation wavelength and 580 nm as emission wavelength. The readings were compared with a standard curve of doxorubicin in the buffers at pH 7.4 and pH 5.5.

Cell culture

Human osteosarcoma MG-63 cells were seeded onto 24-well plates at a starting density of 2000 and 5000 cells/cm² in complete DMEM (supplemented with 10% FBS and 1% P/S), up to 5 days. At the desired time point, cells were rinsed twice with PBS (1X), fixed with 3.7% formaldehyde and stained with 2.5 µg/ml of 4',6-diamino-2-phenylimidazole (DAPI) to highlight the nuclei. Using a Fluorescent Microscope (Olympus IX51) under a DAPI filter, 250 images per sample were acquired on average. The images were subsequently processed through ImageJ software (www.rsbweb.nih.gov) to count the cells and obtain a growth curve.

Cell morphology

In order to visualize the structure of the cells and the production of the extracellular matrix proteins, samples were permeabilized with 0.4% Triton for 8 minutes and incubated for 30 minutes in 1% BSA solution of rabbit polyclonal to fibronectin (1:200 dilutions, Abcam, Cambridge, MA), as the primary antibody. After rinsing twice with PBS (1X), samples were incubated for 30 minutes in 1% BSA solution of Cy3 goat anti-rabbit IgG (1:100 dilutions, Jackson Immuno), as secondary fluorescent antibody. After rinsing twice with PBS (1X), cells were stained for 20 minutes with Alexa Fluor 488 phalloidin (1:100 dilution in PBS, Invitrogen) to highlight the actin structure. Lastly, cells were incubated in 2.5 µg/ml of DAPI to stain the DNA. The samples were imaged using the Olympus IX51 Fluorescent Microscope under the DAPI, Alexa Fluor 488 and PI filters.

Cell motility

Human osteosarcoma MG-63 cell motility in the presence or in the absence of HGC_(0.185) nanoparticles was assessed. Briefly, cells were plated in 35 mm tissue culture plates in complete DMEM (supplemented with 10% FBS and 1% P/S) at a seeding density of 5000 cells/cm². After attachment overnight the media was replaced with serum free DMEM containing HGC_(0.185) nanoparticles at different concentrations (500 and 1000 µg/ml). After 1 and 3 hours of incubation, the samples were rinsed with serum free DMEM to wash away the non internalized nanoparticles.

In the presence of CO₂ independent medium (supplemented with FBS, 200 mM L-glutamine and PenStrep) cells were imaged with the Olympus IX51 Fluorescent Microscope in the phase contrast mode. Time lapses of 2 hours with 1 image every 3 minutes were acquired. The images were subsequently processed through ImageJ software (www.rsweb.nih.gov) to track the nuclei of the cells, visualize their path and compute the average cell speed and their displacement under the different conditions. Samples plated in complete DMEM and in serum free DMEM were also considered as controls. The statistical significance of the findings between experimental groups and control was determined by two-tail Student's *t*-test considering unequal variances and $p < 0.05$ as statistically significant.

Cellular nanoparticle uptake in monolayers

Human osteosarcoma MG-63 cells were plated on 13 mm glass coverslips at a starting density of 7000 cells/cm² and let attached overnight in complete DMEM. Cy5.5-HGC_(0.0115) and Cy5.5-HGC_(0.185) nanoparticle containing medium was applied to the cells for different incubation time, prior bath-sonication for 10 minutes to allow a good dispersion of the polymeric vehicles. At the desired time point, cells were rinsed with serum free DMEM to remove the unbound nanoparticle, washed twice with PBS (1X) and fixed in 3.7% formaldehyde for 20 minutes. The glass coverslips were subsequently mounted on microscope glass slides with Fluoromount G (Southern Biotech, Alabama). To visualize the near-infrared nanoparticles internalized in the cancer cells, the samples were observed under a Leica TCS SP5 Confocal Laser Scanning Microscope (Leica Microsystems, Ontario, Canada). All images were acquired with a 63X oil immersion lens, at speed of 10 Hz and at a resolution of 1024x1024 pixels. The confocal imaging was conducted at the Center for Functional Materials at Brookhaven National Laboratory.

Lysosomal vesicle staining

To investigate the intracellular fate of the fluorescently labelled polymeric nanoparticles, a co-localization study with lysosomes was performed. MG-63 cells were plated on 13 mm glass coverslips at a starting concentration of 70000 cells/cm² and let attached overnight. The media was replaced with Cy5.5-HGC_(0.0115) and Cy5.5-HGC_(0.185) containing media for different incubation periods (15 and 30 minutes, 1 and 3 hours). At the desired time points, cells were rinsed with serum free DMEM to wash away the non internalized nanoparticles and incubated with 50 nM of

LysoTracker[®] Green (Thermo Fisher Scientific) for 15 minutes at 37 °C, according to the supplier's protocol. Subsequently, cells were washed twice with PBS (1X), fixed in 3.7% formaldehyde and mounted on microscope glass slides with Fluoromount G (Southern Biotech, Alabama). The samples were analyzed with a Leica TCS SP5 Confocal Laser Scanning Microscope (Leica Microsystems, Ontario, Canada). All images were acquired with a 63X oil immersion lens, at a speed of 10 Hz and at a resolution of 1024x1024 pixels. The confocal imaging was conducted at the Center for Functional Materials at Brookhaven National Laboratory.

Nanoparticle cytotoxicity on cell monolayers

Human osteosarcoma MG-63 cells were seeded in 24-well plates at a starting density of 10000 cells/cm² in complete DMEM and let attach overnight at 37 °C in the presence of 5% CO₂. Serum free, phenol red free DMEM containing HGC_(0.185) nanoparticles at concentrations ranging from 0.075 to 226 µg/ml was added into the wells. Samples remained in constant contact with the nanocomplexes up to 72 hours. The cytotoxicity of the empty nanovehicles was evaluated using the MTS assay (Promega, Madison, WI). In this colorimetric assay, a tetrazolium compound, [3-(4,5-dimethylthiazol-2-yl)-5-(3-carboxymethoxyphenyl)-2-[(4-sulfophenyl)2H-tetrazolium] and an electron coupling reagent (phenazine methosulfate, PMS) were directly added to the wells (25 µl). The MTS was reduced into a formazan product, soluble in the tissue culture media, by the metabolically active cells. Depending on the number of viable cells in the sample, the medium would assume a purple-brown color after 3.5 hours of incubation at 37 °C. The diluted medium was placed in a 96-well plate and the absorbance at 490 nm was recorded by means of a plate reader (Tecan Infinite[®] 200 PRO, Switzerland). Data are expressed as the percentage of viable cells compared to the control group and are presented as means ± s.e. The statistical significance of differential findings between experimental groups and control was determined by Student's *t*-test considering unequal variances and $p < 0.05$ as statistically significant.

Free drug delivery to the monolayer cancer cell culture

With the aim of assessing the free drug uptake and its intracellular distribution within the human osteosarcoma MG-63 cell monolayer, doxorubicin was administrated at different concentrations (1, 3 and 10 µM) and for various time points (1, 3, 6 and 24 hours). Briefly, cells were plated on glass coverslips at a concentration of 7000 cells/cm² and let attach overnight in

DMEM complete media. Afterwards, the media was changed with serum free, doxorubicin containing DMEM and samples were kept in incubation at 37 °C and 5% CO₂ atmosphere. At the desired time points, cells were rinsed with PBS (1X), fixed in 3.7% formaldehyde and stained with 2.5 µg/ml of 4',6-diamino-2-phenylimidazole (DAPI) to highlight the nuclei. The actin staining was performed as previously described. Subsequently, the coverslips were mounted on microscope glass slides with Fluoromount G (Southern Biotech, Alabama) and analyzed under the Olympus IX51 Fluorescent Microscope. Moreover, in order to achieve a more detailed understanding on the intracellular/intranuclear distribution of the free drug, samples were imaged under a Leica TCS SP5 Confocal Laser Scanning Microscope (Leica Microsystems, Ontario, Canada). All images were acquired with a 63X oil immersion lens, at a speed of 10 Hz and at a resolution of 1024x1024 pixels. The confocal imaging was conducted at the Center for Functional Materials at Brookhaven National Laboratory.

Encapsulated drug delivery to the monolayer cancer cell culture

To evaluate the cellular distribution of the encapsulated drug, doxo-HGC_(0.185) nanocomplexes were delivered to human osteosarcoma MG-63 cell monolayer, at different concentrations (24.3, 81.1 and 243.4 µg/ml equivalent to 1, 3 and 10 µM of doxorubicin, respectively) and for various time points (1, 3, 6, 24, 48 and 72 hours). The amount of HGC vehicles needed for the experiment was calculated considering the loading content (LC%) previously obtained for this drug-amphiphilic polymer system. The cell plating and the administration of the nanotherapeutics to the cancer cell monolayer was performed as previously described. In addition, to assess the co-localization of the complexes with intracellular vesicles, LysoTracker[®] Green (Thermo Fisher Scientific) staining was conducted (50 nM for 15 minutes at 37 °C). The samples, fixed and mounted on microscope glass slides, were imaged under a Leica TCS SP5 Confocal Laser Scanning Microscope (Leica Microsystems, Ontario, Canada). All images were acquired with a 63X oil immersion lens, at a speed of 10 Hz and at a resolution of 1024x1024 pixels. The confocal imaging was conducted at the Center for Functional Materials at Brookhaven National Laboratory.

Cytotoxicity of free and encapsulated drug on the monolayer cancer cell culture

Human osteosarcoma MG-63 cells were seeded in 24-well plates at a starting density of 10000 cells/cm² in complete DMEM and let attach overnight at 37 °C in the presence of 5% CO₂. Serum free, phenol red free DMEM containing free doxorubicin at concentrations ranging from 0.01 to 30 μM was added into the wells. Samples remained in constant contact with the anticancer compound up to 72 hours. Cells incubated in serum free, phenol red free DMEM as well as in complete DMEM were considered as controls. The cytotoxicity of the free doxorubicin was evaluated using the MTS assay (Promega, Madison, WI), as previously described. Data are expressed as the percentage of viable cells compared to the control group and are presented as means ± s.e. The data presented were normalized with respect of the serum starved, untreated control sample of each day. The statistical significance of differential findings between experimental groups and control (three independent experiments) was determined by Student's *t*-test considering unequal variances and $p < 0.05$ as statistically significant.

To assess the effect on the monolayer cell viability of the encapsulated drug, doxo-HGC_(0.185) nanocomplexes were administrated to human osteosarcoma MG-63 cells following a similar protocol. The concentration of the loaded vehicles was ranging from 0.081 to 243.4 μg/ml, to match the amount of free drug used, calculated considering the loading content (LC%) previously obtained for this drug-amphiphilic polymer system. The cytotoxicity of the doxo-HGC_(0.185) nanocomplexes was evaluated using the MTS assay (Promega, Madison, WI), as previously described. Data are expressed as the percentage of viable cells compared to the control group and are presented as means ± s.e. The data presented are normalized with respect of the serum starved, untreated control sample of each day.

2.3 Results and Discussion

Hydrophobically modified glycol chitosan micelles have been synthesized and characterized in terms of morphology and physicochemical properties

The synthesis of the amphiphilic chitosan derivative has been performed through hydrophobic modification of glycol chitosan (GC) with 5- β -cholanic acid via EDC and NHS chemistry, as presented in Figure 2.1. In addition, a cyanine fluorophore was added to favor the micelle visualization (Figure 2.2). In order to check the success of the synthesis, FT-IR spectrum of the HGC powder has been compared with the spectra of the two starting components. In Figures 2.6 and 2.7 the overlays of the acquired spectra of the substances in the region of interest are reported. Vibrational spectroscopy is a powerful tool for the identification of frequencies characteristic of well-defined functional groups. A linear molecule consisting of N atoms has $3N-5$ fundamental vibration modes, while a non-linear molecule presents $3N-6$ fundamental vibration modes. Many factors may influence the frequencies of a molecular vibration, such as the mass of the molecule and the steric effect of the substituents, as well as the phase of the material (condensed phase, solution, gas). Moreover, when atoms pertaining to two different bonds are close to one another in the molecule, vibrational coupling can occur.¹⁶⁷ As a result, the labeling of the group frequencies can be challenging. In this case the bands of interest have been assigned as in Table 2.1. The amide I band refers to the stretching of the carbonyl group involved in the amide linkage, while the amide II band is related to the N-H deformation vibration. The other representative band is constituted by the C = O stretching vibration of the carbonyl group in the carboxylic acid at 1723 cm^{-1} . As visible from the spectra in Figure 2.7 and the data in Table 2.1, the HGC conjugate presents the band at 1725.6 cm^{-1} pertaining to the carboxyl group of the cholesterol moiety. Although the contribution of the peak is smaller than the one obtained from the 5- β -cholanic acid spectrum, this can be considered a hallmark for the conjugation between the GC and the hydrophobic molecule. In addition, the HGC conjugate presents both amide bands slightly shifted, if compared with the pure GC. This further supports the hypothesis that an amide bond between the glucosamine and the cholesterol compound was formed during the reaction. The data reported in Table 2.2 represent the area (baseline corrected) underneath the peaks: both amide bands in the HGC are associated to a larger area, validating the conjugation. A term of comparison between the pure GC and the functionalized one can be obtained by considering the sum of the total area of the amide peaks

(total amide) divided by the area of the C – O stretching peak at 1055 cm^{-1} (considered as a reference). From the calculated values (0.0676 for the GC and 0.1042 for the HGC), appears visible that a higher content of amide linkage is present in the HGC conjugate. Taken together, these data suggest the successful conjugation of the 5- β -cholanolic acid to the glycol chitosan chain and the synthesis of the amphiphilic chitosan derivative.

Chitosan is a positively charged polysaccharide which interacts with water molecules primarily upon inter- and intra-molecular interactions, such as hydrogen bonds and Van der Waals forces. Due to its polyelectrolyte behavior, the physicochemical properties of chitosan can be controlled acting on pH, ionic strength and temperature of the solution.¹⁶⁸ In a water-based environment, at $\text{pH} < 6.5$ the molecules are solvated due to the presence of protonated amino groups. At higher pH values, fewer groups get protonated and the hydrophobic character becomes stronger. This behavior arises from the contemporary presence on the chitosan backbone of slightly hydrophobic segments, the acetamide groups, and hydrophilic segments, the amino groups, which may lead to chitosan self-aggregation in acetate buffer solutions. Several strategies have been implemented to modulate chitosan behavior in solutions, either to increase its water solubility by introducing hydrophilic groups, or to increase its self-aggregation potential by grafting hydrophobic moieties onto the reactive functional groups ($-\text{NH}_2$ and $-\text{OH}$). In fact, hydrogen bonding between water molecules and hydroxyl or carboxyl groups on the chitosan-derivative chain is responsible for enhanced water solubility, while intra-molecular hydrogen bonding and electrostatic repulsion between the charged chain segments tend to favor its aggregation in solution.¹⁶⁸ Amphiphilic molecules possess the capability of forming aggregates in which the hydrophobic segments are oriented within the cluster, while the hydrophilic domains are pointed towards the solvent. The presence of either cholesterol-like moieties or alkyl segments grafted to a polymeric chain has been shown to favor the self-organization of the macromolecules into nanoparticulate systems (as shown in the schematic reported in Figure 2.4).^{63, 81, 96, 98, 104, 120} Moreover, the content of rigid, hydrophobic pendants in glycol chitosan derivative nanoparticles has been shown to influence micelle serum stability and deformability, critical factors in the design of efficient drug delivery agents, able to survive blood circulation and extravasate in tumor interstitium.¹⁶⁹ We hypothesized that the extent of the hydrophobic substitution can modulate the behavior of the macromolecules in a water-based environment, affecting the self-assembly process and, thereby, the morphology and the physicochemical features of the resulting system. A lower

degree of hydrophobic substitution should be correlated with a lower micelle stability while the presence of more hydrophobic substitutions should improve the micelle surface activity and stability.¹⁶⁸ Based on the work published by Kwon *et al.*,¹²⁰ two different mol/mol feed ratios have been considered in the synthesis process, 0.0115 and 0.185, where the number indicates the moles of 5- β -cholanic acid over moles of amino sugar residues present in the glycol chitosan chain. Those ratios should be associated with a degree of substitution (DS) of about 1.10% and 5.21% < DS < 6.42%, respectively.¹²⁰

To obtain the polymeric nanoparticles, the resulting HGC powders were suspended in HPLC water at a concentration of 1 mg/ml and ultrasonicated with a probe-type sonifier. During this step, the dispersion of the amphiphilic polymeric chains is promoted: the hydrophobic domains on the HGC chains tend to preferentially cluster in the center, away from the water molecules, while the hydrophilic GC domains are distributed on the outer layer, facing the water environment. The nanoparticle suspensions were subsequently filtered (0.8 and 0.2 μ m) and sonicated in a water bath to allow homogeneous dispersion of the nano-vehicles. The resulting systems were characterized in terms of size and morphology through Dynamic Light Scattering (DLS) and Transmission Electron Microscopy (TEM). The average diameter of the HGC_(0.185) vehicles was 288.6 ± 21.8 nm (Table 2.3) and it remains stable up to two weeks of shelf life when stored at 4°C (data not shown). The zeta potential measurements highlighted the positive charge of the surface ($+13.2 \pm 0.2$ mV), as expected considering the polycationic nature of the main matrix component. For the case of the lower degree of substitution, HGC_(0.0115) nanoparticles presented a bigger average diameter of 339.38 ± 2.8 nm (Table 2.3). This result indicates the formation of a less stable and more loose micellar structure, probably due to the presence of less numerous hydrophobic domains in the core. In addition, the zeta potential analysis revealed a less positive value, $+4.47 \pm 0.52$ mV, which further confirms the lower surface activity of this system. The TEM morphological analysis showed HGC_(0.185) micelles with an elongated spherical shape and a compact structure (Figure 2.5).

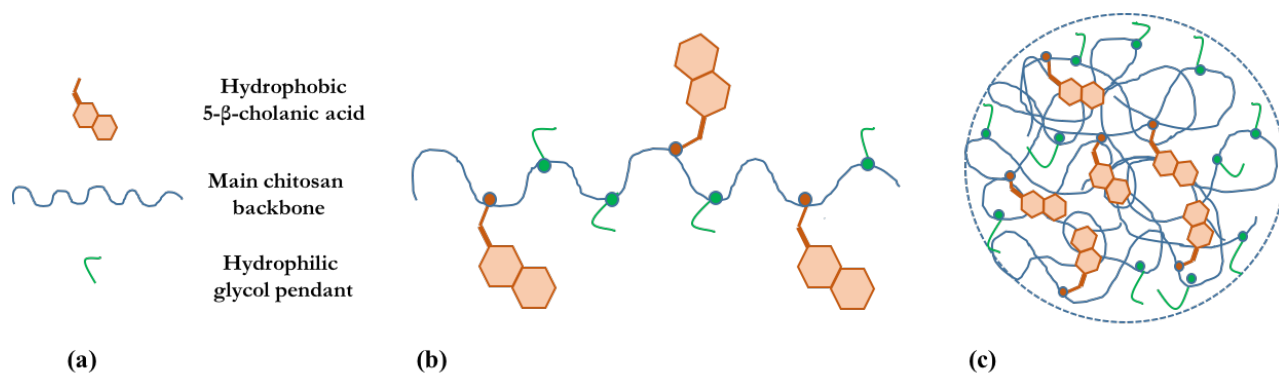


Figure 2.4 Schematic depicting the self-assembly process of amphiphilic polymeric chain: (a) building blocks of the system, (b) resulting polymer chain, and (c) micellar structure with the hydrophobic core containing the 5- β -cholanic acid pendants and the hydrophilic shell presenting the glycol residues.

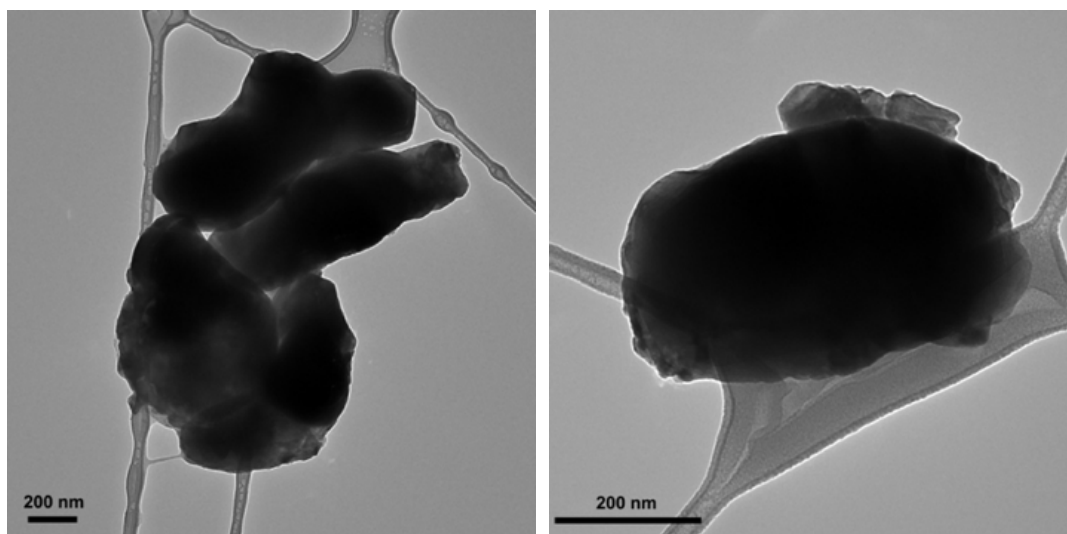


Figure 2.5 TEM micrographs of $HGC_{(0.185)}$ self-assembled complexes depicting ellipsoid-shaped nanoparticles with faceted contours. The average hydrodynamic diameter measured by DLS is 288.6 ± 2.8 nm and the average zeta potential is $+13.2 \pm 0.2$ mV. Scale bar 200 nm.

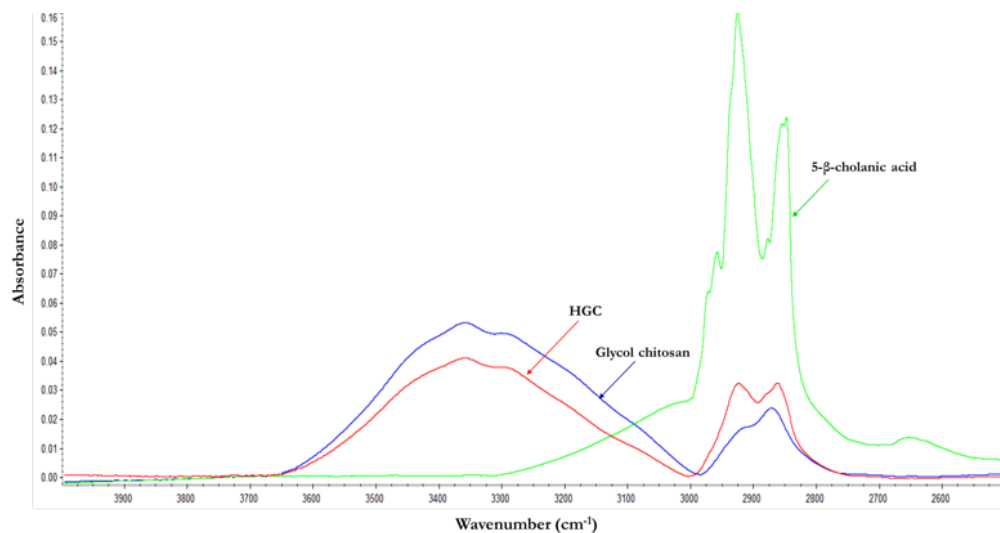


Figure 2.6 IR spectra: overlay in the region 4000-2500 cm^{-1}

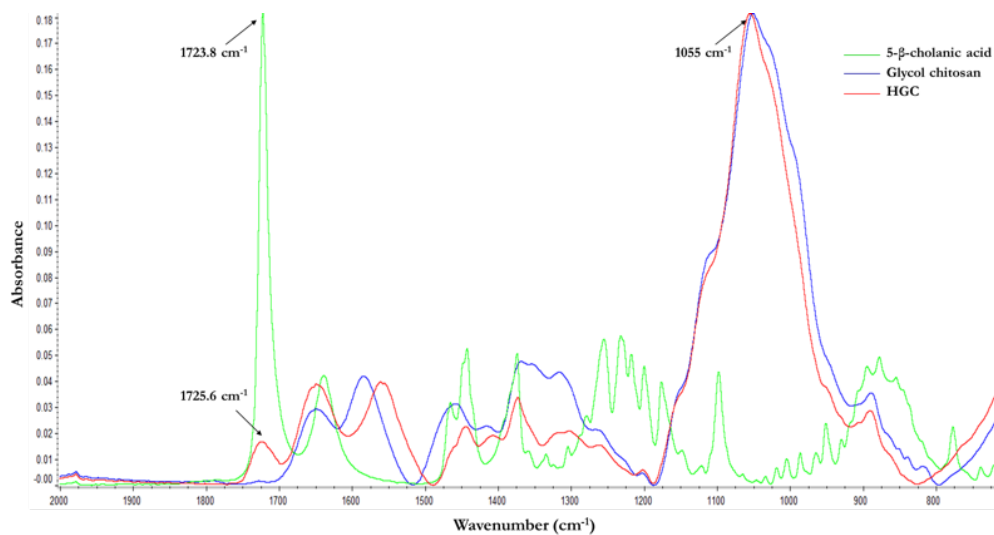


Figure 2.7 IR spectra: overlay in the region 2000-700 cm^{-1}

Table 2.1 IR frequencies of the representative functional groups expressed in cm^{-1}

	<i>-CH₃ and -CH₂ stretch</i>	<i>-NH and -OH stretch</i>	<i>O-CH₂ stretch (ether)</i>	<i>C=O stretch</i>	<i>Amide I</i>	<i>Amide II</i>	<i>-C-O stretch (alcohol)</i>	<i>-CH₂-NH₂ bend</i>
<i>GC</i>	no peak	3360.6	2872.2	no peak	1651.5	1585.7	1052.5	1459.5
<i>5-β-cholanic acid</i>	2926.3	no peak	no peak	1723.8	no peak	no peak	no peak	no peak
<i>HGC_(0.185)</i>	no peak	3360.2	2862.5	1725.6	1650.8	1562.7	1055.1	1445.5

Table 2.2 Area associated with the IR frequencies of the representative groups

	<i>-CH₃ and -CH₂ stretch</i>	<i>-NH and -OH stretch</i>	<i>O-CH₂ stretch (ether)</i>	<i>C=O stretch</i>	<i>Amide I</i>	<i>Amide II</i>	<i>-C-O stretch (alcohol)</i>	<i>-CH₂-NH₂ bend</i>
<i>GC</i>	no peak	18.42	2.22	no peak	0.506	1.173	24.85	0.729
<i>5-β-cholanic acid</i>	11.123	no peak	no peak	4.935	no peak	no peak	no peak	no peak
<i>HGC_(0.185)</i>	no peak	13.417	3.57	0.343	1.089	1.407	23.967	0.361

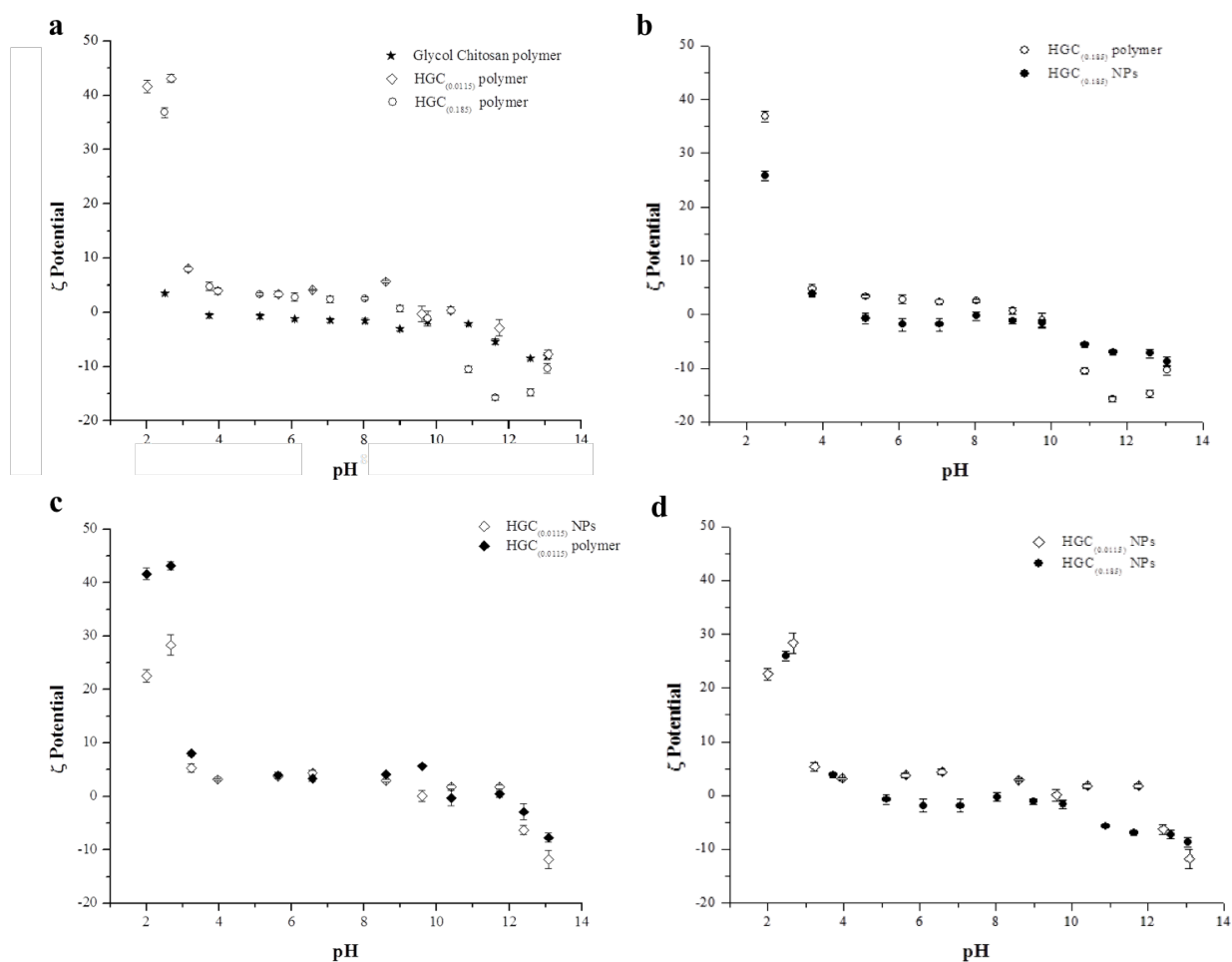


Figure 2.8 Comparison of the zeta potential titration curve (zeta potential vs pH) for (a) the glycol chitosan, HGC_(0.0115) and HGC_(0.185) polymeric systems and the nanoparticulate systems: (b) HGC_(0.0115) polymer and nanoparticles, (c) HGC_(0.185) polymer and nanoparticles, (d) HGC_(0.0115) and HGC_(0.185) nanoparticles. Error bars represent s.e. of 9 measurements.

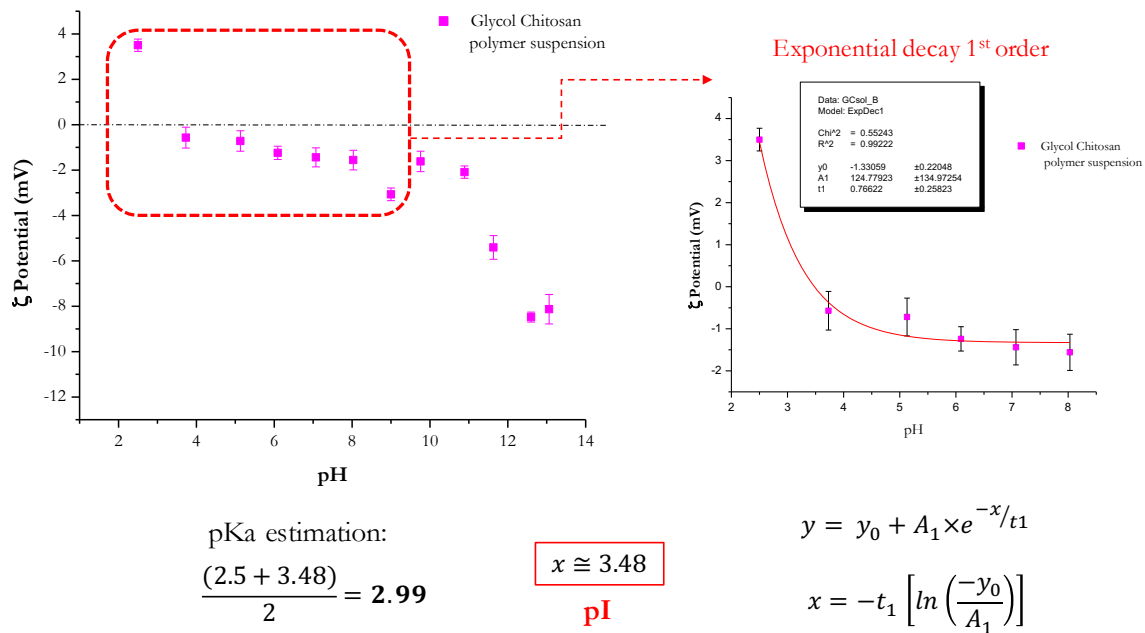


Figure 2.9 Glycol chitosan polymer suspension: zeta potential titration curve and derivation of the isoelectric point (pI) for the system.

Table 2.3 Physical properties of the chitosan-derivative polymers and nanoparticles

	<i>pI</i>	<i>pKa</i>	<i>Avg Diameter (nm)</i>	<i>Avg ζ_{pot} (mV)</i>
<i>Glycol chitosan</i>	3.48	2.49		
<i>HGC_(0.0115) polymer</i>	6.69	4.35		
<i>HGC_(0.0115) NPs</i>	4.6	3.3	339.38 ± 10.19	+4.47 ± 0.52
<i>HGC_(0.185) polymer</i>	9.64 < x < 9.76	5.85		
<i>HGC_(0.185) NPs</i>	4.7	3.6	288.6 ± 2.8	+13.2 ± 0.2

With the purpose of characterizing the pH responsiveness and the stability in solution of the naked glycol chitosan (GC) and its synthesized derivatives, a series of titration curves were obtained. Briefly, several suspensions of GC, HGC_(0.0115) and HGC_(0.185) polymers were prepared at different pH values, ranging from 2.5 to 13. The pH values of the water were adjusted by adding drop-wise NaOH 0.1 M or HCL 0.1 M, as needed. Afterwards, 5 ml of the acidic or basic water were transferred in a scintillation vial and the polymer powder was added to form a polymer water suspension of 5 mg/ml. Zeta potential measurements were recorded. For the case of the hydrophobically modified GC polymers, the same polymer suspension was used to prepare NPs by means of probe-type sonication, as described above. These micellar suspensions were also characterized in terms of their zeta potential. Figure 2.8 reports the comparison of the zeta potential titration curves (ζ potential vs pH) for each polymer suspension and its corresponding micellar suspension. The dotted lines on the graphs help the identification of the pH value at which the ζ potential is zero (the system has no residual surface charge).

The GC polymer presented good solubility in both acidic and neutral water, as expected considering the high hydrophilicity of the material, conferred by the –OH residues on the glycol pendants. A similar behavior was observed for the case of the HGC_(0.0115) polymer, indicating that a degree of substitution of cholanic acid of about 1% is not enough to affect the water solubility of the basic polymer. On the other hand, the HGC_(0.185) polymeric chains did not completely solubilized in water, and only appeared to be slightly more well dispersed in basic water environments (pH > 11). In this case, a degree of substitution of about 5% was sufficient to modify the macromolecule dispersion and stability.

As visible from Figure 2.8a, at low pH GC does not show a high positive charge ($+3.5 \pm 0.27$ mV at pH 2.5), while the HGC_(0.0115) and the HGC_(0.185) polymers possess a more polycationic behavior, with charges of $+41.64 \pm 1.13$ mV and $+36.84 \pm 0.95$ mV at pH 2.5, respectively. Moreover, when considering the ζ potential values of the polymeric suspension at pH 13 (Figure 2.8a), the negative charge passes from -8.13 mV, to -7.68 , to -10.35 as the degree of hydrophobic substitution increases, indicating the enhanced pH responsiveness of the functionalized systems, which can switch from a high positive surface charge, when exposed to lower pHs, to a negative one, when in contact with a basic environment. A similar behavior is maintained when the polymeric chains are complexed in micelle-like structures, as noticeable from the curves in Figure 2.8b and Figure 2.8c, in which the comparison between the polymeric suspensions and the

corresponding nanoparticle suspensions are presented. The delta between the zeta potential values recorded at the lowest and at the highest pHs were 34.34 mV and 34.67 mV for the HGC_(0.0115) and the HGC_(0.185) nanoparticles, respectively (micellar system comparison reported in Figure 2.8d), further validating the pH-responsiveness of the hydrophobically functionalized systems. Figure 2.9 represents the analysis of the titration curve of the glycol chitosan polymer and the derivation of the isoelectric point, as example. This parameter indicates the value of pH at which the charge of the molecules is null. For pHs < pI the overall charge of the system is positive (the system is protonated), while at pHs > pI the molecules carry a net negative charge, with implications on the solubility of the polymeric chains and on the resulting stability of the micelles. A portion of the graph, containing values of zeta potential above and below the 0 point, was isolated and fitted with an exponential curve (1st order decay). The value of the isoelectric point was obtained from the fitting, considering the y value (which represents the zeta potential) at zero. For the pKa (the logarithm of the acid dissociation constant) estimation, the mid value between the lowest pH and the pI was considered. This parameter gives a quantitative measure of the strength of an acidic material in solution: larger pKa values are correlated to a weak acid, less prone to dissociate and form ions at a given pH.

The procedure for the GC polymer is reported in Figure 2.9, as example. This analysis was performed on the three polymers and on the two micellar systems, and the resulting data are reported in Table 2.3. The isoelectric point of the polymers increases with the degree of hydrophobic substitution, passing from 3.48, to 6.69, to about 9.7, while both micelles presented comparable pI values of about 4.6. This outcome might indicate a possible effect of the macromolecule conformation and assembly in solution on the pH-responsiveness of the system: the protonable amine groups within the micellar matrix could be subjected to intra-molecular interactions, which would be less probable to occur when the polymeric chains are well dispersed and surrounded by solvent molecules. These results suggest that HGC nano-micelles, when internalized into intracellular compartments, usually presenting acidic pHs ranging from 6.5 to 4.5, can get protonated. As a result, two possible, parallel outcomes can be envisioned: the protonated groups on the cationic chains are able to buffer the pH inside the vesicles, recalling an influx of counterions that can cause osmotic swelling and, ultimately, vesicle membrane rupture. In a similar scenario, the protonated molecules can electrostatically interact with the negatively charged vesicle membrane, leading first to micellar swelling and then to vesicle rupture. In both cases, the

HGC micelles would undergo a surface and a structure instability, which would ultimately lead to their endosomal escape and their cargo molecule release in the cytosol. Despite a similar pI value, the HGC_(0.185) micelles appeared to be a more promising candidate for the design of an effective drug delivery system, considering their smaller average diameter, their more compact structure and their higher positive surface charge. In addition, a greater variation in the sizes of those micelles at different pHs has been recorded, passing from an average diameter of 191.4 nm at pH 12.6 to 470.8 nm at pH 2.5, validating the hypothesis of protonated carboxyl and amide group-associated swelling and consequent disruption of the hydrophobic core integrity (data not shown).

A model hydrophobic anti-cancer drug was encapsulated in the HGC micelles and the system was characterized in terms of morphology and physicochemical properties

The hydrophilic shell-hydrophobic core structure of the self-assembled micelles supports the accommodation inside the clusters of hydrophobic molecules, such as anti-cancer compounds, due to favorable hydrophobic interactions. The solubility and bioavailability of the cargo molecules would be improved, while protecting them from degradation and burst release during the nanoparticles' delivery. With the aim of assessing the ability of our micellar system to encapsulate a hydrophobic anti-neoplastic agent, doxorubicin was used as a model. This potent anti-tumor antibiotic from the class of anthracyclines has been intensively studied in the past decades, in terms of its cytotoxic potential and mechanisms,^{76, 170-172} and its chemical modifications to overcome multi-drug resistance phenomena.^{39, 173, 174} Doxorubicin and its derivatives were first isolated from *Streptomyces* strains in the 1960s. Since their approval by the US Food and Drug Administration in 1974, they have emerged as successful chemotherapy treatments of solid and hematopoietic tumors. The rigid structure of the molecule, presenting a four-ringed 7,8,9,10-tetrahydrotetracene-5,12-quinone, allows its intercalation between adjacent base pairs in the DNA, inhibiting topoisomerase II and macromolecular biosynthesis.^{175, 176} Moreover, anthracyclines have been observed to promote apoptosis, by influencing p53 and Bcl-2 expression¹⁷⁰ and to lead to high cardiotoxicity and chronic cardiac injury as a consequence of oxygen-derived free radicals-associated cell membrane damage.¹⁷² Therefore, strategies have been implemented to complex the active anthracyclines with prodrugs or polymeric delivery systems, to enhanced the cancer cell targeting ability, while reducing the overall toxicity, potentially harmful for the patient's life.¹⁷¹

In the past decades, doxorubicin has been used in combination with different nanoparticulate formulations for the design and development of drug delivery systems, able to specifically target cancer cells *in vitro*.^{41, 105, 106, 114, 177-180} We hypothesized that the amphiphilic behavior of our micelles would allow an efficient drug encapsulation, depending on the degree of hydrophobic modification introduced with the synthesis. Moreover, the pH-responsiveness of the chitosan-derivative nano-vehicles would allow a sustained release of the drug molecules in an acidic environment.

To test our hypotheses, doxorubicin-loaded HGC complexes were prepared through a mixing and dialysis method (Figure 2.3). Briefly, a suspension of HGC polymer in DMSO was added drop-wise with doxorubicin (3.5 mg/ml in DMSO). The amount of doxorubicin was 5% wt. with respect to the polymer. A drop of triethylamine was added to favor the de-complexation of the doxorubicin molecules from the hydrochloride salt. The system was kept under stirring for 5 hours in the dark, to allow the complexation between the drug molecules and the hydrophobic residues on the polymeric chains. To facilitate the formation of self-assembled micelles, 50 ml of HPLC water were slowly added to the system, while keeping the mixture under a cold water / ice bath, to reduce the increase in the temperature associated with the isothermal reaction. During this step, cloudiness of the suspension was observed, indicating that a phase separation was occurring: the hydrophobic domains of the HGC micelles would cluster in the center, entrapping the hydrophobic drug molecules in the core, while the hydrophilic glycol pendants would face the solvent, where water molecules are predominant. After stirring overnight in the dark, the suspension was transferred in dialysis cassettes to eliminate the loosely complexed doxorubicin molecules, and let dialyze for 24 hr against HPLC water. Afterwards, the purified material was lyophilized for 3 days and ground into powder. During the dialysis step, for the case of doxorubicin-HGC_(0.185) micelles, aggregates were visible in the dialysis cassette membrane, indicating their successful formation and their stability in suspension for over 48 hours. Moreover, the resulting final powder presented an intense pink-orange color, due to the presence of doxorubicin. On the other hand, during the synthesis of doxorubicin-HGC_(0.0115) micelles, few aggregates were visible, suggesting that the amount of hydrophobic modification was not sufficient to obtain stable, self-assembled structures. In addition, the final powder presented a light pink color, suggesting that a lower content of doxorubicin was successfully encapsulated within the micelles.

To assess the encapsulation efficiency and loading content of doxorubicin in our complexes, a modified protocol from Jeong *et al.*¹¹⁴ was implemented. Briefly, 2 mg of the freeze-dried powder were dispersed in 2 ml of HCl 0.1 M, to allow micelle structure disruption, by means of the mineral acid-driven hydrolysis. The resulting solution was then diluted with 8 ml of DMSO, to favor doxorubicin solubilization. Aliquots were transferred in a 96-well plate for recording of the fluorescence emission at 580 nm. Results were compared with a standard curve of free drug in DMSO:HCl (10:2, v/v), previously obtained, while the contribute of the plain HGC micelles to the total fluorescence emission was considered as blank. The data reported in Table 2.4 and the TEM micrographs of Figure 2.10 further validate our hypothesis on the dependency of the encapsulation efficiency on the hydrophobic content: the degree of substitution affects the micelle formation, their stability in water-based environment and their ability to complex hydrophobic molecules in the inner core. The bigger average diameter observed for the doxorubicin-loaded HGC_(0.0115) NPs is imputable to the less densely packed structure, associated with weaker hydrophobic-hydrophobic interactions.

Considering this outcome, a release kinetics experiment was carried out *in vitro* only for the doxorubicin-HGC_(0.185) micelles, following a modified protocol from Jeong *et al.*¹¹⁴ Briefly, the freeze-dried powder was re-suspended in 4 ml of phosphate-buffered saline (PBS, pH 7.4) at a concentration of 1 mg/ml, and the suspension was placed in a dialysis tubing (MWCO 10,000 Da) tied up with clips at the extremities. The sealed tube was then immersed in a beaker containing 40 ml of PBS at pH 7.4 and the system was kept under gentle shaking, at room temperature, in the dark. At predetermined time intervals (each 5-15 minutes for the first 2 hours, hourly measurements for up to 6 hours, then daily measurements for up to 6 days), 3 ml were taken from the beaker for evaluation and were replaced with fresh buffer, to maintain the sink conditions. To observe the effect of the pH on the release behavior of the micellar system, and with the aim of mimicking intracellular vesicle harsher conditions, a parallel experiment was performed re-suspending the doxorubicin-loaded HGC_(0.185) freeze dried powder in 6 ml of KH₂PO₄ – Na₂HPO₄ buffer (pH 5.5) at a concentration of 1 mg/ml. Fluorescence emission at 580 nm was considered for the detection of the released drug molecules, and the measurements were compared with a standard curve of doxorubicin, previously obtained in the corresponding buffers. The results presented in Figure 2.11 clearly showed the release rate dependency from variations in the pH of the media: 49.5% of the drug was released after 4 hours at pH 5.5, suggesting the pH-

responsiveness of the chitosan-derivative nano-vehicles, and a sustained release was kept until day 6. On the other hand, under neutral pH conditions, 28.7% of the initial drug was measured to be released after 3 hours of incubation, and only 43% was released after almost a week, indicating the higher stability of the micelles and their active molecule protection role in this environment.

HGC nanocomplex delivery to a human osteosarcoma model cell line in monolayer revealed a time and concentration dependent uptake

With the aim of assessing the cellular internalization ability, HGC NPs have been delivered *in vitro* to a human osteosarcoma MG-63 model cell line. The micelles were synthesized and prepared as mentioned in the method section. For this uptake experiment, labeling with a near IR dye, Cy5.5, aided the visualization and tracking of the nano therapeutics inside the living hosts. We hypothesized that both the cellular uptake mechanism and the intracellular fate of the nano therapeutics are dependent on the physicochemical and morphological features of the engineered systems. Moreover, when delivered to a two-dimensional model cell line, micelle concentration and treatment duration should play a crucial role in the uptake and internalization process. Under these assumptions, cellular uptake was evaluated as a function of NPs concentration (500 and 1000 $\mu\text{g/ml}$) and incubation time (15, 30 minutes and 1 and 3 hours). From the confocal micrographs in Figures 2.12 and 2.13, the time and concentration dependency of the uptake is visible for both Cy5.5-HGC_(0.0115) and Cy5.5-HGC_(0.185) micelles. While a dim fluorescent signal is already detected after 15 minutes of treatment (Figure 2.12 a, e and Figure 2.13 a, e), the HGC NPs appeared to be distributed throughout the entire cell body after only 1 hour of incubation, at both concentrations (Figure 2.12 c, g and Figure 2.13 c, g). After 3 hour of delivery, the cytosol of the MG-63 cells in monolayer looked completely lighted up, due to the intense fluorescent signal coming from the clusters of internalized micelles (Figure 2.12 d, h and Figure 2.13 d, h). The good internalization ability might be associated with the chemistry of the basic polymeric material. In fact, chitosan and its derivatives have been shown to present strong affinity for phospholipids, common components of the cell membrane. Thus, in a process involving electrostatic forces and hydrophobic interactions, chitosan might promote local distortion of the phospholipid layer, causing its local, transient disruption, and creating a route of entry in the cell.^{168, 181} Interestingly, the hydrophobic modification appeared to have an effect on the ability of the nano therapeutics to

be internalized into the cells: probably due to their smaller average diameter and their more positive surface charge, Cy5.5-HGC_(0.185) NPs showed a more efficient internalization into MG-63 osteosarcoma cells.^{8, 120, 182-184} A similar conclusion was reached by Huang *et al.*¹⁸⁴ in their work on the evaluation of chitosan nanoparticles' uptake into lung adenocarcinoma A549 cells. The chitosan NPs were differing in terms of molecular weight, degree of deacetylation, size and zeta potential. Preferential cellular internalization was observed for the case of NPs presenting higher degree of deacetylation (correlated to a higher number of protonable, free amine group), an increased zeta potential (around +34 mV), and smaller sizes (ranging from 163 to 249 nm), suggesting the critical role of a favorable electrostatic interaction between the negative cell membrane and the positive NP surface in the uptake of the chitosan carriers.

In a following experiment, with the aim of gaining some insights into a possible endocytic pathway of the HGC NPs, their entrapment into lysosomes was considered. The understanding of the mechanisms involved in the uptake, as well as the post-internalization fate, are crucial for the design of an effective drug delivery system.^{125, 130} In fact, to be effective, nano therapeutics should be able to either escape from the lysosomal degradation pathway or activate the release of the cargo molecule and its transfer to the cytosol. In this study, MG-63 cells were treated with Cy5.5-HGC_(0.0115) and Cy5.5-HGC_(0.185) NPs, at concentrations of 500 and 1000 µg/ml and for different time points. Afterwards, samples were washed to remove non-internalized micelles and incubated with LysoTracker Green. This weak, basic amine is permeant to the cell membrane and preferentially accumulates in spherical organelles and acidic compartments, where it gets protonated. The MG-63 samples were observed under the confocal microscope to detect co-localization of the Cy5.5-HGC NPs and the lysosomal vesicles. In Figure 2.14, confocal images of samples treated for 1 hour with 500 µg/ml of either HGC_(0.0115) NPs or HGC_(0.185) NPs are reported as example. Also in this case, the fluorescent signal intensity pertaining to the micelles was concentration and time dependent, and the differential uptake between the two hydrophobically modified micelles was further confirmed. In fact, a brighter and more well-defined red signal was observed for the case of cells administrated with HGC_(0.185) NPs, which appeared to be more easily internalized in the cytoplasmic region. Spherical bright yellow spots were clearly identifiable after 1 hour of treatment, suggesting that some of the red-labelled HGC vehicles might have been captured into the green-stained lysosomal compartments. Although confocal microscopy constitutes a useful tool for the observation of nanoparticles within cells,

techniques with higher resolution, such as structured illumination microscopy, should be employed, to carefully confirm the co-localization with the intracellular vesicles, and to obtain qualitative and quantitative measurements of the co-localization events. In addition, a further study involving the use of endocytosis inhibitors, which selectively impair a specific uptake mechanism, might be beneficial to elucidate the preferential route of entry of our engineered micelles, with respect of their physicochemical and morphological features.

Table 2.4 Comparison between the doxorubicin-polymer systems

	<i>Avg Diameter (nm)</i>	<i>Loading Content (%)</i>	<i>Encapsulation Efficiency (%)</i>
<i>Doxo-HGC_(0.0115) NPs</i>	254.3±1.7	0.35	2.2
<i>Doxo-HGC_(0.185) NPs</i>	216.6±19.9	7.15	99

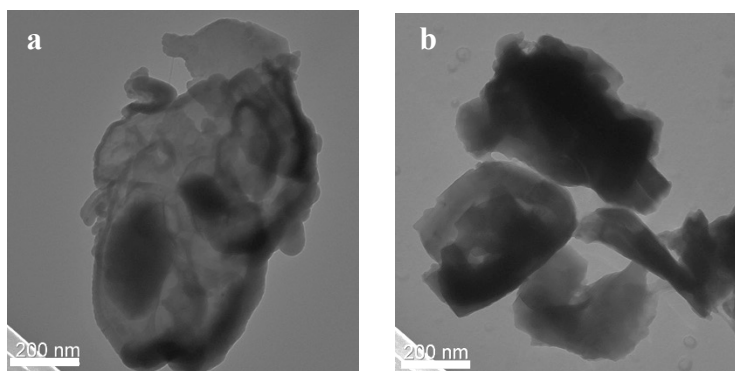


Figure 2.10 TEM micrographs of self-assembled (a) Doxo-HGC_(0.0115) and (b) Doxo-HGC_(0.185) nanocomplexes. Scale bar 200 μ m.

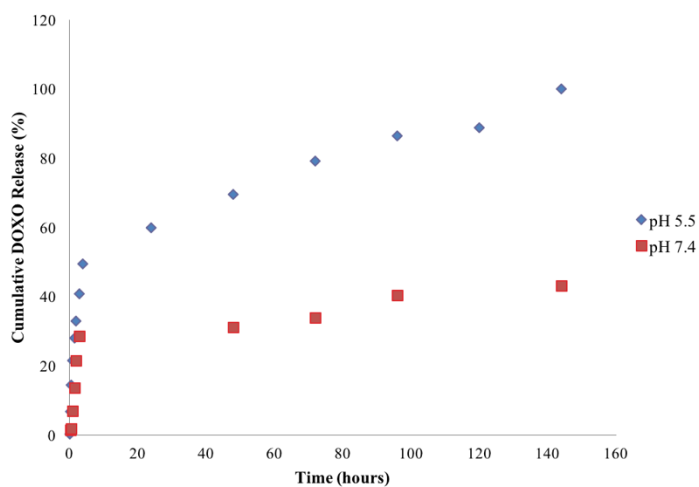


Figure 2.11 Release kinetics of doxorubicin from doxorubicin-HGC_(0.185) NPs in PBS (pH 7.4) and KH₂PO₄ – Na₂HPO₄ buffer (pH 5.5).

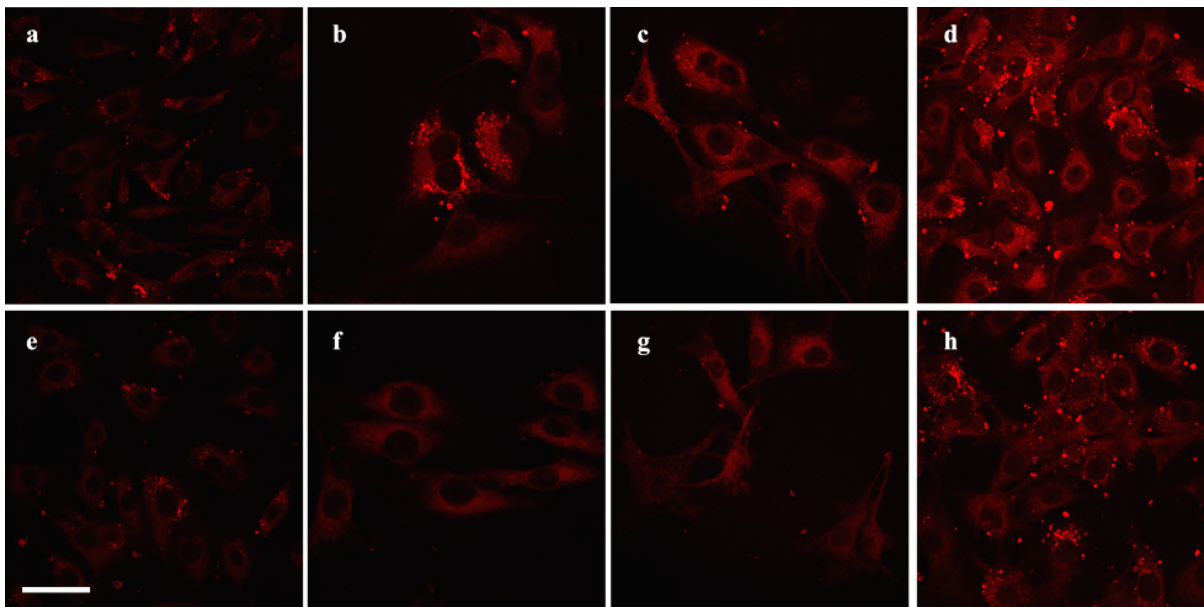


Figure 2.12 Effect of the administration time and NP concentration on the uptake of Cy5.5-HGC_(0.0115) NP into MG-63 cells: 500 µg/ml (a-d) and 1000 µg/ml (e-h) delivered for 15 minutes (a,e), 30 minutes (b,f), 1 hour (c, g) and 3 hours (d, h). Scale bar 50 µm.

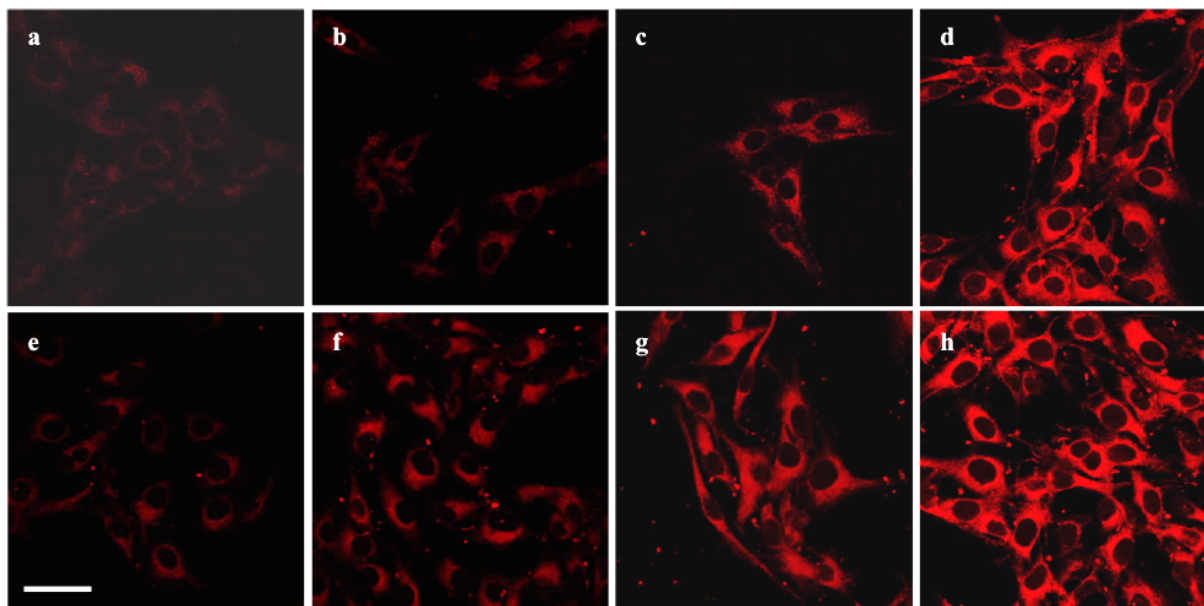


Figure 2.13 Effect of the administration time and NP concentration on the uptake of Cy5.5-HGC_(0.185) NP into MG-63 cells: 500 µg/ml (a-d) and 1000 µg/ml (e-h) delivered for 15 minutes (a,e), 30 minutes (b,f), 1 hour (c, g) and 3 hours (d, h). Scale bar 50 µm.

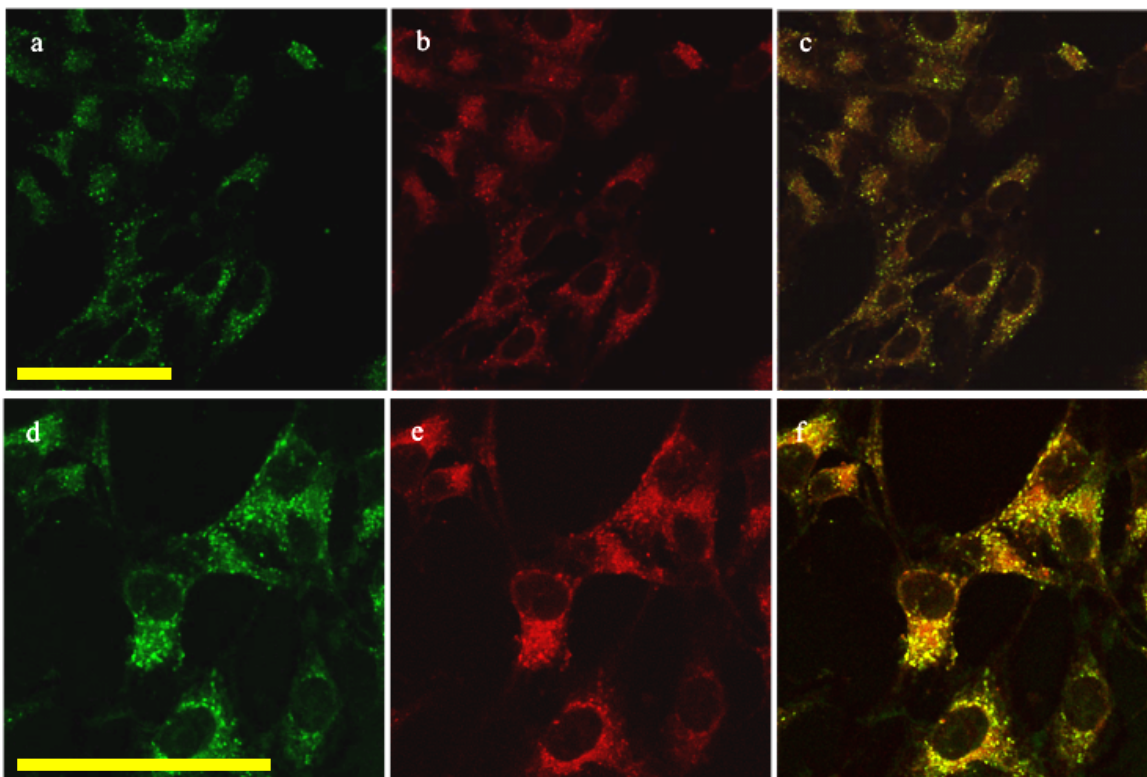


Figure 2.14 Intracellular fate of the nanocomplexes: HGC_(0.0115) NPs (a-c) and HGC_(0.185) NPs (d-f) delivered for 1 hour at a concentration of 500 $\mu\text{g}/\text{ml}$: Lysotacker Green (a, d), Cy5.5-HGC micelles (b, e) and merge images (c, f). Scale bar 100 μm .

Human osteosarcoma cyto-morphology and migration functionality were assessed in the presence of HGC micelle treatments

MG-63 cells are characterized by high metastatic potential and by a fast growth rate, reaching 80% of confluence three days post-plating (data not shown). In addition, their elongated cell shape, with many filopodia protruding from the main body, suggests the propensity of these cells to sense the environment and move with respect with it. Ideally, an empty nano-vehicle, not functionalized with targeting moiety or cell recognition molecules, should not perturb the functionalities and the properties of the cells in which they are internalized. In order to observe the presence of alteration in structure and function, MG-63 cells were treated with empty HGC_(0.185) NPs for 1 and 3 hours at concentrations of 500 and 1000 µg/ml, and stained for actin and fibronectin. Since the delivery of the NPs is performed in serum-free media, to limit possible protein adsorption at the nano-vehicle surface which can reduce their internalization, serum starved samples, untreated, were considered as control. Actin filaments constitute, together with the microtubules and the intermediate filaments, the cytoskeletal architecture of mammalian cells. Those dynamic filaments, constantly assembling and disassembling, provide structural support to the whole cell and are critically involved in several fundamental processes, such as cell division, movement and differentiation. More specifically, fibronectin, a fibrous glycoprotein in the extracellular matrix, binds to the transmembrane protein integrins through its RGD sequence, to form the *so-called* focal adhesion complexes, essential for cell-matrix attachment, as well as cell migration and differentiation.¹⁸⁵ In Figure 2.15 fluorescent microscopy images of the MG-63 morphological analysis are reported: the elongated spindle-like shape is clearly identifiable in the isolated cells. Thin cell membrane protrusions (filopodia) are visible (white arrows), suggesting the preserved tendency to sense the environment and migrate. No significant disruption of the actin architecture was noticeable after the NP treatment, indicating the maintained cytoskeleton integrity. In addition, the distribution of the fibronectin-rich domains within the cellular clusters did not appear affected by the empty, non-functionalized HGC micelles' presence, validating the use of those micellar constructs as drug delivery agents.

In order to assess MG-63 cell motility under different conditions, time lapse videos of live samples, treated with 500 or 1000 µg/ml of HGC_(0.185) nano-vehicles for 1 and 3 hours, were acquired. To account for the role of the serum in the media, control samples incubated for 1 and 3

hours in serum deprived media, as well as control samples kept under normal proliferation conditions, were considered. Considering the previous results on the micelle physicochemical properties, delivery of the HGC_(0.0115) NPs was not pursued further on, for the checking of cellular functionality preservation or cell viability. As a measurement of the cell motility, the analyzed displacements of the cell nuclei were overlaid and considered with respect of an origin coordinate (Figure 2.16). Longer tracking lines, referring to longer distances spanned by the cells, were mostly obtained for the case of the control sample (Figure 2.16a), which was kept under normal proliferation conditions, whereas shorter lines, indicating progressively shorter movements, were obtained when samples were subjected to serum deprivation for 1 hour (Figure 2.16b) and 3 hours (Figure 2.16c). A similar outcome was observed for the NP treated samples, where more confined movements appeared prevalent for the case of the cells administrated for 3 hours with the highest concentration of micelles, under serum-free conditions (Figure 2.16g). This results might suggest a combined effect of the serum deprivation and the chitosan delivery on the MG-63 cell monolayer motility *in vitro*. In addition, the average cell speeds, obtained from the manual tracking of two sets of experiments, were calculated and plotted (Figure 2.16h). The effect of the serum starvation appeared visible once again. The average speed of the control cells ($0.336 \pm 0.047 \mu\text{m}/\text{min}$) was considerably higher than the average speed of the serum starved samples ($0.259 \pm 0.045 \mu\text{m}/\text{min}$ and $0.256 \pm 0.045 \mu\text{m}/\text{min}$, for 1 and 3 hr control, starved samples, respectively). Similarly, with respect of the control sample, the HGC_(0.185) NP administrated cells presented lower average cell speeds, with values ranging from 0.300 and 0.266 $\mu\text{m}/\text{min}$. Interestingly, the delivery of the chitosan micelles *per se* did not seem to significantly (p value < 0.01) affect the motility of the MG-63 cells, if compared to the corresponding serum starved-control samples, suggesting that the serum deprivation might play a more important role in limiting the migratory functions of this cell line. This outcome further corroborates the potential use of the chitosan-derivative micelles in the design of drug delivery nano therapeutics.

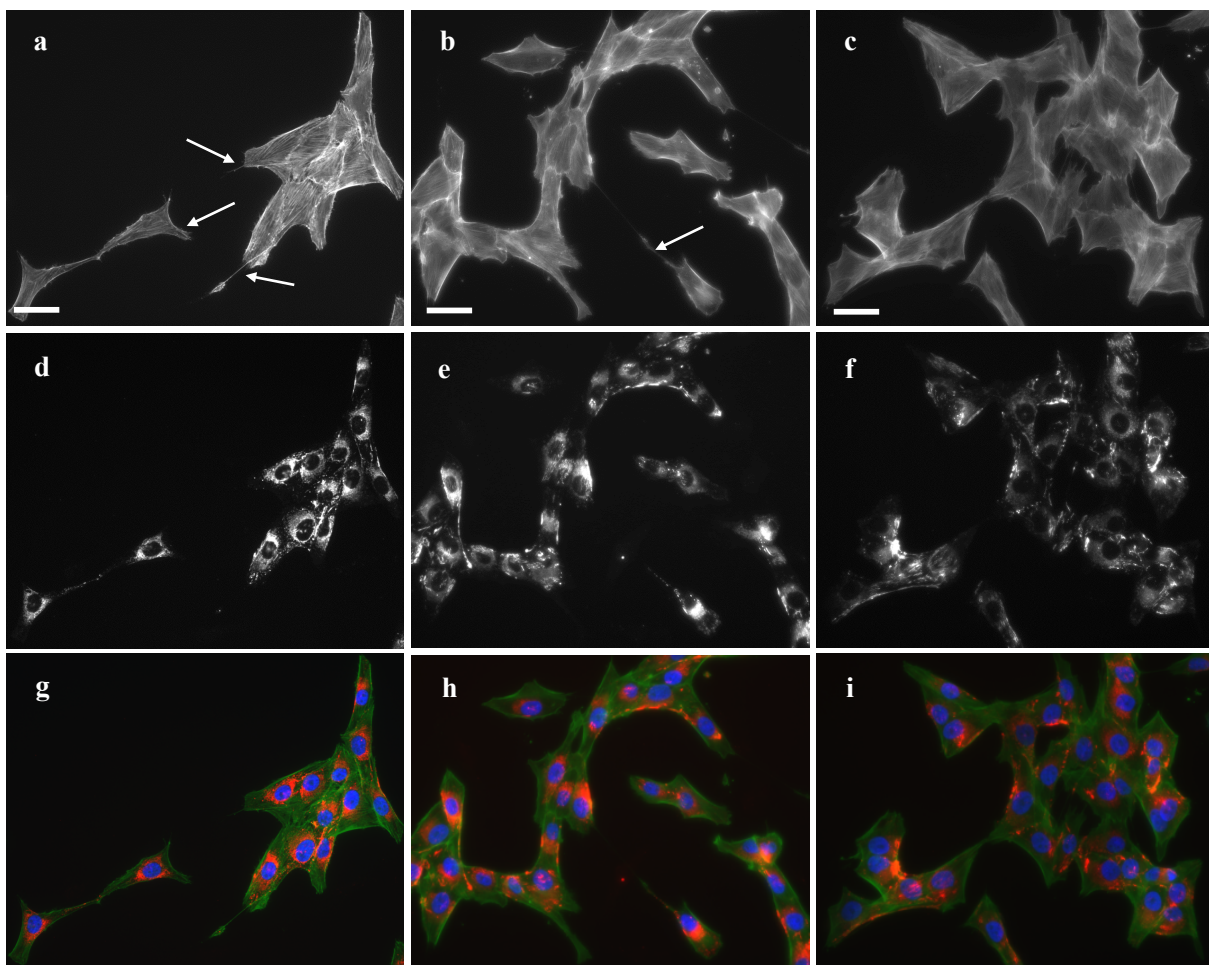


Figure 2.15 Morphological analysis of MG-63 cells: actin staining (top panel), fibronectin staining (middle panel) and merged channel (lower panel). Control, serum starved cells (a,d,g), cells treated with 500 $\mu\text{g/ml}$ (b,e,h) and 1000 $\mu\text{g/ml}$ (c,f,i) of HGC_(0.185) NPs for 3 hours. The elongated spindle-like shape is clearly identifiable in the isolated cells. Thin cell membrane protrusion (filopodia) are visible (white arrows), especially in the serum starved-cells. No significant disruption of the actin architecture is visible after the NP treatment. Scale bar 100 μm .

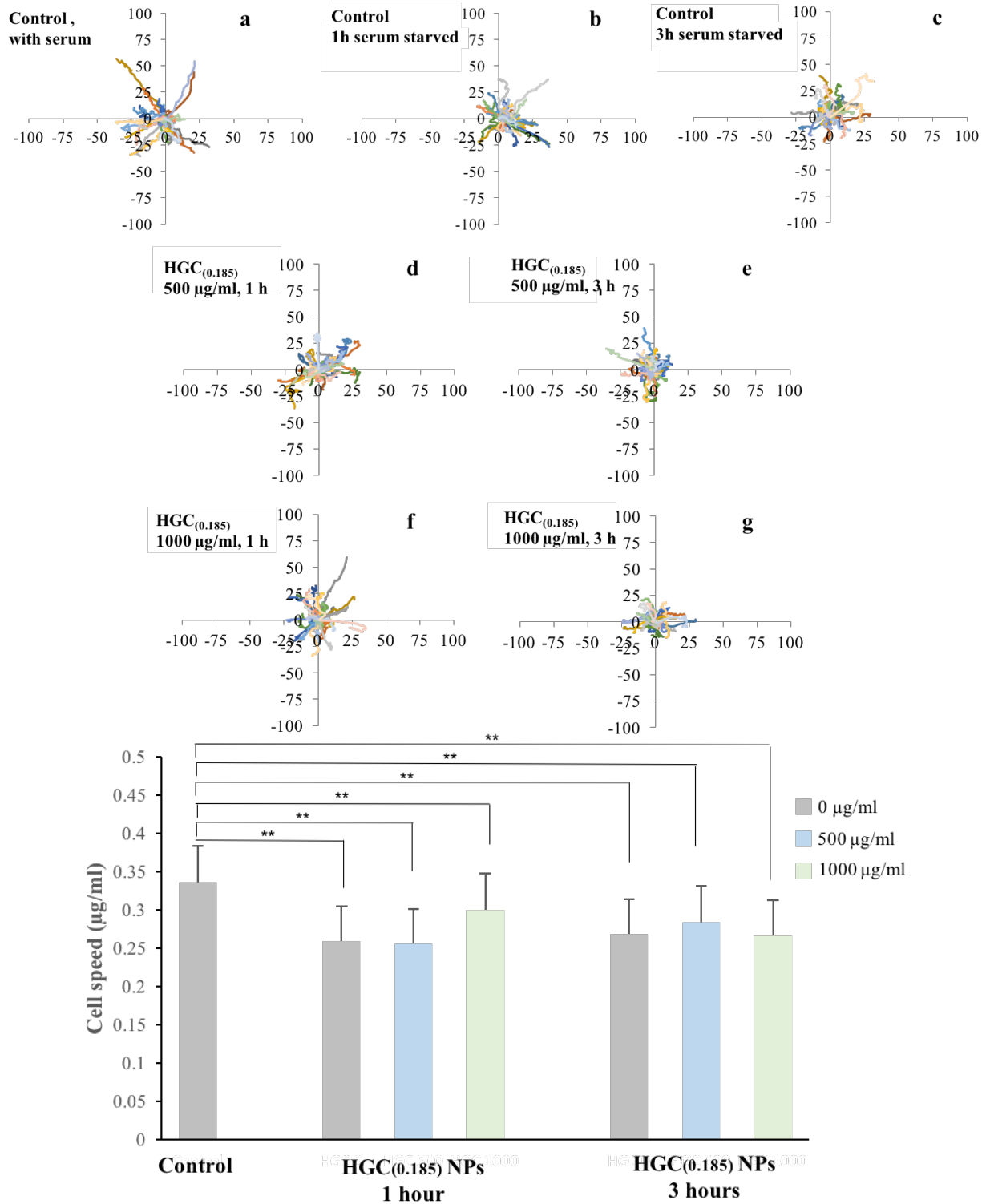


Figure 2.16 Displacement from the origin of MG-63 cells treated with HGC_(0.185) NPs at various time and concentration NPs (a-g), and their corresponding average cell speeds (h). A Student's *t*-test was conducted considering a *p* value < 0.01 (**), comparing each treatment condition with the untreated control sample.

Free and encapsulated doxorubicin have been delivered to a human osteosarcoma model cell line in monolayer: the imaging study revealed the drug intracellular distribution and the time- / dose-dependent uptake

With the aim of assessing the internalization ability and the intracellular distribution profile of the model drug, doxorubicin was delivered to MG-63 cells in monolayer for various time points (ranging from 1 to 24 hours) and concentrations (ranging from 1 to 10 μM). Samples were imaged under a fluorescence microscope, with DAPI, FITC and PI channels, to observe for its distribution with respect of the cell nuclei and the cytosolic compartment. In Figure 2.17, the time- and dose-dependency of the free drug uptake is noticeable, as revealed by the increase in the fluorescence signal (gray scale panels). Interestingly, when delivered at the lowest concentration (1 μM) and for the shortest time point (1 h), doxorubicin appeared to be rather homogeneously distributed in the cytosol, whereas after longer incubation times it preferentially localized within the cell nuclei, where it can exploit its action. Despite the rather limited resolution of the fluorescence microscope, the colored frames of Figure 2.17 allow the observation of the co-localization phenomenon, as distinguishable by the color of the nuclei, which passes from blue (the DAPI signal), to light purple, to bright pink (as result of the DAPI and PI signals' overlay). It is important to mention that, in order to exert their cytotoxic function, the rigid doxorubicin molecules need to reach the nuclei of the cells, where they can intercalate between adjacent base pairs and stop biomolecule synthesis. Once in the nuclei, the fluorescence intensity increases, as a result of the favorable drug molecular packing (π - π stacking of the aromatic rings). This phenomenon can be appreciated with the higher magnification confocal micrographs in Figure 2.18: for the case of 1 μM of doxorubicin delivered for 1 hour or 24 hours (Figure 2.18 a, d) a faint signal was registered, mostly distributed in the cell cytosol. The nuclear localization was favored at higher concentrations and longer time points, as represented by the bright red signal.

A following experiment was focused on the cellular distribution of the encapsulated drug. Doxorubicin-HGC_(0.185) nanocomplexes were delivered to MG-63 cell monolayers at concentrations of 24.3, 81.1 and 243.4 $\mu\text{g/ml}$, equivalent to a content of 1, 3 and 10 μM of doxorubicin, respectively. The doxorubicin-HGC_(0.0115) nanocomplexes were not considered for further delivery, due to their poor encapsulation efficiency. The confocal imaging was performed on samples treated for 24, 48 and 72 hours, to allow for sufficient internalization. Figure 2.19

clearly shows the cytosolic distribution of the doxorubicin-loaded vehicles. In this case, the red signal is pertaining only to the intrinsic fluorescence of the drug (no fluorophore was tagged on the polymeric chains). Accumulation of nanoparticle clusters is visible, suggesting an effective internalization of the nano therapeutics. Surprisingly, on the other hand, only in monolayers treated with 243.4 $\mu\text{g/ml}$ of doxorubicin-HGC_(0.0115) NPs for 48 and 72 hours (Figure 2.19 f, i) a slight fluorescence signal started to be visible in the nuclei. This outcome might suggest that few drug molecules are released from the nano-vehicles to the cytosol in this time frame, to slowly penetrate into the nuclei where their signal would be enhanced. The release kinetics experiment previously showed the liberation of nearly 50% of the drug from the micelles after 4 hours, when incubated in a pH 5.5 buffer. Possible data interpretations can be either associated to limitations in the instrument detection (few free drug molecules are not efficiently visualized) or to a longer stability of the drug-polymer complex once internalized in the cytosol (where the pH is less acidic). Interestingly, the results of our imaging study are comparable with work published in literature. In their study, Dai and co-workers,¹⁸⁶ demonstrated the use of fluorescence lifetime imaging microscopy (FLIM) for the detection and the discrimination of free and encapsulated doxorubicin inside living cells. This technique probes the average time of a fluorophore in its excited state, and can give insights into intramolecular interactions (protein binding) and local physicochemical environment effects (pH changes, quenchers).^{186, 187} Free doxorubicin delivered for 24 hours at a concentration of 0.01 mg/ml presented strong nuclear accumulation in HeLa cells, displaying a lifetime of 1.8 nanoseconds in the cytoplasm and 3.5 nanoseconds in the nuclei. The delivery of doxorubicin-loaded micelles (PEGylated poly-L-lysine adipamide), at an equivalent drug concentration, led to their accumulation in the cytosol (lifetime of \sim 3.5 nanoseconds), with no doxorubicin signal detected into the nucleus after 72 hours of treatment. The free drug molecule nuclear accumulation is imputable to a diffusion process, whereas the encapsulated drug has to be internalized via endocytosis mechanisms, which might lead to intracellular vesicle entrapment, longer cytoplasmic residing time and negligible nuclear penetration.

Strategies for improvement can be obtained either by decorating the engineered micelles with nuclear localization factors¹⁸⁸ or with cell surface recognition molecules to favor the endocytosis process and the internalization into pre-determined degradation or recycling pathways. LysoTracker Green staining was performed on samples administrated with doxorubicin-HGC_(0.185) NPs (Figure 2.20). From the overlaid confocal micrographs, the presence of intracellular vesicle

co-localization of the nanocomplexes was hypothesized. However, a more systematic study, with the aid of super resolution microscopy, should be conducted, to validate this preliminary outcome.

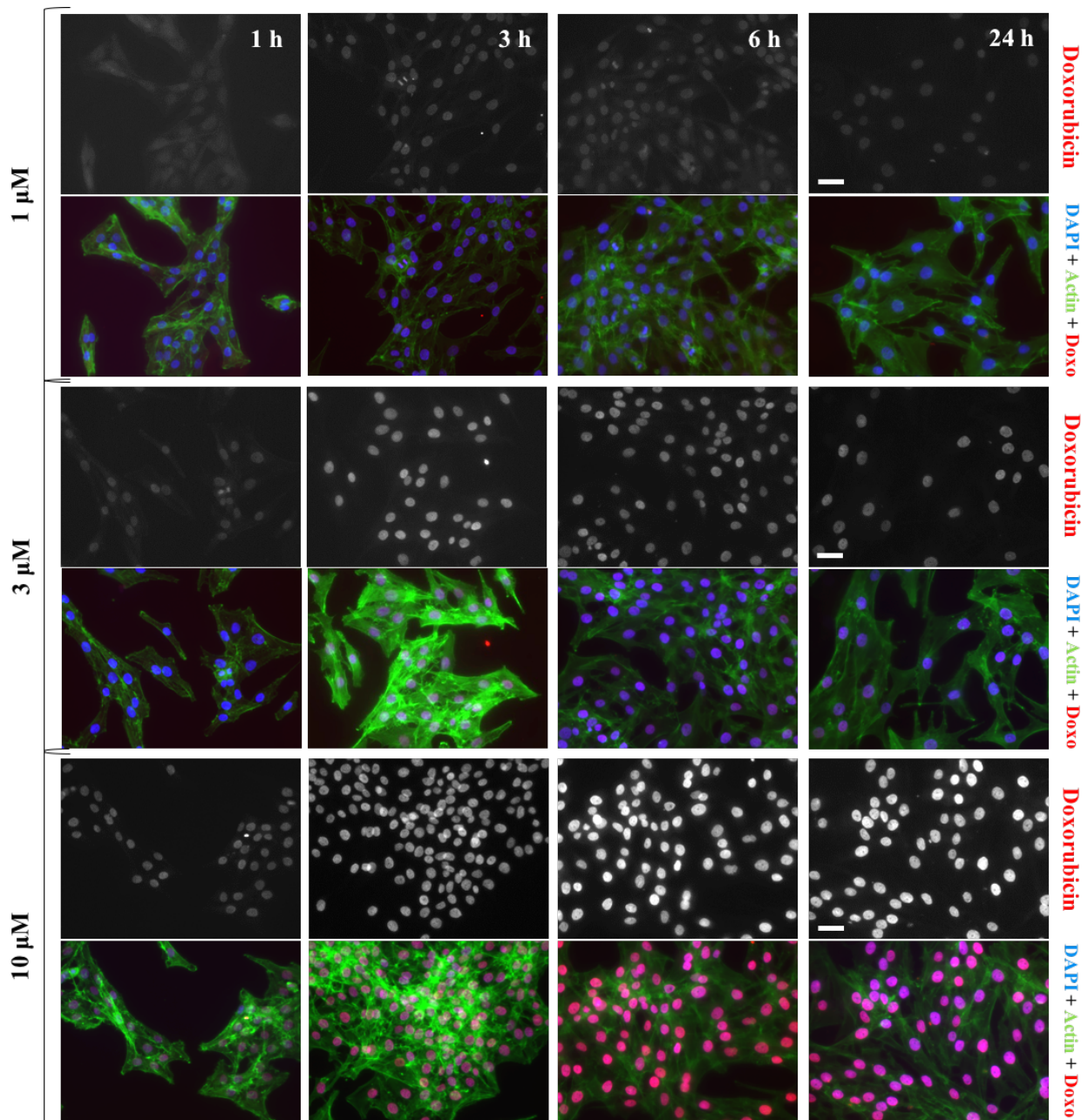


Figure 2.17 Fluorescent microscope images of MG-63 cells treated with free doxorubicin at concentrations of 1 μM , 3 μM and 10 μM , for different delivery time. The grey scale images show the doxorubicin channel (observed under the PI filter), while in the colored images the overlay of actin fibers (FITC), nuclei (DAPI) and doxorubicin (PI) is reported. Scale bar 100 μm .

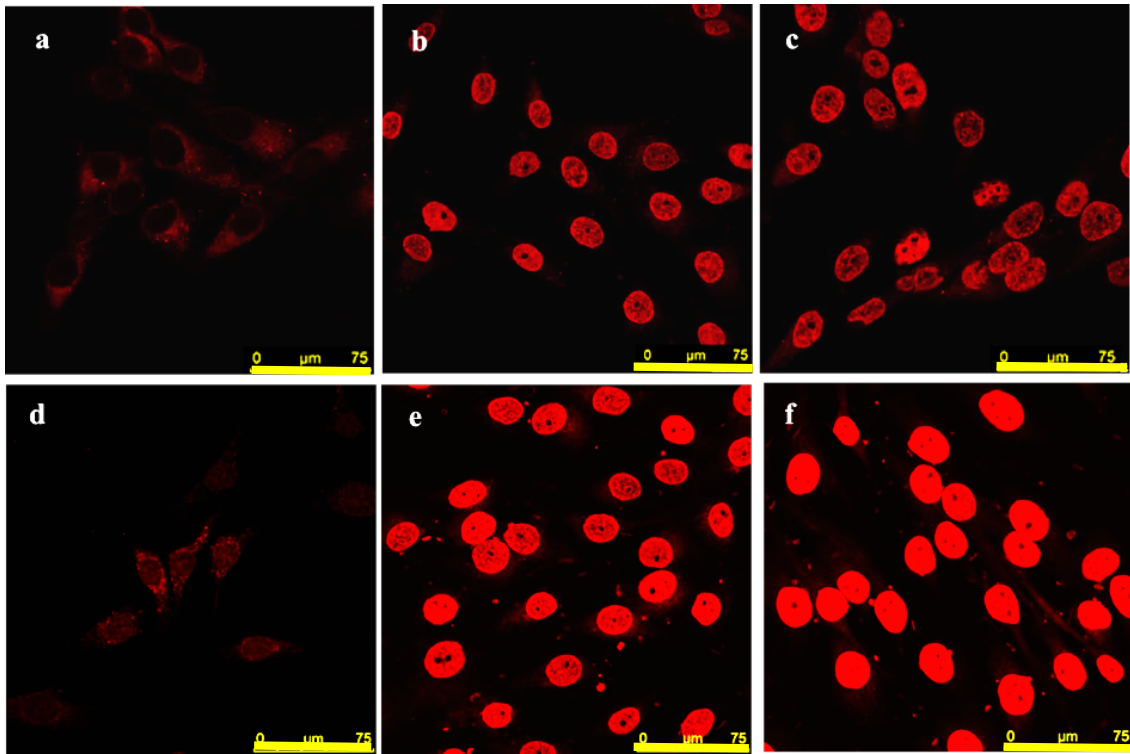


Figure 2.18 Confocal micrographs of MG-63 cells treated for 1 hour (1-c) and 24 hours (d-f) with free doxorubicin at concentrations of 1 μ M (a,d), 3 μ M (b,e) and 10 μ M (c, f). Scale bar 75 μ m.

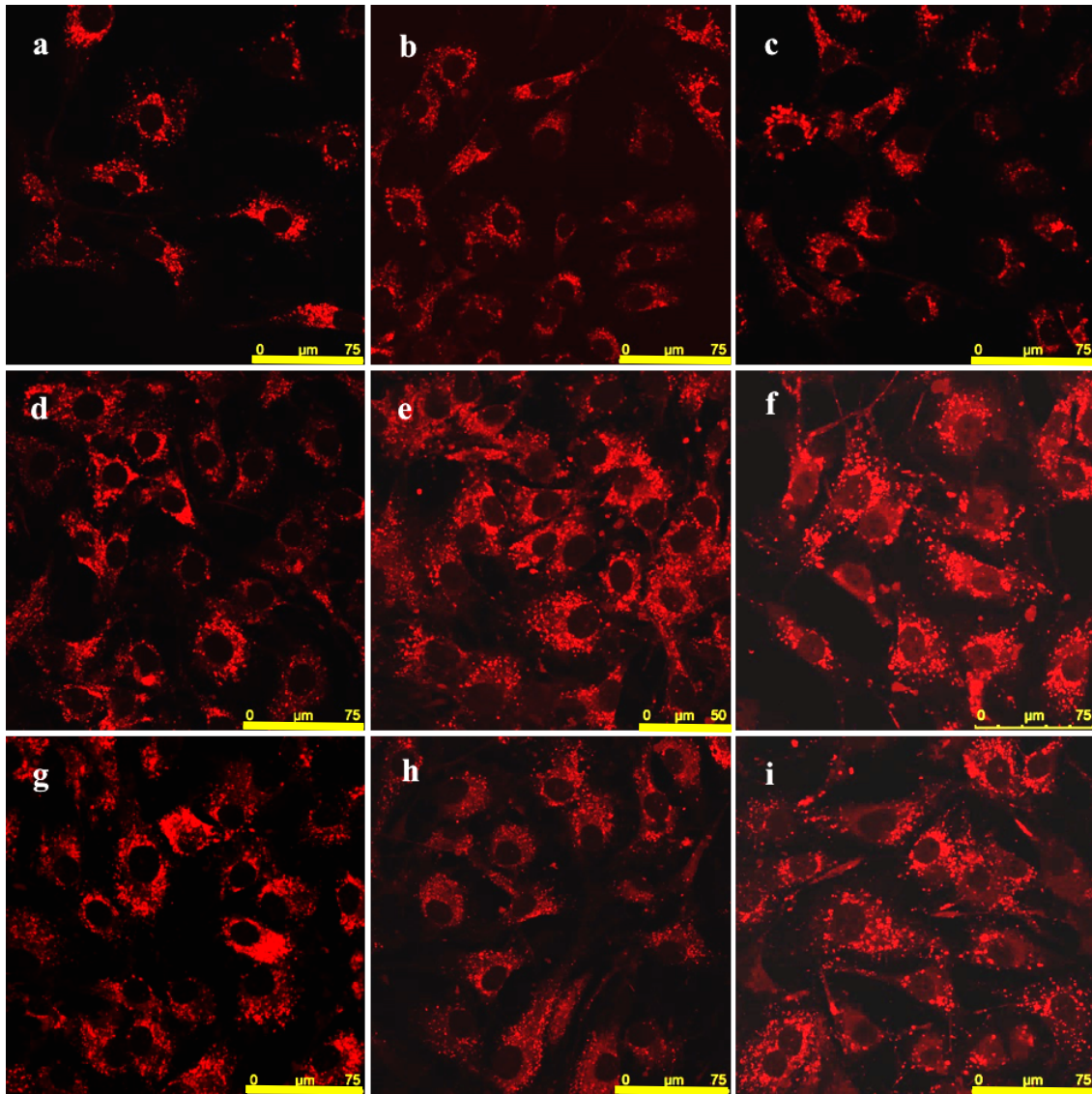


Figure 2.19 Confocal micrographs of MG-63 cells treated for 24 hours (a-c), 48 hours (d-f) and 72 hours (g-i) with doxorubicin-HGC_(0.185) NPs at concentrations of 24.3 µg/ml (left panel, a-d-g), 81.1 µg/ml (middle panel, b-e-h) and 243.4 µg/ml (right panel, c-f-i). Scale bar 75 µm, and 50 µm for image (e).

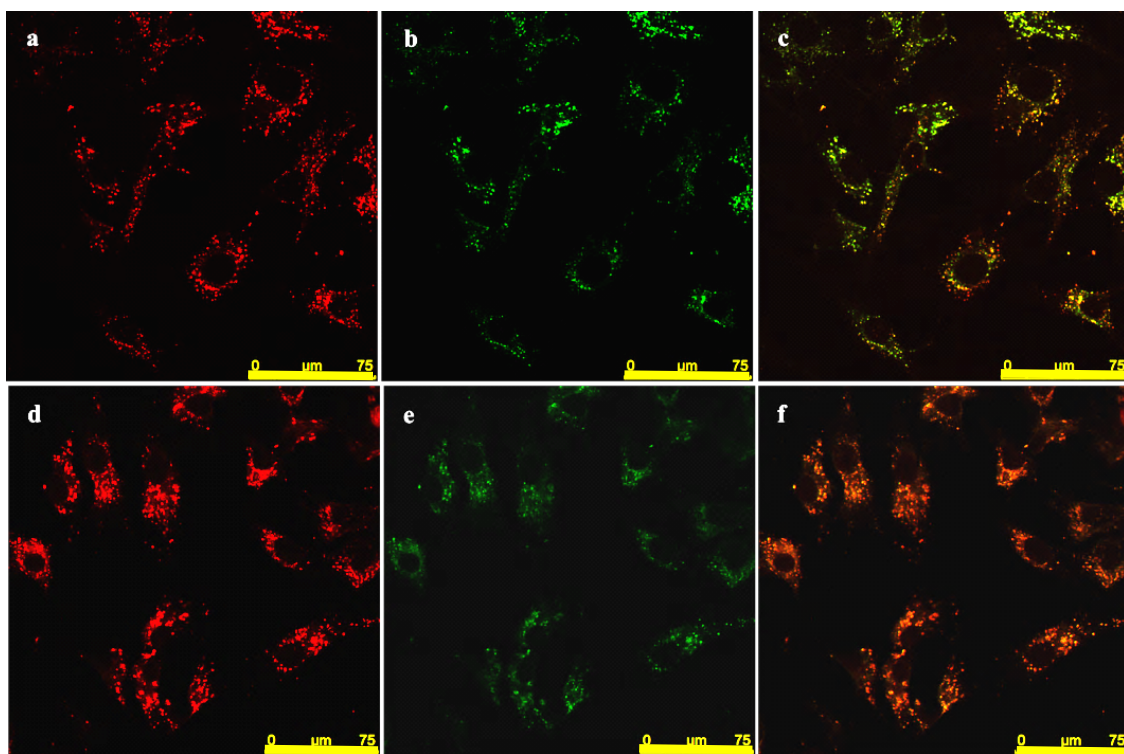


Figure 2.20 Confocal micrographs of MG-63 cells treated for 24 hours with Doxo-HGC_(0.185) NPs at concentrations of 24.3 μg/ml (a-c), 81.1 μg/ml (d-f). Doxorubicin is visualized under the TRITC channel (red), while the lysosomal vesicles are stained in green. The right panel depicts the overlays. Scale bar 75 μm.

Cytotoxicity studies conducted on a human osteosarcoma model cell line in monolayer showed the potential of the chitosan-derivative micelles as drug delivery agents

Amphiphilic micelle-based nano therapeutics have been shown to protect the anti-cancer cargo molecules during their delivery in water-based media and during their cellular uptake. Once internalized in a tumor cell cluster, the release of the active compound should result in efficient cytotoxic potential.

The effect of the unloaded HGC_(0.185) NPs on the human MG-63 osteosarcoma cells in monolayer has been evaluated through a cytotoxicity study. The rationale for such experiment is that empty nanovehicles should exert their carrying function without causing any significant additional toxicity. MG-63 cells were exposed to different NP concentrations (ranging from 0.075 to 226 µg/ml) for up to 72 hours, continuously. The media containing the NPs was serum deprived, to avoid the adsorption of serum proteins on the NPs, which would favor aggregation and limit cellular internalization. Control samples with cells plated in complete DMEM were also considered. To evaluate the cytotoxicity of the empty polymeric vehicles, an MTS assay was performed. Results are reported in Figure 2.21, as average of three independent experiments. Due to the critical role of the serum in the media highlighted in the cell migration experiment (Figure 2.16), data were normalized with respect of the serum starved, untreated samples. No significant decrease in cell viability was observed for samples treated up to 24 hours, over the whole range of concentrations tested. Impaired cell viability was observable only after 72 hours of continuous treatment with 226 µg/ml of HGC_(0.185) micelles (the highest concentration used in the study), suggesting the potential employment of the chitosan-derivative vehicles as safe drug delivery agents. These results confirm the outcome obtained in a study from Kim *et al.*,¹²⁸ in which hydrophobically modified chitosan derivative micelles were delivered *in vitro* to B16F10 melanoma cells: 99% of the cells remained viable after being administrated with 10 µg/ml of empty vehicles for 72 hours. In a similar work, Jeong *et al.*¹¹⁴ delivered PEG-g-carboxymethyl chitosan micelles to C6 glioma cells, observing about 100% cell viability after treatment with up to 500 µg/ml for 48 hours.

The free anthracycline was delivered to the osteosarcoma cell monolayer at concentrations ranging from 0.01 to 30 µM for up to 72 hours, continuously, and similar experimental approach and data analysis were conducted. Figure 2.22 shows the drug concentration-dependent

cytotoxicity for the model cell line used in this study. A concentration of 3 μM of free doxorubicin, administered for 48 – 72 hours, appeared sufficient to start lowering the cell survival in monolayers. A viability of 60% was reached with the delivery of 10 μM for 48 hours, in accordance with similar studies conducted on C6 glioma cells,¹¹⁴ HeLa and HepG2 cells,¹⁸⁸ and squamous carcinoma cells.¹⁸⁹ A further decrease in the MG-63 cell viability to about 25% resulted from the treatment with 30 μM of drug for 72 hours.

In a third round of experiments, doxorubicin-HGC(0.185) nanocomplexes were delivered, with concentrations ranging from 0.081 to 234.3 $\mu\text{g/ml}$ (corresponding to drug equivalents of 0.01 – 30 μM). Interestingly, for the first 24 hours of treatment cells appeared slightly affected by the presence of the nanocomplexes (60% of the cell viability was observed), although the effect was not concentration-dependent (Figure 2.23). On the other hand, at day 2, MG-63 cells in monolayer only showed a decrease in viability when treated with 81.1 – 234.3 $\mu\text{g/ml}$ of doxorubicin-HGC(0.185) micelles. The analysis at 72 hours post-treatment revealed a more pronounced decrease and 27% of the cell viability was recorded for samples administered with 234.3 $\mu\text{g/ml}$ of drug-polymer constructs. Comparison of the resulting cell viability after MG-63 cell monolayer treatment with empty HGC(0.185) nano-vehicles, free doxorubicin and doxorubicin-HGC(0.185) nanocomplexes are reported in Figures 2.24, 2.25 and 2.26. From the plots, it is noticeable that empty chitosan-derivative micelles did not affect the overall cell viability, up to 75 $\mu\text{g/ml}$, suggesting their potential use as safe delivery agents. More interestingly, when loaded into the polymeric vehicles, doxorubicin appeared to affect the cell viability over a broader range of concentrations, if compared to the free drug molecule alone, especially after 72 hours of treatment. These results indicate the efficient design of our engineered system and the preserved functionality of the active agent.

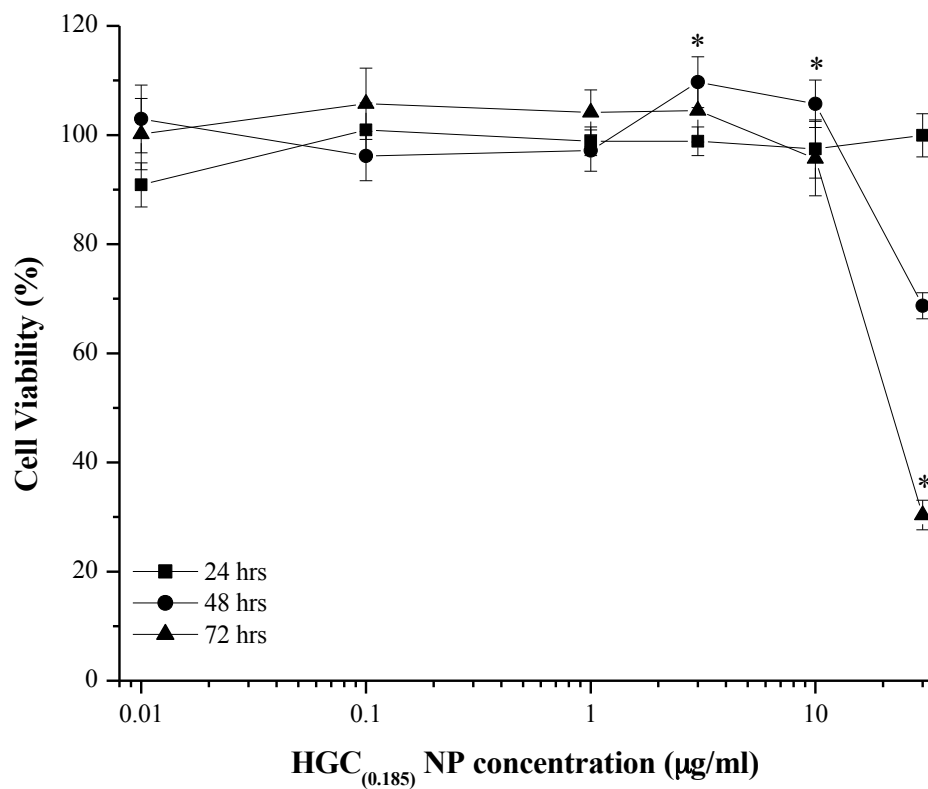


Figure 2.21 Cell viability of MG-63 cell monolayers treated with HGC_(0.185) NPs at different concentrations, up to 72 hours. The results presented are the average of three independent experiments and a Student's *t*-test was performed considering $p < 0.05$ (*). Data comparison and statistics were conducted between each HGC_(0.185) nanoparticle concentration and the corresponding control, serum starved sample at the same time point.

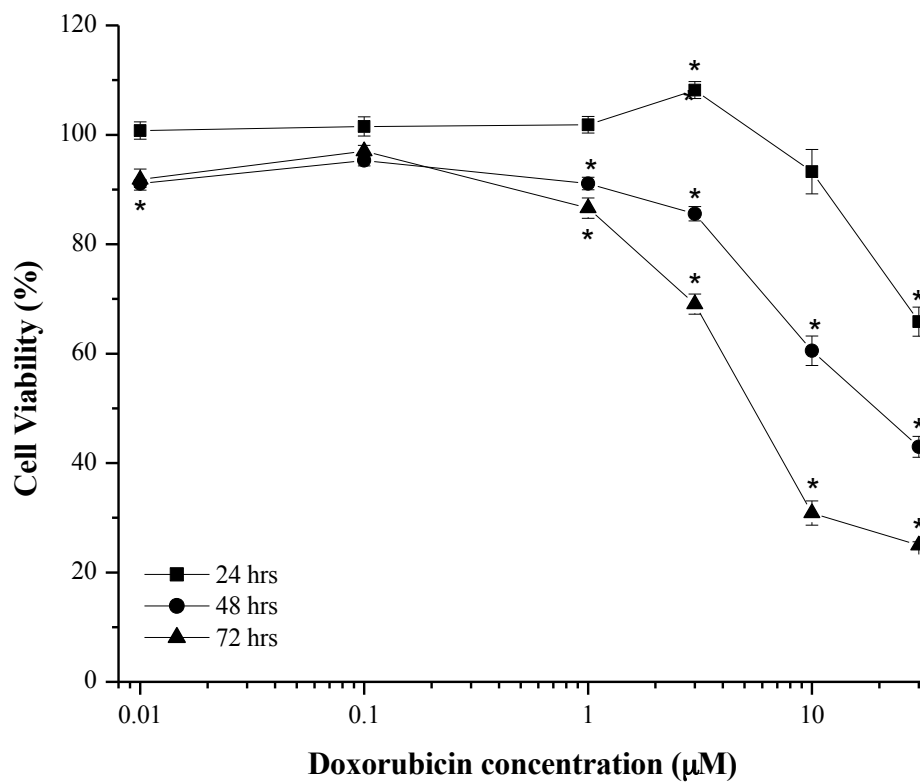


Figure 2.22 Cell viability of MG-63 cell monolayers treated up to 72 hours with free doxorubicin at different concentration, up to 72 hours. Data represent the average of three independent experiments and a Student's *t*-test was performed considering $p < 0.05$ (*). Data comparison and statistics were conducted between each free drug concentration and the corresponding control, serum starved sample at the same time point.

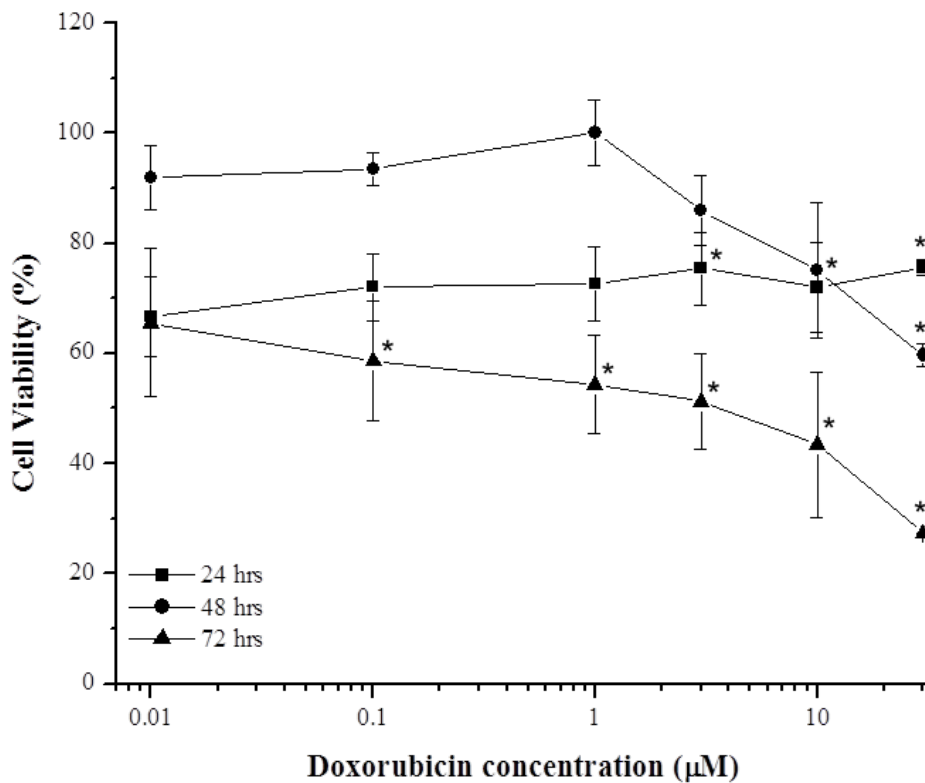


Figure 2.23 Viability of MG-63 cell monolayer treated up to 72 hours with doxorubicin-HGC_(0.185) NPs at different concentrations, up to 72 hours. The results presented are the average of three independent experiments and a Student's *t*-test was performed considering $p < 0.05$ (*). Data comparison and statistics were conducted between each doxorubicin-HGC_(0.185) concentration and the corresponding control, serum starved sample at the same time point.

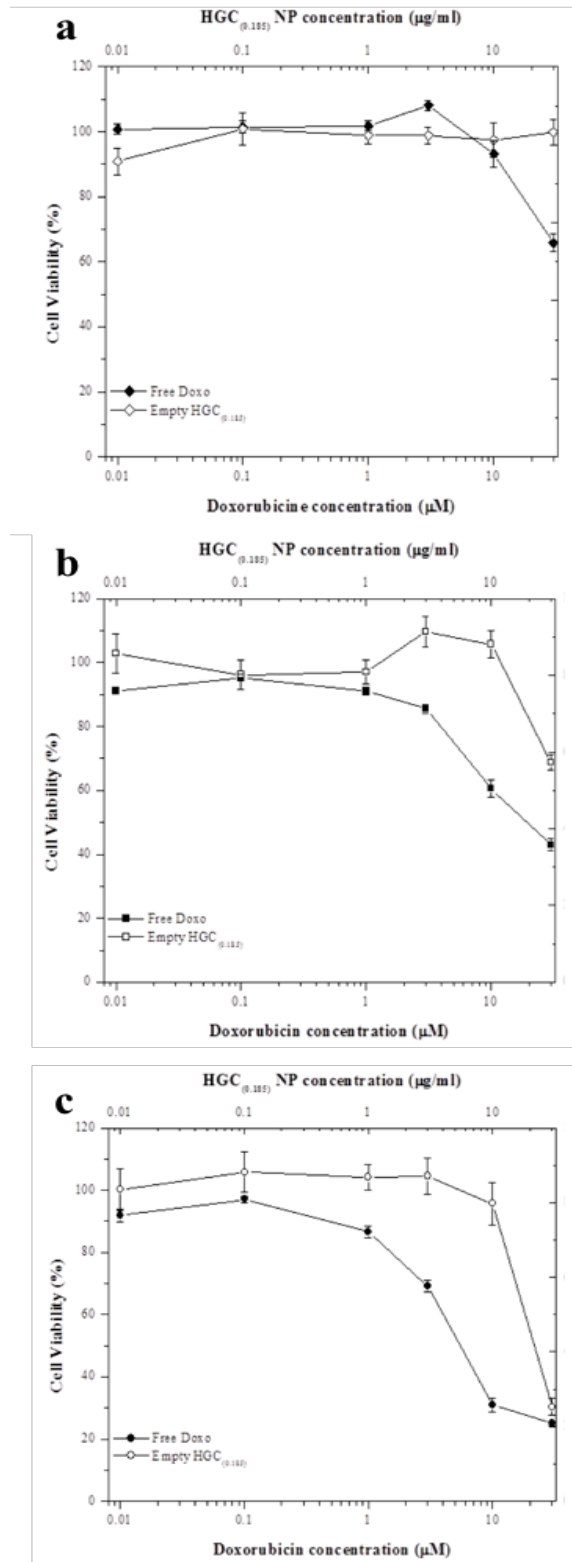


Figure 2.24 Comparison of the viability of MG-63 cell monolayer treated for 24 hours (a), 48 hours (b) and 72 hours (c) with either free doxorubicin (solid markers) or empty HGC_(0.185) nano-vehicles (hollow markers).

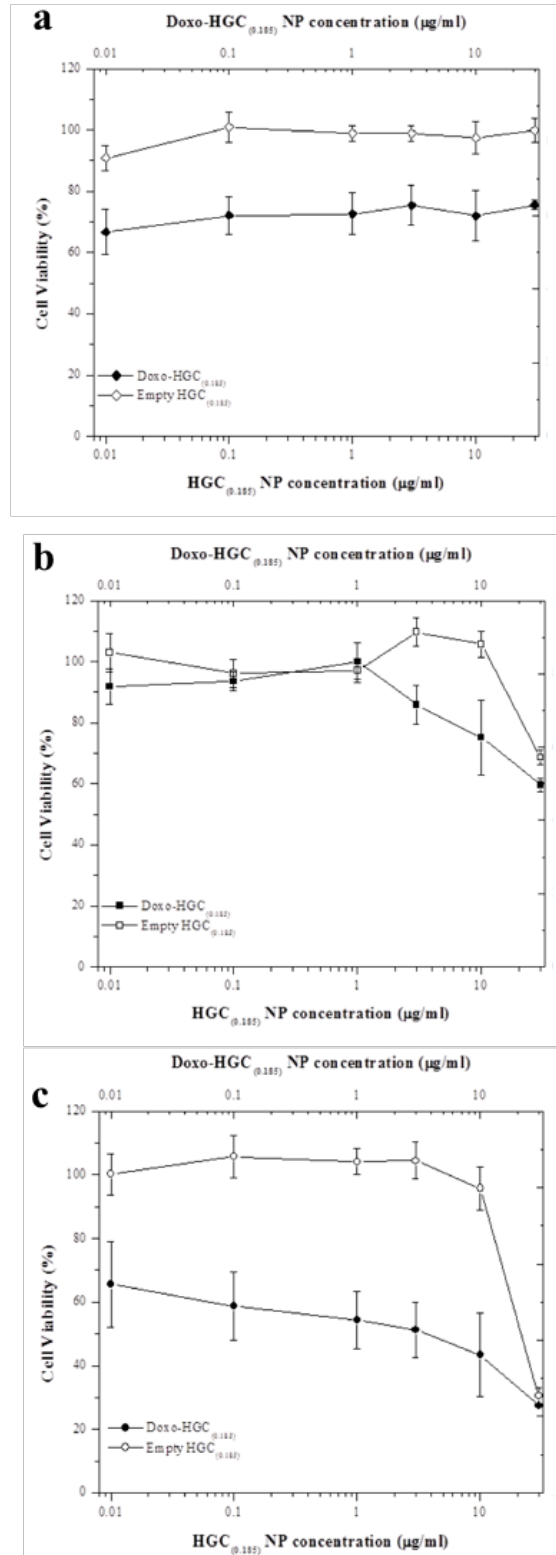


Figure 2.25 Comparison of the viability of MG-63 cell monolayer treated for 24 hours (a), 48 hours (b) and 72 hours (c) with either empty HGC_(0.185) nano-vehicles (hollow markers) or doxorubicin-loaded HGC_(0.185) nanocomplexes (solid markers).

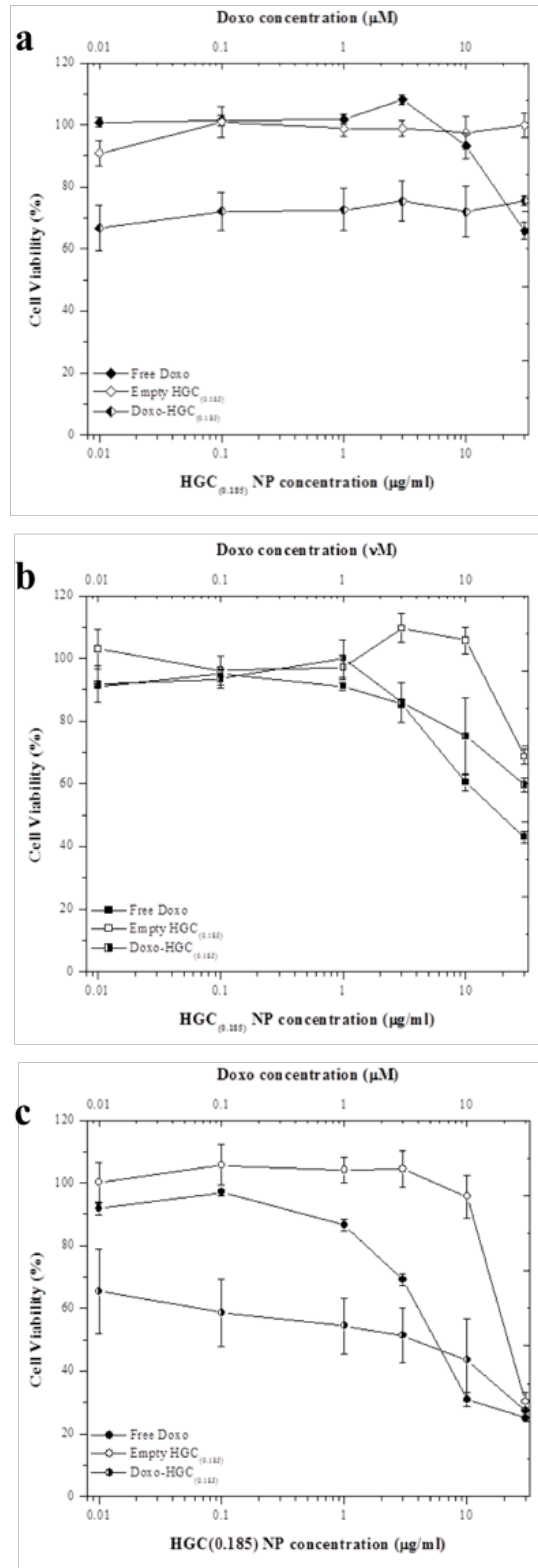


Figure 2.26 Comparison of the viability of MG-63 cell monolayer treated for 24 hours (a), 48 hours (b) and 72 hours (c) with either free doxorubicin (solid markers), empty HGC_(0.185) nano-vehicles (hollow markers), or doxorubicin-loaded HGC_(0.185) nanocomplexes (bi-color markers).

2.4 Conclusions and Future Perspectives

In this study, hydrophobic modifications of glycol chitosan were performed, in order to obtain amphiphilic molecules (HGC) able to self-organized in aqueous environment. Polymeric self-assembled nanoparticles were characterized in terms of size, morphology, pH responsiveness and ability to encapsulate and subsequently release a hydrophobic model drug. Results revealed a correlation between the material chemistry and the resulting physicochemical properties.

With the aim of proposing these polymeric complexes as anti-cancer compound delivery nano-vehicles, the second part of the study was dedicated to the administration of empty, non-functionalized HGC NPs to a human osteosarcoma cell line, to evaluate the nano-micelle cellular internalization ability and their cytotoxicity. Results showed null or minimal cytotoxicity of the empty vehicles towards MG-63 cells, over a broad range of nanoparticle concentrations tested, up to 72 hr post-treatment. Moreover, no significant changes in the cell morphology, motility and their ability to produce the extracellular matrix protein fibronectin were observed to be associated with the HGC nano-micelle administration, suggesting the potential use of our construct in living systems. Interestingly, doxorubicin-micelle nanocomplexes, successfully synthesized and internalized by the cells in monolayers, showed comparable cytotoxicity with the free model drug alone, indicating the preservation of the drug functionality and activity. This constitutes a promising outcome for the further formulation of our nanoparticulate engineering construct. In fact, thanks to its dimension and physicochemical properties, our system would more likely to provide passive targeting of tumor masses (the so-called EPR effect), and bypass the reticulum endoplasmaticum clearance, allowing longer circulation and bioavailability. Moreover, the HGC micelles, when properly decorated with a functional molecule, would also be able to selectively target the surface of tumor cells, be internalized within them while still protecting and delivering in a sustained manner functional anti-cancer molecules (exploiting the so-called *Trojan horse* function). The enhancement and evaluation of the HGC nano-micelles' targeting ability will be the focus of Chapter 3.

Confocal microscopy allowed the visualization of the Cy5.5-HGC NPs, efficiently internalized into the osteosarcoma cells. The uptake dependence on incubation time and nanoparticle concentration was noticed. Lysosomal vesicle staining revealed that some HGC NPs may have co-localized with those intracellular compartments. A more systematic study, involving

multiple vesicle staining and higher resolution image acquisition, should be carried out, to confirm the preliminary outcome and gain more insights into the chitosan-derivative micelle routes of entry into the cells (e.g. clathrin-mediated endocytosis, caveolin-mediated endocytosis and micropinocytosis), and their following degradation pathway. Further experiments with the application of endocytosis inhibitors (e.g. chlorpromazine, filipin and amiloride) can be considered, to elucidate which mechanisms of uptake are predominantly involved in the case of the chitosan-derived micelles. In fact, understanding the mechanisms involved in the NPs cellular uptake and intracellular fate constitutes an essential step towards the establishment of effective nano therapeutics with a controlled cellular pharmacokinetics.^{29, 31, 125, 130, 190}

Strategies to improve the micelle uptake specificity can be implemented, to favor an active, preferential internalization in tumor cells, without leading to healthy tissue accumulation. Due to the versatile chemistry of the chitosan-derivative system, which allows either covalent linkage of functional groups or physical complexation with different components, functionalization with surface recognition molecules or active biomolecules can be developed. In the following chapters of this thesis work, examples of modifications in the synthesis process will be presented, to properly decorate the engineered HGC nano-constructs according to a specific drug delivery application (see Chapter 3 and Chapter 5).

To explore a different cellular approach, three-dimensional spheroids can be used to study the chitosan-derivative micelles penetration into a solid, complex cell network, which replicates some morphological and structural features of the tumor microenvironment.^{187, 191-194} In fact, the cell monolayer poorly reflects the *in vivo* cellular assembly conditions. On the other hand, microtissues *in vitro* can exhibit actual tumor microenvironment features, such as gradient in the oxygen content and in the pH, differential nutrient penetration, cell-to-cell signaling and matrix deposition. Thus, these cellular tools might help to gain a deeper understanding of the nano-vehicle interactions with the heterogeneous milieu and their actual application for a successful tumor penetration and therapy. In a following chapter of this thesis work, with the aim of addressing this biological question, the development of MG-63 three-dimensional multi-cellular systems for a more complete analysis of the HGC penetration ability will be presented (see Chapter 4).

Chapter 3:

Multifunctional, chitosan-based micelles to target breast cancer cell invasiveness

3.1 Introduction

Affecting about 1.6 million people every year, breast cancer is one of the most common malignancy among women worldwide. While the 5-year survival for patients with localized cancerous masses reaches 98%, the survival percentage of women presenting advanced diseases, with proximal (lymph nodes) or distant (bone, lung) metastatic lesions dramatically decreases to 83.6% and 23%, respectively.^{195, 196} This poses the attention of the scientific and clinical communities towards the development of new strategies to target cancer metastasis.

During a metastatic process, cancer cells disseminate from the primary tumor to a distant tissue, interacting with and remodeling the extracellular matrix (ECM) in the surroundings. Cancer cells that have acquired invasive capacities are able to breach the basement membrane, a cross-linked network (about 50 – 100 μm thick) of proteoglycans and type-IV collagen, separating epithelial cells from connective tissues (Figure 3.1).¹⁹⁷ First, the ventral surface of the cells develops invadopodium-like processes, to invade within the physical barrier constituted by the matrix (Figure 3.1b). In a second step of the metastases formation, cancer cells move through the interstitial tissue (type I collagen being the main component of the three-dimensional network) with a mesenchymal invasion mode, characterized by the extension of the lamellipodia protrusions in the direction of the migration (Figure 3.1c). The pericellular region undergoes proteolysis, mediated by metalloproteinases, a class of molecules from the family of the zinc-dependent endopeptidases, and the resulting proteolytic tracks serve as guidance to support further cell invasion.¹⁹⁷ Collective cancer cell migration as multicellular sheets is also possible, based on the maintenance of cell-to-cell contacts and MMP-associated matrix remodeling. In addition, in an antithetical scenario, individual cell migration via amoeboid motion has been correlated to myosin-II-dependent contractility.¹⁹⁷ After penetrating through the ECM, invasive cancer cells enter the bloodstream, to subsequently extravasate into a new tissue site, where a metastatic tumor mass can be established (refer to Chapter 1, Figure 1.1, for metastasis formation process).¹⁹⁸

Matrix metalloproteinases (MMPs) are involved in ECM remodeling events, such as wound repair, tissue morphogenesis during development, and physiological mediation of immune responses. However, MMPs' dysregulation has been identified as a driving factor for cancer progression, metastasis formation, and poor patient prognosis and survival.¹⁹⁹ In the past decade, the traditional concept of genetic mutation-driven cancer cell proliferation and survival potential has been widened by understanding the key role of the tumor microenvironment in actively supporting the disease progression.²⁰⁰⁻²⁰³ Among the biochemical and biophysical cues, exchanged reciprocally between the cells and the surrounding ECM, and transmitted from the cell membranes to the nuclei through the cytoskeleton components, matrix metalloproteinases appeared to be implicated in basement membrane breaching, interstitial tissue invasion, and angiogenesis promotion.¹⁹⁹

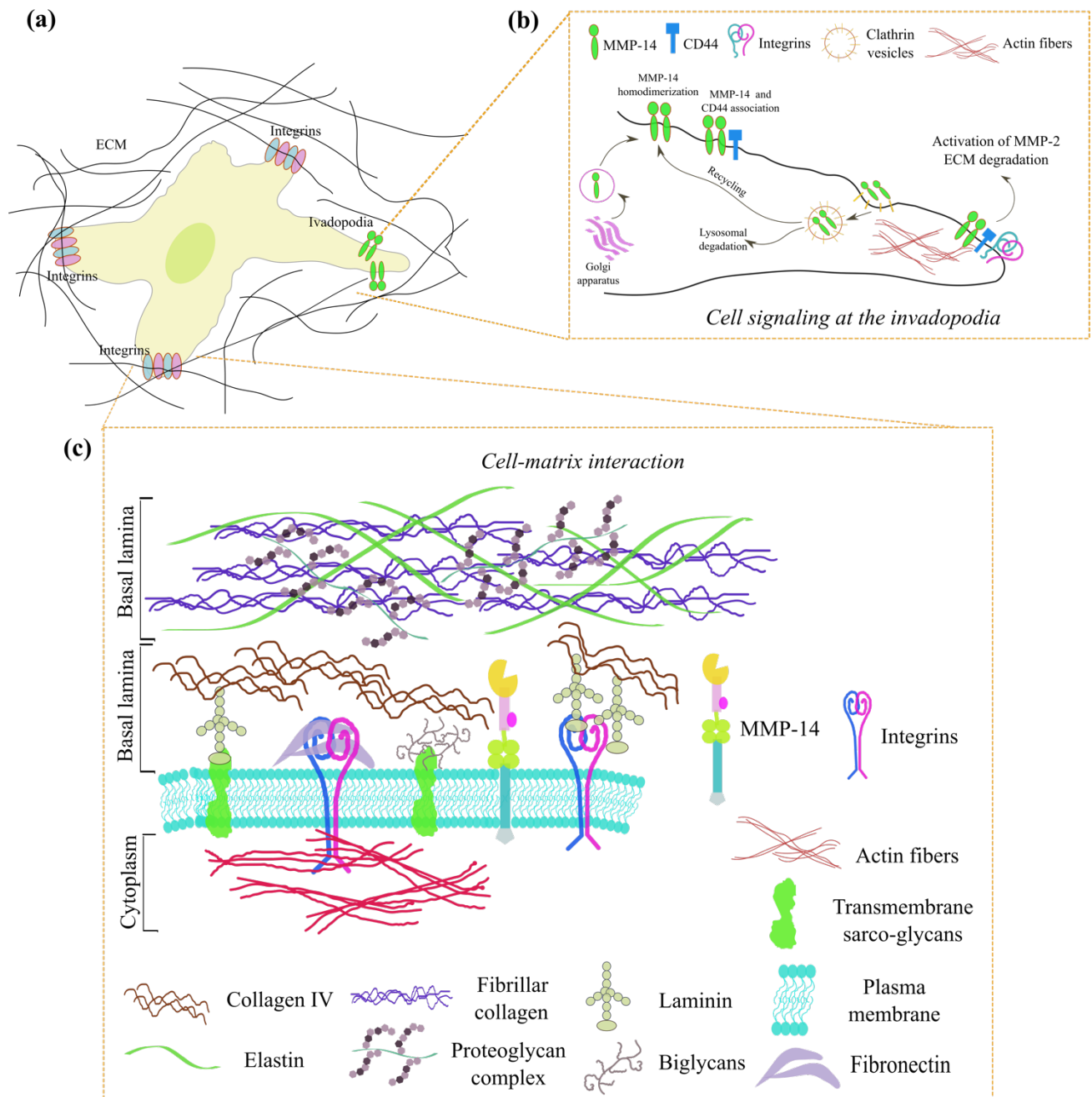


Figure 3.1 Schematic of the cell-matrix interaction: (a) a cell surrounded by ECM; (b) cell signaling at invadopodia, with MMP-14 associated ECM degradation and cell migration processes; (c) basal lamina and ECM components.

Within this family of 25 members, the enzyme substrate preference gives a classification method for the different subgroups. In Figure 3.2 a-e, the generic structures of the various subgroups are presented. Collagenases (MMP-1, MMP-8, MMP-13 and MMP-18) can cleave fibrillary collagen types I, II and II, and aggrecan. Gelatinases (MMP-2 and MMP-9) present a proteolytic action toward gelatin, elastin and fibronectin, while stromelysins (MMP-3, MMP-10, MMP-11 and MMP-12) act on proteoglycans, laminin, casein, gelatin and fibronectin. On the other hand, matrilysins (MMP-7 and MMP-26), active both intracellularly and as secreted molecules, are involved in cell adhesion and in matrix components' hydrolysis processes. Lastly, membrane-bound proteinases (MMP-14, MMP-15, MMP-16 and MMP-25) not only present enzymatic activity toward fibronectin, collagen and laminin, but are also involved in regulating complex signaling pathways, due to their strategic localization at the cell surface.^{199, 204} Several structural elements are conserved among all the MMPs: (1) a signaling sequence at the N-terminal, (2) a propeptide region, (3) a catalytic domain with a calcium-dependent active site for the zinc coordination, (4) a linker, and (5) a hemopexin domain (PEX) involved in protein-protein interactions. While the catalytic segments are highly preserved among the different proteinases, the PEX domain is the least homologous, conferring high substrate specificity.^{197, 199} In addition, MMP-14 and MMP-15 are distinguished from the soluble proteinases, due to the presence of a transmembrane domain and a short cytoplasmic tail at the C-terminal. In the case of matrix metalloproteinase-14 (also known as MT1-MMP) the 64 kDa proMT1-MMP is converted into the active 55 kDa enzyme in the trans-Golgi network via furin-mediated proteolysis. Once transported at the cell membrane, MMP-14 homo-dimerizes and starts a signaling cascade which leads to the activation of the secreted collagenases MMP-2 and MMP-13. In addition, MMP-14 is directly responsible for the cleavage of various components of the extracellular milieu and for the association with cell surface proteins, such as CD44 and integrins. The regulation cycle of MMP-14 includes cellular internalization, usually via clathrin-mediated or caveolae-mediated endocytosis and entrapment into early and late endosomal compartments. A fraction of the proteinase is degraded in late endosomes and lysosomes, while another fraction enters a recycling pathway within the Golgi apparatus and storage vesicles, which leads to subsequent cell surface expression.^{197, 205} MMP-14 and activated MMP-2 have been shown to preferentially accumulate at invadopodia, specialized plasma membrane extensions rich in actin, adhesion molecules and tyrosine kinases, present in invasive cancer cells and accountable for ECM degradation.^{206, 207} This

brought new insight into the regulation of mesenchymal migration mechanisms, and opened the door for new, potential pharmacological targets to address metastatic disease progression.

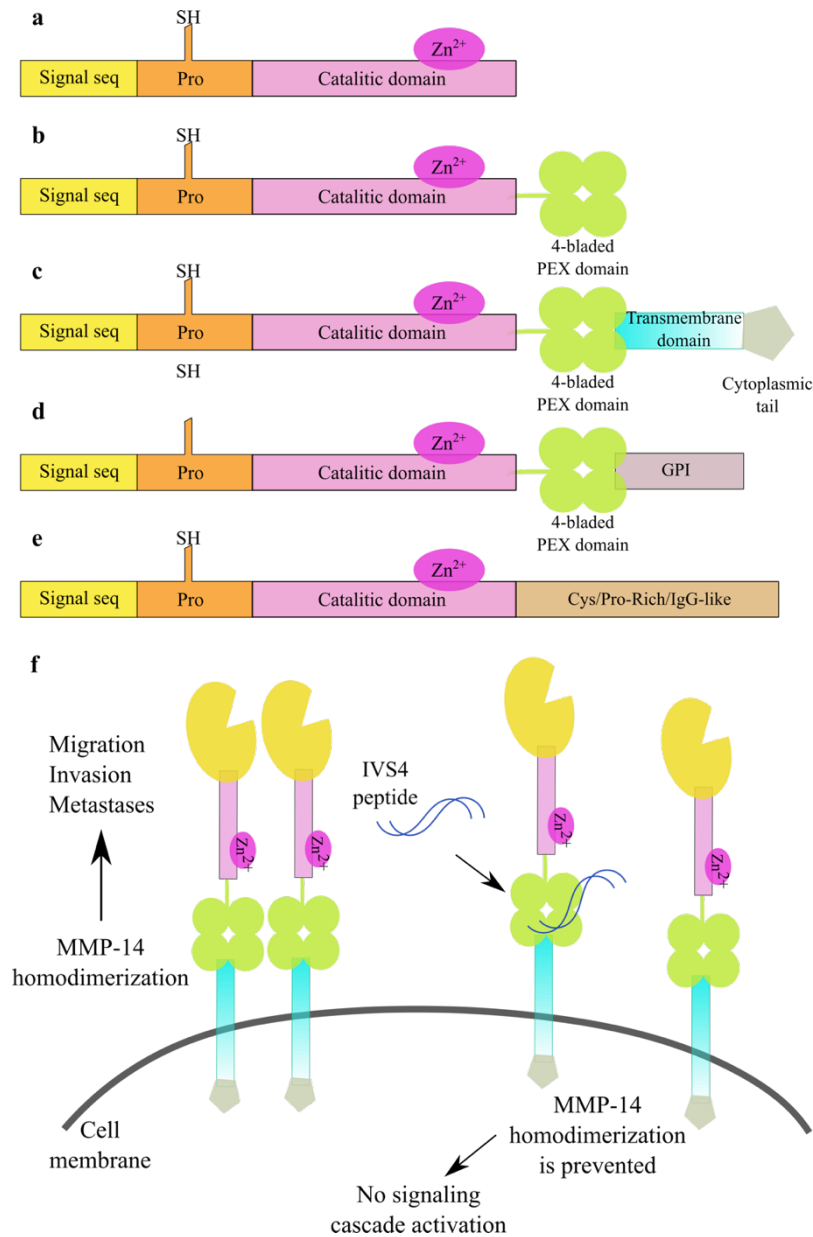


Figure 3.2 General structures of matrix metalloproteinases' subgroups: (a) minimal domain of MMP-7, -26; single-hemopexin (PEX) domain of MMP-1, -2, -8, -9, -13, -3, -10, -11, -12, -19, -20, -22, -28; (c) transmembrane MMP-14, -15; (d) glycoposphatidylinositol GPI-anchored MMP-17, -25; (e) Cys/Pro-Rich/IgG-like MMP-23. In panel (f) the homodimerization of MMP-14 allows the activation of the signaling cascade which leads to cell migration, invasion of the ECM and metastasis formation. The binding of the IVS4 peptide at the PEX domain interferes with the homodimerization process, preventing MMP-14 associated cellular functions.

Matrix metalloproteinase-14 is overexpressed in several tumors, such as small cell lung cancer, head and neck carcinoma, bladder, prostate, breast and ovarian cancer. Moreover, this up-regulation correlates with poor patient prognosis, invasive metastases formation²⁰⁸ and, ultimately, shorter survival time.²⁰⁵ In the past decades, clinical trials have been carried out to study the ability of small molecules, antibiotics, and monoclonal antibodies to target the catalytic activity of a broad spectrum of MMPs. Unfortunately, due to a lack of specificity of the designed inhibitors, and the structural homology of the catalytic domain, which did not allow a successful discrimination of the MMPs to target, no significant improvement in the symptomatic progression or in the patient survival was observed and the clinical trials were cancelled.¹⁹⁹ A shift in the direction of investigation, focusing the attention on the more diverse hemopexin (PEX) domain, led to the establishment of more promising strategies.^{204, 209, 210} The PEX domain presents four propeller-like blades, disposed to form a central funnel-like tunnel. Each blade is constituted of four β -strands, being β 4 the least preserved across different proteinases, suggesting its mediation role in specific protein interactions.^{199, 209, 210} In fact, homodimerization of MMP-14 occurs via the outermost strand of blade IV, while its association with CD44 molecules is mediated by the outermost strand of blade I. Since both processes induce cytoskeleton rearrangements necessary for the activation of the invasion machinery, targeting the PEX domain to prevent further molecular associations of the MMP-14 appears a feasible and potential approach. Small peptides such as IS4 (acetyl-Val-Met-Asp-Gly-Tyr-Pro-Met-Pro-NH₂) and IVS4 (acetyl-Gly-Tyr-Pro-Lys-Ser-Ala-Leu-Arg-NH₂), mimicking the outermost motif of blade I and IV of the PEX domain, have been observed to inhibit MMP-14-associated migratory functions, decrease tumor size and metastatic foci number, when administrated *in vitro* or to animal models (Figure 3.2 f).^{199, 205, 209} These inhibitors can constitute a valid strategy to modulate the MMP-14-dependent disease promoting features, while allowing the physiological activity of the proteinase.

With 230,500 new breast cancer cases in 2011 in the USA, breast cancer constitutes the second leading cause of tumor mortality among women, representing a major public health issue. The aggressiveness of the pathology resides in the development of metastatic foci in several tissues and organs, such as lymph nodes, liver, lung, bone and brain.²¹¹ While significant progresses have been made in understanding the biological features of various subgroups of breast cancer (e.g. the expression of cell surface receptors, their response to chemotherapies, their invasive behavior), and improvements in local treatments or surgeries have been obtained, little advance has been

achieved in treating patients with metastatic breast cancer. Currently, cancer nanomedicine has emerged to bring new nano-technological insights into the picture for the treatment development of this highly invasive disease.^{190, 211, 212} Recently, advances in drug delivery design have brought attention to the formulation of bio-engineering constructs with high binding affinities for MMPs and suitable pharmacokinetics profiles. Polymeric nano-micelles, conjugated to a selective cellular marker, able to respond to the tumor microenvironment cues and to encapsulate a cytotoxic agent, have emerged as innovative and successful approach to target cancer cell invasiveness. Focus of this study was the development of a peptide-decorated chitosan-based micelle for the targeted delivery of an antineoplastic compound to a model invasive breast cancer cell line.

In our approach, chitosan-based micelles are functionalized with the inhibitory peptide IVS4, mimicking the outermost motif of the PEX domain.²⁰⁹ The glycol chitosan derivative nanomicelles fabricated in our laboratory have shown rapid cellular internalization *in vitro*, stability in enzyme-containing environment,²¹³ and hemocompatibility.¹⁶⁶ Moreover, thanks to the chemical tailorability of the polymeric chain, functional groups and targeting moieties can be easily included to exert a specific biological goal.¹⁶⁶ The IVS4 peptide has been shown to interact with the MMP-14 expressed at the surface of the invadopodia fronts in human breast cancer cells *in vitro*. The binding would limit its homodimerization and impair the consequent activation of the migratory signaling cascade. Triple-negative breast cancers, accounting for about 15% of total patients, do not present estrogen and progesterone receptors and do not express the gene for HER2 (human epidermal growth factor). Poor prognosis associated to a high rate of metastasis formation and the lack of response to hormonal or HER2-targeting therapies are associated with a low patient survival.²¹² Therefore, the need for a new strategy to overcome the current therapeutic limitation is of great importance. Our proposed construct would selectively bind MMP-14, potentially undermining the associated migratory activities and preventing the cell invasiveness. In addition, the chitosan-based micelle would be internalized into the cytoplasm and enter intracellular pathways, while being coupled with the proteinase. Once internalized, the pH responsiveness of the engineered system would allow the release of an encapsulated anticancer compound, to effectively obtain a cytotoxic effect (Figure 3.3). More specifically, we have opted for the encapsulation of ansamitocin-P3 (AP-3), a potent antitumor drug from the class of maytansinoids, extracted from the fermentation broth of microorganisms and mosses.²¹⁴⁻²¹⁶ The drug, presenting a macrolactam structure attached to a chlorinated benzene, showed antitumor activity against

Lewis lung carcinoma, melanocarcinoma, multiple myeloma,^{217, 218} sarcoma and lymphocytic leukemia²¹⁴ at considerably low doses (IC₅₀ in the range of pmol/L – few nmol/L), both *in vitro* and in animal model. In their study, Venghateri *et al.*²¹⁹ provided elucidation on the AP-3 anti-proliferative mechanisms of action against a plethora of cells in culture, which responded to half-minimal inhibitory concentrations, in the range of 20 pM - 150 pM. Ansamitocin P-3 disrupts interphase and mitotic microtubule (MT) polymerization by binding at the vinblastine binding site of the MT dimer. In addition, activation of the p53 apoptotic pathway has been observed. Due to the promising biological functionalities as a microtubule-depolymerizing agent, immune-conjugates^{217, 218, 220, 221} and AP-3 derivatives and prodrugs have been proposed for clinical trials.²¹⁵ However, due to the poor solubility of the molecule and the potent cytotoxicity, no significant benefits were observed for the patients,²¹⁴ suggesting the need of further system modification. In addition, the lack of a strong chromophore group, requires sensitive analytical methods of detection, in order to obtain info on the pharmacokinetics of AP-3 molecules.^{215, 222} Our engineering construct AP-3 loaded Cy3-HGC-IVS4 nano-complexes would combine the IVS4-targeting ability with the ansamitocin cytotoxic potential, allowing easy fluorescent tracking and protection of the cargo molecule during the delivery.

Considering the above mentioned premises and the physicochemical characteristics of the material system under study, we formulated the following hypotheses.

- Hypothesis (a): the modification of the HGC micelles with the IVS4 peptide, via biotin-avidin interaction, would lead to the formulation of spheroid-like micelles, able to selectively target cells expressing MMP-14 at their surface membrane.
- Hypothesis (b): the presence of the targeting moiety on the micellar engineered construct would allow its coupling with the membrane-bound MMP-14. Moreover, the intracellular fate would be dictated by the physicochemical properties of the HGC micelles, favoring the escape from degradation pathways.
- Hypothesis (c): the encapsulation of a microtubule-depolymerizing agent, active in the cytosolic compartment, would lead to the formulation of an effective drug delivery agents, towards MMP-14 expressing cancer cells.

In order to test our hypothesis, four cell lines, either expressing endogenous MMP-14 or lacking of its coding gene, have been used. An extensive microscopy study has been performed, to observe the intracellular uptake and the enhanced targeting ability of the micelles. In addition,

functional assays and cell viability experiments have been carried on, to assess the effect of our nanoconstructs on the MMP-14 associated cellular functions.

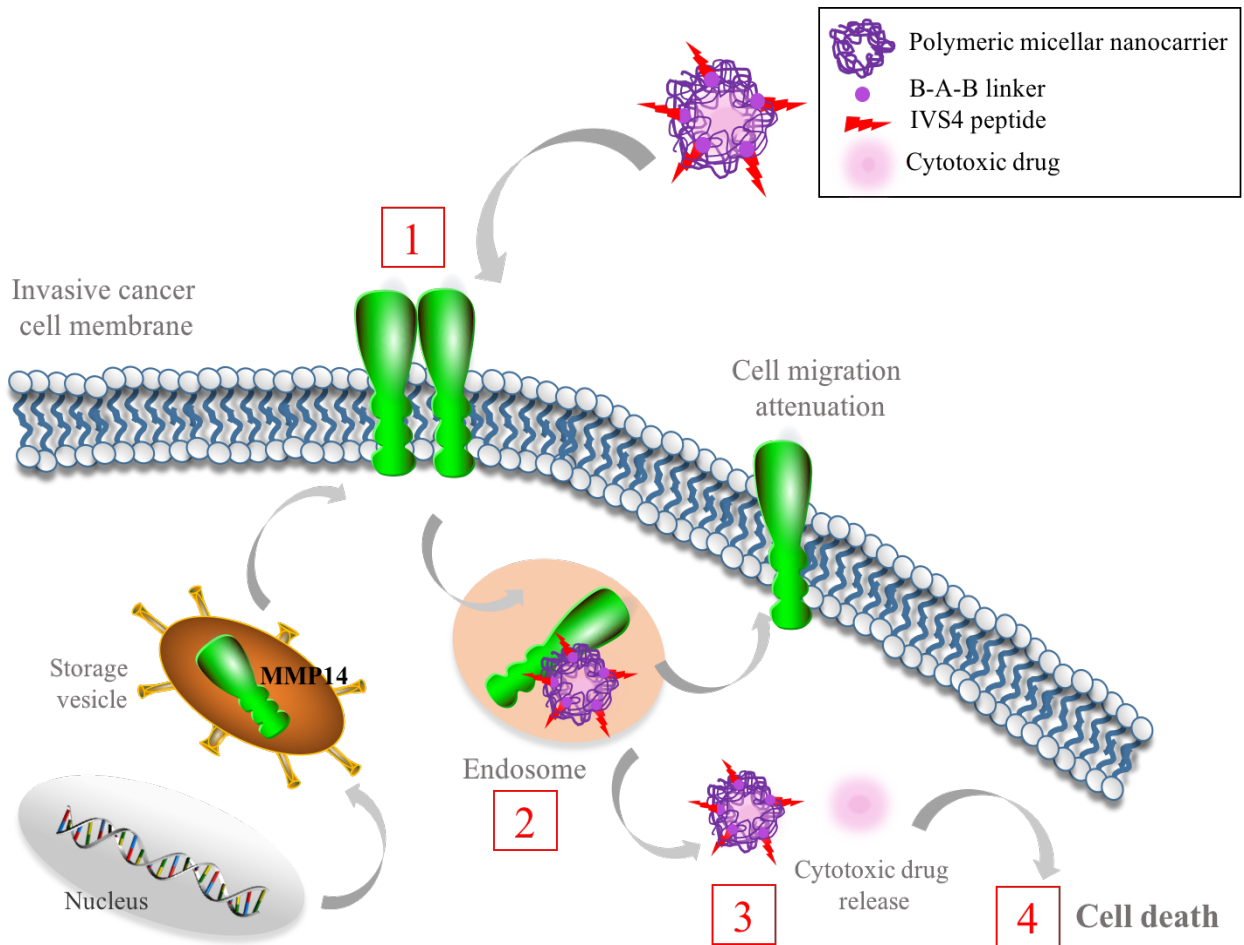


Figure 3.3 Hypothetical mechanism of uptake, internalization, and action of the IVS4-decorated HGC nanomicelles, interacting with a cancer cell expressing MMP-14 at its surface. (1) Micelle interaction with the MMP14, *via* PEX domain, over-expressed at the membrane of invasive cancer cells; (2) internalization process and trafficking, involving association with endosomes and intracellular vesicles; (3) endosome escape and cytotoxic drug release in the cytosol, which can lead to effective cell death (4).

3.2 Methods

Materials

Glycol chitosan (250 kDa molecular weight, degree of deacetylation > 60%), 5 β -cholanolic acid, N-(3-dimethylaminopropyl)-N'-ethylcarbodiimide hydrochloride (EDC), N-Hydroxy-Succinimide (NHS) were purchased from Sigma-Aldrich (St. Louis, MO). Monoreactive hydroxysuccinimide ester of Cyanine 3 (Cy5.5-NHS) was obtained from Lumiprobe (Hallandale Beach, FL). Analytical grade methanol was acquired from Pharmco-AAPER (Brookfield, CT). Biotin-4-fluorescein (B4F) is obtained from Biotium (Hayward, CA). Anhydrous dimethyl sulfoxide (DMSO) is purchased from EMD Chemicals (Darmstadt, Germany). The biotinylated-IVS4 peptide (Biotin-GYPKSALR-NH₂, 1116.37 Da) and the biotinylated control peptide (Biotin-GIHTEIGK-NH₂, 1079.31 Da) were purchased from EZBiolab (stock solution of 0.01 M in DMSO).

Synthesis of hydrophobically modified glycol chitosan (HGC)

The hydrophobic modification of glycol chitosan (GC) with 5- β -cholanolic acid is carried out as presented in Figure 2.1, following the synthesis procedure from Chin *et al.*²¹³ Briefly, glycol chitosan (500 mg) is dissolved in HPLC water (60 ml). In a separate beaker, 5 β -cholanolic acid (150 mg), N-hydroxysuccinimide (NHS, 72 mg) and N-(3-Dimethylaminopropyl)-N'-ethylcarbodiimide hydrochloride (EDC, 120 mg) are dissolved in methanol (60 ml). The hydrophobic modification is completed by slowly adding the cholanic activated solution to the glycol chitosan solution. The removal of the reaction by-products was performed by means of dialysis cassettes (10 kDa molecular weight cut off, ThermoScientific) for 1 day against a water/methanol mixture (1/4, v/v) and for 1 day against pure water. The resulting system was centrifuged for 30 minutes at 2790 rpm, lyophilized for 3 days to obtain the GC-5- β -cholanolic acid conjugate (HGC), and then finely ground into powder. Subsequently, the HGC was labeled with a cyanine dye that emits in the red light range of the electromagnetic spectrum (Cy3-NHS, ex = 555 nm, em = 570 nm). One mg of activated NHS-ester of the cyanine dye was dissolved in 250 μ l of DMSO. In a separate beaker HGC (100 mg) was dissolved in DMSO (40 ml) and the Cy3 solution was added drop-wise. The resulting system was kept in the dark for 6 hours at room temperature under constant stirring. The N-hydroxysuccinimide ester reacted with the free amine on the HGC

chain to form an amide bond. After dialysis, freeze-drying and grinding, an intense pink powder was obtained.

Synthesis of the peptide-decorated nanomicelles

The inhibitory peptide of interest (IVS4) and a scramble peptide as control were tagged onto the polymeric backbone via a series of chemical functionalization steps involving biotin-avidin reaction. Briefly, glycol chitosan (GC, 500 mg) was dissolved in 60 ml of HPLC water. Seventeen mg of sulfo-NHS-LC-Biotin (556.59 Da, ThermoScientific) were dissolved in 2 ml of HPLC water and added drop-wise to the GC solution. The system was let reacting for 3 hours and was subsequently loaded into dialysis cassettes (10kDa molecular weight cut off, ThermoScientific). After 48 hours of dialysis, the system was centrifuged for 30 minutes at 2790 rpm, lyophilized for 3 days and ground into powder, to obtain the biotinylated-glycol chitosan (B-GC). In the second step of the synthesis, avidin was added into the system. Briefly, 300 mg of B-GC were dissolved in 50 ml of HPLC water. Eighty ml of avidin were dissolved in 10 ml of HPLC water and subsequently added drop-wise to the B-GC solution. The system was let reacting for 2 hours. Afterwards, the solution was diluted by adding extra 36 ml of HPLC water: this would favor the preparation of aliquots for the following centrifugation step, and would allow a more efficient yield. The solution was transferred in 8 Amicon tubes, containing a filter membrane with 100 kDa molecular weight cut off. Centrifugation was performed at 5000xg for 30 minutes. The resulting retentate was freeze-dried and ground into powder to obtain biotinylated-avidinated-glycol chitosan (AB-GC). In the third step of the synthesis, the system was hydrophobically modified. Briefly, 200 mg of AB-GC were dissolved in 25 ml of HPLC water. In a separate beaker, 60 mg of 5- β -cholic acid were dissolved in 25 ml of methanol and 48 mg of EDC (1-Ethyl-3-[3-dimethylaminopropyl]carbodiimide hydrochloride) and 29 mg of NHS (N-hydroxysuccinimide) were added to activate the mixture. The activated 5- β -cholic acid was slowly added to the AB-GC solution and the system was let stirring overnight. To eliminate 5- β -cholic acid molecules, dialysis was performed as presented before (with dialysis cassettes, MWCO of 10 kDa), and the final product (AB-HGC) was obtained after lyophilization and grinding. The last step of the synthesis process involved the functionalization with the peptide of interest and with the fluorophore. Briefly, 60 mg of AB-HGC were dissolved in 40 ml of DMSO. The cyanine3 dye was added drop-wise to the system (120 μ l of 5 gm/ml of stock solution in DMSO) and let stir for

6 hours in the dark at room temperature. Afterwards, 77 μ l of biotinylated-IVS4 peptide were added drop-wise to the mixture and let reacting for 2 hours in the dark at room temperature. The system was then loaded into dialysis cassettes and dialyzed against HPLC water for 48 hours. Upon centrifugation, lyophilization and grinding, a pink powder of Cy3-HGC-IVS4 complex was obtained. A similar protocol was used for the tagging with a control, scramble peptide.

Preparation of the drug loaded, peptide-decorated nanomicelles and evaluation of the loading efficiency

In order to encapsulate the anti-cancer compound of interest into the peptide-decorated polymer nanocomplexes the following steps were carried out. In a round bottom flask, Cy3-HGC-IVS4 powder (30 mg) was dissolved in dimethyl sulfoxide (DMSO, 9 ml) for 1 hour. One mg of Ansamitocin P-3 (Ansamitocin P-3 from *Actinosynnema pretiosum*, Sigma Aldrich) was dissolved in 0.5 ml of DMSO and added drop-wise to the polymer mixture. After 5 hours of stirring, 21 ml of HPLC water was added in the flask: to the presence of hydrophilic and hydrophobic domains on the polymeric chains, in contact with water molecules and DMSO molecules, would favor the self-assembly into micellar structures. The system is kept under stirring overnight, in the dark at room temperature. To eliminate drug molecules loosely complexed with the Cy3-HGC-IVS4 polymeric chains, the suspension was loaded into dialysis cassettes (3.5 kDa molecular weight cut off, ThermoScientific) and dialyzed against HPLC water for 48 hours. The purified system was centrifuged for 30 minutes at \sim 3000 rpm and lyophilized for 3 days to obtain the AP3-loaded-Cy3-HGC-IVS4 complex, and then finally ground into powder. This synthesis was kindly performed by Weiyi Li. To assess the drug encapsulation efficiency, 2 mg of AP3-Cy3-HGC-IVS4 complex were dissolved into 2 ml of 0.1 M HCl. After the immediate dissolution in the acidic environment, 8 ml of methanol were added, to form a mixture of methanol:HCl (4:1, v/v). Aliquots were transferred to a 96-well plate and absorbance was recorded at 250 nm and 280 nm. The results were compared with a standard curve of the free drug in methanol and with the absorbance of empty Cy3-HGC-IVS4 nanocomplexes in the methanol:HCl mixture. The evaluation of the encapsulation efficiency was performed considering the following equation:

$$EE\% = \frac{W_{Doxo \text{ in micelles}}}{W_{feed \text{ Doxo}}}$$

Physicochemical characterization of nanomicelles

The HGC conjugate was suspended in serum free media and vortexed. The suspension was then probe-type sonicated for cycles of 2 minutes x 3 times and cycles of 5 minutes x 2 times. To prevent the increase in the temperature the particle suspension was kept on an ice bath. The self-assembled HGC nanoparticles were passed through syringe filters (pore sizes 0.8 and 0.2 μm , Pall Corporation) as a sterilization method for the following characterization and cell culture delivery. The size distribution and the surface charge of HGC nanocomplexes suspension were determined at 25 °C by Dynamic Light Scattering (DLS, Zetasizer Nano, Malvern Instruments Ltd., Westborough, MA). The morphology was obtained by placing few drops of HGC nanoparticle suspension on Lacey Carbon Film on 300 mesh copper grids and the extra solution is blotted with filter paper and air dried. The grids are observed under the Transmission Electron Microscope (JEM-1400LaB6, JEOL) with an accelerating voltage of 60kV. The characterization of the HGC vehicles was carried out at the Center for Functional Nanomaterials at Brookhaven National Laboratory.

In order to quantify the amount of biotin molecules successfully attached to the glycol chitosan polymeric chain, a HABA assay was performed. When HABA (4'-hydroxyazobenzene-2-carboxylic acid) is complexed with avidin, it adsorbs light at 500 nm. When a biotin-containing sample is brought into contact with the HABA complex, the biotin displaces the HABA (due to its higher affinity for avidin) and a decrease in the absorbance is observed. Various dilutions of B-GC in PBS were prepared, and the absorbance results were obtained via spectrophotometry (InfiniteM200Pro Tecan, Switzerland)

Cell culture and nanomicelle delivery

Triple negative breast cancer MDA-MB-231 cells, breast epithelial MCF-10A cells, and COS African green monkey epithelial cells were purchased from ATCC. COS cells were stably transfected using retroviral approach with either vector control (pQXCIP, Clontech) or vector bearing MMP-14, to obtain COS-pQ and COS-MMP14 cells (stably expressing the matrix metalloproteinase-14), respectively. When reaching a confluence of about 60%, cells were plated on glass coverslips and let attach overnight in Dulbecco's Modified Eagle Medium (DMEM, Gibco) containing 1% of pen/strep and 10% of Fetal Bovine Serum. MCF-10A cells were plated

in DMEM:F12 (v/v, 1:1) media (Gibco). After overnight adherence, cells were treated with Cy3-HGC, Cy3-HGC-IVS4 and Cy3-HGC-control peptide nanocomplexes at various concentrations ranging from 0.5 µg/ml to 50 µg/ml and for different time points (8 hours and 24 hours). Samples were then washed twice with PBS to remove non internalized nanomicelles, fixed with 4% of paraformaldehyde and Hoechst stained (1:2000 dilutions). The glass coverslips were mounted on microscope glass slides. Imaging was conducted under a Zeiss LSM 510 Meta NLO Two-Photon Laser Scanning Confocal Microscope, equipped with a red laser (543 nm) and a Chameleon tunable laser (810 nm). The cell plating and Hoechst staining was performed by Jillian Cathcart, while the imaging and the experiment design were carried out in collaboration

MMP-14 association mechanism study

Triple negative breast cancer MDA-MB-231 cells were plated on glass coverslips and let adhere overnight at 37 °C (Figure 3.4). Afterwards, cells were transferred at 4 °C for 15 minutes to pre-adapt and then were treated, on ice, with 2.5 µg/ml of Cy3-HGC-IVS4 nanocomplexes in DMEM serum free. In addition, cells were treated with a primary antibody for MMP14 (1:100 dilutions, rabbit-anti-MMP14, Millipore). Samples were transferred at 4 °C for 1 hour, to allow nanoparticle adsorption at the cell surface. Subsequently, cells were washed with ice cold PBS to remove the unbound nanoparticles and were incubated at 37 °C for different time points (2. 5. 10 and 30 minutes). At the desired time point, cells were fixed with 4% paraformaldehyde for 20 minutes at room temperature and permeabilized with Triton 0.02% for 7 minutes. After PBS washings, samples were incubated in 1% BSA and 5% normal goat serum for 30 minutes, and 1 hour with 200 µl of secondary antibody (FITC-goat-anti-rabbit, 1:1000 dilutions). Afterwards, nuclei were stained with Hoechst (1:2000 dilutions). The incubation was carried out by flipping the coverslips on a parafilm sheet in a humid chamber. Samples were imaged with a Nikon N-SIM Super Resolution Microscope equipped with a red laser (543 nm), a green laser (488 nm) and blue laser (405 nm). The plating was performed by Jillian Cathcart, while the staining, the imaging and the experiment design were conducted in collaboration.

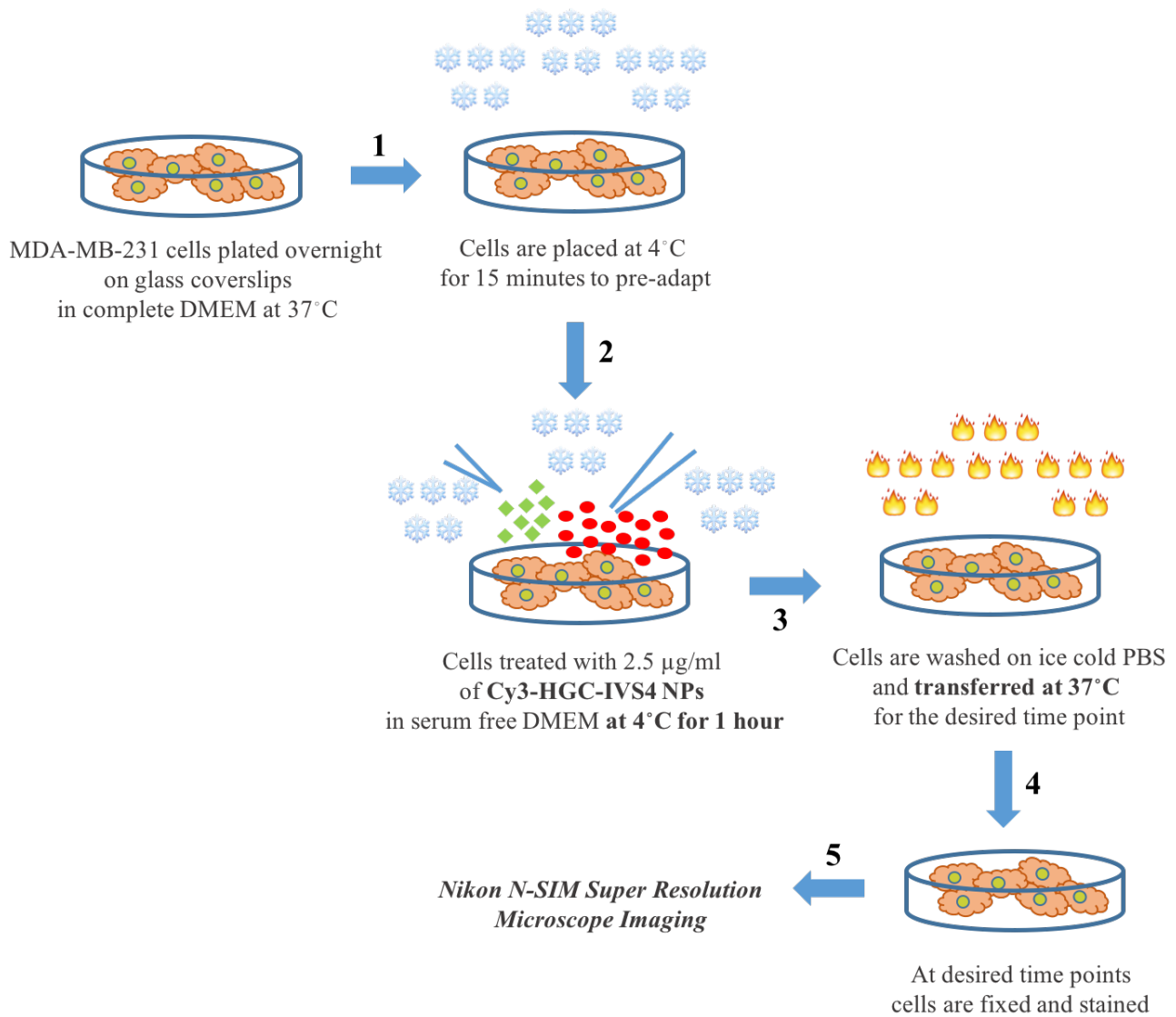


Figure 3.4 Flow diagram depicting the plating, treatment and post processing of the internalization mechanism experiment. MDA-MB-231 cells were treated with 2.5 µg/ml of Cy3-HGC-IVS4 NPs and with the primary antibody for MMP-14. The first incubation was carried out at 4 °C, to slow down the internalization process and endocytic recycling.

Endocytosis mechanism study

A similar experimental set-up was implemented for the study of the endocytosis mechanisms involved in the nanomicelles uptake. Triple negative breast cancer MDA-MB-231 cells were plated on glass bottom dishes and let adhere overnight at 37 °C. Afterwards, cells were transferred at 4 °C for 15 minutes to pre-adapt and then were treated, on ice, with 2.5 µg/ml of Cy3-HGC-IVS4 nanocomplexes in DMEM serum free. Samples were transferred at 4 °C for 1 hour, to allow nanoparticle adsorption at the cell surface. Subsequently, cells were washed with ice cold PBS to remove the unbound nanoparticles and were incubated at 37 °C for different time points (30 min, 1 hour, 3 hours, 8 hours, 18 hours and 24 hours). At the desired time point, cells were fixed with 4% paraformaldehyde for 20 minutes at room temperature and permeabilized with Triton 0.02% for 7 minutes. After PBS washings, samples were incubated in 1% BSA and 5% normal goat serum for 30 minutes. Cells were stained with 200 µl of either a primary antibody for early endosomes, EEA1 (BD Bioscience, 1:400 dilutions, 2 hours) or a primary antibody for lysosomes, LAMP1 (Stressgen, 1:250 dilutions, 2 hours). The secondary antibodies (Alexa Fluor 488-goat-anti-mouse, Molecular Probes) were applied for 1 hour at a dilution of 1:2000 and the cells were stained with Hoechst (1:2000 dilutions). Cells were stored in PBS. Samples at time zero (no incubation at 37 °C) was considered and directly fixed and stained after 1 hour of incubation at 4 °C. Control samples, in which cells were not treated with Cy3-HGC-IVS4 nanoparticles were also considered for time points 0 and 24 hours, as comparison. Samples were imaged with a Nikon N-SIM Super Resolution Microscope equipped with a red laser (543 nm), a green laser (488 nm), and blue laser (405 nm). A similar experiment was performed with the purpose of staining for the Golgi apparatus. In this case, samples were prepared and treated with Cy3-HGC-IVS4 NPs as mentioned above. At the desired time points (0, 8, 18, 24 hours) cells were fixed with 4% paraformaldehyde for 20 minutes at room temperature and permeabilized with Triton 0.02% for 7 minutes. After PBS washings, samples were incubated in 1% BSA and 5% normal goat serum for 30 minutes. Cells were stained with 200 µl of either a primary Golgi marker (Anti-Giantin, Abcam, 1:1000 dilutions, 2 hours). The secondary antibodies (Alexa Fluor 488-goat-anti-mouse, Molecular Probes) were applied for 1 hour at a dilution of 1:2000 and the cells were stained with Hoechst (1:2000 dilutions). The plating and staining was performed by Jillian Cathcart, while the imaging and the experiment design were conducted in collaboration.

Cytotoxicity study

To assess the cytotoxic potential of the engineered nanomicelles, MDA-MB-231 cells, MCF-10A cells, COS-pQ cells and COS-MMP14 cells were plated at a concentration of 1000 cells/well in white 96-well plates and let attach overnight. Cy3-HGC NPs, Cy3-HGC-IVS4 NPs, Cy3-HGC-control peptide NPs and Cy5.5-HGC-Biotin NPs were administrated for up to 72 hours at concentrations of 0.5 $\mu\text{g/ml}$, 1 $\mu\text{g/ml}$, 10 $\mu\text{g/ml}$, and 50 $\mu\text{g/ml}$. The nanoparticle suspensions were prepared with a stock solution in serum free media, and 10% FBS was added to the desired dilutions, to limit the possible cell death due to lack of serum during the assay. Negative controls with untreated cells and positive controls with Staurosporine (ATP-competitive kinase inhibitor and apoptosis inducer) treated cells were also considered for each data point. CellTiter-Glo® Luminescent Cell Viability Assay (Promega) was used to quantify the metabolically active, viable cells present in the culture, upon analysis of the ATP released in the media. Briefly, 100 μl of the reagent were directly added to well and let incubate for 30 minutes. The plate was gently shaken before luminescence reading. The cell plating and the viability assay were performed by Jillian Cathcart, while the nanoparticle administration and the experiment design were carried out in collaboration. Three independent experiments were performed, each presenting data in triplicates. Data are reported as mean value \pm standard error of a representative experiment. A Student's *t*-test was performed considering a *p* value < 0.05 (*) or *p* value < 0.01 (**). A similar approach was conducted for the cytotoxicity assessment of the drug-loaded engineered nanomicelles. In this case, MDA-MB-231 cells and MCF-10A cells were plated onto 96-well plates at a cell density of 1000 cells/well. Free ansamitocin P-3, AP3-loaded Cy3-HGC-IVS4 NPs and empty Cy3-HGC-IVS4 NPs were delivered at concentrations of 100 pM, 250 pM, 375 pM, 500 pM, 750 pM and 1 nM (expressed in terms of drug concentration equivalent). CellTiter-Glo® Luminescent Cell Viability Assay and data analysis were performed as mentioned above. Three independent experiments were performed, each presenting data in triplicates. Data are reported as mean value \pm standard error of a representative experiment. A Student's *t*-test was performed considering a *p* value < 0.01 (**).

Cell migration study

To assess the effect of the nanomicelles on the migration ability of MDA-MB-231 cells, two-dimensional collagen dots were prepared. Briefly, cells were re-suspended in DMEM containing either Cy3-HGC-IVS4 NPs or Cy3-HGC-control peptide NPs at concentrations of 0.0001 µg/ml, 0.0005 µg/ml, 0.1 µg/ml, 0.25 µg/ml, 0.5 µg/ml, 0.75 µg/ml, and 1 µg/ml for 30 minutes. Afterwards, cells were counted and centrifuged to obtain a concentration of 70,000 cells/µl. In a separate Eppendorf tube, 70 µl of distilled water and 50 µl of 5X DMEM were mixed with 125 µl of 6 mg/ml Type 1 collagen from rat tail in 0.2 N acetic acid. The system was kept under an ice bath, to prevent collagen hardening at room temperature. Two to three µl of 1 M NaOH were added to the mixture to bring the pH to neutral. Subsequently, in a separate Eppendorf tube, 10 µl of cell suspension were combined with 10 µl of collagen solution and homogenized through careful pipetting. 1.2 µl of the mixture were pipetted in the center of the well of a non-TC treated 96-well plate to form a 2D cell-collagen dot. The collagen concentration in the dot was 3.75 mg/ml. The dots were incubated at 37 °C for 7-8 minutes to allow solidification of the matrix, prior addition of 100 µl of DMEM containing the nanomicelles. The 2D cell-collagen dots were incubated for 8 hours at 37 °C and fixed for 20 minutes with 8% paraformaldehyde containing 2.5 µg/ml of DAPI. Under a fluorescence microscope the counting of the number of cells escaped from the outer border of the collagen matrix was performed, by means of ImageJ software (www.rsweb.nih.gov), ITCN plugin (Figure 3.5). Three independent experiments were performed, each presenting data in triplicates. Data are reported as mean value ± standard error. A Student's *t*-test was performed considering a *p* value < 0.05 (*) or *p* value < 0.01 (**). Plating and data analysis was performed by Jillian Cathcart, while the design of the experiment was conducted in collaboration.

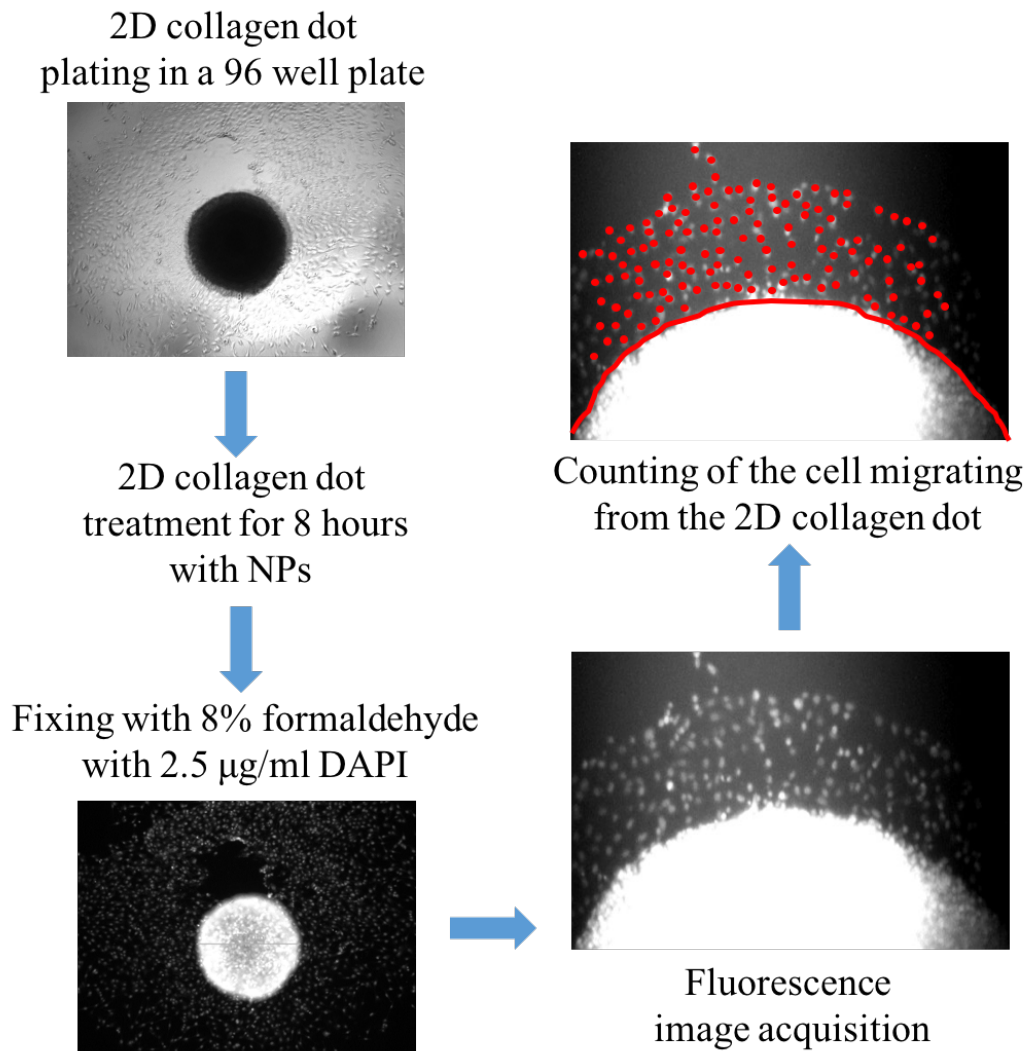


Figure 3.5 Cell migration assay: 2D collagen dots are plated in 96 well plates and treated with various concentration of nanoparticles (NPs) for 8 hours. Samples are fixed in 8% formaldehyde containing 2.5 $\mu\text{g/ml}$ of DAPI, to highlight the cell nuclei. Fluorescence image acquisition of zoomed area allows the identification of the cells migrating and escaping from the bulk mass. Cell counting is performed via ImageJ software, with a ITCN plugin.

3.3 Results and Discussion

Peptide-decorated nanocomplexes have been synthesized through biotin-avidin interaction and the system showed targeting ability for MMP14-expressing cells

In order to functionalize our chitosan-based micelles with the inhibitory peptides of interest via biotin-avidin interaction, a series of reaction steps was conducted (Figure 3.6). The use of the water soluble glycol chitosan (GC) as starting material allowed the performance of the reactions in a water-based environment. First, GC was conjugated to sulfo-NHS-LC-biotin through the formation of amide linkages at the primary amines of the D-glucoamine residues. In a second step, the water-soluble biotinylated glycol chitosan (BGC) is let reacting with avidin. Subsequently (Step 3, Figure 3.6), a cholesterol-derivative, 5 β -cholanic acid, is conjugated to the avidinated-biotinylated glycol chitosan (AB-GC), to yield a hydrophobic modified compound (AB-HGC), which presents an amphipathic behavior. In fact, while the hydrophilic biotin-avidin pendants and the glycol residues on the main backbone favor water solubility, the hydrophobic cholanic acid facilitates the self-assembling of the polymeric chains into micellar structure. Lastly, (Step 4, Figure 3.6), the resulting system is let reacting with the biotinylated-peptide (either the biotin-IVS4 or the biotin-control peptide). A fluorescent molecule (Cy3-NHS-ester) is also added to the reaction mixture, to favor the visualization of the micelles. After purification through dialysis and lyophilization, a fine, intense pink powder is obtained.

Probe-type sonication in water-based culture media of the plain Cy3-HGC NPs (no biotin-avidin linkage present) yielded to self-assembled micelles with an average diameter of 218.9 ± 4.8 nm, while the bio-polymeric compound lead to micelles presenting an average diameter of 202.1 ± 0.9 nm for the case of the Cy3-HGC-IVS4 NPs, and 247.1 ± 0.45 nm for the case of the Cy3-HGC-control peptide NPs (Table 3.1). As expected, the Zeta Potential measurements (Table 3.1) revealed the positive charge of the micelles, given the presence of the polycation glycol chitosan as base material. More specifically, values of +32.1 mV, +30.5 mV, and +22 mV were obtained for the plain Cy3-HGC NPs, the Cy3-HGC-IVS4 NPs, and the Cy3-HGC-control peptide NPs, respectively.

The TEM imaging analysis (Figure 3.7) confirmed the range of nanoparticle dimensions obtained by Dynamic Light Scattering. Moreover, uniform distribution of nanoparticles, in terms of morphology, spheroid-like shape and dimensions was observed. Taken together, those results

indicate that the addition of the avidin-biotin linked peptide moieties did not alter the micellar configuration, validating the success of our bio-polymer synthesis approach, as well as the reproducibility of the micellar fabrication process.

With the aim of assessing the targeting ability of the IVS4 peptide-decorated micelles for cancer cells presenting matrix metalloproteinase-14 expressed at the cell surface, a micelle uptake experiment was performed. Four different cell lines were selected: (1) triple negative breast cancer MDA-MB-231 cells, expressing endogenous MMP-14 at the cell membrane, (2) epithelial breast tissue MCF-10A cells, lacking of the gene for MMP-14, (3) COS-pQ cells, African green monkey epithelial cells, stably transfected with a vector control and (4) COS-MMP14 cells, African green monkey epithelial cells, stably transfected with a vector bearing MMP-14. The rationale behind the use of cells (1) and (2) is represented by the comparison of different internalization behaviors in cancerous and non-cancerous breast cells. In addition, this experiment would allow to investigate how the presence of MMP-14 on cancerous cell membranes might substantially increase the uptake of the IVS4-bearing NPs. In a second, parallel experiment, the use of cells (3) and (4) was set up in order to elucidate the role of transmembrane MMP-14 in determining the nanoparticle uptake process in normal epithelial cells.

Confocal imaging study of cells treated with various concentrations of Cy3-labelled nanoparticles revealed the presence of a clear pattern in the uptake. For the case of the MCF-10A cells treated for 8 hours with 2.5 $\mu\text{g/ml}$ of NPs (Figure 3.8 a-c), a faint red signal is observed in the cytosol, indicating a general poor micellar uptake. On the other hand, MDA-MB-231 cells (Figure 3.8 d-f) presented a more intense and punctate red fluorescence signal throughout the cytoplasm, when administrated for 8 hours with 2.5 $\mu\text{g/ml}$ of Cy3-HGC-IVS4 NPs, indicating a preferential internalization of the peptide functionalized nanoparticles in the MMP-14 expressing cancer cells. In Figure 3.8, the difference in the internalization between panel (c), showing epithelial breast cells, and panel (f), depicting breast cancer cells, is striking. A similar uptake pattern was noticed after 24 hours of treatment (Figure 3.8 g-i and l-n). At this time point, triple negative breast cancer cells (Figure 3.8 g, h, i) appeared to be able to generally internalize more nanoparticles than their non-cancerous counterpart (Figure 3.8 l, m, n), with a Cy3 fluorescent signal becoming more intense and highlighting the whole cytosolic compartment when IVS4-decorated micelles were administrated.

For the case of African green monkey epithelial cells, Cy3-HGC-control peptide NPs did not seem to be effectively internalized in neither of the two cell lines (Figure 3.9 b, e, h, m). Moreover, no substantial difference in the uptake was observed for the case of the Cy3-HGC NPs (Figure 3.9 a, d, g, l), which did not present any targeting moiety at their surface. On the other hand, Cy3-HGC-IVS4 NPs (Figure 3.9 c, f, i, n) were predominantly uptaken by COS-MMP14 cells, when delivered at a concentration of 1 $\mu\text{g/ml}$ for 8 hours (Figure 3.9 c,f) or 24 hours (Figure 3.9 i, n). This result further confirms the fundamental role of the transmembrane MMP-14 expression in favoring the internalization of nanomicelles bearing the inhibitory peptide IVS4 as recognition, targeting agent.

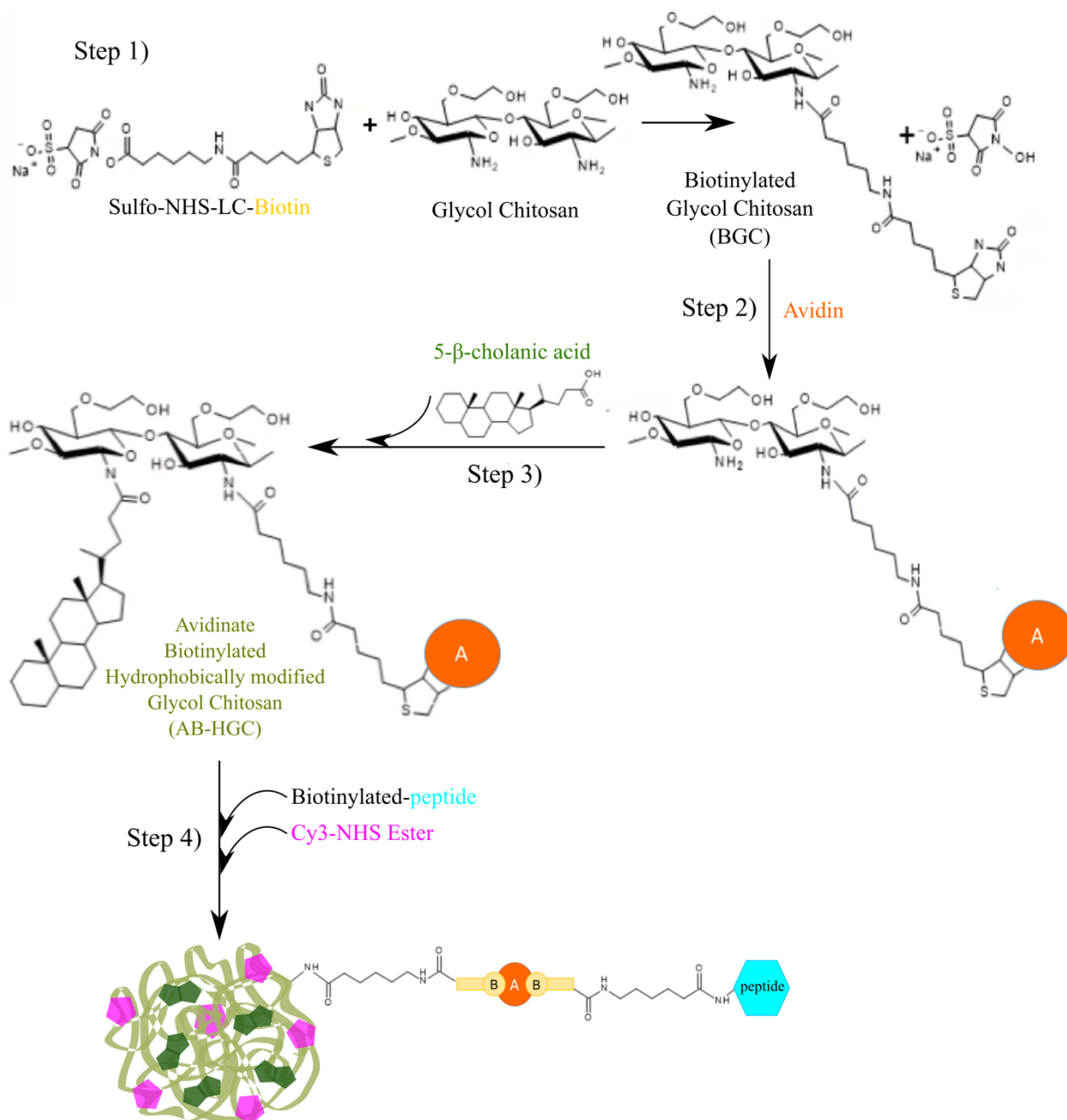


Figure 3.6 Synthesis of peptide decorated-HGC: (1) glycol chitosan is biotinylated in water with sulfo-NHS-LC-biotin to form BGC; (2) the first biotin-avidin bond is allowed to form in water, by mixing for 2 hours the dialyzed and lyophilized BCG product with avidin; (3) the resulting material is hydrophobically modified *via* reaction with 5-β-cholanic acid in methanol, in the presence of NHS and EDC as catalyzers; (4) the biotinylated peptide is added, together with the fluorophore, to complete the functionalization of the system.

Table 3.1 Average diameter and average surface charge measurements of nanomicelles

	<i>Cy3-HGC NPs</i>	<i>Cy3-HGC-IVS4 NPs</i>	<i>Cy3-HGC-control peptide NPs</i>
Average Diameter (nm)	218.9 ± 4.8	202.1 ± 0.9	247.1 ± 0.45
Average ζ-potential (mV)	$+32.1 \pm 1.6$	$+30.5 \pm 1.5$	$+22.0 \pm 1.4$

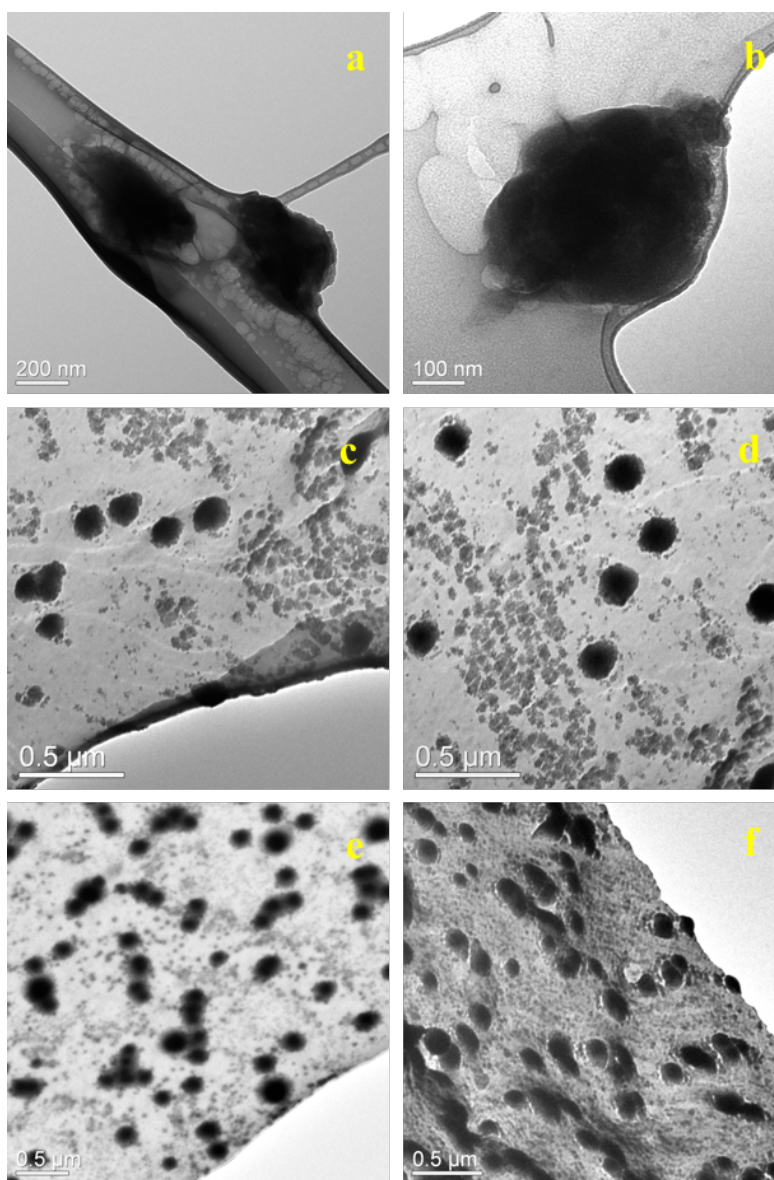


Figure 3.7 TEM micrographies of HGC micelles (a,b), HGC-IVS4 micelles (c, d) and HGC-control peptide micelles (e,f).

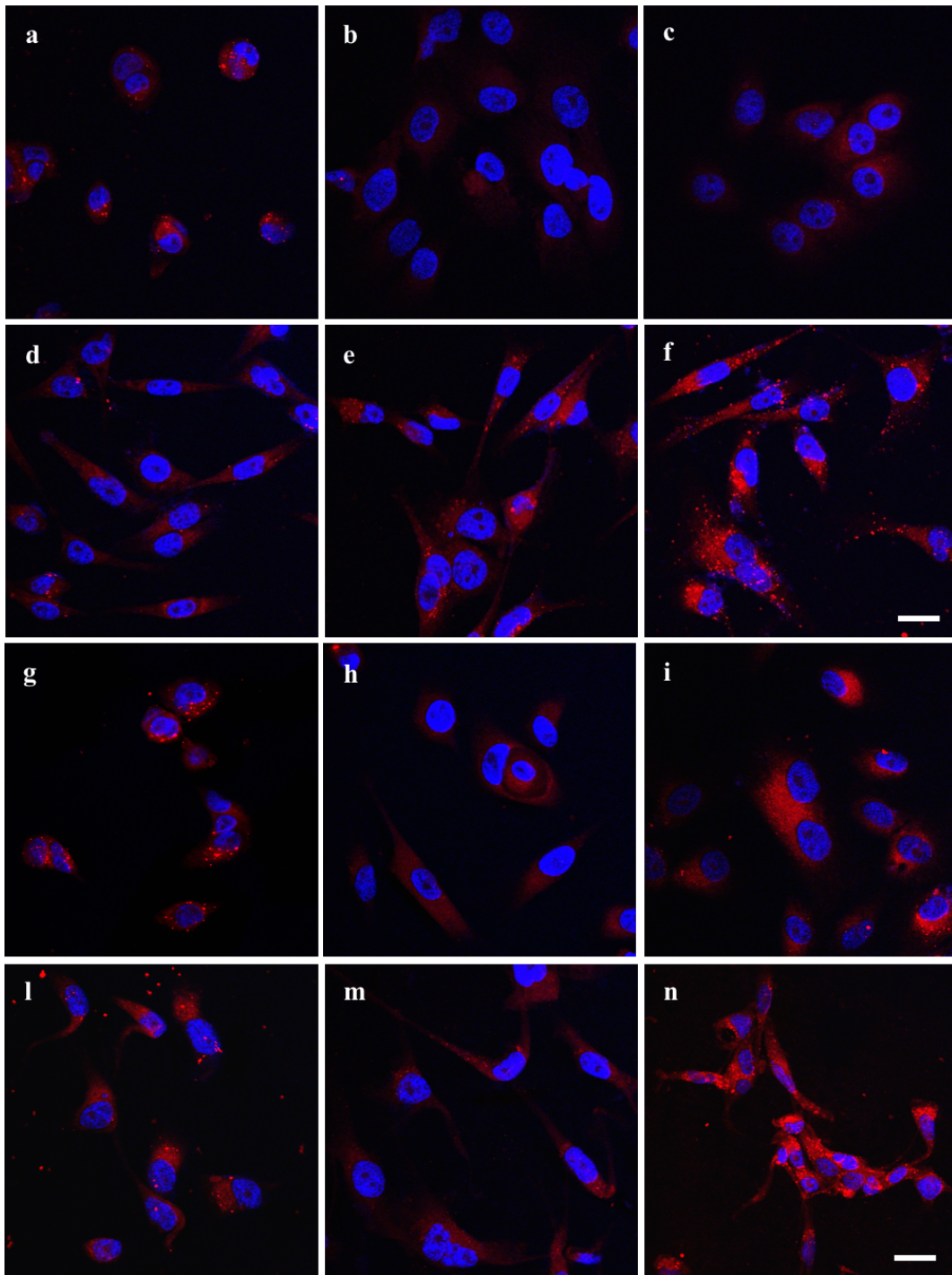


Figure 3.8 Confocal images of MCF-10A cells (a, b, c, g, h, i) and MDA-MB-231 cells (d, e, f, l, m, n) treated for either 8 hours (a-f) or 24 hours (g-n) with 2.5 $\mu\text{g}/\text{ml}$ of Cy3-HGC NPs (a, d, g, l), Cy3-HGC-control peptide NPs (b, e, h, m) and Cy3-HGC-IVS4 NPs (c, f, i, n). Images are representative of 3 independent uptake experiment. Scale bar 30 μm .

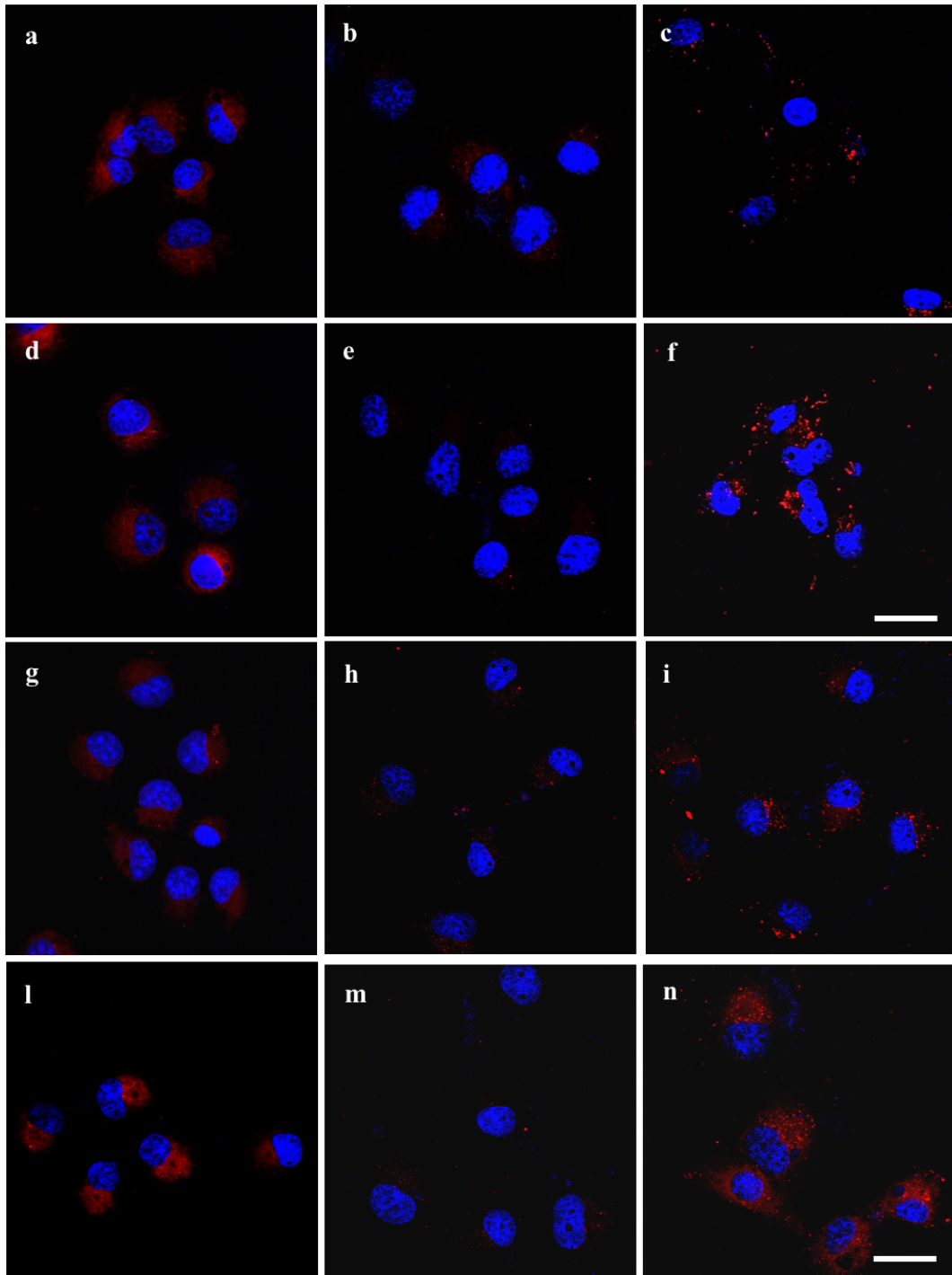


Figure 3.9 Confocal images of COS-pQ cells (a, b, c, g, h, i) and COS-MMP14 cells (d, e, f, l, m, n) treated for either 8 hours (a-f) or 24 hours (g-n) with 1 $\mu\text{g}/\text{ml}$ of Cy3-HGC NPs (a, d, g, l), Cy3-HGC-control peptide NPs (b, e, h, m) and Cy3-HGC-IVS4 NPs (c, f, i, n). Images are representative of 3 independent uptake experiment. Scale bar 30 μm .

Peptide-decorated nanocomplexes did not cause significant cell viability impairment, when delivered to four model cell lines

With the aim of assessing the cytotoxic potential of the engineered nanomicelles, a cell viability study was carried out on the four model cell lines. For this experiment, cells were plated in white 96 well plate and let attach overnight. The following morning, nanoparticles were delivered at different concentrations, ranging from 0.5 $\mu\text{g/ml}$ to 50 $\mu\text{g/ml}$, in DMEM containing 10% FBS, to limit cell death imputable to the lack of serum. Samples were continuously exposed to the media containing NPs for up to 3 days. Controls were considered by either leaving cells in normal DMEM, to check for good culture conditions, or in contact with staurosporine, an apoptosis inducer molecule as negative control. The cell viability was assessed with a CellTiter-Glo® Luminescence kit, which allows the quantification of the number of viable cells in culture by quantifying the ATP present and released by metabolically active cells. Representative results for each cell line are reported in Figures 3.10, 3.11, 3.12 and 3.13, in terms of luminescence counts obtained with a Gemini IM plate reader (a.u.). The results are grouped in bar graphs depending on the nanoparticle treatment performed, to facilitate the visualization of their effect with respect to the concentration and the time of the administration.

Triple negative breast cancer cells did not appear to be significantly affected by either Cy3-HGC NPs or Cy3-HGC-IVS4 NPs, over the range of concentrations tested (Figure 3.10 b, c). In fact, a stable increase in the number of viable cells was observed passing from day 1 to day 3 of culture. When treated with Cy3-HGC-control peptide NPs (Figure 3.10 d), MDA-MB-231 cells presented a lower viability compared to the control, at day 1 (decrease of 16%) and day 2 (decrease of 27%) of culture. This pattern was not observed at day 3, suggesting a possible recovery of the system.

Figure 3.11 shows representative results for MCF-10A cells. Also in the case of the breast epithelial cells, no significant effect on the overall viability was noticed, indicating that the different engineered nanoparticles can be used as safe delivery agents. The overall slightly higher susceptibility of the MDA-MB-231 cells to the empty nanoparticle treatment, compared to the MCF-10A cells, might correlate with the general tendency of the breast cancer cells to uptake more easily the nanomicelles than the breast epithelial cells (Figures 3.8 and 3.9).

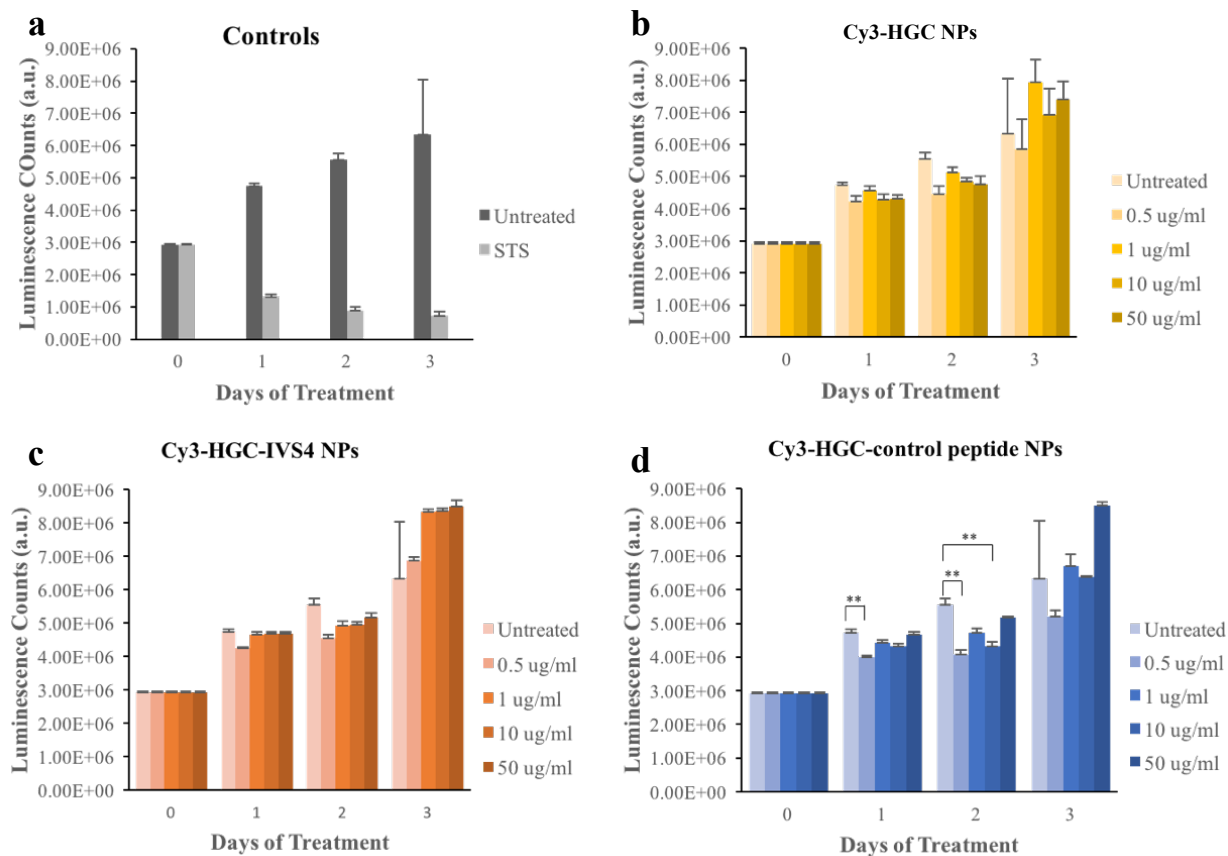


Figure 3.10 Cell viability of MDA-MB-231 cells treated with different nanoparticles (NPs) continuously for up to 3 days. Error bars represent s.e. of 3 independent experiments. Student's *t*-tests were performed between the treated samples and the control, untreated sample, at each time point, considering a *p* value < 0.01 (**).

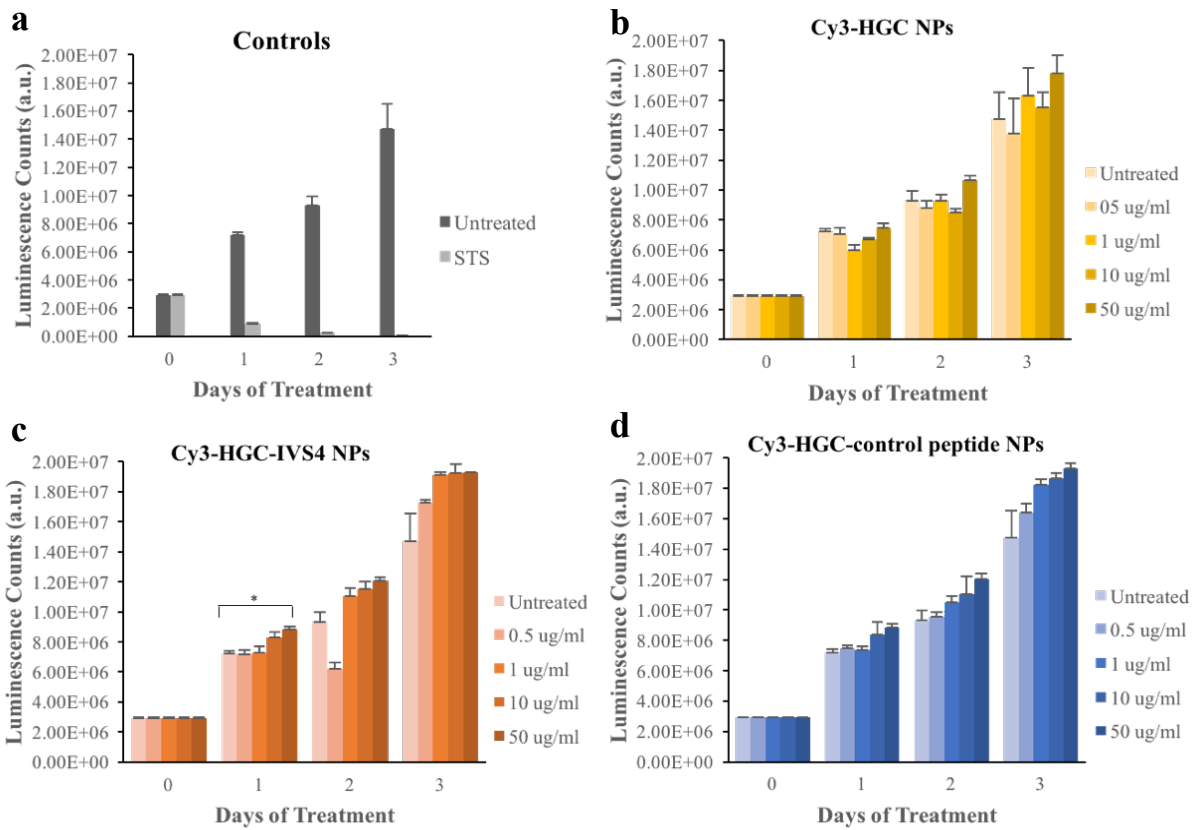


Figure 3.11 Cell viability of MCF-10A cells treated with different nanoparticles (NPs) continuously for up to 3 days. Error bars represent s.e. of 3 independent experiments. Student's *t*-tests were performed between the treated samples and the control, untreated sample, at each time point, considering a *p* value < 0.05 (*).

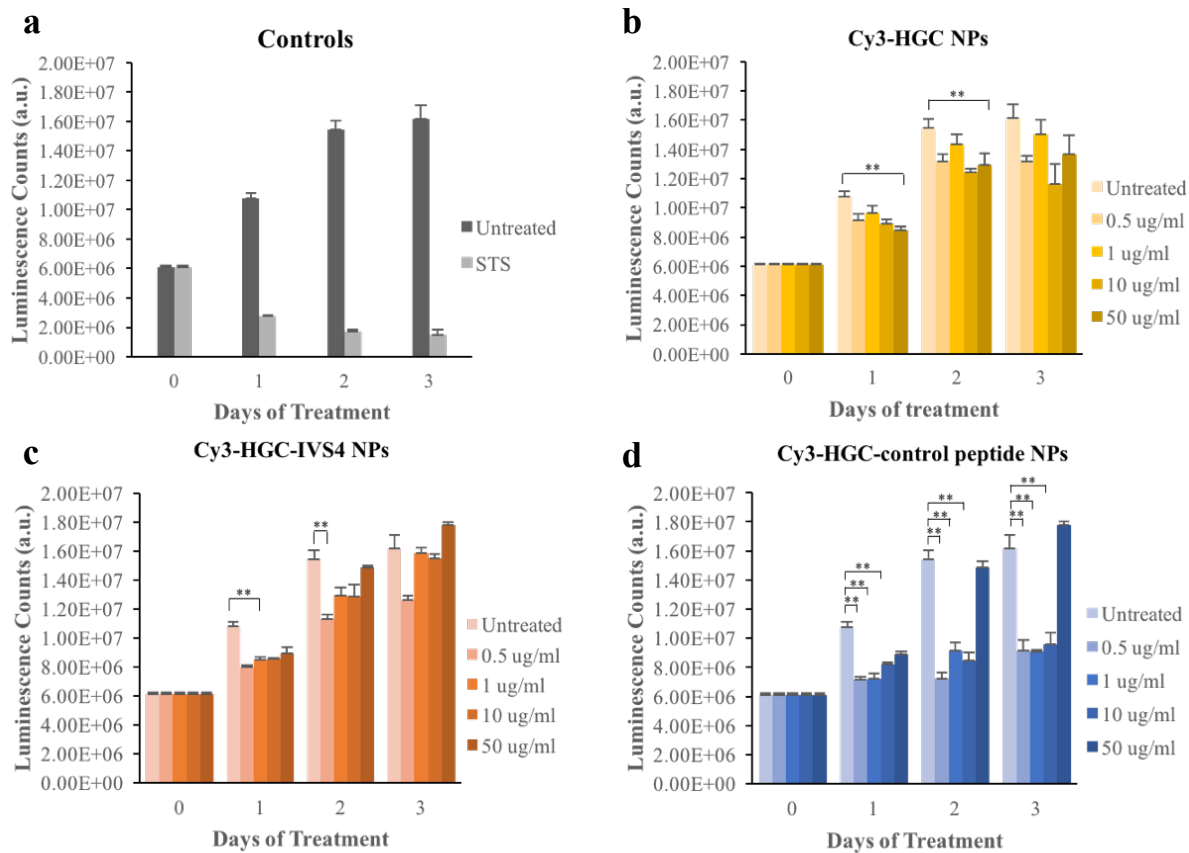


Figure 3.12 Cell viability of COS-MMP14 cells treated with different nanoparticles (NPs) continuously for up to 3 days. Error bars represent s.e. of 3 independent experiments. Student's *t*-tests were performed between the treated samples and the control, untreated sample, at each time point, considering a *p* value < 0.01 (**).

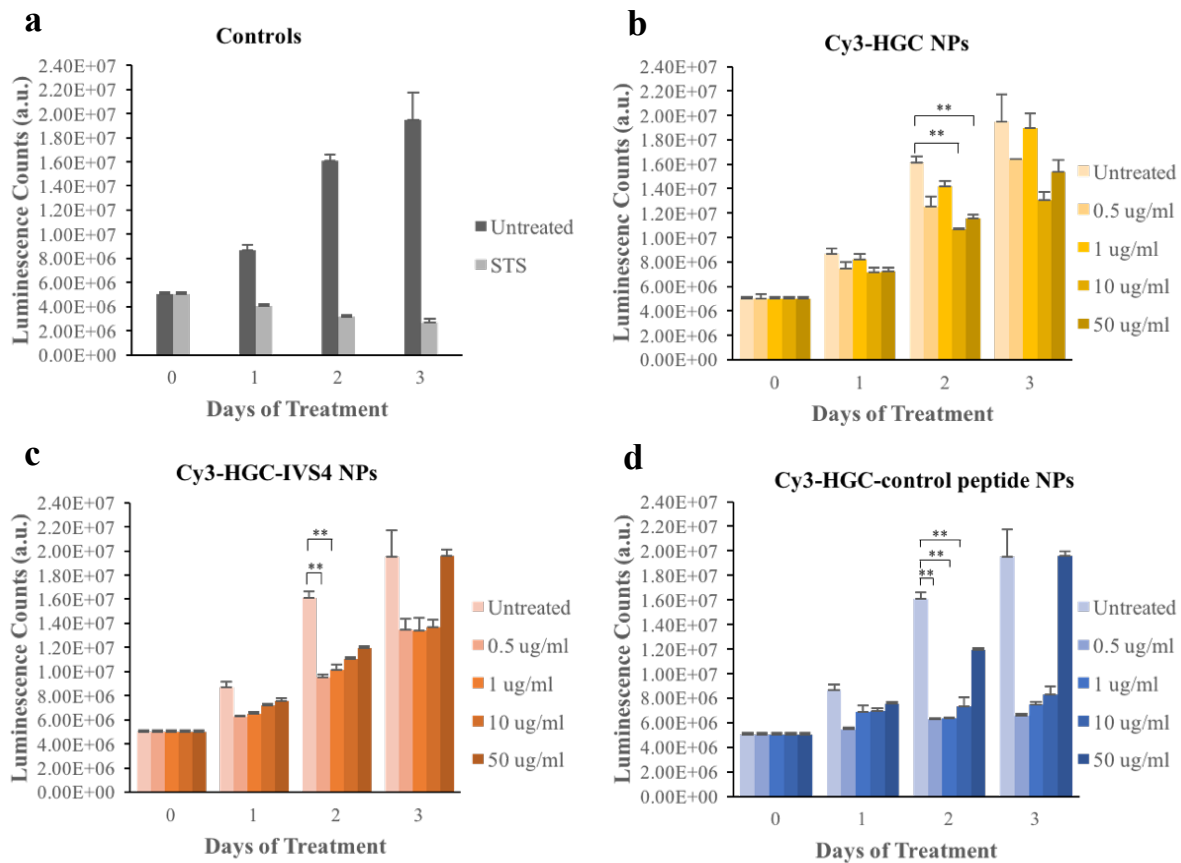


Figure 3.13 Cell viability of COS-pQ cells treated with different nanoparticles (NPs) continuously for up to 3 days. Error bars represent s.e. of 3 independent experiments. Student's *t*-tests were performed between the treated samples and the control, untreated sample, at each time point, considering a *p* value < 0.01 (**).

The cell viability assay performed on COS-pQ and COS-MMP14 cells (Figure 3.12 and 3.13) revealed that both cell lines presented significantly lower viability with respect to the control, when treated with Cy3-HGC NPs at the highest concentration, up to day 2 of culture (Figure 3.13 b). At day 3, high concentrations of Cy3-HGC NPs appear to slightly decrease the number of viable cells (Figure 3.13 b). However, the outcome is not significantly different from the control, suggesting a possible recovery of the system. Surprisingly, Cy3-HGC-control peptide NPs seemed to affect COS cell viability (Figure 3.13 d), when administrated at 0.5 $\mu\text{g/ml}$, 1 $\mu\text{g/ml}$, and 10 $\mu\text{g/ml}$, while a concentration of 50 $\mu\text{g/ml}$ does not show significant cytotoxicity in both cell lines. This unexpected result should be further confirmed with another set of experiment. Interestingly, the Cy3-HGC-IVS4 NPs did not significantly affect the overall cell viability after 3 days of treatment (Figure 3.13 c), indicating the potential use of this engineered bio-polymeric system as anti-cancer nano-vehicle. The peptide functionalized nanoparticles differ in the chemical structure from the plain HGC nanoparticles, due to the biotin-avidin linkage. During the first step of the synthesis process, 15 mmol of biotin are let react with 1 mmol of glycol chitosan. The HABA assay performed on the resulting material showed that on average 13.8 molecules of biotin are linked to 1 molecule of glycol chitosan. Due to its high molecular weight and its steric hindrance, the avidin moiety is introduced in the system at a molar ratio of 1:1, with respect of the glycol chitosan. This led to the presence of several free LC-biotin pendants, not involved in the interaction with the avidin, dangling from the main glycol chitosan chain, and possibly interacting with the cell membrane.

To elucidate if the presence of this free biotin on the nanoparticles could be responsible for an increased in their uptake and in their cytotoxicity, a separate cell viability assay was carried out. More specifically, Cy5.5-HGC-biotin NPs were synthesized, lacking of avidin moieties and biotinylated-peptides. The delivery to the four model cell lines was performed as above mentioned. Interestingly, while MDA-MB-231 cells and MCF-10A cells did not show susceptibility to the biotin-NP treatment (Figure 3.14 a, b), both COS cell lines showed a significant decrease in the number of metabolically active cells, over the range of NP concentration tested (Figure 3.14 c, d). Interestingly, when treated with propidium iodide (PI) to check for the presence of dead cells after Cy5.5-HGC-biotin NP administration, no significant PI red signal was observed in the COS cell samples (Figure 3.15). This result suggests that the presence of the Cy5.5-HGC-biotin NPs might interact with biotin-receptors at the cell surface, slowing down the metabolic activity of both COS-

pQ and COS-MMP14 cells, without being necessarily correlated to increased cell death.

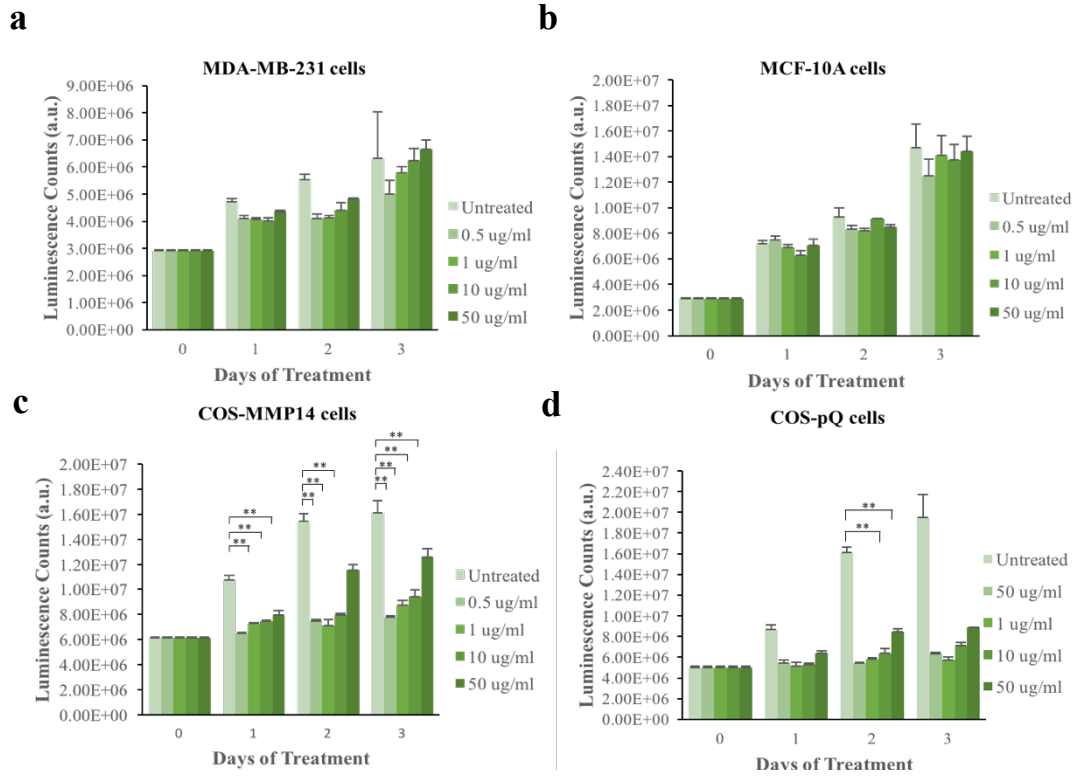


Figure 3.14 Cell viability of cells treated with HGC-Biotin nanoparticles (NPs) continuously for up to 3 days. Error bars represent s.e. of 3 independent experiments. Student's *t*-tests were performed between the treated samples and the control, untreated sample, at each time point, considering a *p* value < 0.01 (**).

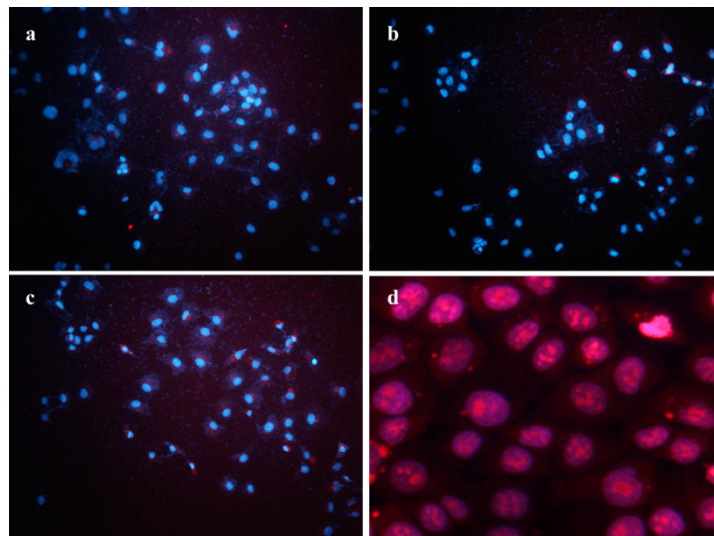


Figure 3.15 Propidium iodide staining (red channel) and DAPI staining (blue channel) of COS-pQ cells untreated (a) or treated with 10 $\mu\text{g/ml}$ (b) or 50 $\mu\text{g/ml}$ (c) of HGC-Biotin NPs. (d) represent the control sample treated with staurosporine.

Peptide-decorated nanocomplexes inhibited MMP14-associated migration activity

The transmembrane matrix metalloproteinase-14 plays a critical role in cancer invasion and in metastasis formation. The protease is predominantly localized at the leading edge of the cells, the invadopodia, and it activates pro-MMP2 and pro-MMP13, which further contribute to the invasion machinery.²⁰⁹ With the aim of assessing if the peptide-decorated micelles were able to inhibit the MMP-14 associated migration activity, a 2D dot migration assay was performed (Figure 3.5). Specifically, MDA-MB-231 cells and COS-MMP14 cells were pre-treated with different concentrations of either Cy3-HGC-IVS4 NPs or Cy3-HGC-control peptide NPs for 30 minutes and plated into 2D collagen dots in 96 well plates. The collagen dots were let incubating in NP containing-DMEM for additional 8 hours and then fixed with 8% formaldehyde and DAPI stained. Fluorescence microscope imaging of the samples allowed the identification of the migration front, presenting cells which have eroded the collagen matrix, have left the bulk of the dot and have started to migrate from it. Figure 3.16 shows representative images of those migration fronts. The MMP-14 expressing cell lines treated with IVS4-bearing micelles showed a limited cell migration (Figure 3.16 c, f), when compared to the untreated samples (Figure 3.16 a, d) and the control-peptide micelle administrated samples (Figure 3.16 b, e). This result correlates with previous findings, where HT-1080 human fibrosarcoma cells, expressing endogenous MMP-14 and undergoing trans-well chamber migration, were significantly arrested by the delivery of the free IVS4 peptide (100 μ M), when compared to the untreated sample or to the control peptide treated sample.²⁰⁹ The effect of the HGC-control peptide NPs and the HGC-IVS4 NPs on the cell migration was quantified in terms of fold changes with respect to the control sample migration (bar graphs in Figure 3.16 g, h). For the case of the MDA-MB-231 cells, 0.1 μ g/ml seems to constitute the most effective concentration of Cy3-HGC-IVS4 NPs for the inhibition of the MMP-14 associated migration activity (fold change of 0.39, compared to 1.1 for the case of the Cy3-HGC-control peptide NPs). For COS-MMP14 cells, a concentration of 1 μ g/ml seems to exert the best result (fold change of 0.13, compared to 0.49 for the case of the Cy3-HGC-control peptide NPs). A range of effective concentrations can be identified, where the lower limit is represented by non-effective, diluted micelles and the upper limit is given by the possible dimerization of the IVS4 peptides, with consequent loss of inhibitory activity. Lastly, the general more intense migration impairment effect of the IVS4-decorated micelles on the COS-MMP14 cells might be

due to the lower metabolic activity of this cell line, as previously noticed with the cell viability assay (Figure 3.13 and Figure 3.14 c, d).

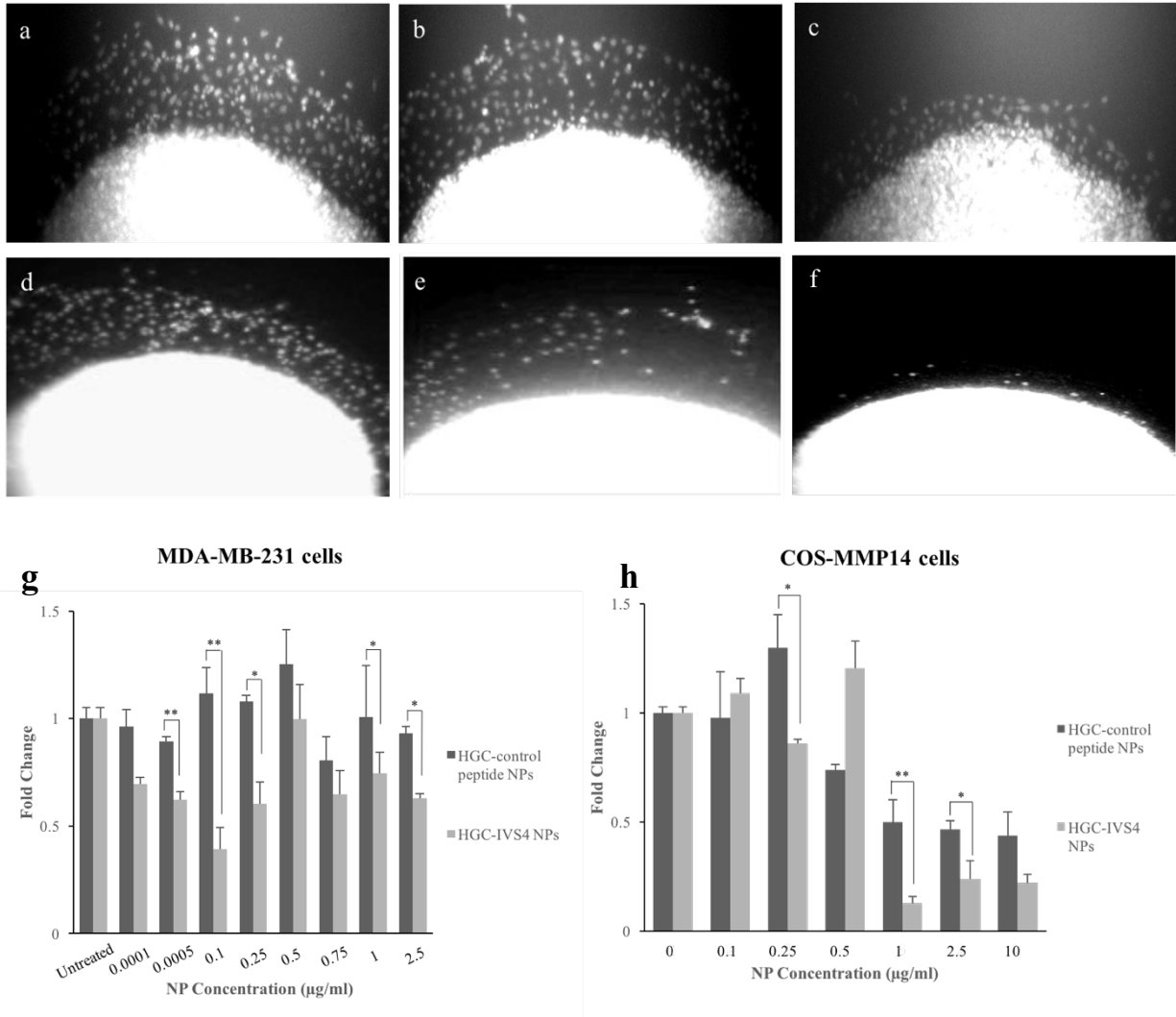


Figure 3.16 2D dot migration assay. Upper panel: fluorescence microscope representative images depicting MDA-MB-231 cells untreated (a) or treated with 0.1 µg/ml of HGC-control peptide (b) or with 0.1 µg/ml of HGC-IVS4 (c). COS-MMP14 cells were either untreated (d) or treated with 2.5 µg/ml of HGC-control peptide (e) or with 2.5 µg/ml of HGC-IVS4 (f). The fold changes in cell migration are reported for both cell lines (g, h). Student's *t*-tests between samples treated with control NPs and with IVS4-NPs were performed, considering *p* values < 0.05 (*) or *p* < 0.01 (**).

The study of the internalization mechanism allowed a direct observation of the coupling with the membrane bound MMP-14

With the aim of assessing the peptide-decorated nano-micelle interaction with the membrane bound matrix metalloproteinase-14, a careful internalization experiment has been conducted. In the past decade, several studies have tried to elucidate the mechanisms involved in the uptake of polymeric self-assembled micelles,^{125, 130, 190} the role of the different cytoskeleton proteins in supporting the formation of intracellular vesicles,²²³ as well as the various intracellular fate pathways that a nano-therapeutics can undergo once internalized.^{19, 29, 32, 183}

In the design of our experiment, MDA-MB-231 cells, endogenously expressing MMP-14, were chosen as model for a metastatic and invasive cancer. Figure 3.4 (Method section, *MMP-14 association mechanism study*) depicts the steps carried out in the internalization experiment. First, cells were plated on a glass bottom dish and let attached overnight. The following morning, cells were incubated at 4 °C for 15 minutes to let them pre-adapt to the cold environment. Afterwards, cells were treated with 2.5 µg/ml of Cy3-HGC-IVS4 NPs, bearing the critical inhibitory peptide of interest for the interaction with the ECM protease. The delivery was performed for 1 hour at 4 °C. In fact, the rationale behind the experiment was to slow down both the MMP-14 recycling and the cellular endocytosis processes, prior to and during the nanoparticle application. As a result, the adsorption of the nanoparticles onto the cell membrane, where MMP-14 is expressed, would be the only phenomenon occurring. In addition, the interaction between the IVS4 residue on the micelles and the PEX domain of the transmembrane MMP-14 would be maximized. Together with the fluorescent nanoparticles, a primary antibody for MMP-14 was added to the glass bottom dishes, prior to the incubation step. This would grant to subsequently stain the protease molecules which were present at the cell surface at time zero. After 1 hour of delivery, cells were washed with ice cold PBS and transferred in an incubator at 37 °C, to allow the internalization of the coupled MMP-14 - IVS4-micelles. At desired time points, ranging from 2 minutes to 30 minutes, samples were fixed, stained with a secondary antibody for MMP-14 and stained for nuclei. Figures 3.17, 3.18, and 3.19 present micrographs of the samples, acquired by structured illumination / super resolution microscopy by means of a Nikon N-SIM.

The high resolution of the structured illumination imaging technique allows the visualization of a single cell and its subcellular compartments. In Figure 3.17 the results of the time course

experiment are reported. Cy3-HGC-IVS4 nanoparticles are visible under the red channel: the limited amount of NPs is imputable to the delivery performed at 4 °C, a Temperature at which the endocytosis processes are slowed down. In fact, one of the main goals of this experiment was to observe the interaction of a single micellar assembly with the membrane bound protease; a high concentration of nanoparticles would mask the phenomenon and impede its observation. The MMP-14 staining is highlighted in the green channel. Interestingly, the staining pattern varies over time, being more punctate and localized at the cell surface at the earliest time points (from 0 to 5 minutes) and then becoming more diffuse and cytosolic as the time of incubation at 37 °C increases (from 10 to 30 minutes) and the MMP-14 turnover pathway is activated. Co-localization between the red signal of the IVS4-micelles and the green signal of the MMP-14 molecules was observed at every time point, as highlighted by white arrows in the merged images in Figure 3.17. The acquisition of *z*-stacks allows to span within the thickness of a single cell and to focus at different focal planes. As an example, Figure 3.18 reports images of a sample incubated for 30 minutes at 37 °C, obtained at various focal planes. The separate channels facilitate the resolution of the signal distribution within the cell. By passing from plane A to plane D the co-localization of the protease clusters with the nano-micellar clusters becomes predominant, as given by the appearance of a yellow signal (Figure 3.18, white circles). To further corroborate this observation, a 3D reconstructed volume was obtained (Figure 3.19). By means of a computer software (NIS-Elements Microscope Imaging Software) it was possible to rotate the reconstructed image and zoom onto the area of interest, to highlight the co-localized signals. The FITC-labelled MMP-14 transmembrane molecules appeared enveloped in the red-tagged peptide bearing nanomicelles (white arrows in Figure 3.19)

Taken together, these experimental observations from the first phase of the study helped to elucidate the presence of an interaction between the membrane bound MMP-14 and the peptide-decorated engineered micelles. This constitutes the first step for a targeted delivery of nano-therapeutics, where a functional moiety is used to specifically target a molecule of interest, overexpressed at the surface of cancer cells. This step would consequently dictate the route of entry of the nano-therapeutics in the cell, and their following internalization and degradation pathways.

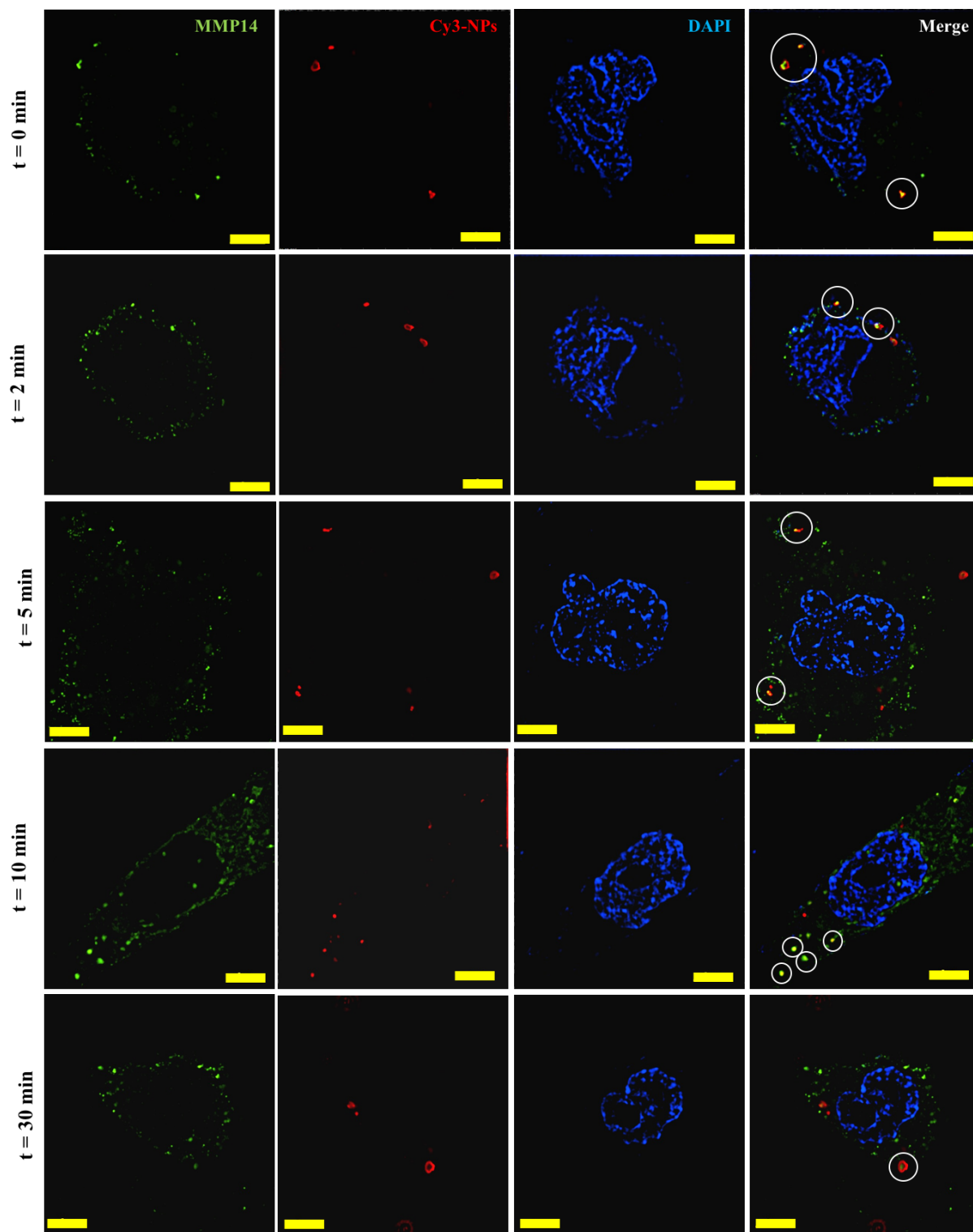


Figure 3.17 Super resolution microscope imaging of MDA-MB-231 cells stained with MMP-14 and treated with Cy3-HGC-IVS4 NPs for different time points (0, 2, 5, 10 and 30 minutes). The green channel shows the MMP14 membrane or intracellular distribution, the red channel depicts the peptide-decorate NPs, while the blue channel shows the cell nuclei. Scale bar 5 μ m.

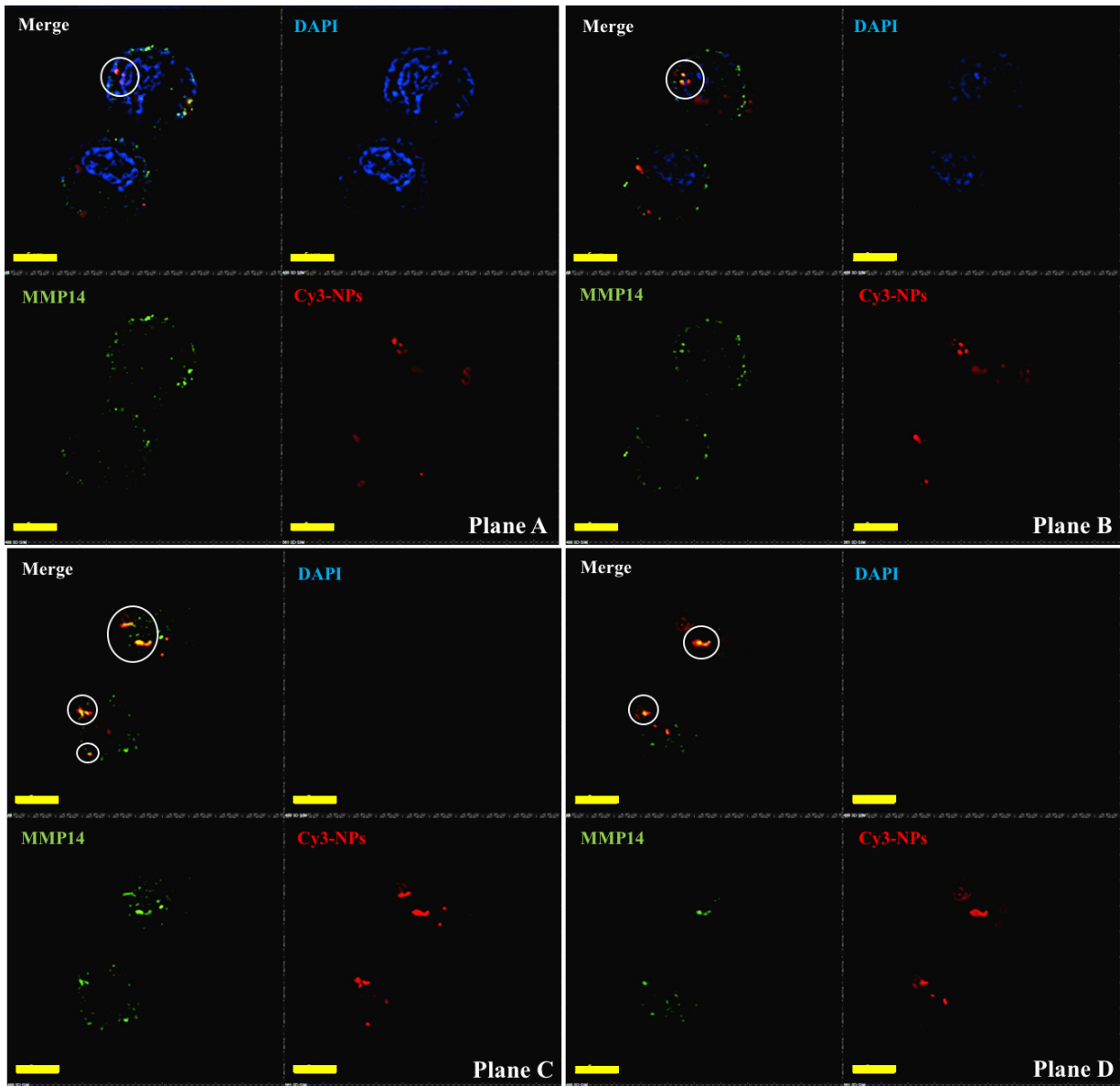


Figure 3.18 Super resolution microscope imaging of MDA-MB-231 cells stained for MMP-14 and treated with Cy3-HGC-IVS4 NPs 30 minutes. The various focus planes allow the visualization of the different intracellular distribution of the matrix metalloproteinase with respect of the peptide-decorate NPs. Separate channels showing MMP14 staining (green), nuclear staining (blue) and Cy3-HGC-IVS4 NPs (red) are presented. Scale bar 5 μ m.

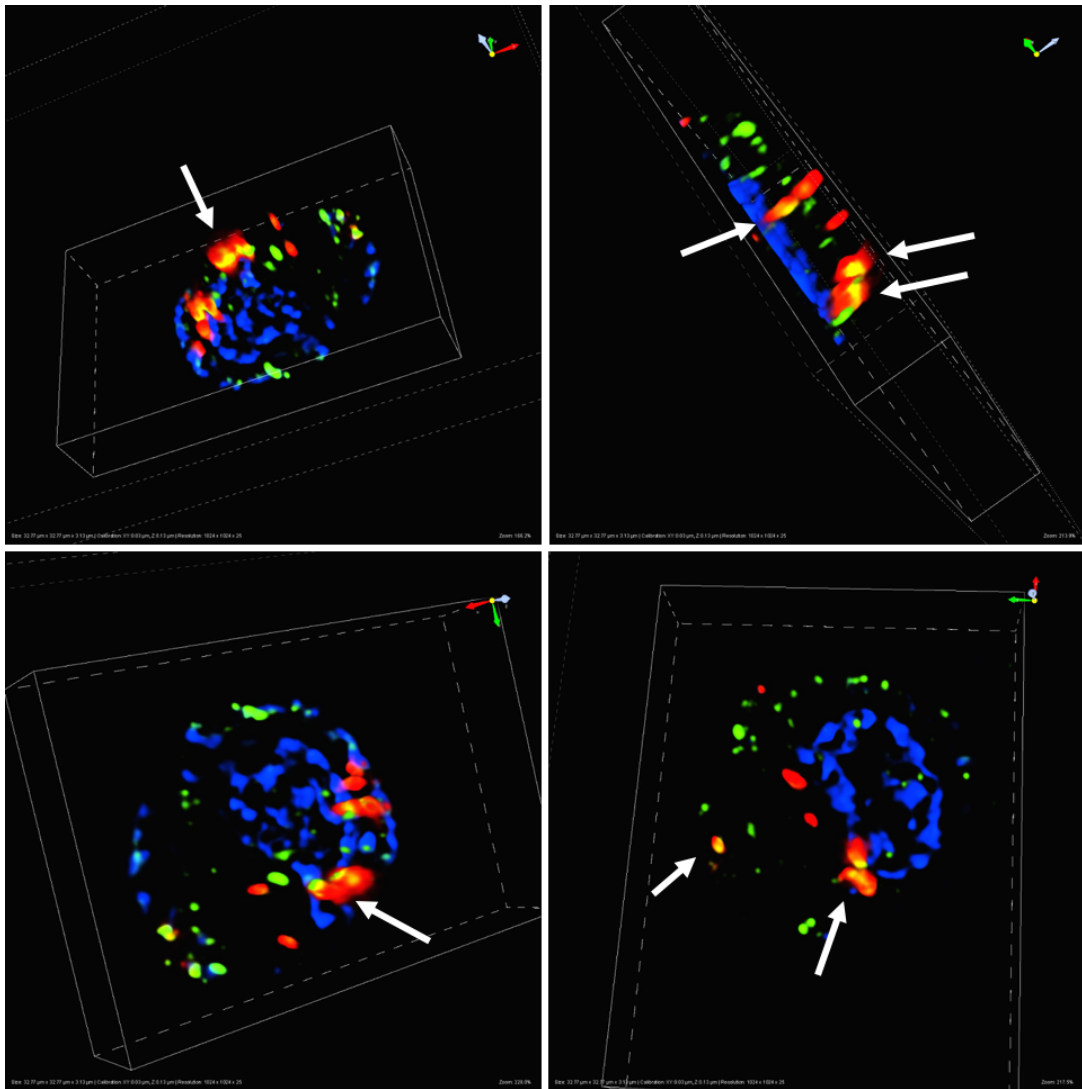


Figure 3.19 Super resolution microscope imaging of MDA-MB-231 cells stained for MMP-14 and treated with Cy3-HGC-IVS4 NPs for 30 minutes. The 3D volume reconstruction allows the visualization of the co-localized signals pertaining to the MMP14 (green) and the Cy3-HGC-IVS4 NPs (red).

The study of the uptake mechanism helped elucidating the nanomicelle intracellular fate

The second phase of the study focused on the understanding of the nano-therapeutics intracellular fate, once internalized. A series of experiments at subcellular levels were designed to gain insight onto the “nano-pharmacological” activity of the engineered micelles. Recently, the concept of “intracellular pharmacokinetics” started to gain attention in the scientific community:¹⁹⁰ the targeted delivery of anti-cancer compounds or active molecules should also consider the subsequent nanoparticle metabolism and the possible segregation in off-target cellular compartments. In fact, this can greatly influence the pharmacological efficacy of the nano-therapeutics and impact on the response of the patient. Under these considerations, a study carefully investigating the interaction between the nano-micelles and the subcellular domains at different time points was conducted.

The same experimental set up used for the MMP-14 – NPs coupling was implemented (as depicted in Figure 3.4), with the delivery of 2.5 µg/ml of Cy3-HGC-IVS4 NPs for 1 hour at 4 °C, to slow down the endocytic processes and allow the coupling of the micelles with the MMP-14 bound at the cell surface. The incubation at 37 °C was performed for 30 minutes, 1 hour, 3 hours, 8 hours, 18 hours, and 24 hours, to span over a longer range of time that would allow the formation of intracellular vesicles and the consequent activation of the degradation / recycling pathways. At the desired time points, samples were fixed and processed to stain for either early endosome (EEA1 marker), or lysosome (LAMP-1 marker) or Golgi apparatus (anti-giantin marker). Early endosomes are vesicles typically formed within 5 minutes of the intracellular uptake, and present a pH of 6.5; they are responsible for material sorting into a catabolic or a recycling pathway. Lysosomes, characterized by pH values ranging from of 5.5 to 4.5, contains several enzymes, critically involved in the degradation of the endocytosed material. The Golgi network, characterized by a slightly acidic pH of 6.5, it is mostly involved in the sorting of endogenous proteins destined for secretion or membrane expression.³³ For the early endosome staining, the super resolution microscopy data are shown in Figures 3.20 and 3.21, while LAMP-1 stained cells are reported in Figures 3.22, 3.23, and 3.24. Lastly, Golgi stained samples are presented in Figures 3.25, 3.26, 3.27, and 3.28.

The EEA1 staining revealed the formation of the early endosomes over time. At the earliest time points (up until 1 hour) the staining appeared as punctate green dots (Figure 3.20, white

arrows) and homogeneously distributed in the cytosol. At 8 and 18 hours of incubation, circular vesicles of different dimensions (ranging from 100 nm to 2 μ m) became visible in the green channel, to then shrink down again to a few hundred nanometers at 24 hours (Figure 3.20, yellow arrows). This evolution in the morphology might be due to two distinct phenomena, the endosomal vesicle membrane fusion or the vesicle bursting.^{19, 27} Association of the red signal pertaining to the peptide-decorated NPs with the endosome marker was first noticeable after 3 hours of incubation (Figure 3.20), but complete internalization was clearly observed only at 8 hours, when the Cy3-HGC-IVS4 NPs appeared surrounded and included into the green endosomal vesicles. Figure 3.21 reports the 3D reconstruction of the volume of an MDA-MB-231 cell treated for 8 hours with Cy3-HGC-IVS4 NPs. The volume was spanned with a *z*-stack acquisition: several NPs were visible within the circular structures (white arrows). No co-localization was observed at longer time points (18 and 24 hours, Figure 3.20), suggesting that a possible endosomal escape of the micelles might have occurred. In fact, the presence of the chitosan derivative as main component of the micelle matrix confers a polycationic nature to the system. Once taken up by intracellular vesicles, characterized by low pH (6.5-4.5) and the presence of enzymes, the material buffering capacity might be activated, to disrupt the vesicle membrane and ensure a successful cytosolic delivery.²⁷

The lysosomal membrane glycoprotein-1 staining (anti-LAMP-1) did not reveal the presence of completely formed vesicles (Figure 3.22, 3.23, and 2.24). As organelles more downstream in the degradation pathway, lysosomes are generally smaller than endosomes, with dimension ranging from 0.1 to 1.2 μ m. Surprisingly, the green channel signal appeared dotted and diffuse throughout the cytosol, not in association with the red nanoparticle signal at any of the time points considered (Figure 3.22). The acquisition of *z*-stacks of samples treated for 18 and 24 hours (Figures 3.23 and 3.24, respectively), confirmed the previous observations. This outcome led to several possible interpretations: (1) the dimensions of the Cy3-HGC-IVS4 NPs after 24 hours of intracellular trafficking do not favor the invagination into the lysosomal membranes,²²⁴ (2) the Cy3-HGC-IVS4 NPs are stable and a more sustained activation of the lysosomal system would be required. In addition, it is possible that the low Temperature experimental conditions, at which the NP delivery was performed in order to control the coupling with the membrane bound MMP-14 molecules, might have partially impaired or slowed down the lysosomal machinery. This result partially differ from the observations of Sitia and co-workers,¹⁹⁰ who recorded HEMA-PCL (poly-

hydroxy-ethyl methacrylate- poly-caprolactone) nanoparticle association with lysosomal membranes after 6 hours of delivery to MDA-MB-231 cells.

To elucidate if the internalized nano-micelles were following a different intracellular recycling pathway, staining of the Golgi complex was carried out, by means of anti-giantin antibody to highlight the perinuclear Golgi walls at different time points (Figure 3.25). Interestingly, the super resolution imaging revealed the association of the red NP signal with the Golgi apparatus. The separate channels and the merge image in Figures 3.26 show the proximity of a nano-micellar cluster with the Golgi wall at 18 hours of incubation, while Figure 3.27 allow the visualization of a more complete association at 24 hours (white circle). Moreover, the 3D reconstruction of a *z*-stack acquisition at 24 hours clearly demonstrates the presence of Cy3-HGC-IVS4 micelles in between the perinuclear Golgi coral reef-like structure, typically observed and resolved under confocal microscope or super-resolution microscope (Figure 3.28). A similar outcome was also observed by Sitia *et al.*¹⁹⁰ The slightly acidic pH of the Golgi apparatus (pH of 6.5) might be sufficient to trigger a micellar structure degradation.

Taken together, these observations suggest that the internalized Cy3-HGC-IVS4 NPs determine the activation of the cellular metabolic machinery. A possible interpretation of the uptake route and intracellular fate of the peptide-decorated micelles could be summarized as follows. First, the coupling with the transmembrane MMP-14 promotes the cell recognition and the micelle internalization. After 3 – 8 hours of incubation the nanoparticles appear to be segregated into endosomes. Afterwards, the *so-called* endosomal escape process, in which buffering of intra-vesicle acidity and vesicle membrane disruption are involved, might be hypothesized. In fact, no further co-localization of the NPs with endosomes was noticeable at longer time points (18 and 24 hours, Figure 3.20), probably due to the physicochemical properties of the micelle matrix (e.g. pH-responsiveness). In addition, no association with lysosomal vesicles was evident at any time points (Figures 3.22, 3.23, and 3.24), suggesting that these organelles are not involved in the degradation pathway of the IVS4-micelles. Lastly, the presence of the NPs in between the Golgi complex's wall was observed after 18 – 24 hours of delivery, indicating that a transport from the cell periphery to the perinuclear area has taken place. Since MMP-14 molecules have shown to be recycled via Golgi apparatus (unpublished results, Prof. Cao's group) our observation might indicate that a coupling with the IVS4-micelles might still persist after 24 hours. To clarify this hypothesis and to observe a further sorting role of the Golgi complex, the

intracellular fate of the nanoparticles at longer time points should be investigated. In addition, as MMP-14 was shown to be preferentially internalized via clathrin-mediated endocytosis,²⁰⁵ a colocalization study between clathrin-coated vesicles and the IVS4-micelle might help to further elucidate the NP uptake mechanisms in triple negative breast cancer cells.

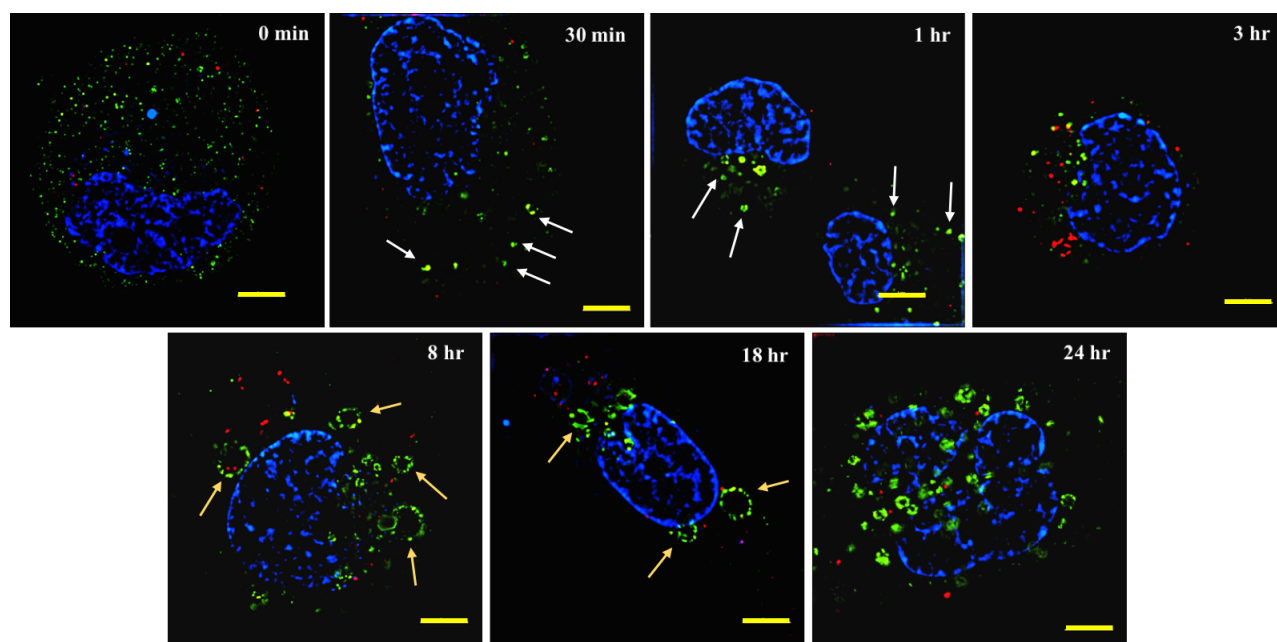


Figure 3.20 Super resolution microscope imaging of MDA-MB-231 cells stained for early endosome (EEA1 antibody, green channel) and treated with Cy3-HGC-IVS4 NPs (red channel) different time points. The blue channel depicts the cell nuclei. Scale bar 5 μm .

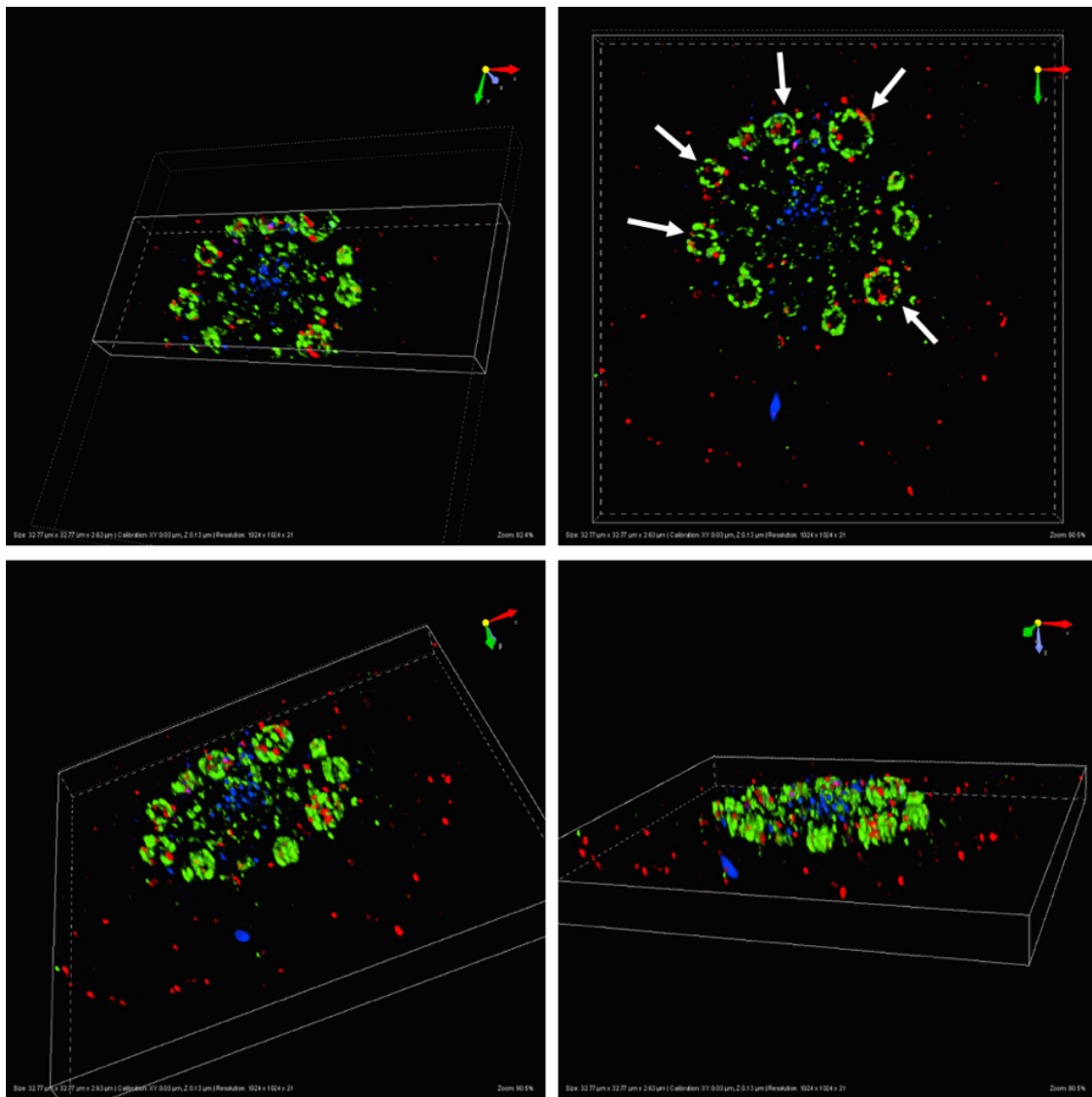


Figure 3.21 Super resolution microscope imaging of MDA-MB-231 cells stained for early endosome (EEA1 antibody, green channel) and treated with Cy3-HGC-IVS4 NPs (red channel) for 8 hours. The blue channel depicts the cell nuclei. The 3D volume reconstruction allows the visualization of the Cy3-HGC-IVS4 NPs enveloped in the endosomal vesicles (white arrows).

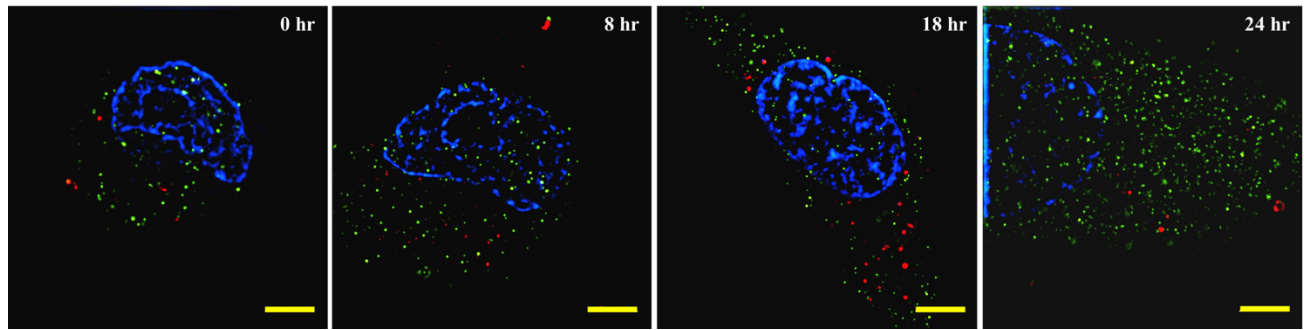


Figure 3.22 Super resolution microscope imaging of MDA-MB-231 cells stained for lysosomes (LAMP1, green channel) treated with Cy3-HGC-IVS4 NPs for different time points. The blue channel depicts the cell nuclei. Scale bar 5 μm .

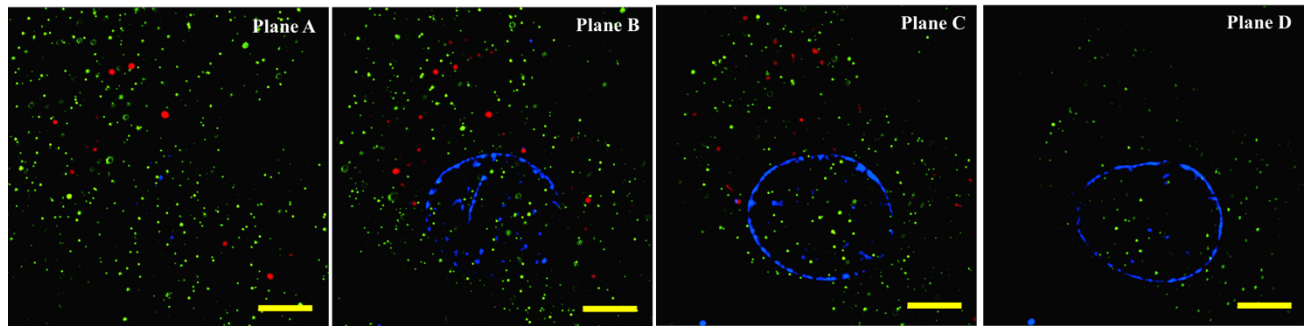


Figure 3.23 Super resolution microscope imaging of MDA-MB-231 cells stained for lysosomes (LAMP1, green channel) and treated with Cy3-HGC-IVS4 NPs 18 hours. The images acquired at different planes of focus allows the visualization of the vesicle intracellular distribution, with respect of the up-taken nanoparticles. The blue channel depicts the cell nuclei. Scale bar 5 μm .

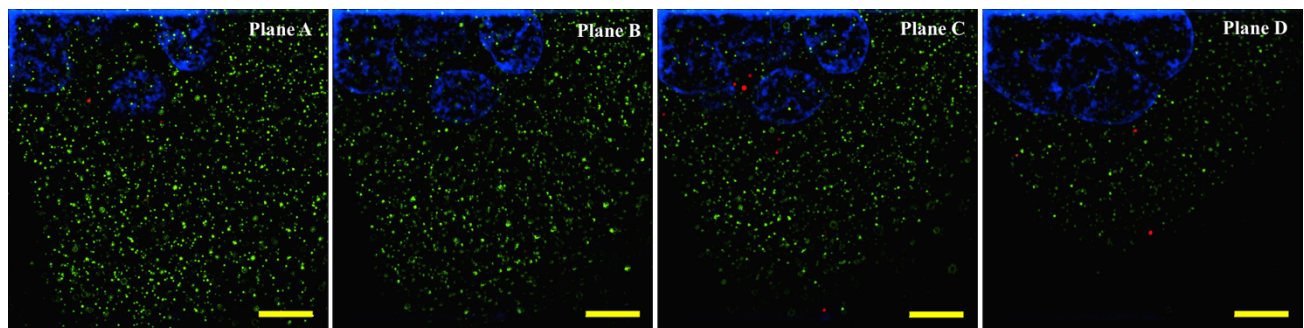


Figure 3.24 Super resolution microscope imaging of MDA-MB-231 cells stained for lysosomes (LAMP1, green channel) and treated with Cy3-HGC-IVS4 NPs 24 hours. The images acquired at different planes of focus allows the visualization of the vesicle intracellular distribution, with respect of the up-taken nanoparticles. The blue channel depicts the cell nuclei. Scale bar 5 μm .

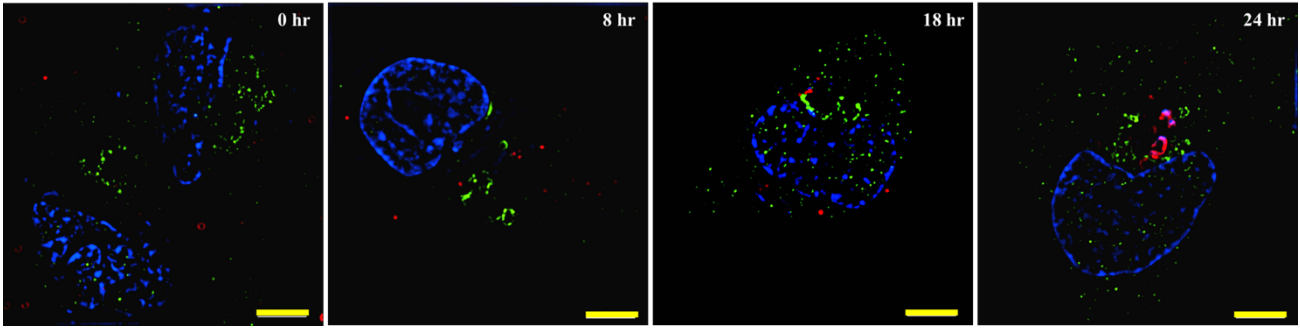


Figure 3.25 Super resolution microscope imaging of MDA-MB-231 cells stained for a Golgi membrane protein (anti-giantin, green channel) treated with Cy3-HGC-IVS4 NPs for different time points. The blue channel depicts the cell nuclei. Scale bar 5 μ m.

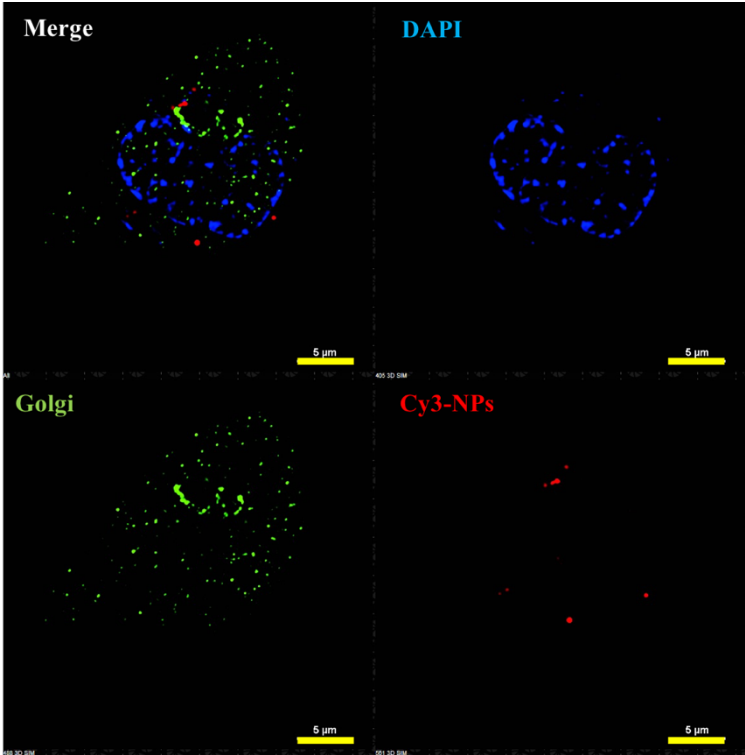


Figure 3.26 Super resolution microscope image of MDA-MB-231 cell stained for a Golgi membrane protein (anti-giantin, green channel) treated with Cy3-HGC-IVS4 NPs for 18 hours (red channel). The blue channel depicts the cell nuclei. Scale bar 5 μ m.

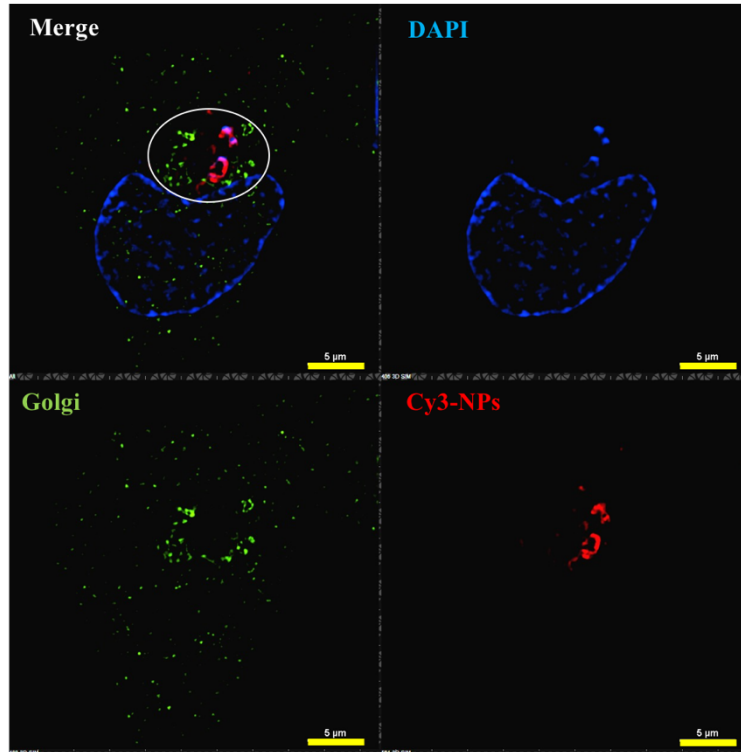


Figure 3.27 Super resolution microscope image of MDA-MB0231 cell stained for a Golgi membrane protein (anti-giantin, green channel) treated with Cy3-HGC-IVS4 NPs for 24 hours (red channel). The blue channel depicts the cell nuclei. Scale bar 5 μm .

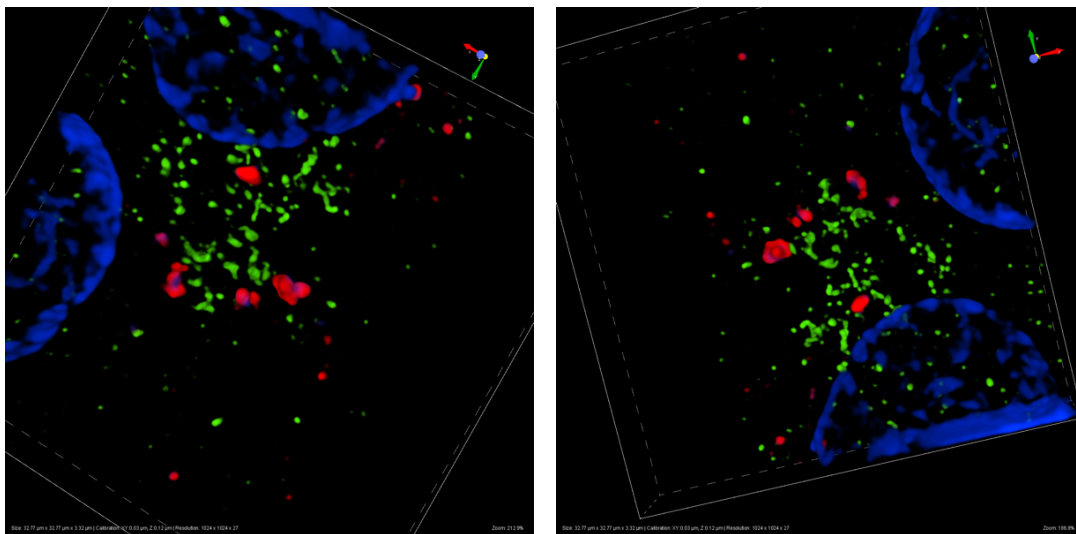


Figure 3.28 Super resolution microscope imaging of MDA-MB-231 cells stained for a Golgi membrane protein (anti-giantin, green channel) and treated with Cy3-HGC-IVS4 NPs (red channel) for 24 hours. The blue channel depicts the cell nuclei. The 3D volume reconstruction allows the visualization of the Cy3-HGC-IVS4 NPs in the close proximity of the Golgi walls.

Drug-loaded, peptide-decorated nanocomplexes showed cytotoxicity, when delivered to an vitro culture model

In this last phase of the study, peptide-decorated micelles have been further functionalized and loaded with a potent microtubule destabilizer, ansamitocin-P3 (AP3), with the aim of assessing the cytotoxic potential of the engineered construct. This maytansinoid derivative has been shown to be highly cytotoxic against multiple myeloma, B-16 melanoma and sarcoma,^{214, 217, 218} with a mechanism of action which affects the polymerization of mitotic and interphase microtubules and sparks the activation of the p53 cascade.

The drug was physically encapsulated by mixing the 30 mg Cy3-HGC-IVS4 with 1 mg AP3 in 9.5 ml of DMSO and by dialyzing for 2 days the mixture. The encapsulation efficiency, calculated as ratio between the mass of AP3 in the micelle and the mass of AP3 in the initial feedstock, was evaluated to be 11%, considering the absorbance of the compound at 250 nm. Our self-assembled system is now consisting of a polymeric matrix (nano-vehicle), tagged with an inhibitory peptide (functional moiety) via biotin-avidin interaction (high molecular weight spacers), labelled with a fluorescent dye via covalent bond (imaging agent), and physically complexed with an anti-cancer compound (therapeutic agent). The rather low value of the encapsulation efficiency might be due to the already densely packed micellar structure, which might impede the accommodation of several molecules of AP3 in the core. On the other hand, the elevated cytotoxic potential of ansamitocin-P3 (in the range of pM)²¹⁹ would allow the use of very diluted drug loaded-micellar suspension. In Figure 3.29 and 3.30, the cell viability study performed on MDA-MB-231 cells and MCF-10A cells are reported, respectively. Bar graphs are grouped per day of culture (up to day 9), to facilitate the comparison between the different treatments: untreated control, free AP3, AP3 encapsulated into Cy3-HGC-IVS4 NPs and empty Cy3-HGC-IVS4 NPs. The homogeneous x axis allows the visualization of the cell growth from day 1 to day 9 of culture treatment. In the y axis the equivalent drug concentrations (either free or encapsulated) in nM are reported. For the calculation of the corresponding amount of Cy3-HGC-IVS4 NPs needed, the encapsulation efficiency and the drug loading content have been taken into account. The cell viability assay was performed as previously described.

Overall, the continuous delivery up to 9 days of the empty, plain nano-vehicles did not impair the viability in both cell lines, as visible from the green bars in Figures 3.29 and 3.30. This result

further corroborates our hypothesis of the peptide-decorated chitosan micelles as safe delivery agents. For the case of the MDA-MB-231 cells, the administration of the free ansamitocin P-3 (blue bars) seemed to affect the cell viability starting from day 1, at almost all the concentrations tested (ranging from 0.1 nM to 1 nM). On the other hand, when administrated in combination with the bio-polymeric micelles, AP-3 appears to have a dose-dependent effect (red bars Figures 2.29 and 3.30). The exponential decrease in cell viability is easily visible at day 6 and day 9 and the treatment with 0.75 nM and 1 nM of AP3-loaded micelles showed a better response than the free drug alone (Figure 3.29 c, d).

The cell viability study on the MCF-10A revealed the cytotoxic potential of the free drug, at any concentration tested and over the entire period of administration. On the other hand, the delivery of AP3-encapsulated drug showed a dose-dependent effect on the epithelial cells. However, this effect is mostly visible after 9 days of treatment (Figure 3.30 d), and it is less significant than the case of the MDA-MB-231 cells. In fact, after treatment with 1 nM of AP3-loaded micelles for 9 days, the cell viability of MCF-10A cells is reduced to a 15.8%, while the value reaches 5.4% for the case of the triple breast cancer cells. In addition, encapsulated ansamitocin did not show higher cell viability impairment, when compared to the free drug. The observed cytotoxicity might be due to the fact that NPs are kept in continuous contact with the monolayer of cells for up to 9 days, and stagnant media, containing the potent microtubule depolymerizing agent, might have contributed to the cell death.

Our AP3-loaded Cy3-HGC-IVS4 nano-vehicles have shown a cytotoxic potential comparable or higher than the free AP-3, especially when delivered for 6 days to a highly metastatic breast cancer cell line, at low concentrations such as 0.5 nM, 0.75 nM, and 1 nM. In the future, release kinetics data should be paired with the cell viability data, to confirm the presence of a sustained release of the active compound from the bio-polymer micellar system.

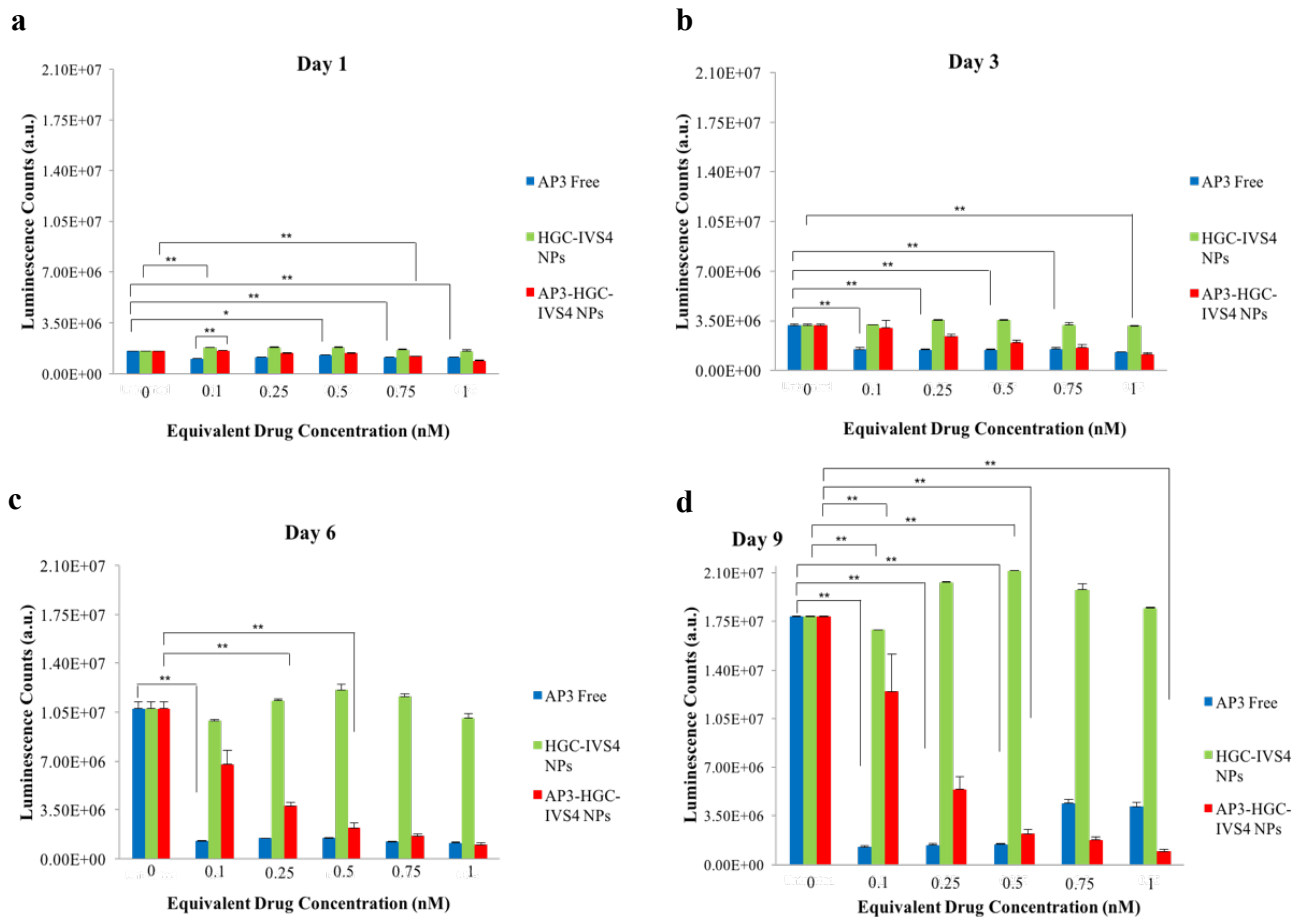


Figure 3.29 Cell viability of MDA-MB-231 cells treated with free Ansamitocin P-3 and with empty and drug-loaded NPs continuously for up to 9 days. Error bars represent s.e. of 3 independent experiments. Student's *t*-tests were performed between the treated samples and the control, untreated sample, at each time point, considering *p* values < 0.05 (*) or < 0.01 (**).

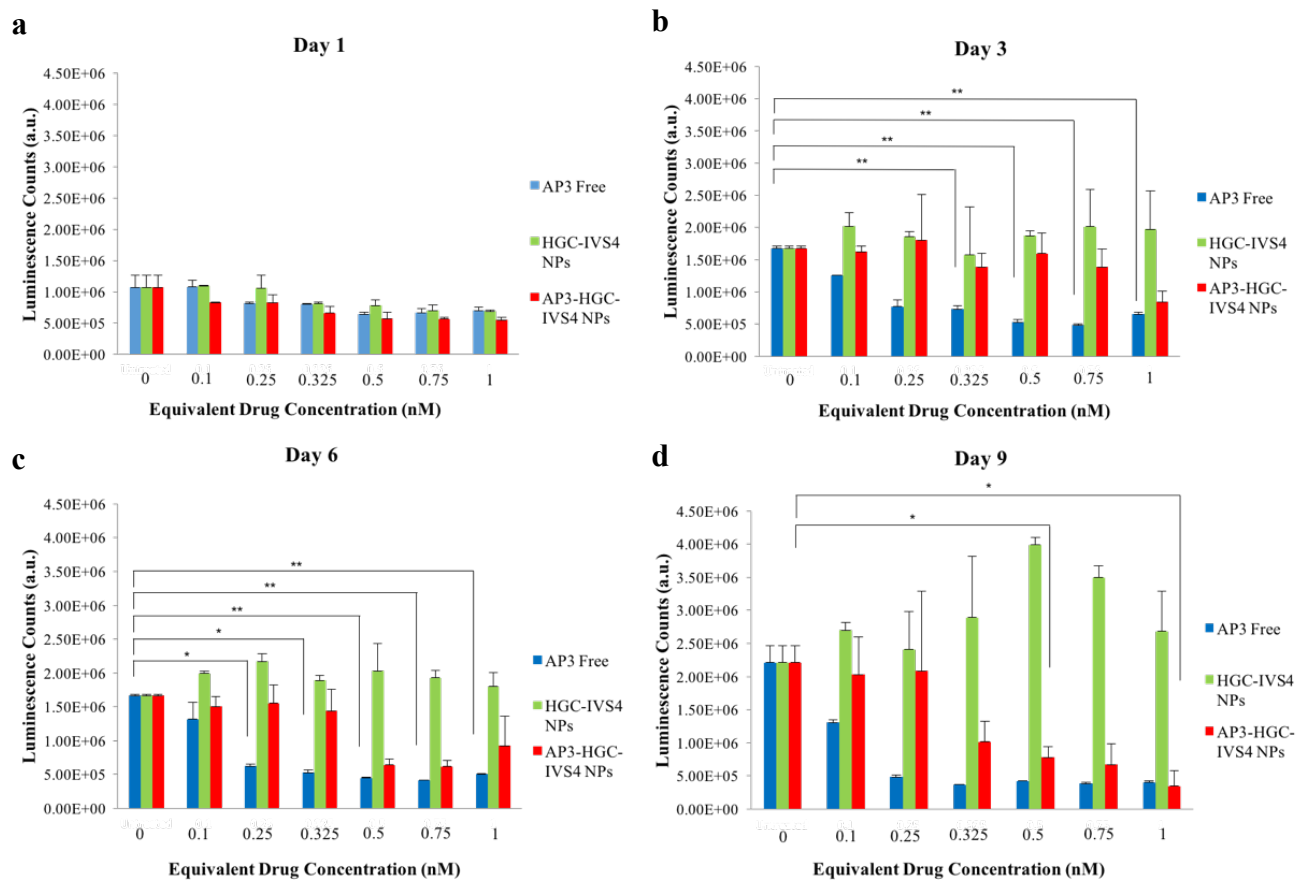


Figure 3.30 Cell viability of MCF-10A cells treated with free Ansamitocin P-3 and with empty and drug-loaded NPs continuously for up to 9 days. Error bars represent s.e. of 3 independent experiments. Student's *t*-tests were performed between the treated samples and the control, untreated sample, at each time point, considering *p* values < 0.05 (*) or < 0.01 (**).

3.4 Conclusions and Future Perspectives

Cell migration and invasion involve the travelling of cells over an ECM substratum, achieved by extension of the leading edges, cell adhesion via binding of integrins to the corresponding ligands, detachment of the trail protrusions, and consequent movement. The surrounding ECM environment is subjected to degradation by the proteases preferentially located at the leading edges of the invasive cells, the *so-called* invadopodia. Membrane bound matrix metalloproteinase-14 (MMP-14) has shown to play a critical role in the activation of the migratory cascade, by activation of pro-MMP2 at the surface of tumor cells.^{197, 205, 210} Recently, Zarrabi *et al.*^{209, 210} unraveled the unique role of an inhibitory peptide (IVS4), mimicking the binding motif of the hemopexin domain (PEX) of the MMP-14 protease.

In this thesis study, IVS4-decorated HGC micelles have been synthesized, characterized and delivered to four model cell lines, to assess their internalization ability and their potential as cytotoxic targeting delivery agents, when compared to non-functionalized nano-carriers. The IVS4-HGC micelles presented preferential uptake into MMP-14 expressing cells, such as African green monkey epithelial COS-MM14 and human triple-negative breast cancer MDA-MB-231 cells. The super resolution microscopy analysis allowed the visualization of the coupling between the peptide-tagged fluorescence micelles and the MMP-14 expressed at the cell surface, validating the use of our engineered construct for targeting delivery. The intracellular fate experiment showed internalization of the Cy3-HGC-IVS4 NPs within early endosome after 8 hours of delivery, and association with the Golgi complex at longer time points (18 and 24 hours). To assess for a further sorting or degradation role of the Golgi apparatus, longer time points should be investigated. Moreover, the initial complexation with the membrane protease might lead to the internalization via clathrin-mediated endocytosis; thus, the staining for this intracellular vesicle protein might help to gain more insight into the IVS4-NPs uptake mechanism in triple negative breast cancer cells.

The successful encapsulation of a microtubule depolymerizing agent, the ansamitocin P3, into our nano-vehicles, have revealed micelle cytotoxic potential comparable to or higher than the free drug, especially after 6 days of delivery to MDA-MB-231 cells, at low concentrations such as 0.5 nM, 0.75 nM, and 1 nM. Release kinetics data should be collected, to confirm the presence of a sustained release of the active compound from the bio-polymer micellar system.

A cytotoxicity study on Sk-3rd cells involving the free drug, AP3-loaded micelles and empty peptide-decorated vehicles, is currently being conducted. These human breast cancer tumor initiating cells (TICs) grow in mammosphere-like assemblies and can undergo conversion from stationary cells to invasive cells, especially when cultured under hypoxic conditions. In their work, Li *et al.*²²⁵ reported cell surface redistribution of matrix metalloproteinase-14 from the cytoplasmic storage pools under low O₂ content, which coincided with TICs enhanced invasion ability. The delivery of IVS4-NPs to Sk-3rd cells under either hypoxic conditions or normoxia might further elucidate the critical role of the MMP-14 – IVS4 coupling at the cell surface, validating the active targeting capability of our construct.

With the purpose of assessing the cytotoxic potential of the AP3-loaded Cy3-HGC-IVS4 nano-micelles *in vivo*, an experiment involving chicken embryos is currently under development. A chorioallantoic membrane (CAM) angiogenesis assay constitutes an effective biological tool to observe possible cancer cell invasion across the membrane (mostly collagen-based) and formation of blood vessels associated with tumor growth.²⁰⁹ This experiment would provide critical information on the efficacy of our bio-polymer micellar system for the targeting of breast cancer invasiveness *in vivo*, and perhaps open the route for the implementation of a new strategy to prevent cancer dissemination.

Chapter 4:

Hydrophobically modified glycol-chitosan micelles as drug delivery agents: application to a three-dimensional bone cancer model

4.1 Introduction

The design and development of drugs and drug delivery systems have to follow a sequence of screening steps, often time consuming, in order to carefully investigate the suitability of a new compound for a certain therapeutic strategy, and to ultimately assess the usefulness for human patients.²²⁶ Usually, preclinical testing of a new nanomedicine first involves *in vitro* analysis with model cell lines, to evaluate potential toxicity and intracellular mechanisms; in a second step, animal models are employed, to investigate pharmacological properties, such as metabolism, absorption, distribution and excretion.²²⁶ Afterwards, the nanomedicine has to pass through various stages of clinical trials, to determine its effects on humans and its ultimate safety. Although promising during preclinical studies, several drugs fail in clinical development (with a Phase I to bedside probability of 8%²²⁷), suggesting that the available 2D *in vitro* approaches and animal models might constitute poor predictors of a nanomedicine efficacy and toxicity in humans.²²⁸ Due to the relevant high cost of the whole drug development process (about 1 billion US dollars for the approval of a new anticancer compound),²²⁶ it is crucial to sieve out potentially poorly functioning nanomedicines early in the evaluation stage. Therefore, efficient, cost-effective and high-throughput preclinical screening methods, able to accurately mimic the physio-pathological features of live tissues and tumor microenvironment, should be established to obtain a more informed prediction of a nanomedicine candidate performance. To bridge the gap between the oversimplified monolayer cultures, and the animal models, often complex and expensive, three-dimensional multicellular platforms have recently gained the attention of the scientific and clinical communities, with the aim of easing the translation from basic research to industrial applications.

Conventional 2D culture systems, developed by Harrison in early 1900s²²⁶ are based on the monolayer culture of cell lines onto substrates, where cells can adhere and acquire a flat and extended morphology. However, this culture configuration lacks of cell-to-cell and cell-to-matrix interactions, which can greatly affect the overall cancer cell response, in terms of receptor

expressions, migration and invasion ability and protein secretion. Moreover, the flat architecture does not take into account the presence of oxygen and nutrient gradients, factors involved in the modulation of the live-dead cell population. On the other hand, 3D cellular constructs constitute a versatile platform for the simulation of the physio-pathological features of the native tumor tissue and the surrounding microenvironment, offering a great biological tool to gain a deeper understanding of the molecular effectors involved in cancer progression and to design and evaluate the efficacy of anti-cancer nano therapeutics.^{229, 230}

Three-dimensional cancer cell spheroids are self-assembled spherical cell clusters, with diameters of about 300-700 μm , depending on the cell line and the maturation time. Due to a gradient of oxygen and nutrients from the surface to the core of the cellular aggregate, a stratified, onion-like structure can be identified, with an outer layer of active, proliferating cells, an intermediate region of quiescent, inactive cells, and an inner core of cells undergoing necrosis or apoptosis. In the past decade, several studies have employed spheroids to evaluate drug sensitivity and acquired resistance (as a result of a physical barrier constituted by the cellular layers),²²⁸ as well as nanomedicine penetration ability.²³¹⁻²³⁷ Most of the cells pertaining to healthy tissues in the human body are located within a few micrometers from a blood vessel or capillary. This homeostatic regulation breaks down when a solid tumor is formed, leading to poor vascularization, irregular blood flow and hypoxia, features that ultimately limit the distribution and the efficiency of an anti-cancer nanomedicine.^{228, 232} Moreover, depending on the 3D cellular network and the ECM composition, variation in the cell signaling might lead to the inhibition or the activation of different molecular pathways, with significantly different outcomes than the conventional 2D approaches.^{228, 230, 238} Some of the main characteristics and advantages of 3D cultures are: (1) replication of the three-dimensional arrangement and ECM deposition; (2) cell-to-cell interactions comparable to those *in vivo* (e.g. tight junctions); (3) physiological barrier to mass transport of drugs; (4) possibility of co-culture formation (e.g. with stromal cells, cancer stem cells, endothelial cells) to address the effect of cell population heterogeneity on the nanomedicine efficiency; (5) presence of an hypoxic core.²²⁹ In addition, given the numerous variables present in the multicellular spheroidal aggregates, along with experimental studies, theoretical mathematical models can provide more insights into nanomedicine transport phenomena, kinetics of cellular mechanisms, dynamics of nanoparticle penetration, and rate of cellular proliferation in the different layers of the spheroids. Ultimately, those models can furnish explanations for the limited

or the successful efficacy of nano therapeutics.^{229, 239}

Several challenges are involved in the establishment of 3D spheroids, mostly associated to the delicate and rather long culture procedures.^{240, 241} In fact, in order to maximize the potential ability of these cellular systems to replicate the *in vivo* conditions of the tumor microenvironment, spheroids should present reproducible and uniform sizes, and should be constituted by multiple cell types. Moreover, characterization protocols, nano therapeutic efficacy screening assays and imaging analysis should be carefully tailored from the conventional 2D platforms and adapted to the spheroid aggregates, in order to obtain standardized procedures for a correct comparison of the results within different studies.^{227, 229, 242, 243}

Different culture methods have been implemented to obtain reproducible 3D cancer spheroids: forced-floating system,²⁴¹ hanging drop method,¹⁹² agitation-based approaches, cultures supported by matrices and scaffold,²⁴⁴ and microfluidic²⁴⁵ and organ-on-a-chip cell culture platforms.^{226-229, 240, 246} The forced-floating technique (also known as liquid overlay) is based on the modification of the culture plate surface with a hydrophobic coating, such as agarose²⁴¹ or poly-hydroxyethyl methacrylate,¹⁹⁴ to prevent cell surface attachment and favor cell-to-cell interaction in suspension.^{240, 241} This relative simple and inexpensive method is suitable for high throughput screening and the resulting spheroids are easy to assess, transfer and process. On the other hand, careful coating of the plate and a subsequent dry step are required in order to obtain spheroids with consistent sizes and shapes. In the case of the hanging drop methods, a small aliquot of cell suspension (about 20-60 μ l) is pipetted into a micro well tray. After cell seeding, the tray is inverted, leading to the formation of hanging drops kept in place by surface tension. Cells aggregate into homogeneous spheroids at the liquid-air interface, and moisture needs to be carefully maintained. The media exchange and the spheroid treatment might constitute a challenge, due to the small volume of liquids and the risk of perturbing the cellular assembly. As an attempt to overcome this limitation, Guo *et al.*¹⁹² designed magnetically labeled 3D spheroid culture, to facilitate spheroid manipulation in hanging drop plates. Further improvements were obtained with the development of specialized plates, such as GravityPLUSTM plates (from InSphero, Switzerland)²³⁵ and Perfecta3D hanging drop plates (from 3D Biomatrix, USA). Agitation-based approaches involve spinner flask bioreactors and rotational culture systems (e.g. NASA Rotary Cell Culture System). The cell suspension is placed in a container and kept in constant motion to allow cellular aggregation in the media. A rather large scale production is achievable, and the

spheroids can continuously be in contact with nutrients in transport, allowing an easy media exchange. On the other hand, these techniques do not allow control over the cell number and the resulting spheroid size, and the shear forces created by the suspension in motion might affect the cell physiology and viability. Polymeric matrices and hydrogel scaffolds have been extensively used to provide a three-dimensional support for the cellular growth and assist the formation of the intricate molecular network of the *in vivo* tumor microenvironment. Natural derived matrices, such as Matrigel™, hyaluronic acid, type I collagen, can aid a 3D aggregation of cells, allowing the simulation of the tumor surrounding mechanical features, porosity and nutrient exchange. However, variations in their batch-to-batch composition might lead to the formation of assemblies with low reproducible characteristics.^{235, 244} Synthetic scaffolds, based on the use of biodegradable polymer such as poly-caprolactone, poly-lactic acid and poly-glycolic acid, present more controllable properties and, when functionalized with nutrients and growth factors, can provide a biomimetic cell growth niche.^{236, 244} However, retrieving the formed 3D structure from the matrices poses additional challenges to the implementation of these techniques. Lastly, microfluidic devices have been employed to guide 3D network formation by means of thin channels or chambers.^{245, 246} The main advantage of this approach is the possibility of simulate the physiological cues of the tumor microenvironment, by spatially and temporally control biological factors, nutrients and oxygen flow. In addition, those culture systems might provide insight into collective cell migration in response of a chemical stimulus or to assess the effect of drug treatments in the presence of a convection flow. Despite these versatile application, microfluidic devices require specific and often time consuming fabrication steps (usually microfabrication in cleanroom facilities) and need optimization of the biomaterial and the sterilization process used. In addition, the impossibility of retrieving the spheroids after treatment would limit their further characterization and, as a result, the amount of information obtainable from the assays.²⁴⁴

It is undoubtful that the application of three-dimensional culture systems as platform for the study of the molecular pathways involved in cancer progression is critical. Further improvements, in terms of culture techniques (e.g. co-culturing), imaging modalities and mathematical modeling would allow a deeper understanding of the neoplastic disease and the development of more effective anti-cancer nanomedicine strategies.

The objective of this part of the thesis work was the development of MG-63 osteosarcoma 3D spheroids for the assessment of the HGC_(0.185) micelle ability to penetrate within the three-

dimensional tumor masses and deliver the cytotoxic anthracycline. Human osteosarcoma spheroids have been previously investigated by Rimann and co-workers in a recent study,²³⁶ where they compared SAOS-2, HOS and MG-63 cell lines in terms of proliferation, apoptotic state, and susceptibility to treatment with chemotherapeutics agents (e.g. cisplatin, doxorubicin, taxol, taurolidine, and pemetrexed). In a previous work, Indovina *et al.*^{247, 248} assessed the MG-63 spheroid response, in co-culture with fibroblasts, to hypoxia treatments, in terms of collagen receptors, fibronectin receptors and cell-adhesion properties. Even though these studies constitute good references for the preparation and analysis of MG-63 multicellular aggregates, the delivery of chitosan-based micelles to human osteosarcoma MG-63 cells has not been yet performed. Considering the above mentioned premises and the physicochemical characteristics of the micellar system under study, we formulated the following hypotheses.

- Hypothesis (a): MG-63 human osteosarcoma spheroids can be easily obtained by liquid overlay technique, with high reproducibility. Given the presence of a necrotic core, this 3D multicellular system constitutes an avascular model to assess nanotherapeutics' efficiency *in vitro*.
- Hypothesis (b): thanks to their physicochemical properties, HGC micelles are able to penetrate within the inner regions of the tumor masses, constituting a promising anti-cancer delivery agents.

In this thesis project, the analysis of the MG-63 multicellular aggregate volume is presented to observe the spheroid growth both under normal culture conditions and under various treatments (free drug, empty polymeric micelles and drug-polymer nano complexes). Moreover, live-dead staining was performed to observe the stratified cellular structure. Extensive confocal imaging of the spheroidal masses allowed the visualization of the different nanomedicine uptake patterns.

4.2 Methods

3D Spheroid culture

Three dimensional tumor masses of MG-63 osteosarcoma cells were obtained via the so-called “liquid overlay technique”, based on the use of a hydrophobic coating which favors the cellular self-assembly into networks and highly organized structures. Briefly, a 96 well-plate was coated with 50 μ l of Agarose type I (low EEO, Sigma), previously dissolved in complete DMEM at a concentration of 1.5 % w/v and autoclaved. The agarose was let solidify into the wells for 20 minutes before using the plate. Cells were seeded at different densities (1000, 5000, 10000, 15000, 30000 and 50000 cells/well) by pipetting 100 μ l of cell suspension in each well. To favor cell aggregation and spheroid formation, immediately after plating, the plate was orbitally shaken (amplitude = 6 mm) for 15 minutes at 37 °C. The cells were left in incubation, unperturbed for 3 days at 5% CO₂ and 37 °C to allow the complete spheroid maturation. Media was freshly changed every two days (Figure 4.1).

3D Spheroid growth analysis

In order to evaluate the spheroid formation and growth in complete DMEM over a period of 14 days, the plate was imaged with the Olympus IX51 Fluorescent Microscope in the phase contrast mode at low magnification (4X). Subsequently, the images were analyzed in MATLAB with SpheroidSizer, an image analysis software application developed by Chen *et al.*²⁴⁹. The software accurately and automatically measures the size and the volume of tumor 3D assemblies, by detecting the contours of the spheroids. The identification of the minor and major axes allows the calculation of the spheroid volume as follow:

$$V = 0.5 \times (\text{major axis}) \times (\text{minor axis})^2$$

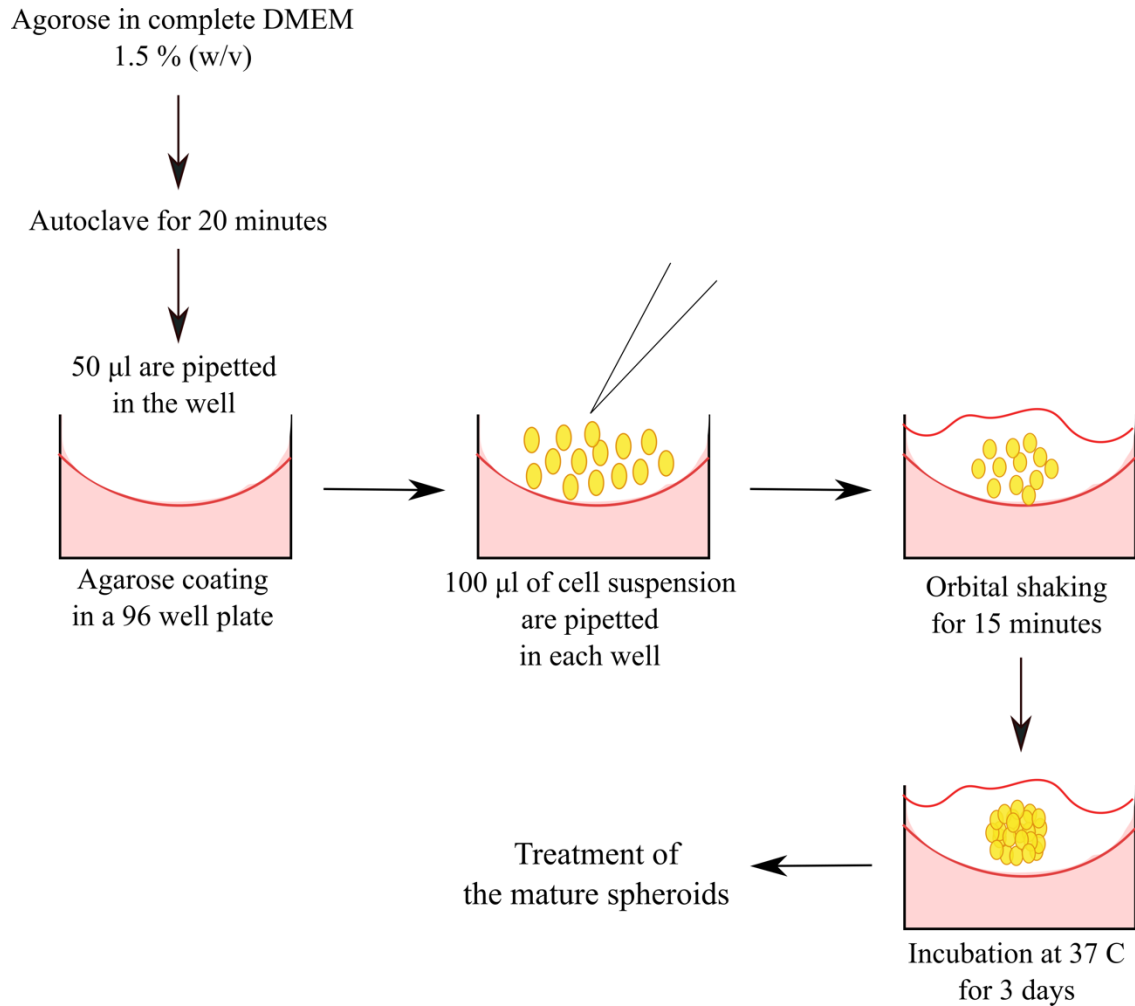


Figure 4.1 Schematic depicting the plating liquid overlay plating protocol for the fabrication of 3D tumor spheroids.

3D Spheroid cell population and morphology

With the aim of assessing the distribution of live cells and to observed the presence of the so-called “necrotic core” in the spheroids, a live-dead staining was performed. Briefly, mature spheroids were rinsed once with PBS (1X) and incubated in serum free DMEM containing 7 $\mu\text{g/ml}$ of fluorescein diacetate (FDA, Thermo Fisher Scientific) and 25 $\mu\text{g/ml}$ of propidium iodide (PI, Thermo Fisher Scientific). The incubation was carried out at 37 °C for 30 minutes in the presence of 5% CO₂. Immediately after incubation the spheroids were rinsed with DMEM to avoid further dye penetration and imaged with the Olympus IX51 Fluorescent Microscope under the FITC filter (green viable cells) and the PI filter (red dead cells). The volume of the whole spheroid mass and the volume of the PI-stained necrotic core were obtained as previously mentioned and the ratio of the volumes was calculated over a period of 7 days of growth. Results are presented in terms of mean \pm standard error.

In order to observe the morphological details of osteosarcoma MG-63 cells assembled in a 3D structure, mature spheroids were washed twice with PBS (1X), fixed with 8% formaldehyde for 20 minutes and stained with Alexa Fluor 488 phalloidin (1:100 dilution in PBS, Invitrogen) for 20 minutes. Consequently, samples were washed twice with PBS (1X), handpicked with a cut pipette tip and transferred to a glass bottom dish (MatTek) previously covered with Fluoromount G (Southern Biotech, Alabama). The spheroids were sandwiched with a glass coverlips and the samples were imaged under a Leica TCS SP5 Confocal Laser Scanning Microscope (Leica Microsystems, Ontario, Canada). A schematic of the spheroid post-culture processing protocol is reported in Figure 4.2. Images were acquired with a 63X oil immersion lens or with 20X and 10X dry lenses, at a speed of 10 Hz and at a resolution of 1024x1024 pixels. The confocal imaging was conducted at the Center for Functional Nanomaterials at Brookhaven National Laboratory.

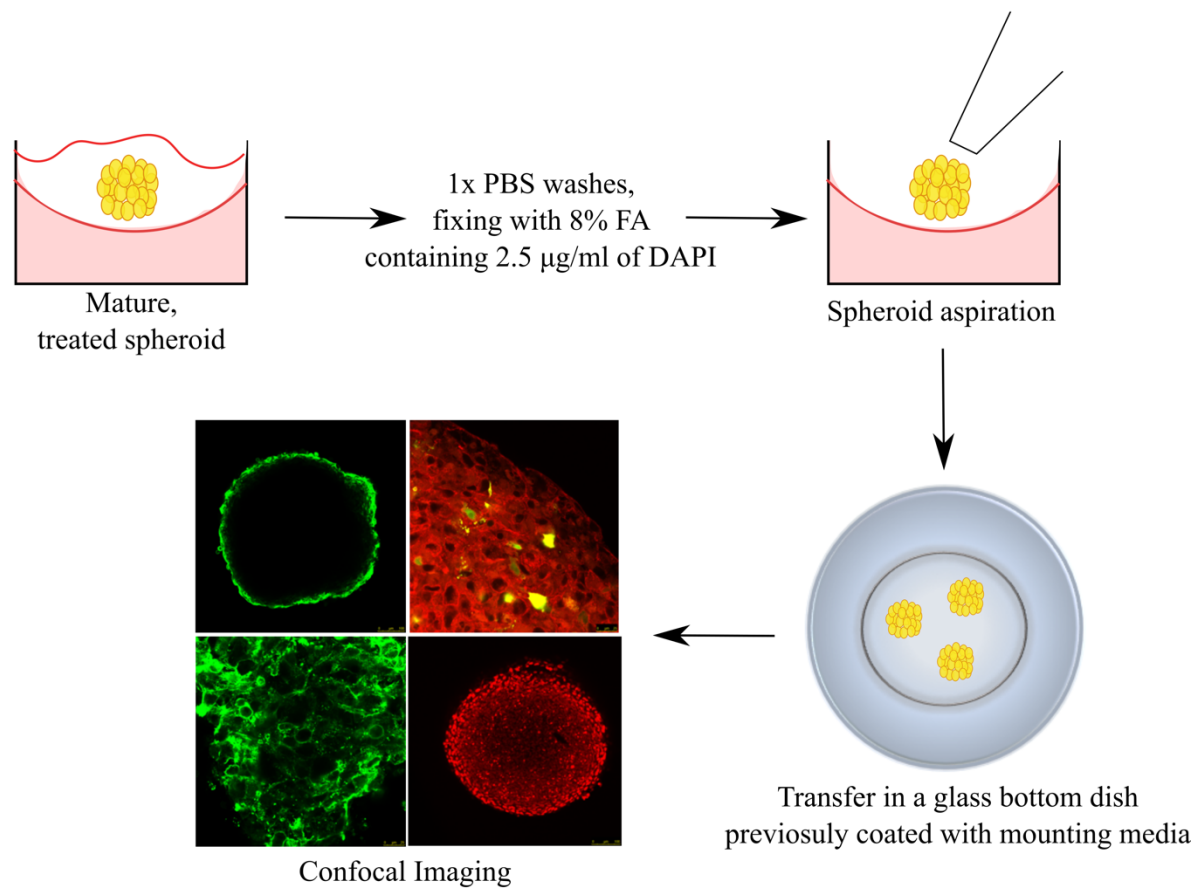


Figure 4.2 Schematic depicting the processing protocol (fixing, staining and mounting) for the imaging sample preparation of 3D tumor spheroids.

Delivery of free doxorubicin to 3D spheroids: cytotoxicity analysis and depth of penetration evaluation

With the aim of assessing the effects of the free drug on the 3D tumor model, human osteosarcoma MG-63 spheroids were obtained via “liquid overlay technique” as previously described. Doxorubicin was administrated at different concentrations (from 0.01 to 100 μM) and for various time points (15 and 30 minutes, 1 hour, 3 hours, 1, 2, 3, 5 and 7 days). The delivery was performed on mature spheroids (3 day old) by adding 100 μl of serum free DMEM containing the corresponding drug concentration to each well. At the desired time points, the plate was imaged with an Olympus IX51 fluorescent inverted microscope in phase contrast mode. Subsequently, the low magnification images were processed in MATLAB with SpheroidSizer package to check for change in size and morphology of the cancer cell assemblies with respect of the drug treatment. Control samples plated in serum free and in serum containing media were also considered. Three independent experiments were carried out. Data are presented in terms of average spheroid volume, with respect of the control, untreated and serum starved samples and a Student’s *t*-test was conducted considering a *p* value < 0.05 (*) or a *p* value < 0.01 (**).

Moreover, in order to observe the drug uptake and its spatial distribution within a three dimensional tumor volume, doxorubicin was delivered at concentrations of 10, 30 and 100 μM to 3 day-old spheroids. At the desired time points (15 and 30 minutes, 1, 3, 24 hours) the spheroids were washed twice with PBS (1X) and fixed with 8% of formaldehyde for 20 minutes, keeping the samples in the dark. After fixation and additional rinsing with PBS (1X) the spheroids were handpicked with a cut pipette tip and transferred to a glass bottom dish (MatTek) previously covered with Fluoromount G (Southern Biotech, Alabama). The spheroids were sandwiched with a glass coverlips and the samples were imaged under a Leica TCS SP5 Confocal Laser Scanning Microscope (Leica Microsystems, Ontario, Canada). Each spheroid was imaged with a 10X dry lens, at a speed of 10 Hz and at a resolution of 1024x1024 pixels. The microscope parameters were kept constant: 543 nm laser at a power of 27%, imaging with TRITC dye ($\lambda_{\text{ex}} = 562 \text{ nm}$, $\lambda_{\text{em}} = 595 \text{ nm}$), smart offset 0%, smart gain 1166.6 V, pinhole 53.07 μm . Z-stacks were acquired with slices equally spaced (2.53 μm step size, 80-100 slices on average per sample) in order to analyze a fixed volume of tumor mass. The depth of penetration and the distribution profile of the free drug was obtained by mapping the fluorescence signal via ImageJ software (www.rsbweb.nih.gov).

Delivery of HGC_(0.185) nanocomplexes to 3D spheroids: cytotoxicity analysis and depth of penetration evaluation

To assess the effects of the empty nanovehicles on the size, morphology and overall viability of the MG-63 3D tumor model, self-assembled nanoparticles were delivered at concentrations ranging from 0.075 µg/ml to 753 µg/ml and for various time points (15 and 30 minutes, 1, 3 hours, 1, 2, 3, 5 and 7 days). The delivery was performed on mature spheroids (3 day old) by adding 100 µl of serum free DMEM containing the corresponding nanocomplexes' concentration to each well. At the desired time points, the plate was imaged with an Olympus IX51 fluorescent inverted microscope in phase contrast mode. Spheroid volume analysis was performed with MATLAB with SpheroidSizer as previously described. Control samples plated in serum free and in serum containing media were also considered. Three independent experiments were carried out. Data are presented in terms of average spheroid volume, with respect of the control, untreated and serum starved samples and a Student's *t*-test was conducted considering a *p* value < 0.05 (*) or a *p* value < 0.01 (**).

To observe the penetration within the three-dimensional cell network of the polymeric nanocomplexes, Cy5.5-HGC_(0.185) nanoparticles were delivered at a concentration of 75.3 µg/ml, 226 µg/ml and 753 µg/ml to 3 day-old spheroids. At the desired time points (15 and 30 minutes, 1, 3, 24 hours) the samples were processed as previously described, imaged under a confocal microscope (Leica TCS SP5 Confocal Laser Scanning Microscope, Leica Microsystems, Ontario, Canada). Each spheroid was imaged with a 10X dry lens, at a speed of 10 Hz and at a resolution of 1024x1024 pixels. The microscope parameters were kept constant: 633 nm laser at a power of 27%, imaging with ATTO 633 dye ($\lambda_{\text{ex}} = 633 \text{ nm}$, $\lambda_{\text{em}} = 684 \text{ nm}$), smart offset -1.5%, smart gain 1050.9 V, pinhole 53.07 µm. Z-stacks were acquired with slices equally spaced (2.53 µm step size, 80-100 slices on average per sample) in order to analyze a fixed volume of tumor mass. The depth of penetration and the distribution profile of the free drug was obtained by mapping the fluorescence signal via ImageJ software (www.rsweb.nih.gov).

Delivery of Doxo-HGC_(0.185) nanocomplexes to 3D spheroids: cytotoxicity analysis and depth of penetration evaluation

To assess the effects of the drug-loaded nanovehicles on the size, morphology and viability of the osteosarcoma 3D tumor model, doxo-HGC_(0.185) nanoparticles were delivered at concentrations ranging from 0.081 µg/ml to 811 µg/ml and for various time points (15 and 30 minutes, 1, 3 hours, 1, 2, 3, 5 and 7 days). The delivery was performed on mature spheroids (3 day old) by adding 100 µl of serum free DMEM containing the corresponding nanocomplexes' concentration to each well. At the desired time points, the plate was imaged with an Olympus IX51 fluorescent inverted microscope in phase contrast mode. Spheroid volume analysis was performed with MATLAB with SpheroidSizer as previously described. Control samples plated in serum free and in serum containing media were also considered. Three independent experiments were carried out. Data are presented in terms of average spheroid volume, with respect to the control (untreated and serum starved samples) and a Student's t-test was conducted considering a p value < 0.05 (*) or a p value < 0.01 (**).

To observe the penetration within the three-dimensional cell network, doxo-HGC_(0.185) nanoparticles were delivered at a concentration of 81.1 µg/ml, 234.3 µg/ml and 811 µg/ml to 3 day-old spheroids. At the desired time points (15 and 30 minutes, 1, 3, 24 hours) the samples were processed as previously described, imaged under a confocal microscope (Leica TCS SP5 Confocal Laser Scanning Microscope, Leica Microsystems, Ontario, Canada). Each spheroid was imaged with a 10X dry lens, at a speed of 10 Hz and at a resolution of 1024x1024 pixels. The microscope parameters were kept constant: 543 nm laser at a power of 27%, imaging with TRITC dye (λ_{ex} = 562 nm, λ_{em} = 595 nm), smart offset 0%, smart gain 1195.6 V, pinhole 53.07 µm. Z-stacks were acquired with slices equally spaced (2.53 µm step size, 80-100 slices on average per sample) in order to analyze a fixed volume of tumor mass.

4.3 Results and Discussion

Tumor spheroids were established as three dimensional cancer model. The morphological features and the cellular structure in the network were extensively analyzed via fluorescence and confocal imaging.

With the aim of replicating some of the tumor microenvironment features, MG-63 tumor spheroids have been established. These multicellular systems present a three-dimensional architecture, in which cells are not fully in contact with a tissue culture substrate surface, but are instead assembled into a solid, self-standing mass, where they can exert cell-to-cell interactions. The ECM proteins, secreted by the cells during the culturing time, confer further stability and structural support to the spheroid, and are responsible for establishing cell-to-matrix signaling. In addition, both the presence of nutrients' gradient across the 3D network and the lack of a continuous oxygen supply to the inner core of the mass, contribute to reproduce *in vitro* the tumor pathological features. In this thesis work, spheroids were plated following a liquid overlay strategy (Figure 4.1, in the Methods section). The wells of a 96-tissue culture plate were coated with agarose, to render the surface hydrophobic and facilitate the cellular self-assembly in suspension. This step has to be carefully performed: in fact, the viscosity of the agarose might impair a smooth application of the coating, and small bubbles might result in the final, cured layer. Any inhomogeneity on the agarose might interfere with the formation of spheroids with reproducible characteristics. The clustering of the cells was optimized by orbitally shaking the plate for 15 minutes at 37 °C. Incubation was carried out for 3 days, to allow the formation of mature, compact spheroids, self-standing in the culture media.

Depending on the purpose of the various experiments, spheroids were either treated and left in the agarose-coated well, for imaging under the fluorescence inverted microscope and size analysis, or treated and post-processed for confocal imaging analysis. The post-culture treatments, such as fixing and staining, were carefully carried out, in order not to disrupt the tumor aggregates and lose information on its morphology. The protocol established in our lab involved a first step of processing (washing, fixing, staining) performed in the same well of the culture. Afterwards, by means of a truncated 200 µl pipette tip, the spheroids were aspirated from the well and gently transferred in a glass bottom dish, previously coated with a layer of mounting media. The transferred spheroids were further embedded in the mounting media and protected by means of a

thin, squared microscope slide (as shown in Figure 4.2, in the Methods section). This set up would ease the subsequent confocal imaging.

A first set of experiments was carried out to analyze the growth profile, in terms of size and morphology of spheroids plated at different cell densities, over 14 days of culture (Figure 4.3). The volume change (percentage of the starting volume at day 3) was also considered, with the aim of assessing the system stability over time. From the plot of the average spheroid volume in Figure 4.3a, it is noticeable that lower plating cell densities (5000 – 15000 cells/well) lead to the formation of more stable tumor masses, not being subjected to volume changes over time. The corresponding phase contrast micrographs in Figure 4.3c offer a good visualization of this phenomenon. However, several cells appeared to be distributed around the periphery of the spheroids, and not included into the main bulk of the mass, almost forming a “sunny-side-up-egg” arrangement (Figure 3.4 c, yellow dotted lines). For the case of the higher plating cell densities (30000 – 50000 cells/well), fluctuations in the volume were recorded. More specifically, the spheroids appeared to shrink by about 10 – 20% between day 3 and day 6 of culture, to maintain a more stable size between day 6 and day 10 and further decrease in size over time, reaching 70 – 80% of the initial volume measured at day 3 (Figure 4.3 a, b). The first, steeper volume decrease might be imputable to the cell compaction in the three-dimensional structure, while the second, slower volume reduction might be due to a partial shedding of the cancer cells from the main tumor mass. A similar outcome was obtained by the work of Gao *et al.*²⁵⁰, in which HeLa cells were plated at different cell densities, ranging from 62 to 100 cells/well. The diameter and volume analysis revealed a spheroid shrinkage between day 1 and day 3 of incubation, and a further size increase until day 10 of culture. In our study, the phase contrast images showed the formation of more homogeneous, spheroid-like cell assemblies, with volumes ranging from 0.12 mm³ to 0.16 mm³ and diameters of about 500 – 700 μm, depending on the starting cellular amount. Despite the observed volume shrinkage, for the following experiments spheroids were plated at higher cell densities, to allow the formation of more compact structure, which would ease both the visualization and the processing (e.g. transferring, hand picking by means of a truncated pipette tip).

Three dimensional tumor spheroids are formed by a non-homogenous cell population. When mature, a layered, onion-like structure can be identified within the system: an outer layer of active, proliferating cells, an intermediate spherical corona of quiescent, non-proliferating cells, and an

inner core of dead cells.²²⁹ Cells in the outer layer often present a more stretched and flat morphology, while cells in the deeper regions of the spheroid dispose in a more 3D configuration. In addition, due to the gradient of oxygen and nutrients across the mass, cancer cells in the core may undergo apoptotic processes or necrosis. Focus of a second set of experiments was the observation of the cellular population within the spheroids, and the quantitative analysis of the necrotic core dimension over time. Propidium iodide (PI) is used to identify dead cells, due to its ability to intercalate between DNA and RNA bases; the compound is membrane impermeant, hence not staining viable cells. On the other hand, fluorescein diacetate (FDA) presents an acetoxymethyl ester group, which can permeate cell membrane. Once inside the cell, FDA is cleaved by nonspecific esterase, and the resulting charged form is retained inside the viable cell where it fluoresces. The live-dead staining was conducted on MG-63 spheroids plated at two different starting cell densities, and images were acquired by means a fluorescent microscope under phase contrast, fluorescein, and PI filters. In Figure 4.4 examples of the staining are reported: the PI appeared to be concentrated in the center of the cellular assembly, where most of the cells undergo oxygen and nutrients deprivation,²²⁹ while a brighter FDA signal was observed in the outer regions, populated by active cells. The evolution of the core was analyzed by acquiring images at day 3, 5 and 7 (Figure 4.5), and by measuring the volume of both the total spheroids and the core by means of MATLAB software (SpheroidSizer package) (Figure 4.6 a, b). Also in this case, a reduction in the average volume was observed for both systems (25000 cells/well and 50000 cells/well). The ratio between the volume of the inner, PI stained core and the total volume of the tumor assembly (Figure 4.6 b) revealed that about 50 – 60% of the mass after 3 days of maturation is already composed of cancer cells undergoing either a necrotic or an apoptosis process. A similar volume fraction was obtained at day 5, whereas after 7 days of maturation the volume of the necrotic core reached about 80% of the total spheroid size. These measurements were obtained from imaging analysis, and should be further validated with more sensitive techniques, such as flow cytometry, which can allow the quantitative determination of the live-dead population, and can discriminate between cells undergoing necrosis or entering an apoptotic pathway which would lead to nuclear chromatin fragmentation, cytoplasm shrinkage and loss of membrane integrity (e.g. staining with propidium iodide and AF488-labelled Annexin V). Precaution should be taken while homogeneously dispersing the tumor masses, not to cause accidental cell death which might bias the result. In addition, confocal microscopy can offer a powerful tool to obtain high resolution

images of the live-dead stained samples. On the other hand, in this case, fixable reagents should be used and the imaging might be affected by possible dye leaking within the mass.

Taken together, the analysis of the spheroid size and morphology, as well as the evolution of the necrotic core over time, allowed to gain insight into the human osteosarcoma MG-63 assembly behavior and features, when exposed to normal growth conditions, an important information for the planning of the following experiments.

Actin staining performed with Alexa Fluor-488 phalloidin on MG-63 spheroids at 10 days of maturation, revealed the three-dimensional arrangements of the cancer cells in the tumor network (Figure 4.7). The circular contours, presenting different dimensions, of the cells suggest their bulking within the mass. The actin fibers are not fully stretched on a substrate surface, but are now entangled in a more complex architecture, which affect the cell ability to migrate, sense the environment and exchange signals. These morphological features differ from the case of the cells in monolayers, where actin fibers appeared well stretched out and aligned one another (Figure 2.15 a, b, c). This intricate network of proteins and cells better mimic the features of the actual tumor microenvironment, constituting a robust model to assess the penetration ability and the therapeutic efficacy of bioengineered nano constructs.²⁵¹

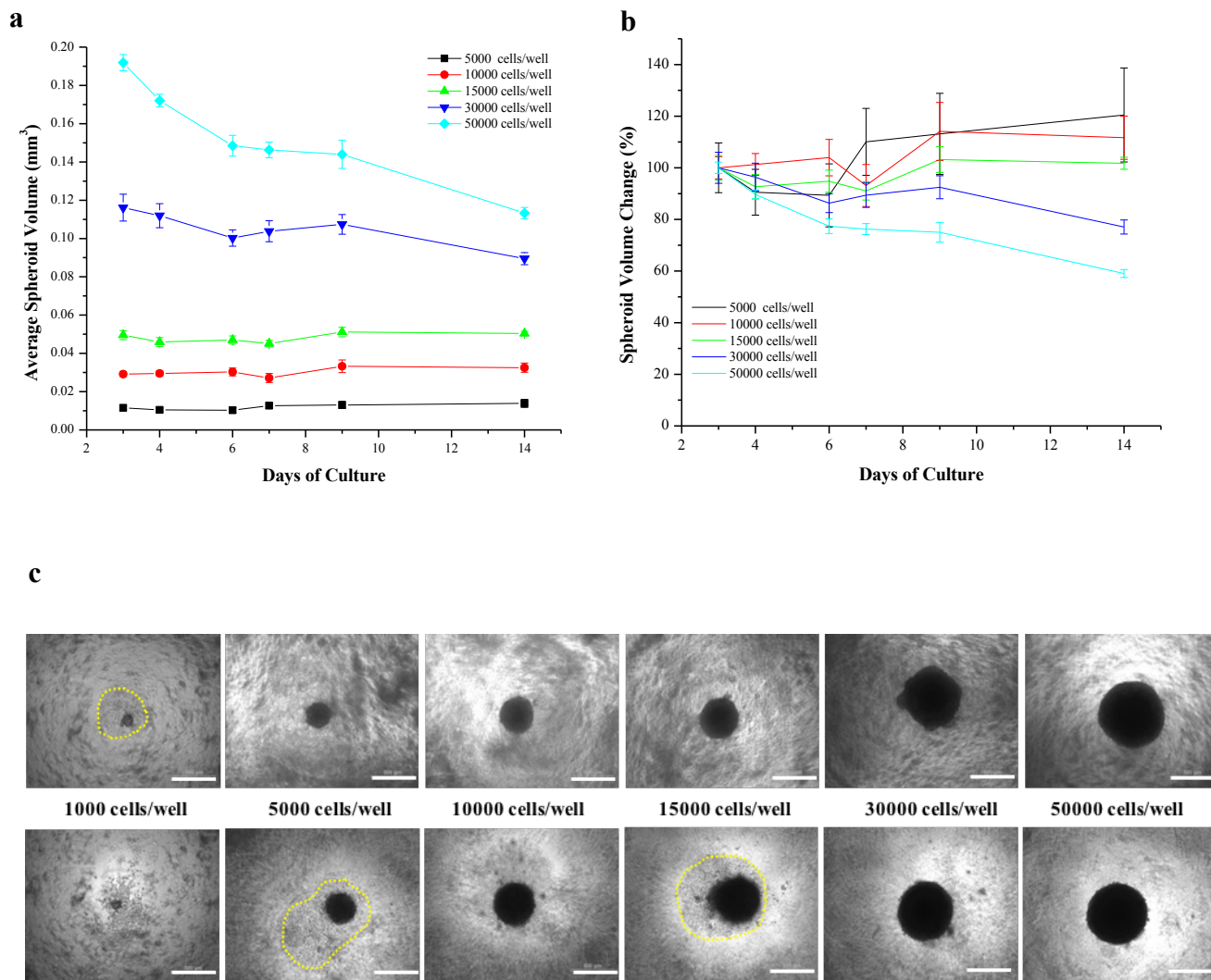


Figure 4.3 3D Spheroids of MG-63 cells plated at different starting cell densities: (a) average spheroid volumes over culture time, (b) change in spheroid volume over culture time, (c) phase contrast images of spheroids at day 3 (upper panel) and day 9 (lower panel) of culture. The dotted lines defined the cells not included in the bulk mass (“sunny-side-up” configuration). Scale bar 500 μm .

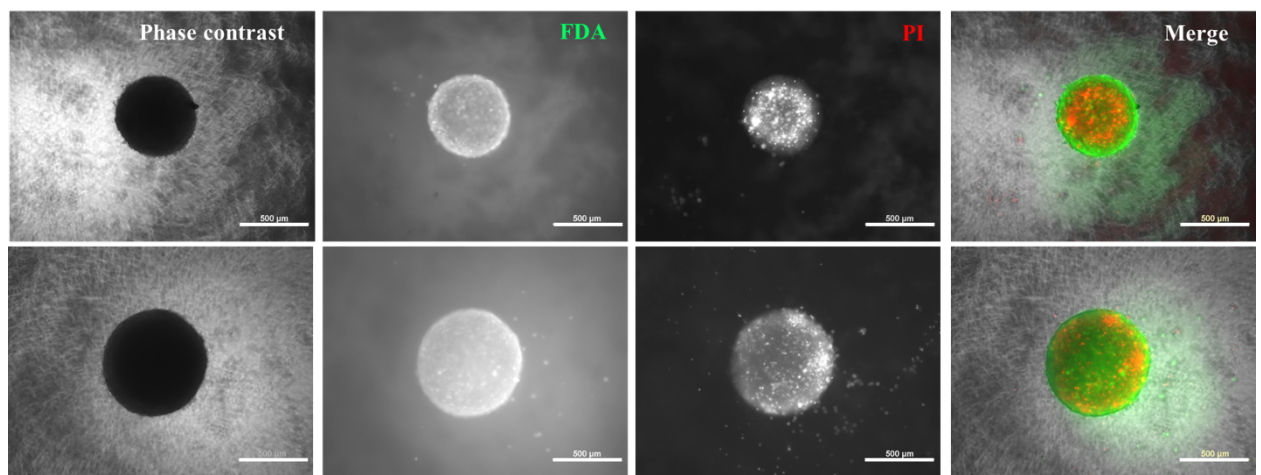


Figure 4.4 Live-dead staining of MG-63 spheroids plated at 25000 cells/well (top row) and at 50000 cells/well (bottom row). The fluorescein molecules (FDA, green channel) stain for the live population of cells, while the propidium iodide (PI, red channel) highlights the necrotic core. Scale bar 500 μm .

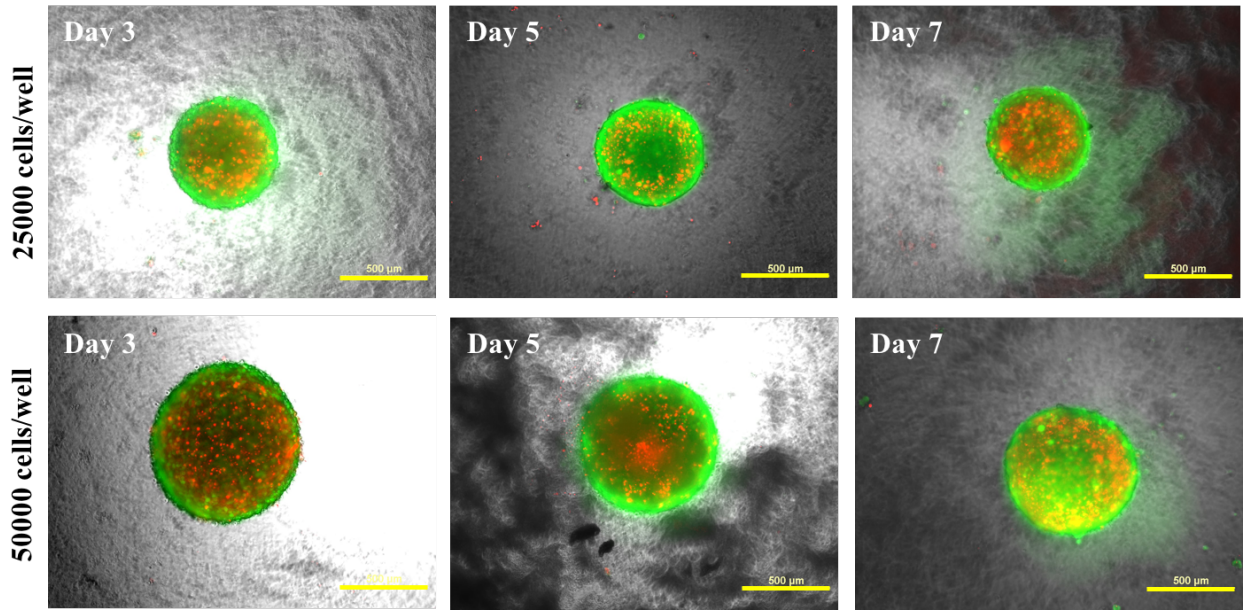


Figure 4.5 Live-dead staining of MG-63 spheroids plated at 25000 cells/well (top row) and at 50000 cells/well (bottom row) and incubated for different time points. The fluprescein molecules (FDA, green channel) stain for the live population of cells, while the propidium iodide (PI, red channel) highlights the evolution of the necrotic core. Scale bar 500 μm .

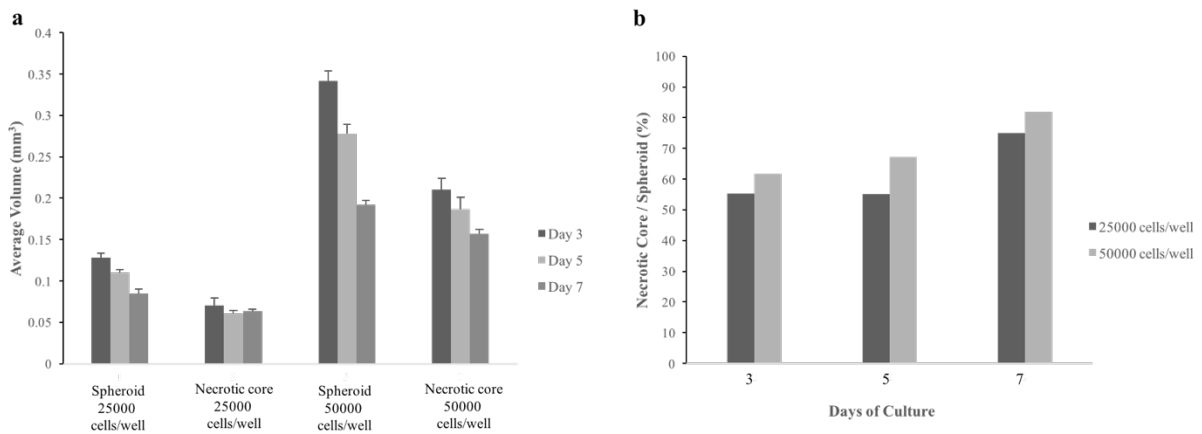


Figure 4.6 Average volume of MG-63 3D spheroids and of the corresponding necrotic cores, with respect to the culture conditions. Errors bars represent s.e. of 12 spheroids (a). Ratio between the volume of the necrotic core and the volume of the spheroids, with respect to the culture conditions (b).

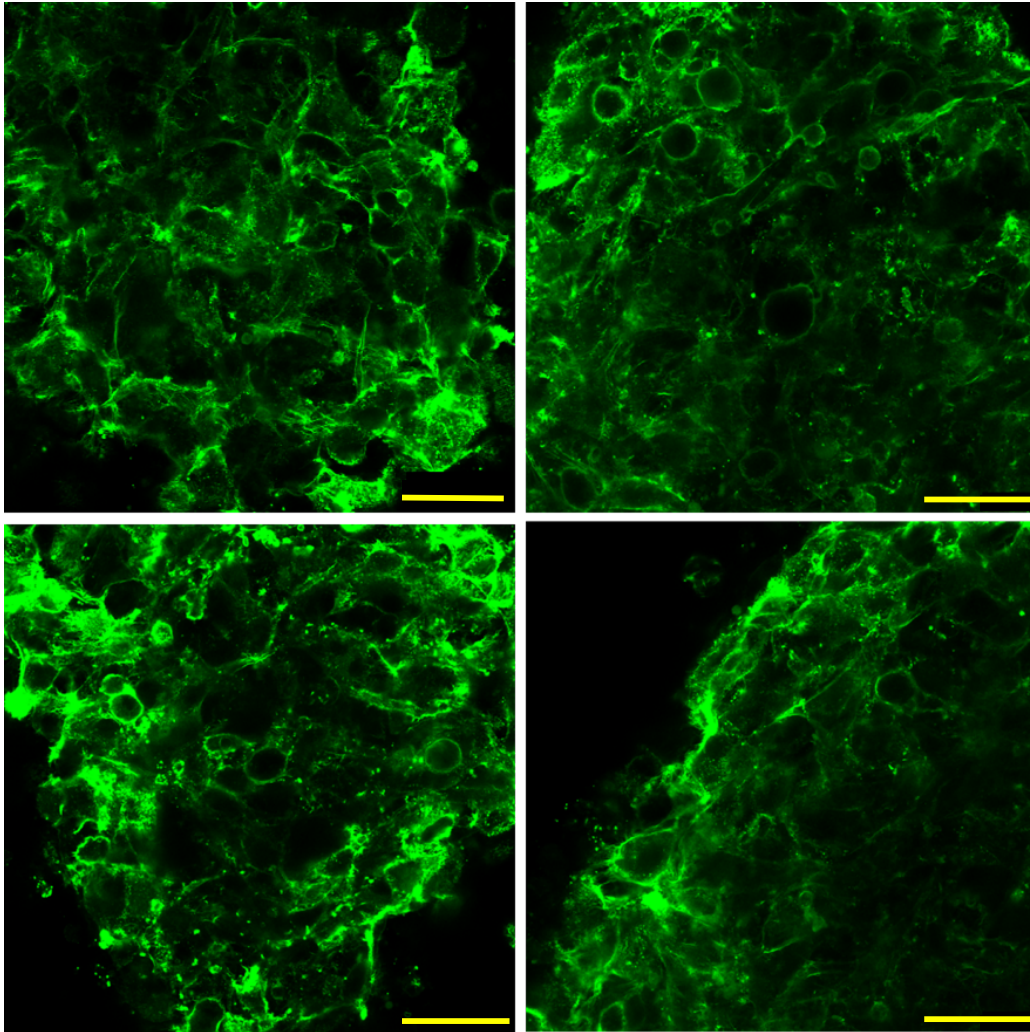


Figure 4.7 Confocal micrographs of mature MG-63 spheroids stained with Alexa Fluor 488 phalloidin to highlight the actin structure. The three-dimensional arrangement of the cytoskeleton and the compact network of cancer cells is visible from the high magnification images (63X). Scale bar 50 μm .

Tumor spheroid culture constitutes a useful tool for the analysis of free, small anticancer compounds, in comparison with the nano-therapeutic efficacy on solid cancer

With the aim of assessing the susceptibility of the MG-63 spheroids to the various treatments, a sequence of experiments has been carried out. Briefly, 3 day-old mature spheroids were treated with either several concentrations of free doxorubicin (ranging from 0.01 μM to 100 μM), or HGC_(0.185) NPs (at concentrations from 0.075 $\mu\text{g/ml}$ to 753 $\mu\text{g/ml}$), or drug-loaded nanocomplexes (ranging from 0.081 $\mu\text{g/ml}$ to 811 $\mu\text{g/ml}$). Three independent experiments were performed, considering triplicates per each condition, up to total 7 days of treatment. The administration of the nano therapeutics was carried out in serum free media, to avoid protein adsorption which would possibly interfere with the micelle penetration. Control samples in complete media were also considered. At each time point, the cell culture plates were removed from the incubator and imaged under a fluorescence microscope equipped with a phase contrast condenser. The contours of the cellular aggregates were analyzed in MATLAB, as previously reported. The analysis of the average volumes and the average volume changes with respect of the treatment dose and duration can give an insight on the response of the three dimensional cell network to the chitosan-derivative micellar system. Results are reported in Figures 4.8 and 4.9. The plots in Figure 4.8 show the variation of the spheroid volume with respect of the treatment time. In this case, a normalization was done referring to the initial volume at time zero of the set of spheroids subjected to a specific treatment (for example, the average volume of the spheroids treated with 0.1 μM of doxorubicin for 3 hours was divided by their average volume at time zero). Since the same spheroids were imaged during the course of the experiment, this data processing would allow to observe variation of the volume with respect to the initial time, before the nano therapeutic administration. From the resulting plots, it is visible that untreated spheroids kept in complete media (black squares) presented a slower volume decrease, while the treated spheroids and the aggregates maintained in contact with serum free media (red circles) showed a steeper decrease in their dimensions. A similar outcome was observed for every treatment (Figure 4.8 a, b, and c), and no particular difference was associated to the concentration of the delivered active agents. As previously observed for the case of the osteosarcoma cells in monolayer, the serum deprivation has a predominant effect on the general viability of the tumor aggregates. It is important to notice that

the spheroids were treated at day 3, after complete maturation and compaction, and the delivery was carried out for 7 days, continuously, refreshing the media every 2 days. Therefore, at the end of the experiments, spheroids were 10 day-old. The reduced efficacy of chemotherapies in 3D systems, in comparison with cell in monolayers, has been previously observed,^{187, 236} and attributed to the limited diffusion posed by the tumor network barrier. Figure 4.9 reports the average spheroid volume with respect to the treatment concentrations. No normalization was performed in this case. Those plots further confirm the previous observation: variations in the average spheroid volume do not appear to be associated to the treatment concentration, and progressive dimension decrease is registered with time. This outcome might suggest that the analysis of the tumor volume does not give a complete picture of the spheroid sensitivity to the drug treatment. Even though the contribution of the shedding off of the cells in the outer layer is considered with this assay, the measurement of the size does not take into account the possible cytotoxic effect on the inner regions, which might still be caused by the nanomedicine treatment. In this regard, spheroid viability could be further assessed via MTS assay, or via flow cytometry, after proper cell dispersion and staining for apoptosis and necrosis markers. In addition, another possible interpretation of the limited doxo-HGC_(0.185) NPs cytotoxic potential can be related to the release of the active drug from the micellar carrier. In fact, the tumor microenvironment is characterized by a lower pH (around 6.8), due to anaerobic glycolysis and fast cell growth, a parameter that greatly affects the drug dissociation from the micelles. A future study with the employment of acidified culture media might elucidate the apparent spheroid resistance to the treatments and give more insight into the efficacy of the delivery agents.^{252, 253} In order to check for the actual penetration of the free drug and the nano vehicles within the tumor masses, a systematic confocal study was conducted and results are presented in the following paragraph.

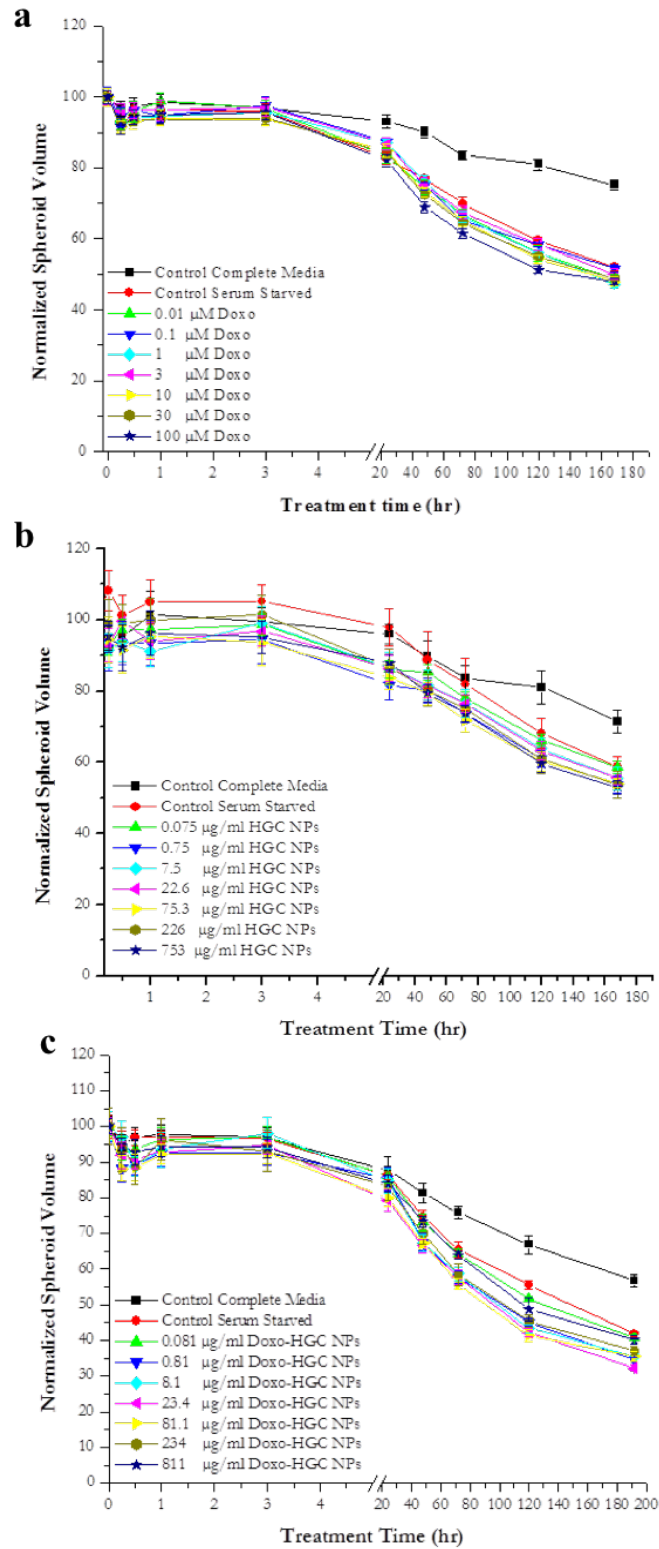


Figure 4.8 Normalized spheroid volume versus treatment time for spheroids treated with (a) free doxorubicin, (b) HGC_(0.185) NPs and (c) doxorubicin-loaded HGC_(0.815) NPs.

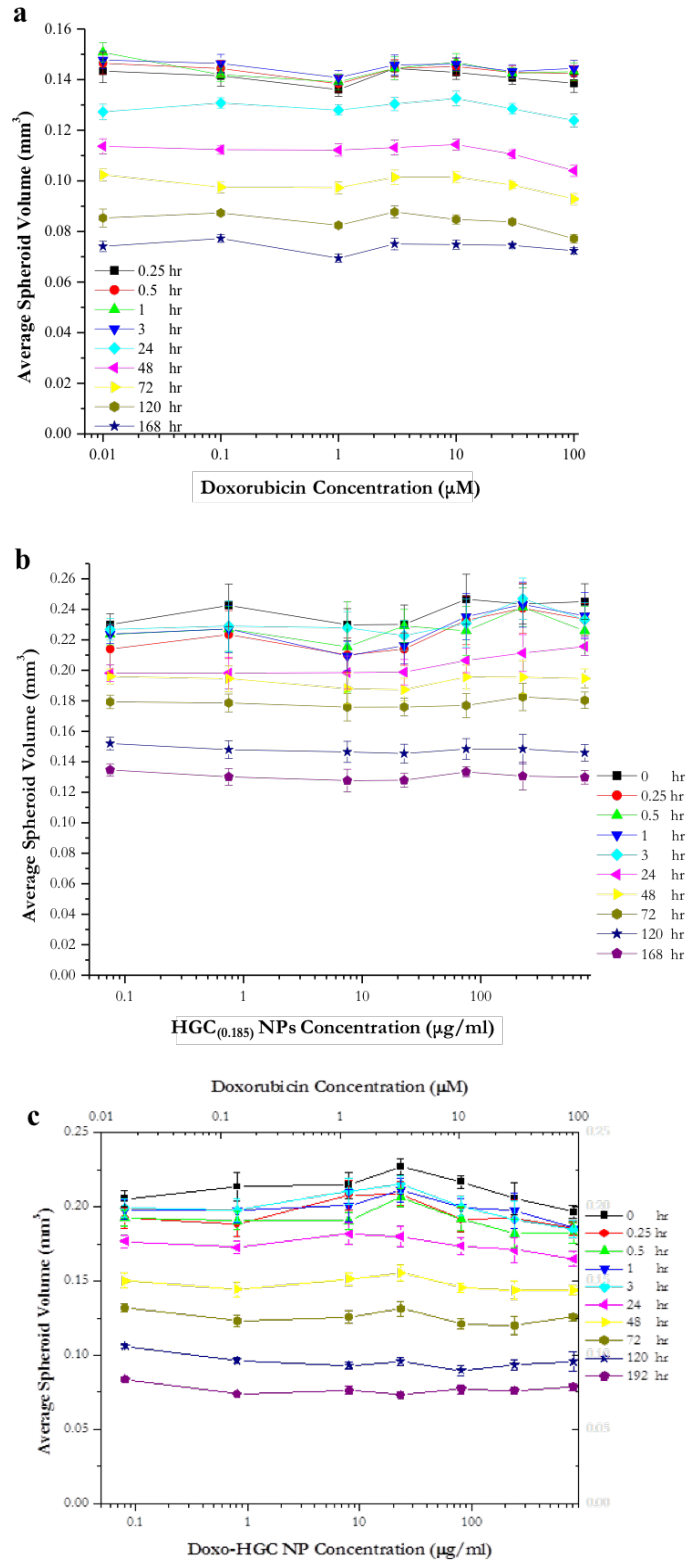


Figure 4.9 Average spheroid volume versus treatment concentration for spheroids treated with (a) free doxorubicin, (b) HGC_(0.185) NPs and (c) doxorubicin-loaded HGC_(0.185) NPs. The double x axis in (c) allows the comparison between the concentration of the free drug and the nanoparticles.

Tumor spheroid culture offers a useful tool for the analysis of the nano-therapeutic penetration into solid cancer

With the aim of assessing and comparing the penetration ability of the free drug and the chitosan-derivative nano-vehicles, an imaging study was performed. Technical challenges are associated with the imaging of the complex, three dimensional cellular structure of the cancer spheroids, which require implementation of more advanced imaging protocols, able to sharply distinguish and define the distribution of nano therapeutics within the sub-regions of the solid masses.^{227, 254, 255} Moreover, increasing imaging depths to limit light scattering should be considered. Several studies have reported the use of *z*-stack analysis via confocal or fluorescent microscopy, to either observe the biodistribution of fluorescently labelled nanomedicines throughout the tumor masses, or to assess for the presence of specific markers after staining.^{187, 191, 250, 256-258} For example, in their work, Ma *et al.*¹⁹¹ performed imaging of live HeLa spheroids (5 μm thick sections) by multiphoton fluorescent microscopy, further reconstructed using tomography. With similar approaches, Gao *et al.*²⁵⁰ and Sarisozen *et al.*²⁵⁶ acquired stacks consisting of 10-20 μm thick slides of spheroids (human glioma and ovarian cancer, respectively), spanning over a total of 140 μm , to obtain the relative intensity plots with respect of the distance from the surface of the spheroids.

In this study, MG-63 spheroids were let maturing for 3 days, before applying the free drug or the nanoparticle treatments. Samples were administrated either with different concentrations of doxorubicin (10 μM , 30 μM and 100 μM), or with the corresponding concentrations of Cy5.5-HGC_(0.185) NPs (75.3 $\mu\text{g/ml}$, 226 $\mu\text{g/ml}$, 753 $\mu\text{g/ml}$), or with the corresponding concentrations of doxorubicin loaded-HGC_(0.185) NPs (81.1 $\mu\text{g/ml}$, 234 $\mu\text{g/ml}$, 811 $\mu\text{g/ml}$). At the desired time points (15 minutes, 30 minutes, 1 hour, 3 hours, and 24 hours) samples were fixed and mounted in glass bottom dishes, as reported in the Methods section. Confocal microscopy was used to acquire *z*-stacks of 2.53 μm thick slices, to span over a total thickness of 200 – 300 μm . The acquisition parameters were kept constant within the sets of samples (see Methods section), to allow the comparison of the penetration profiles with respect to the treatment time and the nanomedicine concentration. Figures 4.10, 4.11 and 4.13 show representative slices of the spheroids' mid planes, imaged at about 100 – 150 μm from the apical surface of the cellular masses, for each condition tested and imaged. As noticeable from the corona-like fluorescent signals in Figure 4.10, free

doxorubicin appeared to be localized at the outermost layer of the spheroids, especially when delivered at 10 μM and 30 μM for shorter time points. At longer incubation times with 100 μM of doxorubicin, the free drug appeared to diffuse further in the tumor masses, as the fluorescence signal interested a thicker layer of cells. After 24 hours of treatment, bright red nuclei were visible in the center of the cross sections, indicating that the anthracycline molecules started to slowly reach inner regions. On the hand, the penetration profile of the Cy5.5-HGC_(0.185) nano-vehicles presented a complete different pattern (Figure 4.11). While the time- and concentration-dependency was observed as expected,^{187, 191} the far-red fluorescent signal pertaining to the NPs appeared to be more homogeneously distributed throughout the tumor assembly. Bright red spots were noticed in the central region of the spheroids, only after 1 hour of incubation with 226 $\mu\text{g}/\text{ml}$ of NPs. In this case, the confocal imaging seems to highlight the presence of sub-regions with lower cell densities, probably resulting from air bubbles formed during the pipetting or the shaking steps. Despite the partial density in-homogeneity of the cellular assemblies, the NPs were successfully uptaken by the osteosarcoma cells in the 3D network. High magnification confocal micrographs from inner regions of the tumor masses reported in Figure 4.12 further confirm our previous observation: clusters of Cy5.5-HGC_(0.185) nano-vehicles were internalized into the cytosol, defining the 3D, spheroid-like cytoskeleton structure of the cells within the network. A similar uptake pattern was observed for the case of the doxorubicin-loaded HGC_(0.185) nano micelles, as reported in Figure 4.13, where the red signal pertaining to the encapsulated drug molecules was also visible in the central areas of the spheroids' cross sections. A possible interpretation of this outcome might be given by the fact that free doxorubicin can be uptaken by active cells, diffuse into their membranes and reach the nuclei to exploit its anti-proliferative function. Multicellular assemblies are constituted by a stratified structure, with an outer layer of active and proliferating cells, an intermediate region of quiescent cells, and an inner core of cells undergoing necrosis or apoptosis.^{191, 237} Free drug molecules can be easily uptaken by the active and proliferating cells, leading to the accumulation of doxorubicin in the outermost layers. By contrast, quiescent cells in the intermediate region might be less responsive to the free drug treatment: a population of cells within the spheroid might acquire drug resistance capability, due to the physical barrier exerted by the 3D network itself. On the other hand, the chitosan-derivative nano vehicles might guide the penetration of a cargo molecule in deeper regions, due to their physicochemical properties, which favor the uptake from cells in the quiescent layer. It is also

necessary to point out that our designed experiments do not take into account the potential effect of convective flows or presence of stromal cells on the nano therapeutic transport and spheroid internalization. Further analysis with co-culture multicellular systems should be implemented to address this biological question.

For the penetration profile analysis, an imaging processing method was implemented, modified from Sagnella *et al.*¹⁸⁷ The approach is presented in Figures 4.14 and 4.15. Briefly, the mid slice of the stack was isolated and 4 intensity profiles were obtained via ImageJ/Fiji software, to account for non-homogeneity in the shape of the tumor mass and in the nanomedicine penetration. In fact, the cancer cell assembly might not present a perfect spheroidal shape and the presence of non-homogeneities at the outer surface might favor or discourage the penetration of the systems under study. The 4 plot profiles were averaged to obtain 1 fluorescent intensity profile per treatment time and concentration. Duplicates were considered for each conditions. In Figures 4.16 and 4.17 the fluorescent intensity plot profiles of free doxorubicin, with respect to the diameter of the spheroids, are reported, while in Figures 4.18 and 4.19 similar plots for the Cy5.5-HGC_(0.185) NP treated spheroids are shown. For the case of the free drug, at each concentration and time point, sharp peaks were identifiable at the extremities of the spheroids, while the fluorescent signal was close to zero in the center (Figure 4.16). Increased fluorescent intensity was observed at longer time points and higher concentrations, as visible from the overlaid plots in Figure 4.17 and the corresponding maximum values of the y axes. When observing the fluorescent intensity plots of the chitosan-NP treated spheroids (Figures 4.18 and 4.19), less defined peaks at the extremities were present, while spikes and smooth peaks in the center of the plots appeared. Although the fluorescent signal maintained a dependency from the time of incubation and the treatment concentration, the non-zero values and the presence of numerous ups and downs in the plots indicated a deep and successful penetration of the micelles within the cancer network. From the fluorescent intensity plots reported (Figures 4.16, 4.17, 4.18 and 4.19), the penetration patterns of the two systems appear to differ greatly, suggesting a higher capability of the chitosan nano micelles to infiltrate within the 3D cellular aggregates. To best of our knowledge, this is the first example of non-targeted, chitosan-based nanomicelles with average diameters of 250 – 300 nm penetrating through the whole cellular mass. For example, in their work, Ma *et al.*¹⁹¹ delivered to Hela spheroids smaller nanoparticles, such as aminoPEG-coated quantum dots and carboxyl-coated quantum dots with diameters of 20 nm, which were only able to penetrate the outer layer

of cells. In another study, Gao *et al.*²⁵⁰ prepared PEG-PCL nanoparticles of about 140 nm in diameter, and administrated them to A549 human adenocarcinoma and U87 human glioblastoma cells: the nanoparticle penetration pattern at 140 μm from the bottom of the spheroids appeared mostly distributed along the spheroid outer shell, and it was only recorded at the center of the tumor mass when the nanoparticles were decorated with a cell penetrating peptide.

To further analyze the plots, an exponential decay of the fluorescent intensity was considered to model the penetration of the free doxorubicin from the outer surface to the inner region of the spheroids. A similar model could not be applied for the case of the Cy5.5-HGC_(0.185) NPs, due to the presence of non-zero values and the absence of well-defined peaks, especially at mid-high concentrations and longer time points. For the case of the free doxorubicin, quantities such as maximum fluorescent intensity (I_{max}), distance from the surface where the maximum fluorescent intensity is reached (x_{max}), half fluorescent intensity ($I_{1/2}$), and distance from the surface where the half value of the fluorescent intensity is reached ($x_{1/2}$) were defined (Figure 4.15). In addition, the difference between x_{max} and $x_{1/2}$ was considered, to indicate the distance of half intensity decay. Reporting a difference between two distances within the spheroid cross section, this parameter can also allow the comparison between spheroids of slightly different sizes. Moreover, when assuming an exponential decay of the fluorescent intensity, a parameter μ , related to the ability of the nanomedicine to penetrate within the tumor mass, can be considered. In Table 4.1 the values of the above mentioned quantities for the free drug and the nano-micelle treatments are reported. Averages refer to the duplicates prepared for the experiments. It is important to recall that, during the confocal imaging acquisition, the microscope parameters were kept constant, for the same set of samples. The density of the MG-63 spheroids is unknown and non-uniform, and, most importantly, subjected to changes over time due to cellular proliferation of the outer layers and cell death of the inner regions. In addition, a modelling of the experimental plots, over a wide range of incubation time was not performed. Therefore, in this case the obtained parameters should not be referred for the calculation of the diffusion coefficients of the different nano therapeutics. However, those quantities constitute a good indication of the penetration ability of the therapeutic treatments into solid tumor masses. From the values in Table 4.1, it is visible that higher penetration depths are reached when longer treatment times (3 hours and 24 hours) and more concentrated drug-containing media are employed (30 μM and 100 μM).

In this fluorescent intensity plot analysis, doxorubicin-treated spheroids were not considered: although the penetration of the drug-loaded micelles was observed, the rather dim signal pertaining to the doxorubicin complexed with the chitosan-micelles did not allowed a precise identification of the peaks, which would lead to a possibly biased result. The weak fluorescent signal pertaining to the doxorubicin molecules might be related to its physical complexation with the polymer matrix. In their work, Sagnella *et al.*¹⁸⁷ delivered doxorubicin-loaded dextran-derivative nano vehicles to human neuroblastoma cell lines. While, under the regular confocal microscope, the free drug molecules were lighting the nuclei of the cells (where the anthracycline fluorescence is enhanced due to favorable molecular packing), the drug-polymer complex was predominantly observed within the cytosolic compartments, both in monolayers and 3D networks, with little drug visibly associated to the nuclei. Therefore, fluorescence lifetime imaging microscopy (FLIM) was employed, to discriminate between the complexed, bound form and the free form of doxorubicin within the cells. By distinguishing between the longer lifetime of the particle-associated doxorubicin and the shorter lifetime of the free drug form, and by observing a time-dependent shift, this technique provides information on the fractional contributions of the two doxorubicin forms, and offers a powerful tool for the observation of the drug release from the nanoparticles, following cellular uptake. A similar experimental approached was also conducted by Basuki and coworkers,²⁴² to monitor the intracellular release of doxorubicin from iron oxide – co-polymer nanocomplexes in MCF-7 breast cancer and H1299 lung cancer cellular systems. Advanced instrumentations, precise experimental protocols and theoretical modelling need to be implemented for the appropriate study of the 3D multicellular networks, to both optimize and maximize the amount of information that can be successfully gathered from this new, promising biological tool.^{254 239, 255}

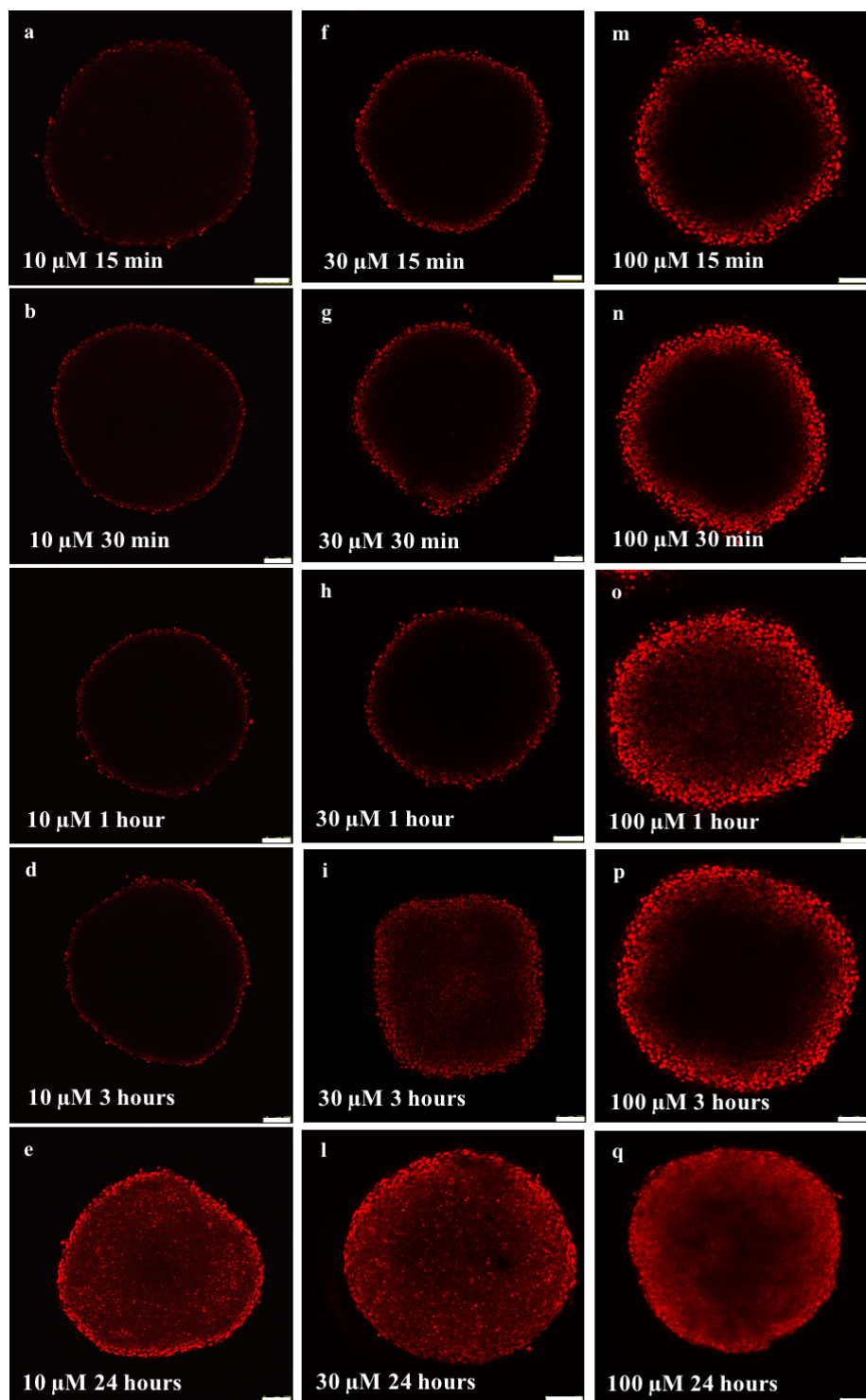


Figure 4.10 Confocal micrographs of MG-63 3D spheroids treated with free doxorubicin at concentrations of 10 μM (a-e), 30 μM (d-l), 100 μM (m-q) for different time points. Images were acquired with a 10X dry lens, at a scan speed of 10Hz and with a resolution of 1024x1024 pixels. Scale bar 100 μm .

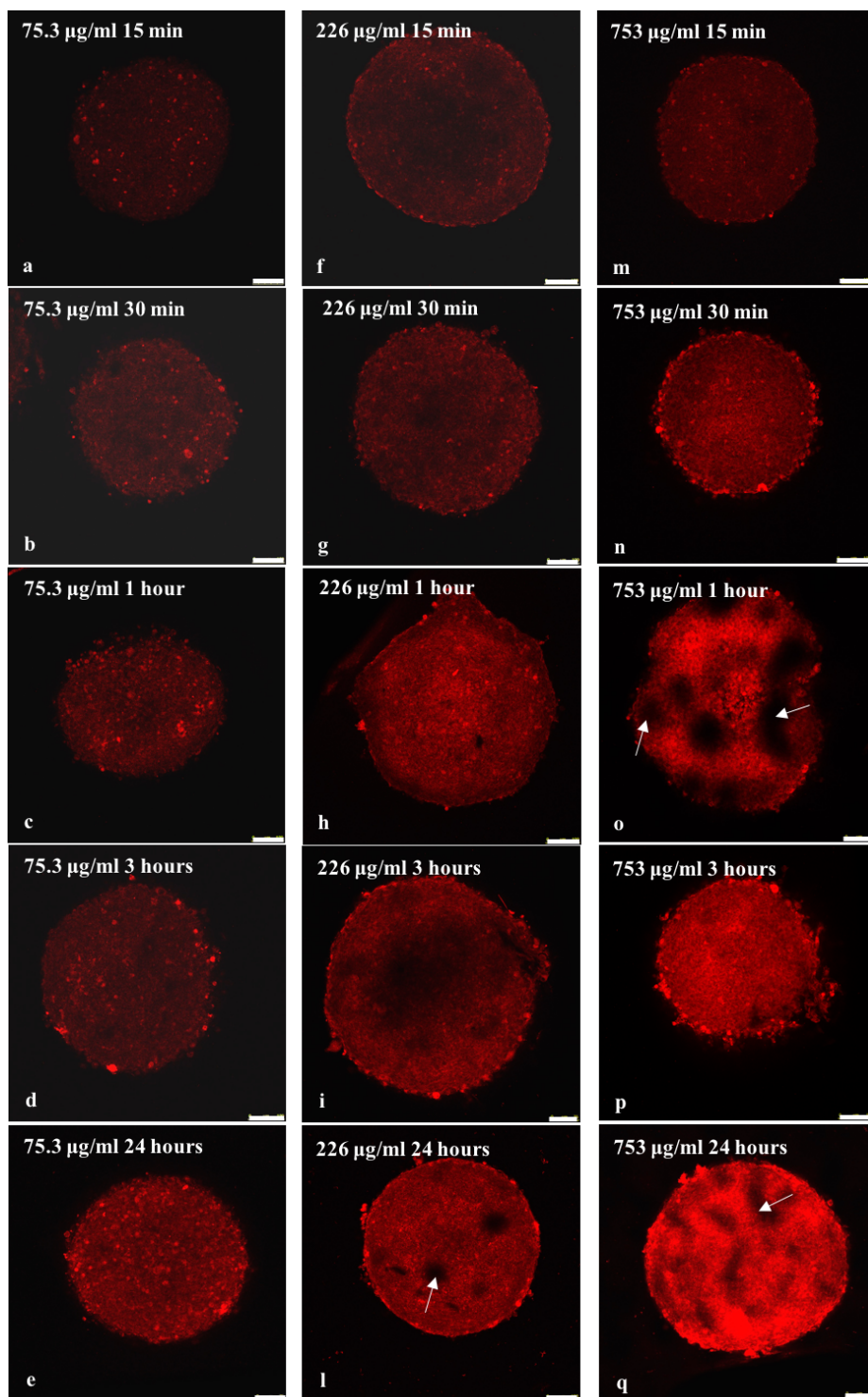


Figure 4.11 Confocal micrographs of MG-63 3D spheroids treated with Cy5.5-HGC_(0.185) NPs at concentrations of 75.3 µg/ml (a-e), 226 µg/ml (d-l), 753 µg/ml (m-q) for different time points. White arrows highlight the presence of voids in the spheroid structure, a possible result of air bubble entrapment during plating. Images were acquired with a 10X dry lens, at a scan speed of 10Hz and with a resolution of 1024x1024 pixels. Scale bar 75 µm for e, l, o, q and 100 µm for the other spheroids.

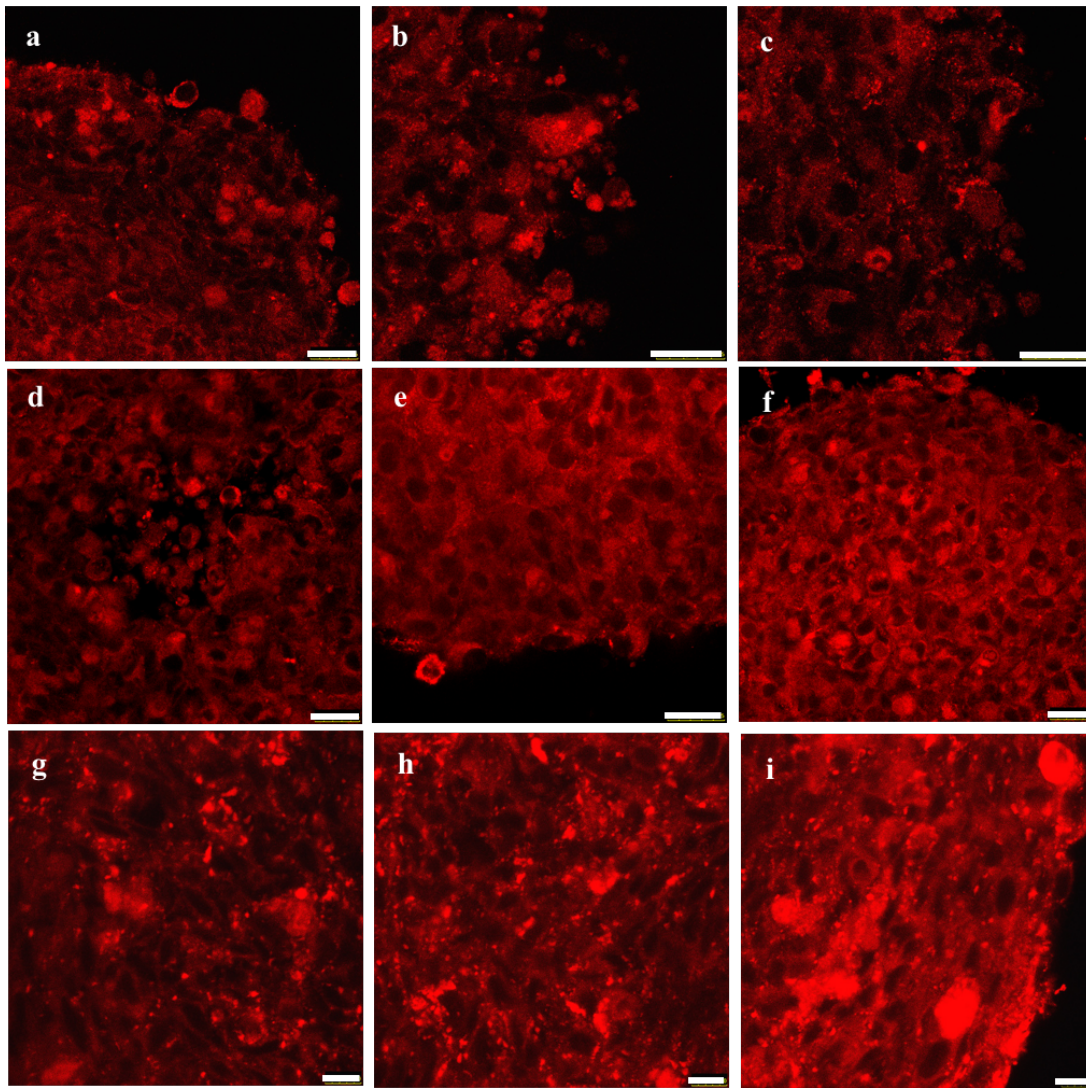


Figure 4.12 High magnification (63X) confocal micrographs of MG-63 spheroids treated with Cy5.5-HGC_(0.185) NPs at a concentration of 226 µg/ml for 1 hour (a-c) and at a concentration of 753 µg/ml for 1 hour (d-f) or 24 hours (g-i), The high magnification allows the visualization of clusters of NPs within the 3D cancer cell network. Scale bar 25 µm for a-f and 10 µm for g, h, i.

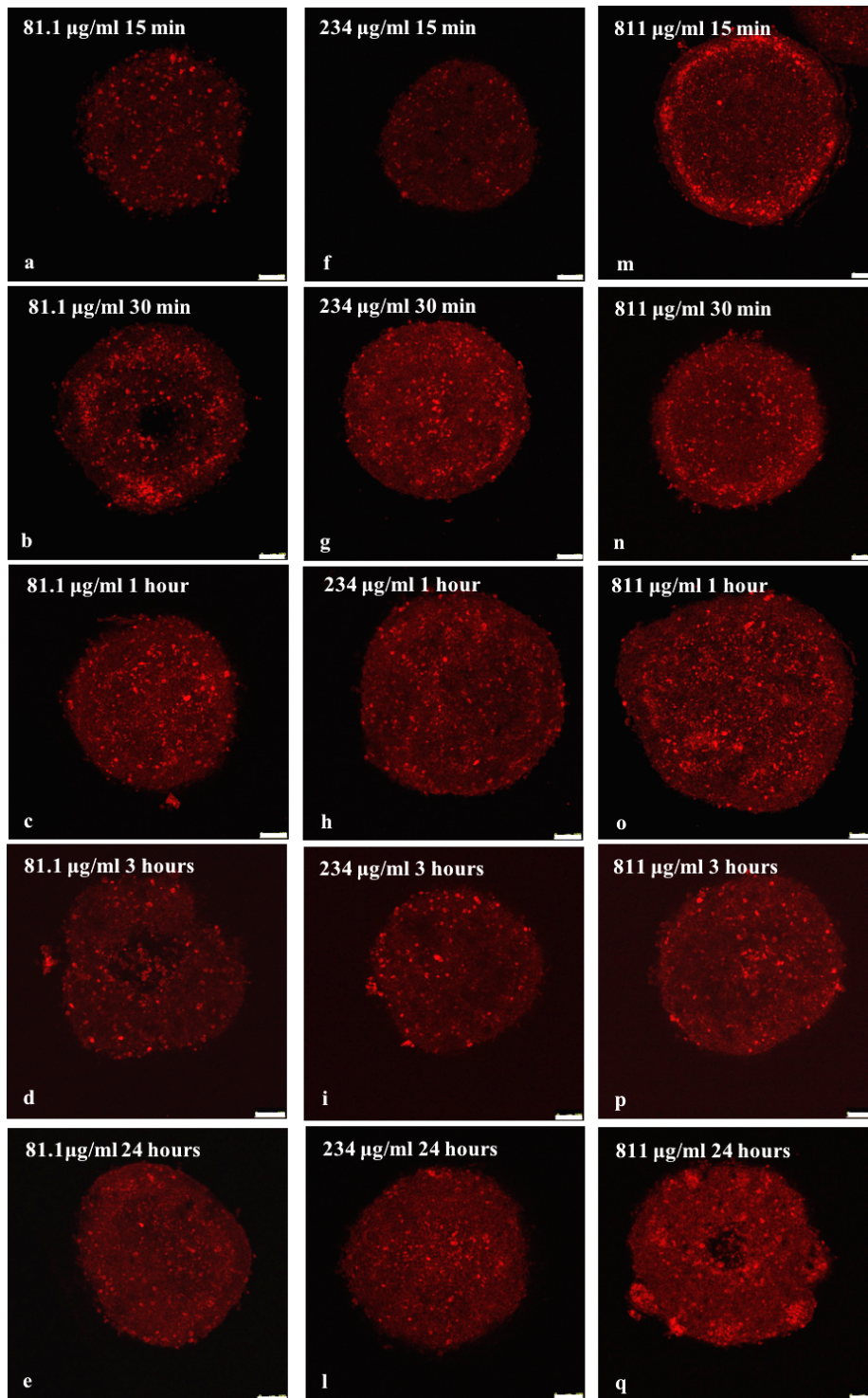


Figure 4.13 Confocal micrographs of MG-63 3D spheroids treated with doxorubicin-loaded HGC_(0.185) NPs at concentrations of 81.1 µg/ml (a-e), 234 µg/ml (d-l), 811 µg/ml (m-q) for different time points. Images were acquired with a 10X dry lens, at a scan speed of 10Hz and with a resolution of 1024x1024 pixels. Scale bar 100 µm.

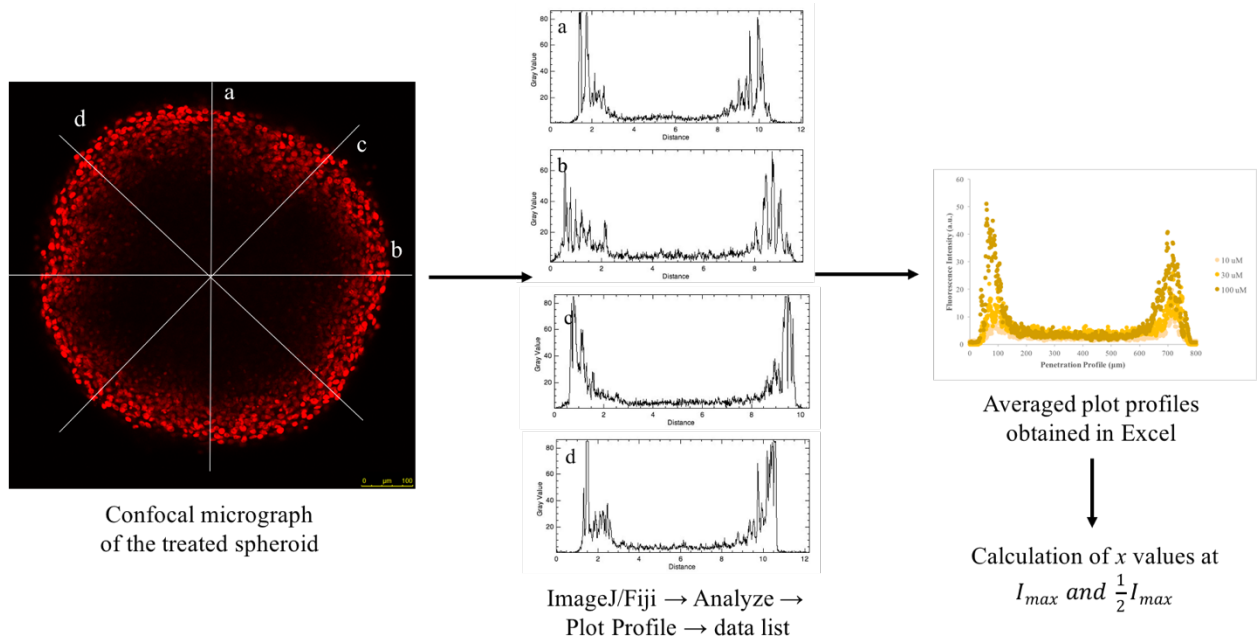


Figure 4.14 Penetration analysis protocol: intensity profiles

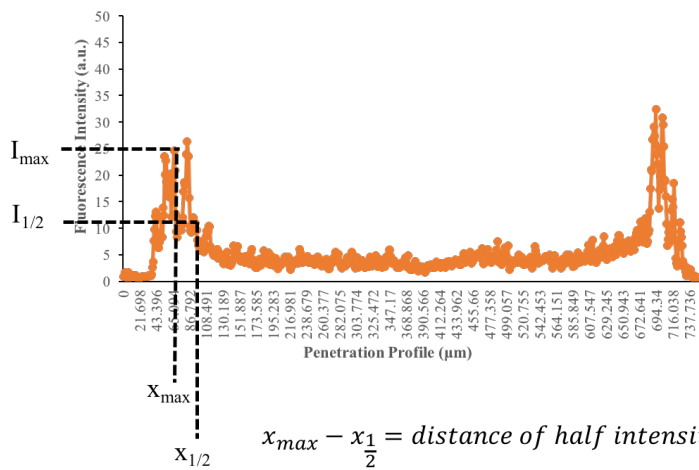


Figure 4.15 Penetration analysis protocol: data processing

If we assume an exponential decay of the intensity:

$$y = y_0 e^{-\mu(x_{max}-x)}$$

Where:
 y = intensity
 y_0 = intensity max
 x = penetration distance
 μ = inverse of penetration depth

At $y = \frac{1}{2}y_0$ we have:

$$\frac{1}{2} = e^{-\mu(x_{max}-x_1)} \cdot \frac{1}{2}$$

$$-\mu(x_{max} - x_1) = -\ln 2$$

$$\mu = \frac{\ln 2}{x_{max}-x_1} \quad \text{inverse of penetration depth } (\mu\text{m})^{-1}$$

$$x_{max} - x_1 = \text{distance of half intensity decay}$$

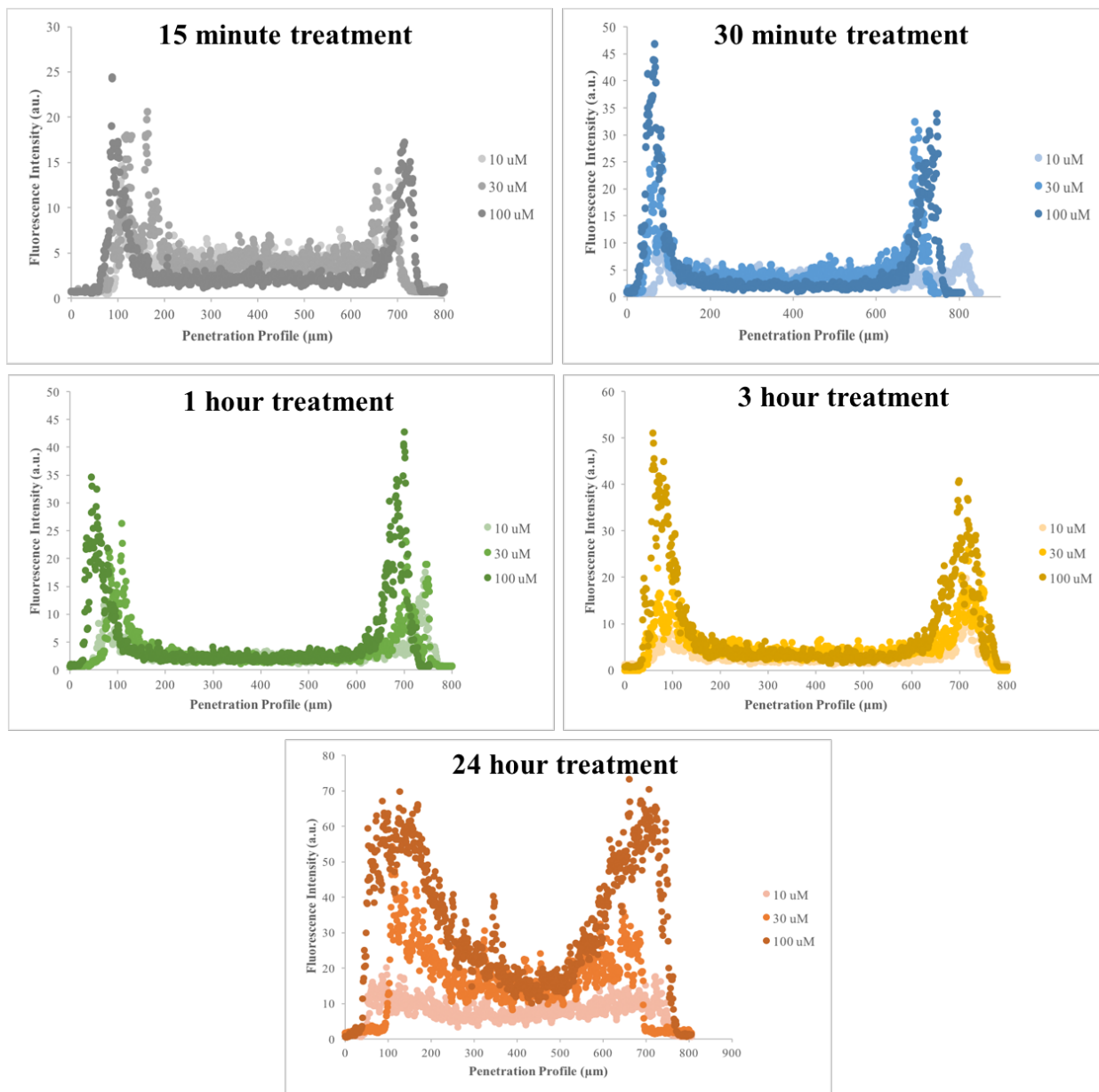


Figure 4.16 Penetration profile analysis of free doxorubicin in MG-63 3D spheroids treated for different time points. The plots were obtained from the mid cross section of the spheroids: four plot profiles, separated of 45 degrees, were drawn and analyzed in ImageJ. The average fluorescent signal was then calculated.

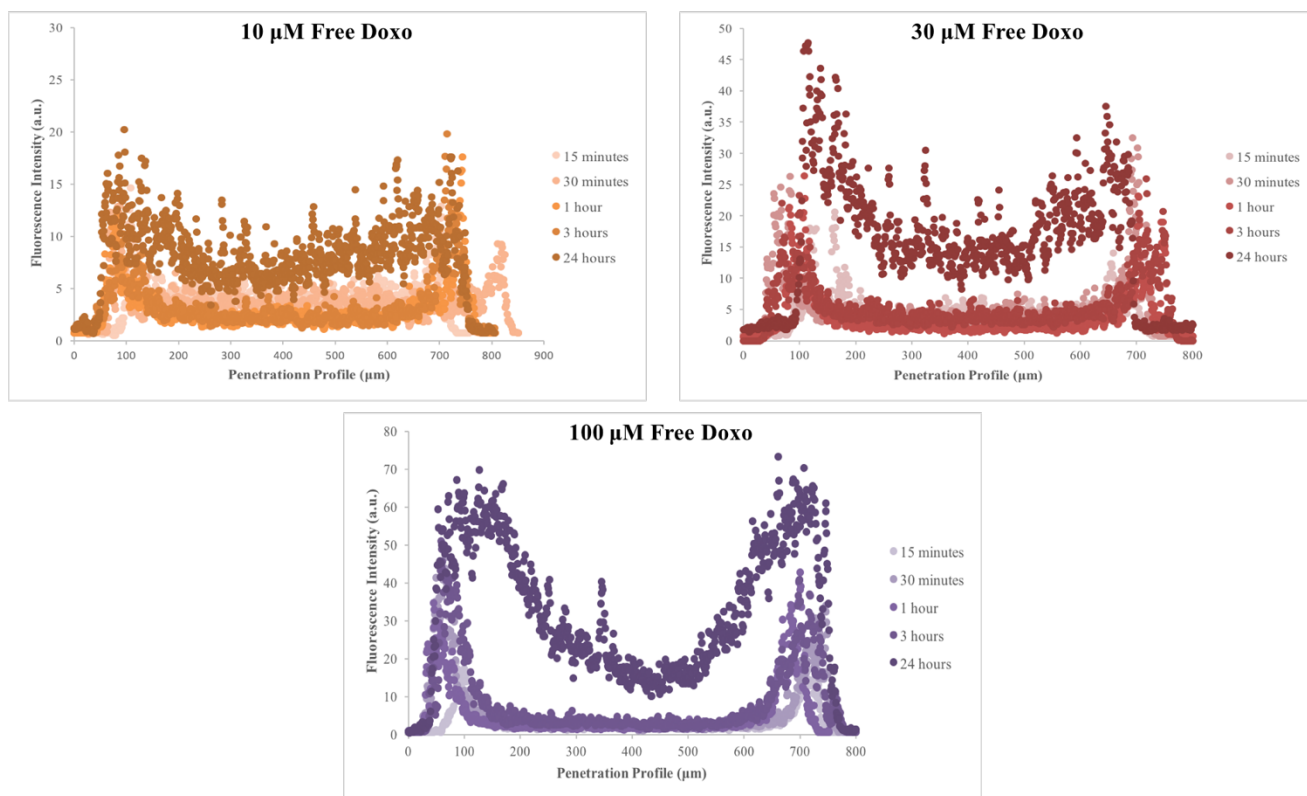


Figure 4.17 Comparison of the penetration profiles of free doxorubicin delivered to MG-63 3D spheroids at different concentrations. The plots were obtained from the mid cross section of the spheroids: four plot profiles, separated of 45 degrees, were drawn and analyzed in ImageJ. The average fluorescent signal was then calculated.

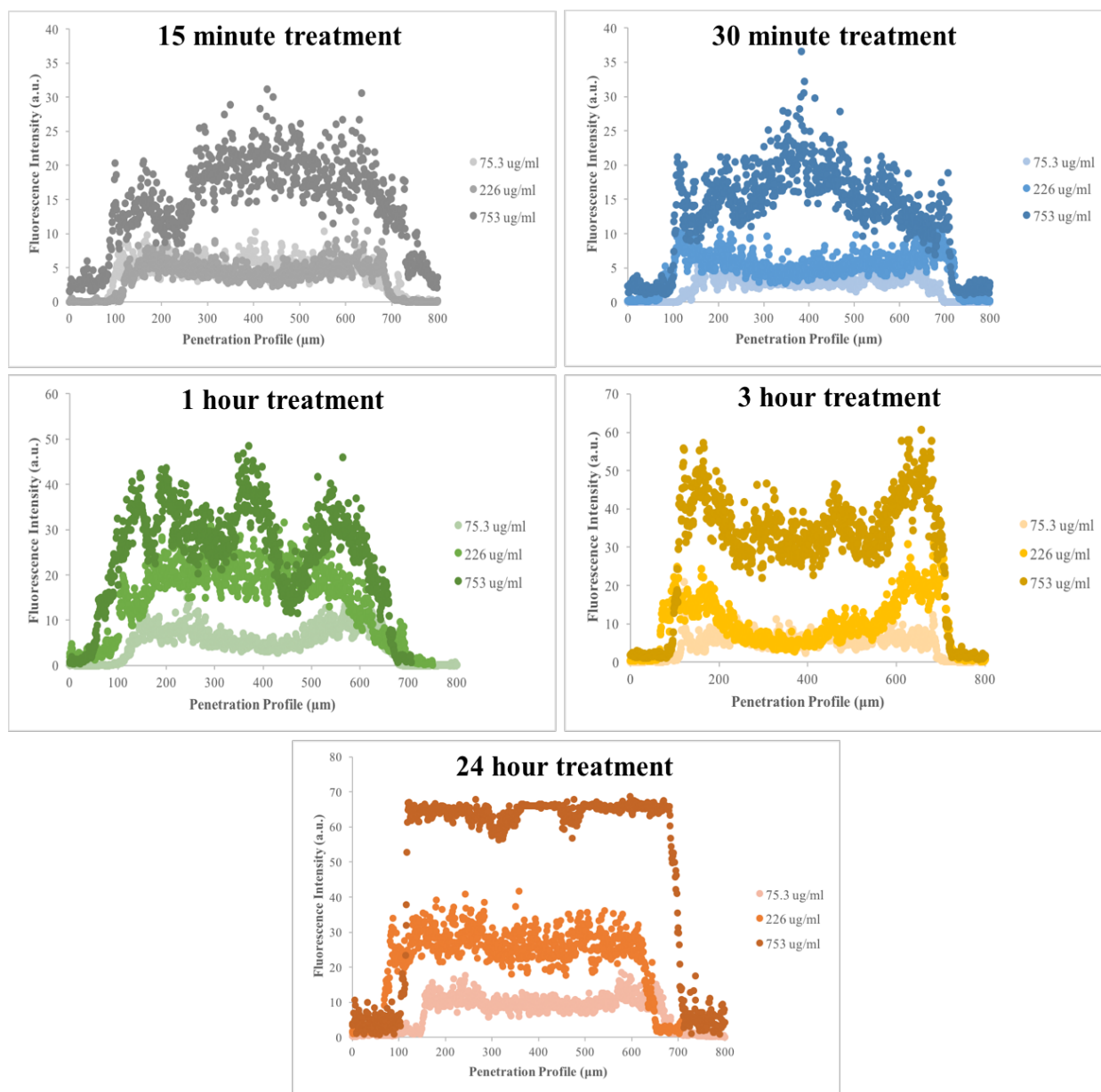


Figure 4.18 Penetration profile analysis of Cy5.5-HGC_(0.185) NPs in MG-63 3D spheroids treated for different time points. The plots were obtained from the mid cross section of the spheroids: four plot profiles, separated of 45 degrees, were drawn and analyzed in ImageJ. The average fluorescent signal was then calculated.

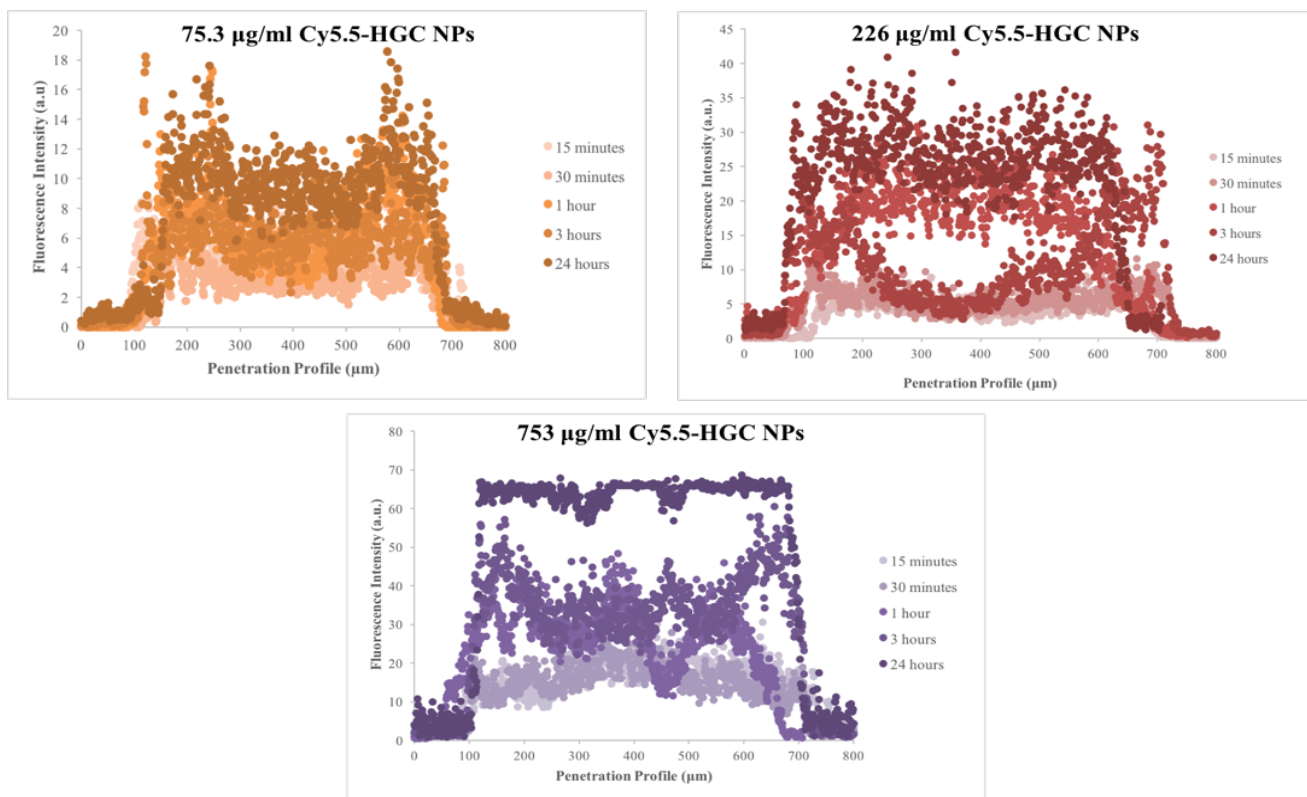


Figure 4.19 Comparison of the penetration profiles of Cy5.5-HGC_(0.185) NPs delivered to MG-63 3D spheroids at different concentrations. The plots were obtained from the mid cross section of the spheroids: four plot profiles, separated of 45 degrees, were drawn and analyzed in ImageJ. The average fluorescent signal was then calculated.

Table 4.1 Penetration profile parameters for the free doxorubicin treated spheroids

Drug conc (μM)	Treatment time	Avg I_{max} (a.u.)	Avg x_{max} (μm)	Avg $I_{1/2}$ (a.u.)	Avg $x_{1/2}$ (μm)	Avg ($x_{\text{max}} - x_{1/2}$) (μm)	$\mu = \ln 2 /$ ($x_{\text{max}} - x_{1/2}$) (μm)⁻¹
10	15 min	14.412	92.938	6.977	107.086	14.148	0.049
10	30 min	16.791	87.234	9.333	98.404	7.9785	0.087
10	1 hr	12.141	78.192	6.056	99.469	21.277	0.033
10	3 hr	16.512	73.936	8.00	87.798	13.862	0.050
10	24 hr	20.134	78.293	10.3335	131.802	53.509	0.013
30	15 min	25.359	117.453	12.229	126.887	9.434	0.073
30	30 min	20.187	69.34	10.801	94.811	25.471	0.027
30	1 hr	21.084	80.66	10.0905	97.17	16.51	0.042
30	3 hr	25.4345	88.129	12.519	109.246	21.117	0.033
30	24 hr	46.3625	86.343	23.034	146.945	60.603	0.011
100	15 min	29.692	88.757	14.561	100.489	11.732	0.059
100	30 min	30.259	65.293	14.248	96.408	31.116	0.022
100	1 hr	38.809	47.791	19.152	70.864	23.073	0.030
100	3 hr	52.059	73.962	24.709	113.684	39.722	0.017
100	24 hr	67.747	93.858	34.282	216.792	122.934	0.006

4.4 Conclusions and Future Perspectives

By mimicking the three-dimensional architecture of the cell-matrix signaling, cancer spheroids present several features of the native environment surrounding a tumor mass *in vivo*.^{191, 192, 236} Hence, these multicellular culture systems have gained recognition as powerful biological tools for the understanding of *in vivo* tumor-like development patterns.^{226, 237, 251, 259} In this study, MG-63 three-dimensional cellular assemblies were established to model and characterize avascular tumor osteosarcoma clusters in terms of morphology, size, cell population and response to different nano therapeutic treatments. Reproducible multicellular systems were obtained via a simple liquid overlay technique, which only required hydrophobic coating and subsequent orbital shaking of the culture plates. Size and morphology of the assemblies were observed to be associated to the starting cell densities, with more compact, easily handled spheroid-like masses with diameters of 500 – 700 μm obtained from 30000 – 50000 cells/well. The live-dead staining allowed the identification of a core-shell structure, with an inner region composed of oxygen and nutrient deprived, dead cells, and an outer layer of live, active cells. Moreover, confocal imaging of actin stained-samples revealed the dense and complex cell arrangement in the tumor mass. Considering those features, 3D spheroids cultures have been applied as promising screening *in vitro* method to verify the chitosan-based micelle ability to penetrate into solid tumors and exert their chemotherapeutic delivery function.

From the extensive confocal imaging study, Cy5.5-HGC_(0.185) micelle penetration was confirmed to interest most of the mass volume homogeneously, with a time- and concentration-dependency. For example, after only 1 hour of treatment with 226 $\mu\text{g/ml}$ of NPs, the fluorescent signal was spanning across the whole spheroid section. Moreover, high magnification imaging allowed the observation of nanoparticle clusters internalized in the cytosol of the MG-63 cells within the 3D network. On the other hand, free doxorubicin molecules were able to mostly permeate only the outer cellular layers of the cancer assembly, as evident from the fluorescent signal disposed to form a hollow corona in the section. The successful penetration of the chitosan-based micelles, compared to the free drug molecules, can be associated to the physicochemical characteristics of the nano vehicles (size, positive charge, surface stability, pH-responsiveness), which favor the cellular internalization and, therefore, the drug transport within the network. However, the image-based analysis seemed to only partially correlate with the volume

measurements: in fact, even though spheroids shrunk over time, no visibly significant reduction in volume was observed, compared to the control, serum starved spheroids. This outcome may lead to several interpretations: (1) the drug resistance observed might be imputable to the multicellular three-dimensional environment, in which the cellular response is differently modulated; (2) the analysis of the tumor volume does not give a complete picture of the spheroid sensitivity to the drug treatment. In fact, while considering the shedding off of the cells in the outer layer, the measurement of the size does not take into account the possible cytotoxic effect on the inner regions. In this regard, spheroid viability could be further assessed via MTS assay, after proper cell dispersion.²⁵⁹ Moreover, embedding, sectioning and staining for ECM proteins, apoptosis markers, proliferation markers or hypoxic markers, may help gaining more insight into the composition of self-assembled multicellular constructs, and the effect of the different treatments on the overall survival of the treated tumor masses.^{236, 237, 259} In addition, since acidification of the tumor extracellular matrixes, resulting from anaerobic glycolysis, has become a well-established targeting feature of the tumor microenvironment, 3D spheroid treatment under low pH conditions should be considered.^{252, 253} Lastly, the employment of more sensitive techniques, such as fluorescence lifetime microscopy, would allow a deeper understanding of the intracellular processes which occur after the drug-loaded nano-vehicles are internalized in the solid mass.^{187, 242}

To further recapitulate the physio-pathological features of the cancer masses *in vivo*, multicellular co-culture systems can be developed.^{233, 260} For example, endothelial cells or stromal cells can be introduced, to mimic the cellular heterogeneity of the tumor microenvironment and to observe how this affects nutrients and oxygen's exchange and, as a result, the size of the necrotic core. Moreover, co-cultured 3D spheroids might constitute a promising biological tool to observe cellular segregation and self-assembly into substructures and sub-regions of the tumor aggregate, and to track collective cell motility within the solid tumor mass. Those aspects can potentially either perturb or enhance the nano therapeutic penetration ability. Ultimately, by offering insights into cell-to-cell and cell-to-matrix communications, this bioengineered three-dimensional cellular model can bridge the gap between the limitations of the over-simplified monolayer cell cultures *in vitro* studies and the complexity associated with *in vivo* pre-clinical models.

Chapter 5:

Micellar nanocomplexes for local delivery of LKB1 to dictate axon development in a neuronal cultural model *in vitro*

5.1 Introduction

In a different project carried out during this thesis work in collaboration with Prof. Shelly (Department of Neurobiology and Behavior, Stony Brook University), micellar nanocomplexes have been tagged with a serine/threonine kinase molecule, involved in several developmental processes, cellular polarization processes, and in tumor progression. More specifically, the nano micelles have been functionalized with LKB1, a tumor suppressor agent, usually mutated in 20-30% of non-small cell lung cancers, involved in the regulation of the lung adenocarcinoma disease,²⁶¹ an mutated in 20% of cervical carcinoma.²⁶² Although the role of LKB1 in the epithelial-to-mesenchymal transtision process and in the metastasis formation is crucial, for the development of this specific research project we have focused our attention on the kinase functionality in neuronal cell polarization and axon formation.

During mammalian embryonic development, neuronal cells undergo polarization to form two morphologically, structurally and functionally distinct compartments, the axon and the dendrites, to serve as the brain's input/output device.^{263, 264} These classes of processes differ in terms of the molecular constituents of their cytoskeletons and their plasma membranes and are interdependent in their synaptic polarity. Axons are thin, long and uniform presynaptic processes, accountable for the release of neurotransmitters. On the other hand, dendrites are short, tapered, contain polyribosomes for protein synthesis and are exclusively postsynaptic, presenting receptors for neurotransmitters.^{263, 265, 266} Breakage of the neuroblast symmetry is a crucial step for the establishment of mature, functional neurons with bipolar morphology. Failure in neuron polarization assists a plethora of severe developmental neuropathologies, characterized by intellectual and motor disabilities, epilepsy and autism spectrum disorders.^{267, 268} In their pioneer work with dissociated hippocampal neurons, Dotti *et al.*²⁶⁵ distinguished five morphological stages for the specification of axons and dendrites *in vitro*: (1) formation of lamellopodia; (2) sprouting

of minor processes (which dynamically extend and retract); (3) outgrowth of one process, rapidly growing, which becomes the axon; (4) dendrite development; and (5) maturation of the fully polarized neuronal cell. In the past decade several studies, based on *in vitro* approaches²⁶⁹⁻²⁷⁴ and *in vivo* observations,²⁷⁵⁻²⁷⁷ have been dedicated to extensively identify the role of proteins and specific molecules in neurite outgrowth and axonal determination.^{278,279} Asymmetric organization and functional polarization of the cell membrane and cytoplasm is fundamental to neuronal development and function. The polarized architecture, which ultimately dictates axonal and dendrite fate, arises from spatial compartmentalization of specific proteins (such as phosphatases, scaffold proteins, kinases, small GTPases) to discrete regions of the cell. In addition, extracellular cues^{264, 271, 280} and stochastic fluctuation of signaling events can trigger intracellular responses that overall concur to determine axon and dendrite outgrowth. Failure in regulating protein compartmentalization may lead to aberrant polarization and, ultimately, to neurobiological disorders.

Pathways implicated in axon formation include the Par (partitioning defective) proteins. The ser/thr mammalian kinase Liver Kinase B1 (LKB1) is the mammalian counterpart of Par-4. This master kinase resides at the top of a signaling cascade that regulates asymmetric localization of Par proteins and their downstream effectors, both *in vitro*²⁸¹⁻²⁸⁵ and *in vivo*.^{275, 277} In cultured hippocampal neurons, preferential accumulation of LKB1 and its phosphorylated analogs in a single neurite has shown to initiate axon development, *via* phosphorylation of SAD (Synapses of the Amphid Defective) and MARK (Microtubule Affinity-Regulatory Kinase) kinases.^{269, 285} More specifically, LKB1 is a 436-amino acid protein, consisting of a kinase domain and a non-catalytic domain at the NH₂-terminal. The COOH terminal presents a regulatory domain, containing phosphorylation sites.²⁸² LKB1 catalytic activity is allosterically regulated by STRAD α (STe20 Related Adapter pseudokinase), an adaptor protein which stabilizes and activates LKB1 upon binding.^{277, 283} The STE20-related pseudokinase (STRAD) is an essential co-factor for LKB1 cytoplasmic activity. For example, Shelly *et al.*²⁸¹ have shown that distinct accumulation of STRAD in an undifferentiated neurite of cultured hippocampal neurons, where it co-localized with LKB1, was highly predictive of axon development of that neurite. Moreover, STRAD down-regulation was responsible for the abolishment of axon formation in cultured hippocampal neurons²⁶⁹ and in the developing embryonic cortex *in vivo*.²⁷⁷ LKB1 and STRAD form a heterotrimeric complex with the highly evolutionarily conserved scaffold protein MO25 (present

in isoforms α and β). This synergy further stabilizes STRAD/LKB1 interaction and, upon complex formation, LKB1 is activated and translocated from the nucleus to the cytoplasm.^{282, 286} Cytoplasmic activity of LKB1 leads to the activation of downstream effector kinases, such as SAD-A and SAD-B (Synapses of the Amphid Defective, mammalian homologs of Par-1), which ultimately results in axon formation *via* phosphorylation of axonal microtubule-associated protein Tau and subsequent regulation of microtubule polymerization (Figure 5.1).

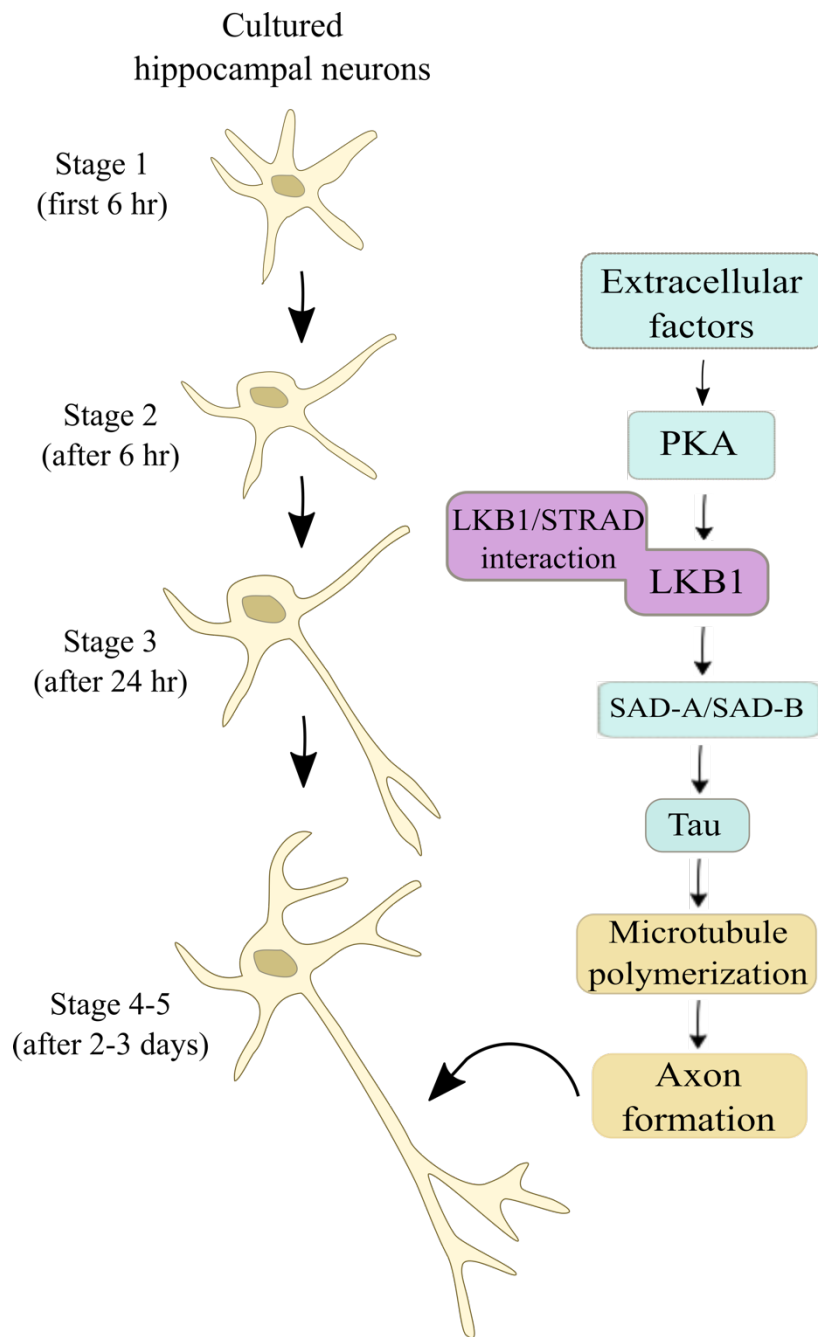


Figure 5.1 Model for local LKB1 activity in undifferentiated neurite of cultured hippocampal neurons: localized activation of LKB1, mediated by its interaction with co-factor STRAD, initiates axon development *via* local SAD and Tau phosphorylation. The resulting microtubule polymerization directs axon formation at the tip of the neurite.

Previous studies in support of the hypothesis that LKB1 signaling cascade underscores neuronal polarization have shown that (1) LKB1 often preferentially accumulated in one of the neurites of cultured hippocampal neurons, an accumulation that was highly predictive of axon development of that neurite;²⁶⁹ (2) down-regulation of LKB1 in cultured hippocampal neurons greatly reduced axon formation;²⁶⁹ (3) over-expression of LKB1 in cultured hippocampal neurons resulted in high percentage of cells that formed multiple axons, and over-expression in cortical progenitors *in vivo* resulted in increased axon formation and branching;²⁶⁹ (4) deletion of LKB1 in embryonic cortical progenitors resulted in striking absence of axon formation in neurons throughout cortical layers *in vivo*.^{269, 285} These findings highlighted the striking importance of localized LKB1 activity as instructive signal for axon formation in undifferentiated neurites. In addition, aberrant nuclear accumulation of LKB1 and abolishment of its cytoplasmic activity have been demonstrated to constitute central etiologic factors in the PMSE neuropathology (Polyhydramnios Megalencephaly and Symptomatic Epilepsy), a developmental disease characterized by epilepsy and mental/motor disability, which results in early childhood mortality.^{267, 268}

Chitosan is a natural polysaccharide material, composed of N-acetyl-D-glucosamine and D-glucosamine monomers. In the past decade, due to facile chemical tailorability, pH-responsiveness, muco-adhesiveness and biocompatibility, chitosan and its derivatives have been broadly applied for the formulation of smart platforms for drug and gene delivery.²⁸⁷⁻²⁹² Amphiphilic chitosan derivatives are known to self-assemble into micellar structures, presenting core-shell morphologies. While the hydrophobic core encapsulates an active compound, the hydrophilic shell is accountable for an efficient transport within the aqueous-based media, until the target site of interest is reached. Furthermore, the cationic nature of chitosan favors cell membrane adhesion, cell uptake and endosomal escape, hence protecting the encapsulated molecules from degradation, and assisting an efficient release in the cytosolic milieu.^{290, 293} Recently, the ability of crossing the blood-brain barrier has drawn the attention of the scientific community towards the development of chitosan-based nanotechnologies for the nose-to-brain administration of drugs and peptides, aimed to the treatment of neurodegenerative disorders.²⁹⁴⁻²⁹⁷

Magnetic nanoparticles (MNPs) have been extensively employed as imaging agents in biomedical research^{298, 299} and clinical applications.^{300, 301} Their high surface area enables functionalization with peptides, sheathing coatings, active molecules or fluorescent lipids, that

enhance MNP cellular targeting ability or facilitate their tracking both *in vitro* and *in vivo*. In the past decades, there has been an increase in the number of studies reporting MNPs applied to neuronal cells in culture, to test for biocompatibility,^{56, 302} internalization pathways and alteration of developmental processes³⁰³⁻³⁰⁷ or to develop nano-delivery systems to target CNS pathologies.^{308, 309} In addition, MNPs have been combined with various polymeric nanostructured matrixes, with the aim of obtaining hybrid nanoparticulate systems for dual imaging modality (e.g. MRI and optical, MRI and near-IR).^{60, 144, 149, 310} In this regard, MNPs can be used as contrast agents to safely evaluate *in vivo* dysfunctions associated to the blood-brain barrier, or to assess the presence of brain tumors and neuroinflammatory pathologies, with the aim of improving brain disease detection, monitoring and treatment.³⁰⁹

Direct demonstration that localized intracellular cytosolic LKB1 activity is indeed needed to instruct axon formation is currently absent. Moreover, LKB1 spatial restriction and localized activity are crucial for the establishment of a polarization process. Nowadays, leading techniques such as molecular genetics or optogenetics fail to accurately manipulate intracellular protein functions to exert an effect on a long-term developmental process. Despite being powerful tools, these approaches present major drawbacks. Cutting-edge molecular genetics techniques work on a diffusion-limited time scale and only allow a whole-cell up- or down-regulation of protein function. On the other hand, with optogenetics strategies, the maintenance of the spatial signaling pattern over time results challenging, due to the diffusion of photo-activable agents in the living cells. In addition, the difficulty in engineering light-sensitive proteins constitutes a further impediment to the optical control of cellular processes. To meet the above-mentioned challenges, one of the ultimate potential application of our engineering construct is to locally deliver LKB1, in a spatially restricted and controlled manner, to ensure the proper axon formation process.

More specifically, in this study we have designed a novel, biopolymeric-based nanotechnology for the targeted and sustained delivery of LKB1 kinase, with the purpose of locally activating LKB1 signaling cascade to direct axon formation in embryonic neurons. To facilitate LKB1 delivery and availability in the cytoplasm, LKB1 has been complexed with the polysaccharide chitosan. By combining the ability of Cy5.5-chitosan amphiphilic molecules to form biocompatible nano-micellar architectures (capable of escaping intracellular vesicle degradation pathways), with the characteristics of MNPs to allow a dual NIRF-MRI imaging modality, an innovative protein delivery system can be design and implemented.

Since localized subcellular LKB1-activity is necessary to dictate axon development in a single undifferentiated neurite, the need for a sustained intracellular delivery of the protein-activity, to dictate a complex and long-term developmental process over a physiologically relevant time scale, has been identified and address in our study.

Considering the above mentioned premises and the physicochemical properties of our micellar system we formulated the following hypotheses.

- Hypothesis (a): the liver kinase LKB1 linked to the HGC chains via avidin-biotin interaction will not modify the physicochemical and morphological characteristics of the resulting nano micelles. Moreover, the LKB1 functionality will be preserved.
- Hypothesis (b): plain HGC nano micelles and LKB1-decorated HGC nano micelles will be rapidly internalized into primary hippocampal neurons *in vitro*, without affecting the cell morphology and viability. In addition, the cytoplasmic delivery of LKB1 will enhance axon formations in primary hippocampal neurons *in vitro*.
- Hypothesis (c): as a proof of concept, to demonstrate the *in vivo* applicability of our engineered construct, plain HGC nano micelles will be delivered via *in utero* electroporation and uptaken by migrating hippocampal neurons.

5.2 Methods

Materials

Glycol chitosan (250 kDa molecular weight, degree of deacetylation > 60%), 5 β -cholanic acid, N-(3-dimethylaminopropyl)-N'-ethylcarbodiimide hydrochloride (EDC), N-Hydroxy-Succinimide (NHS) were purchased from Sigma-Aldrich (St. Louis, MO). Monoreactive hydroxysuccinimide ester of Cyanine 5.5 (Cy5.5-NHS) was obtained from Lumiprobe (Hallandale Beach, FL). Analytical grade methanol was acquired from Pharmco-AAPER (Brookfield, CT). Biotin-4-fluorescein (B4F) is obtained from Biotium (Hayward, CA). Anhydrous dimethyl sulfoxide (DMSO) is purchased from EMD Chemicals (Darmstadt, Germany).

Synthesis of hydrophobically modified glycol chitosan (HGC)

The hydrophobic modification of glycol chitosan (GC) with 5- β -cholanolic acid is carried out following the procedure presented by Chin *et al.*²¹³ Briefly, glycol chitosan (500 mg) is dissolved in HPLC water (60 ml). In a separate beaker, 5 β -cholanolic acid (150 mg), N-hydroxysuccinimide (NHS, 72 mg) and N-(3-Dimethylaminopropyl)-N'-ethylcarbodiimide hydrochloride (EDC, 120 mg) are dissolved in methanol (60 ml). The hydrophobic modification is completed by slowly adding the cholanic activated solution to the glycol chitosan solution. The mixture is kept under stirring for 24 hours at room temperature, to allow the formation of an amide linkage. To eliminate the unreacted cholesterol molecules and the by-products of the reactions, the mixture is loaded into dialysis cassettes (10 kDa molecular weight cut off, ThermoScientific) and dialyzed for 24 hours against HPLC water : methanol (1:4, v/v) and for additional 24 hours against distilled water. The purified system is centrifuged for 30 minutes at \sim 3000 rpm and lyophilized for 3 days to obtain the GC-5- β -cholanolic acid conjugate (HGC), and then finely ground into powder. The HGC is labeled with a cyanine dye that emits in the near-infrared range ($\lambda_{\text{ex}} = 673$ nm, $\lambda_{\text{em}} = 707$ nm). The powdered conjugate (100 mg) is dissolved in dimethyl sulfoxide (DMSO, 40 ml). Subsequently, a solution of Cy5.5-NHS (1 mg) in DMSO (250 μ l) is added drop-wise. The resulting blue solution is kept in the dark and stirred for 6 hours at room temperature. The activated NHS-ester of the cyanine dye reacts with the free amine on the HGC chain to form an amide bond. After dialysis for two days against HPLC water in dialysis cassettes (10 kDa molecular weight cut off, ThermoScientific), the purified precipitate is freeze-dried and an intense blue powder is obtained.

Synthesis of Cy5.5-HGC-BF4

Functionalization of the base HGC material is carried out via avidin-biotin interaction, following a series of steps, which can be considered as modifications of the synthesis process presented above. First, 500 mg of glycol chitosan (GC) are dissolved in 60 ml of HPLC water. In a Falcon tube, 17 mg of sulfo-NHS-LC-biotin are dissolved into 2 ml of HPLC water and consequently added drop-wise to the GC solution. The mixture is let stir for 3 hours at room Temperature and then loaded in into dialysis cassettes (10 kDa molecular weight cut off, ThermoScientific) to dialyzed for 48 hours against HPLC water. The dialyzed biotinylated glycol chitosan (BGC) is freeze-dried and ground into fine powder. In the second step, 300 mg of BGC are dissolved into 50 ml of HPLC water. In a Falcon tube, 80 mg of avidin are dissolved into 15

ml of HPLC water and consequently added drop-wise to the BGC solution. The mixture is let stir for 2 hours at room Temperature and then loaded into filtered Amicon tubes (100 kDa molecular weight cut off, Amicon). After centrifugation at 5000 g for 30 minutes, the filtrate is removed from the membranes and diluted with HPLC water. The avidinated-biotinylated glycol chitosan (AB-GC) is freeze-dried and ground into fine powder. The third step of the synthesis consists in the hydrophobic modification of the AB-GC, by addition of 5 β -cholanic acid. Briefly, 200 mg of AB-GC are dissolved into 25 ml of HPLC water, while 60 mg of 5 β -cholanic acid are dissolved into 25 ml of methanol, and activated with 48 mg of EDC (N-(3-Dimethylaminopropyl)-N'-ethylcarbodiimide hydrochloride) and 29 mg of NHS (N-hydroxysuccinimide). The activated methanol solution is slowly added into the AB-GC solution and mix over night at room Temperature. The mixture is loaded into dialysis cassettes (10 kDa molecular weight cut off, ThermoScientific) and dialyzed for 24 hours against HPLC water : methanol (1:4, v/v) and for additional 24 hours against distilled water. The dialyzed AB-HGC compound is freeze-dried and ground into fine powder. The AB-HGC is dissolved in DMSO at a concentration of 1.5 mg/ml. To couple Cyanine 5.5 NHS ester onto the amine groups of the AB-HGC molecules, 100 μ l of 5 mg/ml stock solution of Cy5.5 NHS in DMSO are added drop-wise. The mixture is stirred for 6 hours in the dark at room Temperature. Consequently, biotinylated Fluorescein (B4F, 10 mg/ml in DMSO) is added drop-wise to the Cy5.5-AB-HGC mixture and the system is kept under stirring for additional 2 hours, in the dark at room Temperature. To remove unbound biotinylated fluorophore, dialysis against HPLC water (10 kDa molecular weight cut off, ThermoScientific) is performed. The resulting Cy5.5-HGC-B4F compound is lyophilized and finely ground into powder. This synthesis was performed with the kind and precious help of Weiyi Li.

Synthesis of HGC-LKB1

Functionalization of the base HGC material with LKB1 kinase is carried out via avidin-biotin interaction, following a series of steps. First, 1 ml of a 0.5 mg/ml solution of sulfo-NHS-LC-biotin is added to a water-based lysate of LKB1. The mixture is stir for 3 hours at room Temperature and then transferred to a dialysis cassette (3.5 kDa molecular weight cut off, ThermoScientific). To remove unbound biotin, dialysis is performed against HPLC water for 48 hours. Biotinylated LKB1 is unloaded from the cassette and stored. One ml of AB-HGC suspension (see previous paragraph) (2.5 mg/ml in DMSO) is placed in a dialysis cassette (3.5 kDa molecular weight cut

off, ThermoScientific) and dialyzed against HPLC water for 48 hours to remove the DMSO. The biotinylated LKB1 solution (2.5 ml) is added drop-wise to the dialyzed AB-HGC solution in water and the mixture is stir for 2 hours. Then, the resulting compound is transferred to filtered Amicon tubes (10 kDa molecular weight cut off, Amicon) and centrifuged at 13000 g for 3 minutes. The centrifugation step is repeated 3 times, to obtain a final volume of 250 μ l of filtrate, containing 2.5 mg of HGC-LKB1. The success of the functionalization was confirmed through immunoblotting. This synthesis was kindly performed by Weiyi Li.

Polymeric nanocomplex preparation

Cy5.5-labelled 5 β -cholic acid-glycol chitosan conjugates are re-suspended in distilled water at a concentration of 1 mg/ml and vortexed for a few minutes. The water-powder suspension is then sonicated with a probe-type sonifier for 3 times (2 minutes each, continuously) and for 2 times (5 minutes each, continuously). The system is kept under ice bath, to prevent sudden increase in Temperature. The self-assembled Cy5.5-HGC nanoparticles are passed through syringe filters (pore sizes 0.8 and 0.2 μ m, Pall Corporation) as a sterilization method for the following cell culture delivery.

SPIONs-HGC nanocomplex preparation

Nano-screenMAG-ARA nanoparticles are purchased from Chemicell (Chemicell GmbH, Germany). These superparamagnetic nanoparticles present a Fe₂O₃ magnetic core, a fluorescent lipid layer ($\lambda_{ex,max}$ = 378 nm, $\lambda_{em,max}$ = 413 nm) and a glucuronic acid coating. In order to encapsulate the SPIONs into the polymeric micelles, a sequence of steps is needed (Figure 5.2), consisting of (1) preparation of different stock solutions; (2) mixing of the components to obtain the desired concentrations and (3) probe-type sonication to favor the self-assembly of the SPIONs-loaded biomagnetic micelles. In order to prevent the aggregation of the magnetic nanoparticles, Pluronic P127 is used as a surfactant: 1 ml of glucuronic acid-SPION suspension (15 mg/mL, in HPLC water) and 1.1 ml of Pluronic P127 solution (20 mg/mL; in HPLC water) are mixed in a Falcon tube. The mixture is then vortexed and bath sonicated for 15 minutes, to achieve a homogeneous suspension. In this step, the mass ratio of Pluronic P127 : SPIONs is 1.46 (based on the experimental method proposed by Balan *et al.*³¹¹). Next, the glucuronic acid-SPIONs-Pluronic mixture is diluted in the serum free Neurobasal media, containing Cy5.5-HGC conjugates, in order

to obtain a desired final concentration of 0.25 mg/ml of Cy5.5-HGC-B4F, 0.25 mg/ml of glucuronic acid-SPIONs and 0.36 mg/ml of Pluronic P127. The final step of the fabrication process consists in the probe-type sonication for 3 cycles of 2 minutes each and for 2 cycles of 5 minute each, consequently. The self-assembled biomagnetic nanocomplexes are passed through syringe filters (pore sizes 0.8 and 0.2 μm , Pall Corporation) as a sterilization method for the following cell culture delivery.

Micelle characterization

The morphology was obtained by placing few drops of HGC and HGC-LKB1 nanoparticle suspension on Lacey Carbon Film on 300 mesh copper grids and the extra solution is blotted with filter paper and air dried. The grids are observed under the Transmission Electron Microscope (JEM-1400LaB6, 120keV TEM, JEOL) with an accelerating voltage of 60kV. The size distribution of the HGC and HGC-LKB1 nanocomplex suspensions were determined at 25 °C by Dynamic Light Scattering (DLS, Zetasizer Nano, Malvern Instruments Ltd., Westborough, MA). The characterization of the HGC vehicles is carried out at the Center for Functional Nanomaterials at Brookhaven National Laboratory.

To evaluate the preservation of the LKB1 kinase activity, a biochemical assay using HeLa cells was performed. These cells do not express endogenous LKB1, SAD-A or SAD-B, but present kinase co-factors, such as STRAD α and MO25 α . After 48 hr of transient transfection for Tau and SAD-A, cell lysate was collected and incubated for 2 hr with HGC-LKB1 micelles or with HGC plain micelles. Tau phosphorylation was detected by immunoblotting with an antibody specific for the phosphorylation site of Tau at Ser-262.

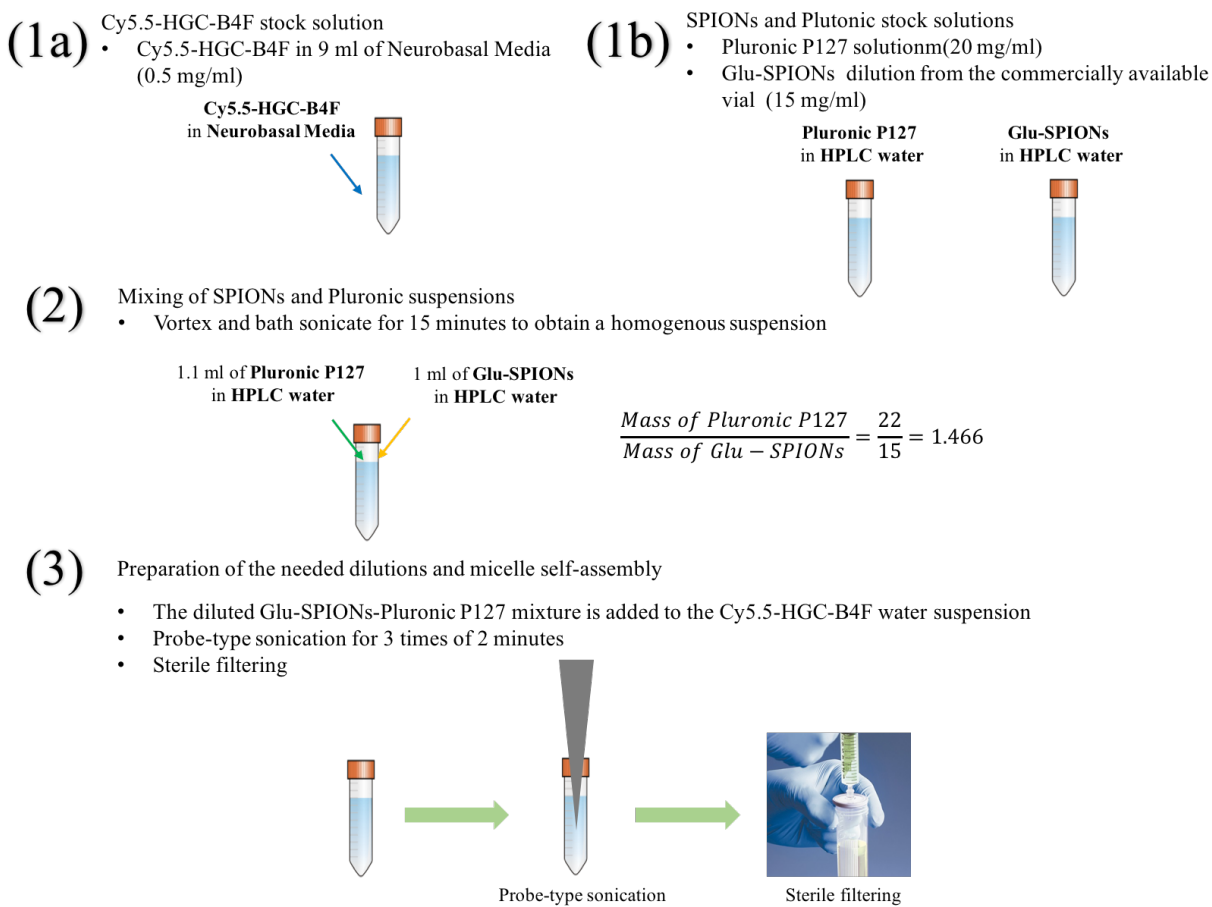


Figure 5.2 Fabrication process of the SPIONs-loaded Cy5.5-HGC-B4F micellar complexes

Hippocampal cell culture and nanocomplex delivery in vitro

To evaluate the suitability of the chitosan-based nanoparticulate system as delivery platform for neuronal cells, embryonic E19 primary rat hippocampal neurons were treated with Cy5.5-HGC plain nanocomplexes. For this first experiment, cells were plated on poly-L-lysine coated coverslips and let attach for 3 hours in Neurobasal media, supplemented with B27, Glutamax and 10% Fetal Bovine Serum (FBS). Afterwards, cells were washed with Neurobasal serum free media and treated with 500 µg/ml of Cy5.5-HGC NPs, under serum free conditions, to avoid nanoparticle clustering in suspension, which could potentially limit cellular uptake. At desired time points, samples were gently rinsed with Phosphate Buffer Saline (PBS) to wash away unbound NPs and fixed with 4% paraformaldehyde for 20 minutes, following mounting in Fluoromount G media onto glass slides. Confocal imaging was performed to observe the NP uptake and the intracellular distribution. In order to assess the effect of MNPs on primary rat hippocampal neurons, an uptake experiment was conducted. Superparamagnetic iron oxide nanoparticles, of 200 nm in diameter, presenting a Fe₂O₃ core, a glucuronic acid shell and a DAPI-labelled lipid coating, were delivered at a concentration of 0.25 mg/ml, under serum free conditions. The cell culture procedure was carried out as mentioned in the previous paragraph. Confocal imaging under DAPI and DIC filters allowed the visualization of the MNPs' uptake pattern. To assess the cellular uptake and the possible co-localization of the three components of the multifunctional nanoparticle (HGC matrix, B4F pendant and encapsulated SPIONs), a delivery experiment was carried out. Embryonic E19 rat hippocampal neurons were plated on poly-L-lysine coverslips and let attach overnight in Neurobasal media supplemented with B27, Glutamax and 10% FBS. Cells were treated with Cy5.5-HGC-SPIONs-B4F nanoparticles for up to 30 hours, under serum free conditions. Afterwards, samples were fixed with 4% paraformaldehyde and mounted on glass slides for confocal imaging observation.

Hippocampal cell culture staining and confocal imaging analysis

To investigate if either the micellar system under study or the magnetic nanobeads were exerting an effect on the morphological development of the neuronal cells, analysis of the neuritic processes was performed. First, primary E19 rat hippocampal neurons were cultured on PLL-coated glass coverslips, placed in 35 mm dishes and immersed into Neurobasal media supplemented with B27, for 2 hours at 37 °C. Afterwards, the following treatments were

considered: (1) Cy5.5-HGC NPs for 18 hours and for 24 hours at a concentration of 0.5 mg/ml; (2) DAPI-glucuronic acid-SPIONs complexed with Cy5.5-HGC-B4F NPs for 24 hours at a concentration of 0.125 mg/ml. At the desired time points samples were fixed with 4% paraformaldehyde for 20 minutes, permeabilized with 0.1% Triton X-100 and blocked with 10% normal goat serum for 2 hours. Cells were then incubated for 1 hour with primary antibody for Tuj-1, a neuron-specific β -tubulin, evenly dispersed throughout the cell. After incubation with FITC-labelled secondary antibody for 30 minutes, samples were washed with 1X phosphate saline buffer and mounted for confocal imaging. Random sampling of immunostained cells were considered. Images were subsequently analyzed using Fiji/ImageJ software, by tracing the cell processes with segmented lines. Statistics was performed considering the following parameters: the three longest neurites, the average neurite number, the average neurite length and the average total length of neurite per cell of each sample. Averages and standard errors were reported for a pool of about 80-90 cells per condition.

With the aim of observing the effect of HGC-LKB1 nanocomplexes on the neuronal culture development in vitro, primary rat hippocampal cells were plated on PLL-coated coverslips and let adhere for 5 hours. HGC-LKB1 NPs were delivered at a concentration of 0.6 mg/ml for 60 hours. Samples were fixed with 4% paraformaldehyde for 20 minutes, permeabilized with 0.05% Triton X-100 in PBS for 10 minutes and blocked with 10% normal goat serum in PBS for 10 minutes. Cells were then incubated with a primary antibody at 4 °C overnight in the blocking solution. Mouse Smi-312 (staining for neurofilament and axonal processes) and Rabbit Tuj (staining for the neuron specific class II β -tubulin) were used as primary antibodies, as dilutions of 1:1000. The next morning, after being washed for 3 times with PBS, samples were incubated with a secondary antibody for 1 hour in PBS at a dilution of 1:1000. Afterwards, coverslips were mounted on glass slides and confocal images at 40X were acquired. Cell tracing was used to assess the presence of axon and dendrite processes. The immunostaining was kindly performed by Dr. Tanvir Khan, while the confocal acquisition was kindly performed by Dr. Maya Shelly.

In utero electroporation of nanocomplexes

In order to deliver in vivo the polymeric micelles, in utero electroporation was performed. Briefly, the day, when animals were mated, was defined as embryonic day Zero (E0). A timed-pregnant Sprague Dawley rat at E17 was deeply anesthetized with isoflurane and its uterine horns

were exposed by laparotomy. The Cy5.5-HGC micelle suspension (500 $\mu\text{g/ml}$) was mixed with Fast Green dye (0.3mg/ml) and loaded to our injection system consisting of a 32G hypodermic needle, syringe and a pico-liter injector (Warner instruments). Approximately 1~2 μl of the chitosan micelle suspension were injected through the uterine wall into the lateral ventricles of each embryo. After the injection procedure, the uterine horns were returned to the abdominal cavity and the open belly sutured. The embryos were allowed being given a birth and sacrificed at postnatal day 2 for the tissue preparation. The procedure, depicted in Figure 5.3, was kindly performed by Dr. Seong-il Lee.

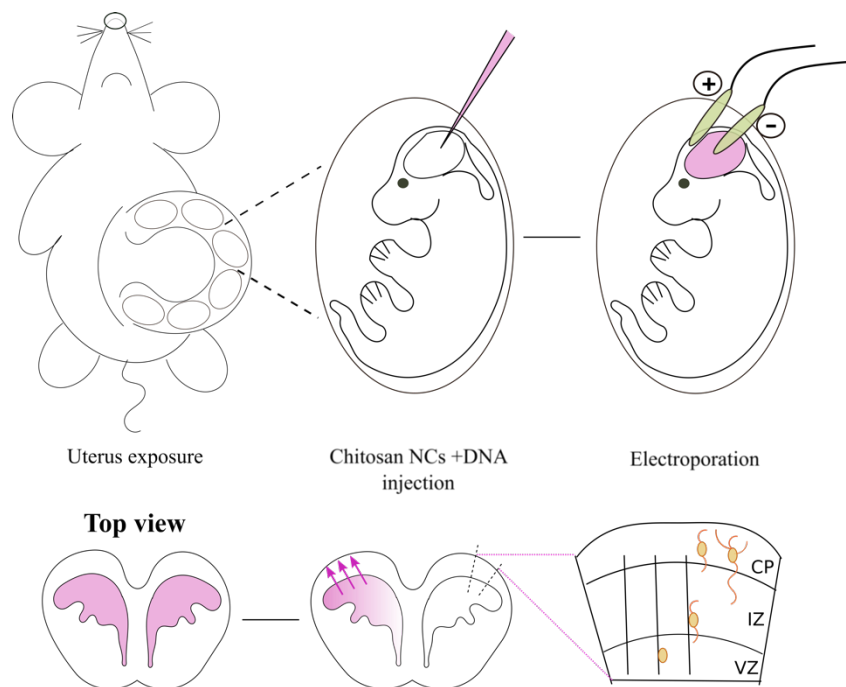


Figure 5.3 Schematic depicting the *in utero* electroporation procedure. First, the uterus of the pregnant rat mother is exposed by laparotomy. Subsequently, the injection into the lateral ventricles of plasmid DNA and chitosan nanocomplexes is carried out by means of a sharp tip. Electroporation (30-50 V) is performed with two electrodes, to temporarily disrupt the cell membrane and favor the passage of the macromolecules through the pores. The embryos are placed back in the abdominal cavity.

5.3 Results and Discussion

LKB1-chitosan nanocomplexes have been synthesized through biotin-avidin interaction and the system retains its kinase functionality

Our system is based on the use of a biocompatible polysaccharide matrix, glycol chitosan, modified with a cholesterol moiety, to form amphiphilic molecular chains able to self-assemble into nano-micelles with core-shell structure upon mixing in an aqueous environment.²¹³ The hydrophobic core would act as a reservoir for cargo molecules or other functional components, while the hydrophilic shell is accountable for the stability of the micellar structure in water-based milieu (e.g. cytoplasm). The facile chemical tailorability of the system allows further functionalization with biomolecules *via* biotin-avidin interactions. Considering this synthesis strategy, LKB1 was complexed to our basic hydrophobic modified glycol chitosan micelles through a series of reaction steps (Figure 5.4). The use of the water soluble glycol chitosan (GC) as starting material allowed the reagent manipulation in a water-based environment. First, GC was conjugated to sulfo-NHS-LC-biotin through the formation of amide linkages at the primary amines of the D-glucoamine residues. The LC moiety would act as a spacer for the following functionalization, limiting the allosteric interactions between the micellar matrix and the LKB1 functional element. In a second step, the water-soluble biotinylated glycol chitosan (BGC) is let reacting with avidin, to allow the formation of the first biotin-avidin bond. Subsequently (Step 3, Figure 5.4), a cholesterol-derivative, 5 β -cholanic acid, is conjugated to the avidinate-biotinylated glycol chitosan (AB-GC), to yield a hydrophobic modified compound (AB-HGC). The presence of small, rigid cholanic molecules confer an amphipathic character to the system. In fact, while the hydrophilic biotin-avidin pendants and the glycol residues on the main backbone favor water solubility, the hydrophobic cholanic acid repels water molecules and grants the self-assembling capabilities to the polymeric chains. In the final reaction (Step 4, Figure 5.4), the resulting amphiphilic system is dispersed in water and let reacting with biotinylated-LKB1, previously purified from cell lysate. Multiple centrifugations allow the separation of HGC-LKB1 nanocomplexes, linked via biotin-avidin-biotin sandwich chemistry, in a pellet form. Probe-type sonication of the bio-polymeric compound yields to self-assemble micelles with a spheroid-like structure and with an average diameter of 285.46 ± 5.33 nm. Such morphological features would likely favor the cellular uptake *via* macropinocytosis, a non-specific endocytic process involving

cell membrane ruffling and usually not resulting in endosomal digestive pathways.

To evaluate whether the LKB1 kinase activity is preserved on the engineered nanocomplexes, an *in vitro* bioreactor-like assay was developed. HeLa cells, not expressing endogenous LKB1, were transiently transfected for 48 hr with various combinations of cDNAs encoding for STRAD α (LKB1 co-factor), for MO25 and for SAD-A and Tau (LKB1 down-stream effectors). Afterwards, cell lysates were prepared and incubated, for 2 hr under gentle agitation, with plain or LKB1-decorated HGC micelles. To initiate its polarization signaling cascade, LKB1 has to activate SAD-A, which subsequently would phosphorylate Tau at the Serine 262 residue (according to Barnes *et al.*²⁸⁵). The immunoblotting results reported in Figure 5.5 show that *only* when HeLa cells are co-transfected with STRAD α , SAD-A and Tau and their lysate buffer is treated with LKB1-chitosan nanocomplexes, a band for phosphorylated Tau at Ser262 appears (the corresponding lane is highlighted by a red rectangle in Figure 5.5). This striking result not only corroborates the preserved kinase functionality of the synthesized bio-polymeric micelles, but also reinforces the crucial role of the LKB1/STRAD α complex synergy in firing the polarization signaling cascade. This result is in accordance with previous works, where the complex formation between STRAD and LKB1 was essential factor for the master kinase activation.^{269, 277} Furthermore, the gel electrophoresis experiment underlined the chemical stability of the designed nanocomplexes. In fact, no unbound LKB1 was detected as free after 2 hours of lysate incubation for the case of the samples treated with HGC-LKB1 (Figure 5.5, IB : LKB1 panel), validating the success of our synthesis approach and indicating the prolonged stability of HGC-LKB1. Based on these outcomes, HGC-LKB1 micelles would be easily internalized by neuronal cells and remain active in the cytoplasm, exerting their sustained kinase function for up to 24-48 hours, a sufficient time for axon formation. The *in vitro* delivery of the kinase-decorated NPs, presented in the following paragraphs, will constitute an additional validation of the immuno-precipitation assay: LKB1 remains active and promotes multiple axon formation in primary hippocampal cells within 72 hours of their development (see Figures 5.12-5.13).

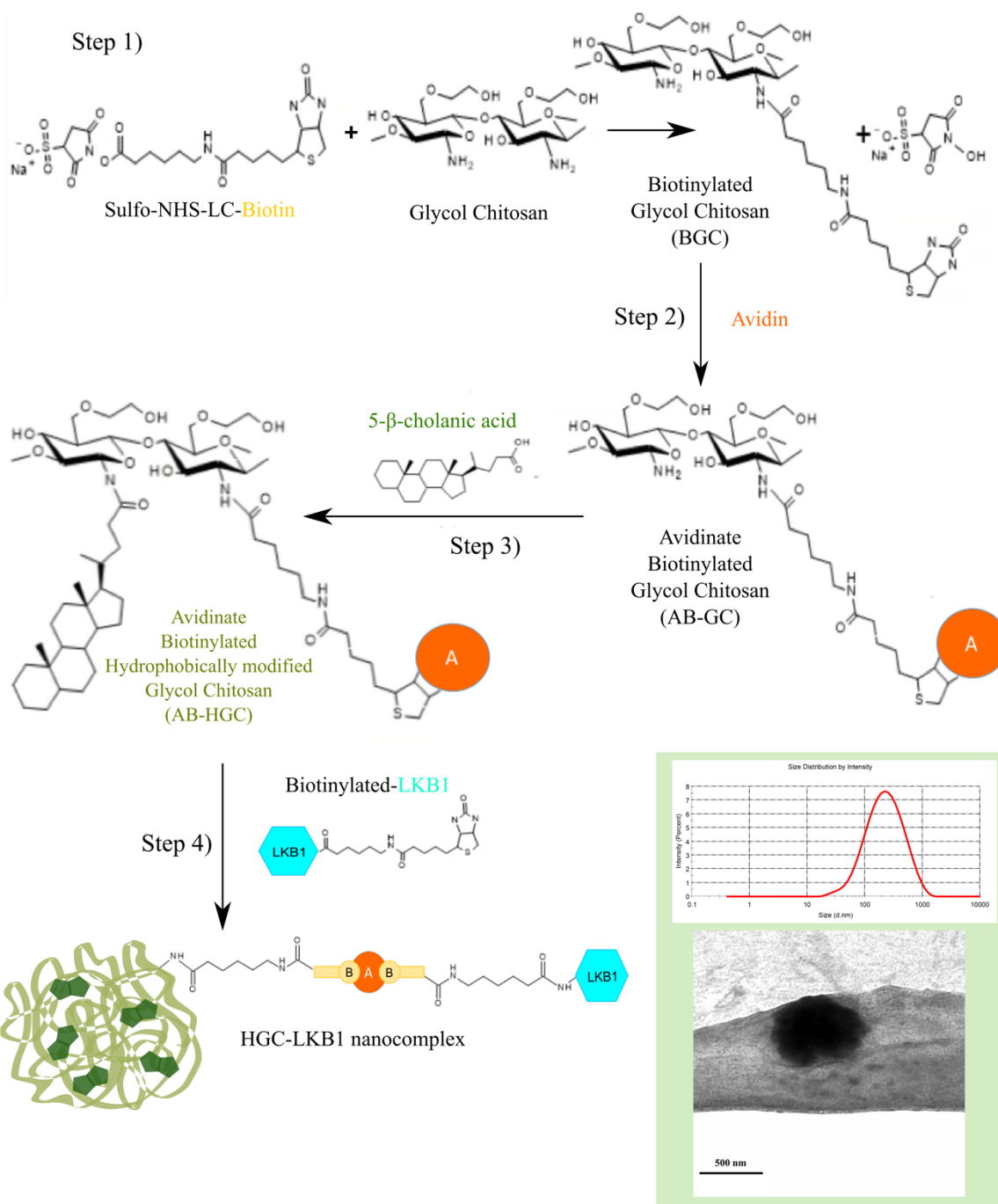


Figure 5.4 Synthesis of HGC-LKB1: (1) glycol chitosan is biotinylated in water with sulfo-NHS-LC-biotin to form BGC; (2) the first biotin-avidin bond is allowed to form in water, by mixing for 2 hours the dialyzed and lyophilized BCG product with avidin; (3) the resulting material is hydrophobically modified *via* reaction with 5-β-cholanic acid in methanol, in the presence of NHS and EDC as catalyzers; (4) a water-based solution of biotinylated-LKB1 is added drop-wise to the avidinate-biotinylated HGC suspension and let stir for 2 hours, to assist the formation of the second biotin-avidin bond. The final product is collected after centrifugation. The inset reports a representative DLS measurement and a TEM micrography.

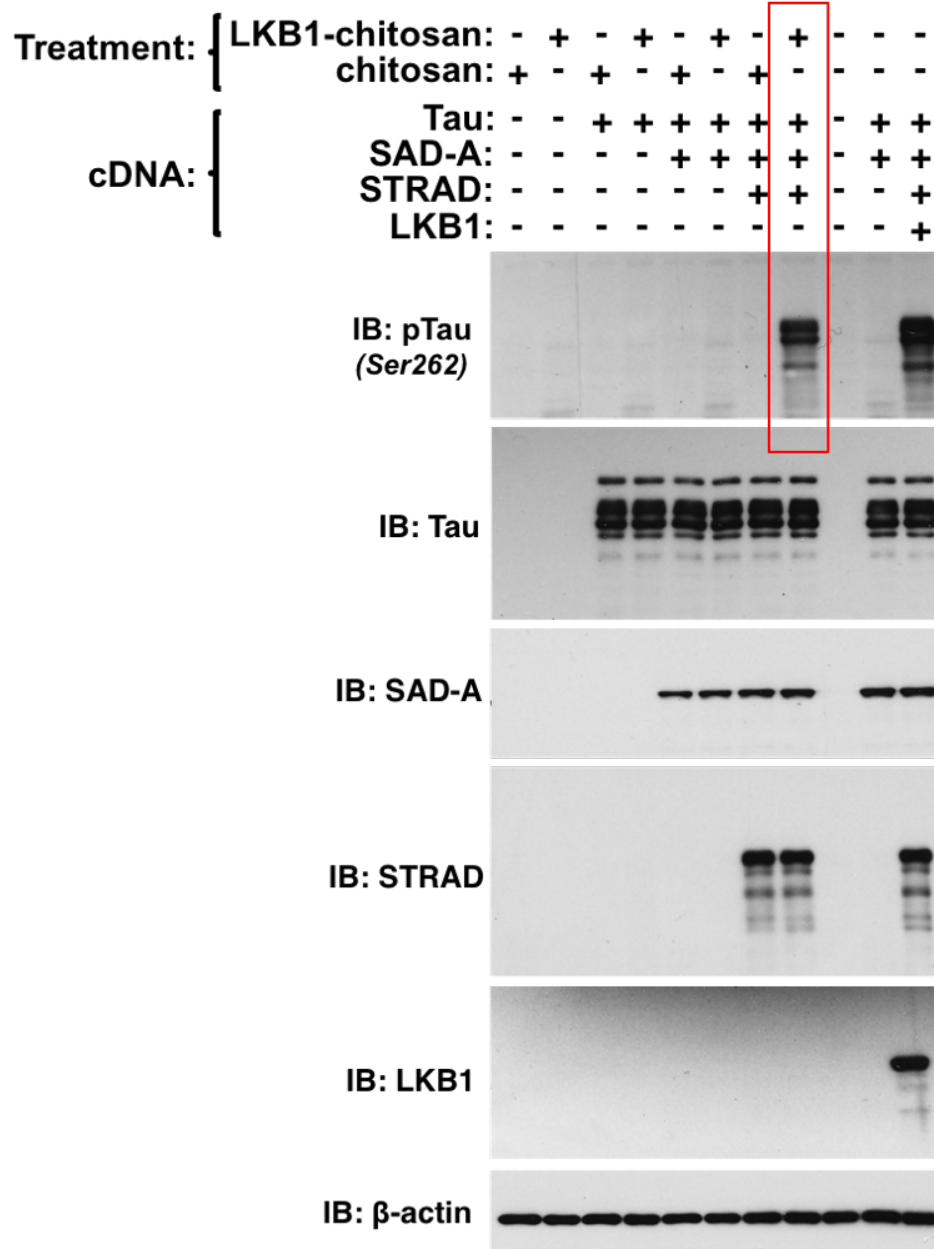


Figure 5.5 Immunoblotting of several molecules of interest, involved in the signaling cascade for axon development. HeLa cells, not expressing endogenous LKB1, have been transfected with different combinations of cDNA for LKB1, STRAD (LKB1 co-factor) and SAD-A and Tau (LKB1 downstream effectors). Consequently, the lysates of the different cell samples have been treated for 2 hours with either plain chitosan nanoparticles or with LKB1-chitosan nanocomplexes. Only HeLa cells transfected with cDNAs for Tau/SAD-A/STRAD and treated with LKB1-chitosan nanocomplexes have shown the presence of phosphorylated Tau at the Ser262 site (red lane), indicating the preserved functionality of the polymer-linked kinase. β -actin represents a control for the lysate volume.

Fluorescently labelled chitosan based micelles nanocomplexes have been synthesized and delivered to cultured hippocampal neurons, exerting no visible cytotoxicity

A first uptake study was conducted with Cy5.5-HGC nanoparticles (non functionalized and non physically complexed with magnetic beads). The fluorescent labelling of the glycol chitosan chains allows the visualization of the micelles and their intracellular distribution. The overlaid micrographs presented in Figure 5.6 show a time-dependent uptake pattern, with a more intense Cy5.5 signal as the incubation time increases from 2 hours to 48 hours. Already at 2-5 hours post-treatment, chitosan nanocomplexes were noticeable at the tip of the growing neuritic extensions, while at 18 hours post-delivery the uptake resulted predominant in the cytoplasm milieu of the soma, surrounding the nuclei. Considering the timing of axon formation *in vitro*, that typically ranges between 12 and 24-48 hours, longer time points were also taken into account. At 24 and 48 hour post-treatment, Cy5.5 signal was distinctly observed in the neuritic processes (Figure 5.6, black arrows). In Figure 5.6 contrast and brightness of the DIC signal were modified to ease the visualization of the fluorescent micelles within the cells.

These results underscore the chitosan micelle capability of penetrating the neuronal cell membrane and be internalized in different cellular compartments and cytoplasmic areas, indicating the suitability of this nanoparticulate system as protein delivery platform for neuronal cells. Furthermore, these preliminary findings show that neuronal cell development up to 48 hours appears not to be affected by the polymeric nanoparticle delivery.

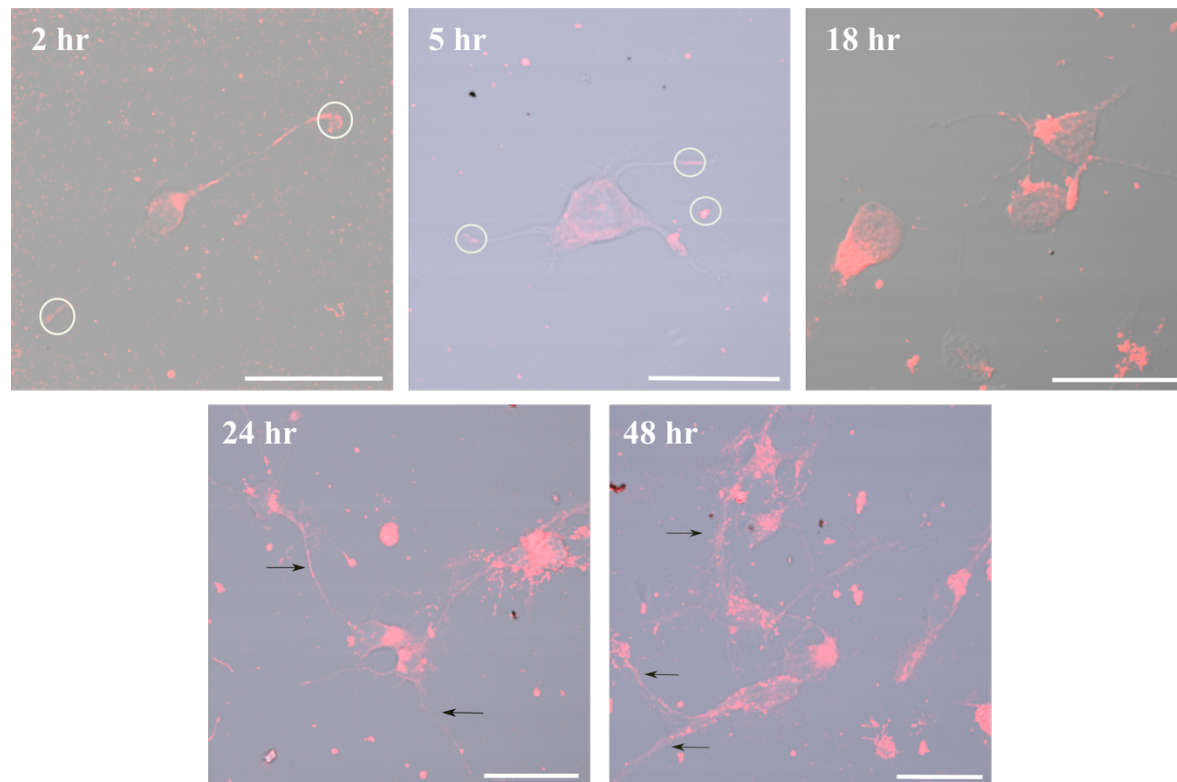


Figure 5.6 Confocal micrographs overlays of Cy5.5 and DIC channels depicting primary E19 rat hippocampal neurons treated with Cy5.5-HGC nanoparticles for different time points. The overlay facilitates the visualization of the nanoparticle intracellular distribution. White circles highlight Cy5.5-HGC NPs internalized at the tip of growing processes at shorter time points, while black arrows are indicating nanocomplexes up-taken within the neurite length at longer time points. Scale bars 30 μm .

Hippocampal cultured neurons treated with SPIONs did not show visible cytotoxicity

In order to assess the effect of MNPs on primary rat hippocampal neurons, an uptake experiment was conducted. Commercially available, superparamagnetic iron oxide nanoparticles, of 200 nm in diameter, presenting a Fe₂O₃ core, a glucuronic acid shell and a DAPI-labelled lipid coating, were delivered at a concentration of 0.125 mg/ml, under serum free conditions. The cell culture procedure was carried out as mentioned in the previous paragraph. Confocal imaging under DAPI filter allowed the visualization of the MNPs' uptake pattern. Although this nanoparticulate system appeared to be easily internalized by neuronal cells, a prevalent accumulation was noticed in the cytosolic compartment of the soma (Figure 5.7, white arrows). Also in this case, from the observation of the morphology of the neurons, neither visible cytotoxicity nor development impairment was detected, up to 48 hour-treatment.

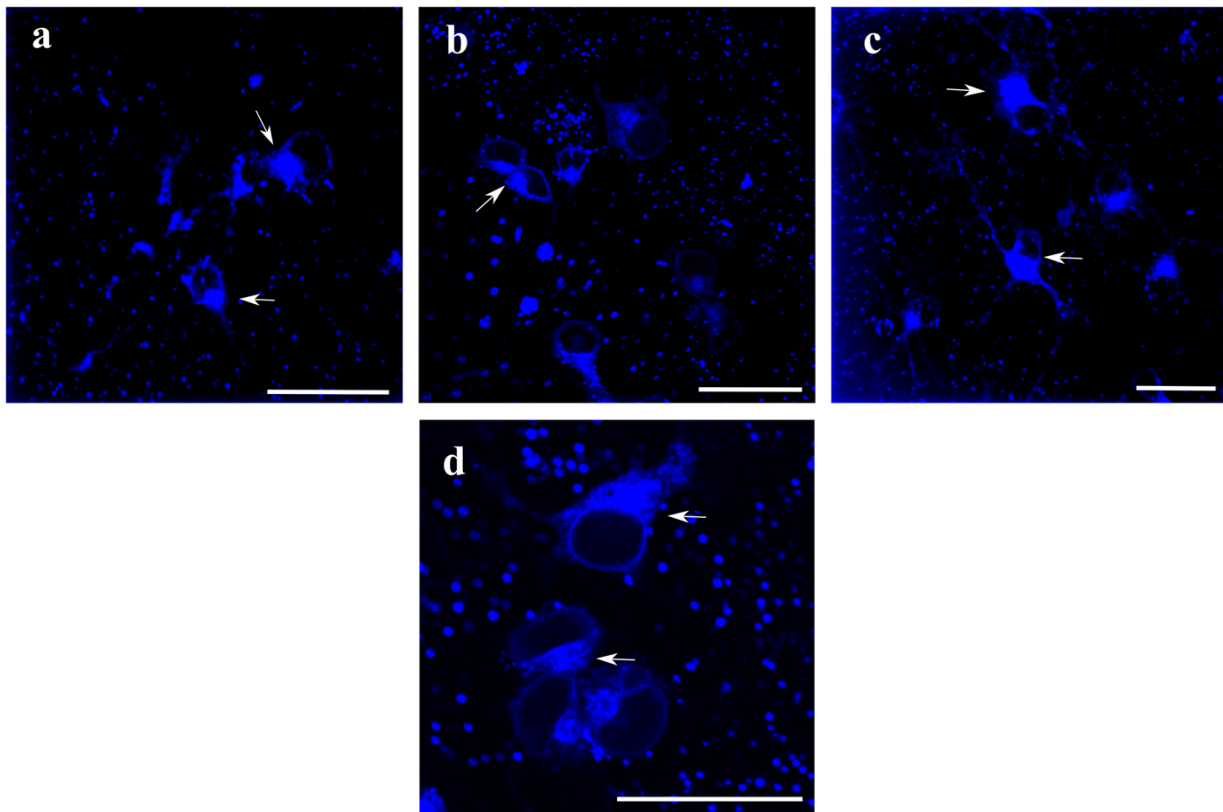


Figure 5.7 Confocal micrographs depicting primary E19 rat hippocampal neurons treated with DAPI-glucuronic acid coated SPIONs for different time points: 18 hours (a); 24 hours (b); 48 hours (c). Arrows are indicating the prevalent accumulation of the MNPs into the cell soma of the neurons. Zoomed image in (d) allows the resolution of the NP clusters within the cell soma. Scale bar 30 μ m.

Fluorescently labelled chitosan based micelles, complexed with SPIONs showed intracellular co-localization when delivered to cultured hippocampal neurons

To obtain our multifunctional nano-micellar delivery system, fluorescently-labelled HGC micelles were decorated with biotinylated fluorescein (B4F) *via* biotin-avidin interactions. The fluorescein moiety served as model molecule to test the intracellular distribution of a functional element linked to the main core-shell structure. In addition, glucuronic acid-SPIONs were complexed to the system, *via* dispersion with Pluronic P127 and subsequent probe-type sonication (as shown in Figure 5.2). The obtained nanocomplexes had an average diameter of 183.24 ± 0.29 nm. To assess the cellular uptake and the possible co-localization of the three components of the multifunctional nanoparticle (HGC matrix, B4F pendant and encapsulated SPIONs), a delivery experiment was carried out. Embryonic E19 rat hippocampal neurons were plated on poly-L-lysine coverslips and let attach overnight in Neurobasal media supplemented with B27, Glutamax and 10% FBS. Cells were treated with SPIONs loaded-Cy5.5-HGC-B4F nanoparticles for up to 30 hours, under serum free conditions. Afterwards, samples were fixed with 4% paraformaldehyde and mounted on glass slides. Confocal imaging observation conducted under Cy5.5, FITC, DAPI and DIC channels at 63X of magnification, revealed the reciprocal distribution of the multifunctional nanoparticles with respect of the cell soma and the neuritic compartments. As previously observed, chitosan-associated signal was present at the tip of growing processes (Figure 5.8e, white arrows). More interestingly, the FITC signal mostly co-localized with the Cy5.5 signal, indicating that the B4F moiety remains attached to the HGC matrix not only during the delivery and the administration step, but also after being internalized (Figure 5.8). The DAPI signal pertaining to the SPIONs was visible in a punctate pattern, indicating the optimal use of the Pluronic as dispersing agent. Moreover, DAPI co-localization with the other channels further confirmed the appropriateness of the bio-polymeric nano-micelles as protein delivery platform for neuronal cells (Figure 5.9).

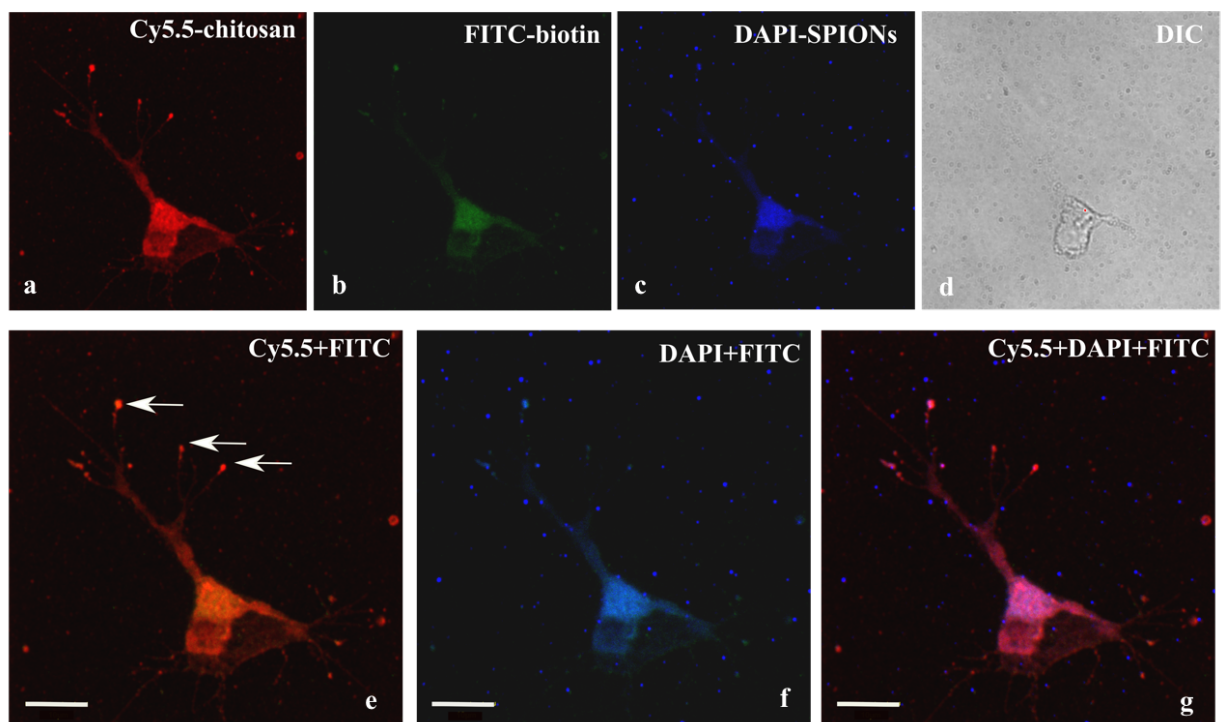


Figure 5.8 Confocal microscopy images of primary hippocampal neurons (E19) treated for 30 hours with SPIONs-loaded-Cy5.5-HGC-B4F nanocomplexes. In the upper panel (a, b, c and d), the separate channels used for the acquisition are shown. In the lower panel (e, f, g), a sequence of images with merged channels are presented. The intracellular distribution of the nanocomplexes at the tip of growing processes is highlighted (white arrows). Scale bar 10 μ m.

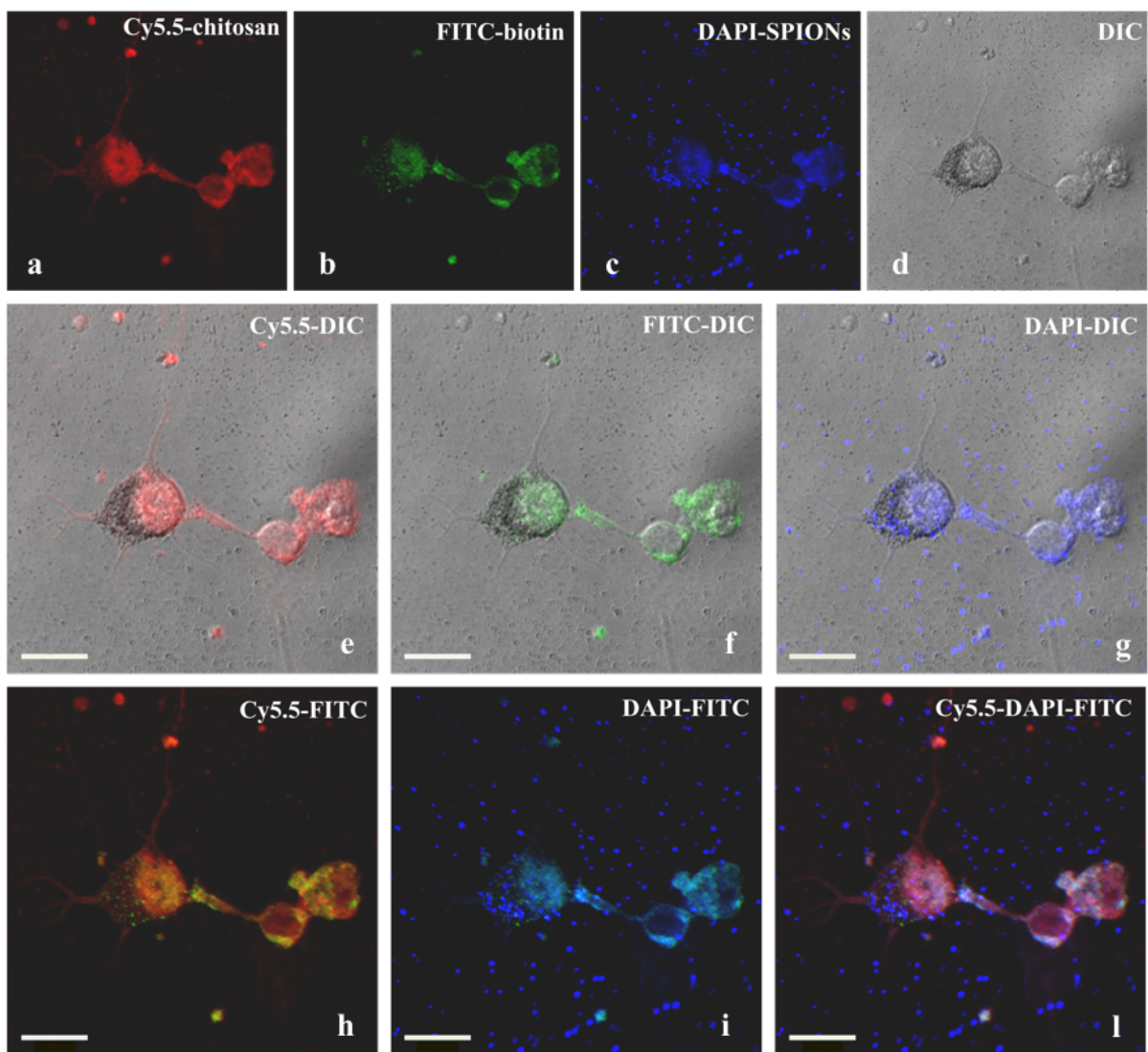


Figure 5.9 Confocal microscopy images of primary hippocampal neurons (E19) treated for 30 hours with SPIONs-loaded-Cy5.5-HGC-B4F nanocomplexes. In the upper panel (a, b, c and d), the separate channels used for the acquisition are shown. In the middle panel (e, f, g), the overlays of the separate fluorescence channels with the DIC allow the visualization of the nanocomplexes distribution within the cells. The bottom panel (h, I, l) presents different combinations of fluorescence channel overlays, to highlight the co-localization of the nanocomplexes' components. Scale bars 10 μ m.

The delivery of the multifunctional bio-magnetic nanocomplexes did not affect the overall morphology and development of the primary hippocampal cultures in vitro

With the aim of assessing the neuronal cell viability upon treatment with our multifunctional systems, several morphological parameters were considered: the length of the three longest processes, the average number of processes per cell, the total length of processes per cell and the average process length. Ideally, these cellular features should be preserved between a control culture and a culture treated with empty, non-functionalized polymeric nanovehicles. For this purpose, four different systems were considered, together with the respective controls: (a) Cy5.5-HGC NPs delivered for 18 hours, (b) Cy5.5-HGC NPs delivered for 24 hours, (c) SPIONs loaded-HGC-BF4 NPs for 30 hours. Systems (a) and (b) constitute the non-functionalized, polymeric micelles, while system (c) contains the model protein linked *via* avidin-biotin bridge and the Fe₂O₃ nanoparticles.

Neuronal tracing performed with ImageJ on the Cy5.5-HGC NP treated samples (47 cells for HGC-18hr and 120 cells for HGC-24hr) did not show any significant difference with the control cultures (77 cells for control-18hr and 86 cells for control-24hr), neither in terms of the length of the three longest processes (presenting dimensions ranging from ca. 35 μm to about 15 μm for both the cultures at 24 hours), nor in terms of average number of neuritic protrusions (3.8 for the HGC NP treated cells and 4.3 for the control after 24 hours of culture). The results summarized in Table 5.1 indicate the good biocompatibility of the plain chitosan micelles.

In the case of the samples treated with SPIONs-loaded Cy5.5-HGC-B4F NPs 15 cells were analyzed, while 20 cells were considered in the control group. Due to a prolonged culturing time (30 hours), control cells presented neuritic processes with average lengths of 49.97 μm (first longest neurite), 26.18 μm (second longest neurite) and 20.00 μm (third longest neurite). On the other hand, neuronal cells treated with the bio-magnetic, fluorescein decorated micelles developed slightly shorter processes (with dimensions ranging from 26 μm to 16 μm), suggesting a possible impairing effect on neuronal growth. However, no significant variation was observed in terms of the average number of processes, indicating that treated cells undergo a healthy neuritic sprouting (results are summarized in Table 5.2).

In addition, to gain a more visual insight of the obtained results and to facilitate the comparison among the different cellular treatments, composite tracings of neurites from random cells were prepared (Figure 5.10). In Figure 5.11, bar graphs reporting the average measurements of all the morphological features analyzed are reported, grouped accordingly to the treatment performed.

Table 5.1 Morphological parameters obtained via neuronal cell tracing for the Cy5.5-HGC NP treated samples and their respective controls

	HGC NPs 18 hours	Control Culture 18 hours	HGC NPs 24 hours	Control Culture 24 hours
<i>1st Neurite length (μm)</i>	31.51 \pm 2.09	26.85 \pm 1.45	33.96 \pm 1.50	35.05 \pm 1.90
<i>2nd Neurite length (μm)</i>	17.94 \pm 1.00	18.41 \pm 0.80	21.75 \pm 0.99	20.84 \pm 1.02
<i>3rd Neurite length (μm)</i>	12.82 \pm 0.65	14.12 \pm 0.59	15.08 \pm 0.64	15.59 \pm 0.76
<i>Total Length of neurites per cells (μm)</i>	66.89 \pm 3.63	70.79 \pm 3.66	81.21 \pm 3.55	88.12 \pm 4.73
<i>Average Neurite Length (μm)</i>	18.94 \pm 0.94	17.53 \pm 0.60	20.91 \pm 0.64	20.48 \pm 0.71
<i>Average number of neurites per cell</i>	3.5 \pm 0.15	4.06 \pm 0.15	3.88 \pm 0.11	4.31 \pm 0.15

Table 5.2 Morphological parameters obtained via neuronal cell tracing for the SPIONs-loaded-Cy5.5-HGC-B4F NP treated samples and their respective controls

	SPIONs-HGC-B4F NPs	Control Culture
	30 hours	30 hours
<i>1st Neurite length (μm)</i>	26.06 ± 2.24	49.97 ± 5.11
<i>2nd Neurite length (μm)</i>	20.76 ± 1.43	26.18 ± 1.99
<i>3rd Neurite length (μm)</i>	15.98 ± 1.21	20.00 ± 2.11
<i>Total Length of neurites per cells (μm)</i>	73.49 ± 11.46	122.17 ± 10.77
<i>Average Neurite Length (μm)</i>	18.13 ± 0.96	25.19 ± 1.84
<i>Average number of neurites per cell</i>	4.5 ± 0.61	4.85 ± 0.32

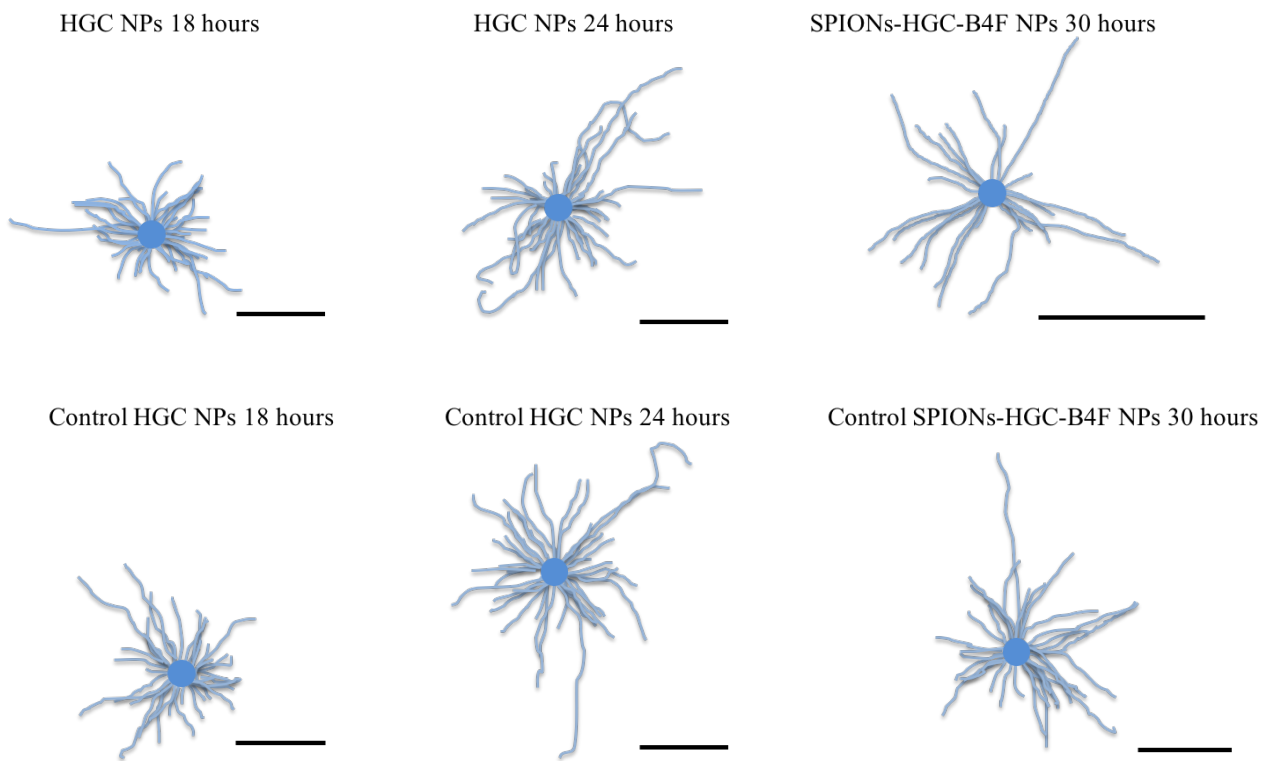


Figure 5.10 Composite tracing of neurites from a random sampling of 10 neurons from each treatment to demonstrate variance in neurite length and number. Scale bar 30 μ m.

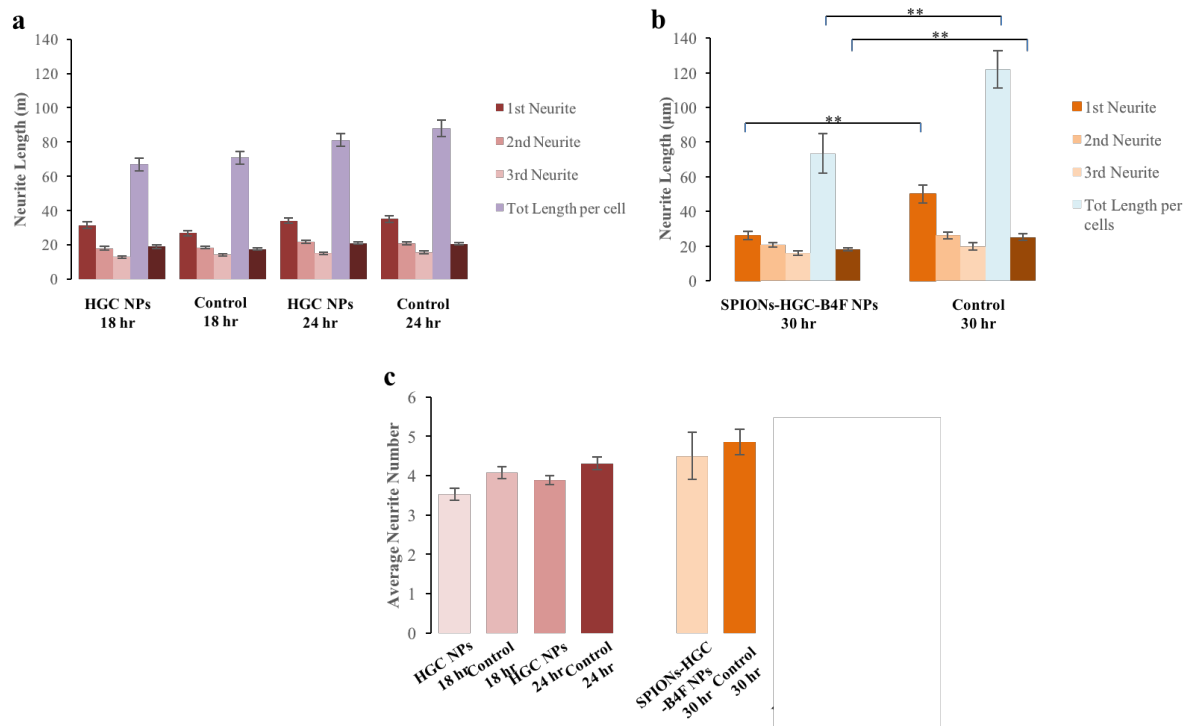


Figure 5.11 Bar graphs representing the variations of the neuronal morphological parameters for the Cy5.5-HGC NP treated samples (a), the SPIONs loaded-HGC-B4F NP treated samples (b). The average number of neuritic processes per cell is reported in (c). Error bars represent the s.e.. A Student's *t*-test between each treated sample and the corresponding control were performed, considering a *p* value < 0.01 (**).

Hippocampal culture neurons treated with HGC-LKB1 nanocomplexes presented multiple axon morphology, indicating the preserved functionality of the kinase

With the aim of assessing the retained functionality of the synthesized kinase-decorated micelles, primary hippocampal neurons were treated *in vitro* with Cy5.5-HGC-LKB1 for up to 72 hours. Confocal imaging allowed the tracing of the cells to check for general, morphological features, such as number, length and ramification of dendrites and axons. In their work, Shelly *et al.*²⁸¹ showed that over-expression of LKB1 in cultured hippocampal neurons resulted in higher number of cells that formed multiple axons. Interestingly, a similar outcome was observed in this case. Upon HGC-LKB1 micelle delivery, 17 over 65 cells presented multiple axon (MA) morphology (corresponding to the 26% of the population of neurons analyzed), while only 4 over 50 cells had more than one axonal process for the control group treated with plain HGC micelles (corresponding to the 8% of the population of neurons analyzed). In a second culture, similar numbers were obtained: 12 cells out of 37 presented MA morphology when treated with LKB-1 NPs (32.43%) while only 7 over 82 cells showed more than one axon for the case of the plain HGC-NPs treatment (8.5%). In Figure 5.12 representative traced cells for both treatments help the visualization of the observed phenomenon. Moreover, the confocal images reported in Figure 5.13 allow a further comparison between the different treatment conditions. In order to confirm the uptake of Cy5.5-HGC-LKB1 nanocomplexes within the neuronal cell soma, overlaid micrographics and zoomed of the separated channels are presented in Figure 5.14.

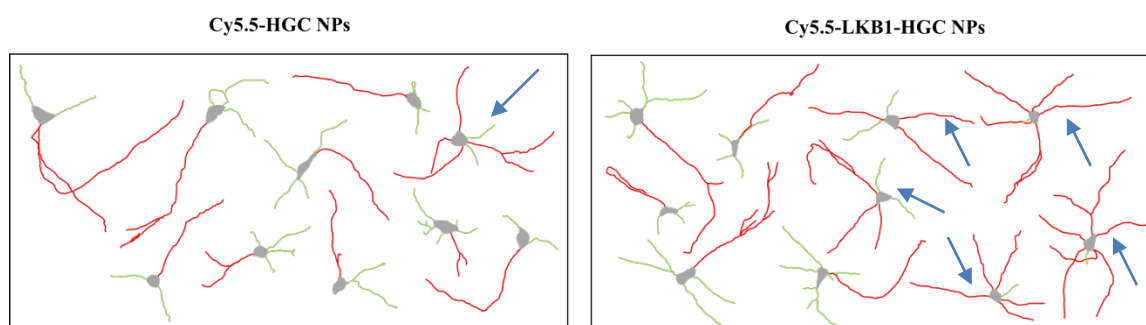


Figure 5.12 Tracing of a representative pool of primary hippocampal neurons treated with Cy5.5-HGC NPs or with Cy5.5-HGC-LKB1 NPs. Axons were traced in red, while dendrites were traced in green. Blue arrows identify the multiple axon cells.

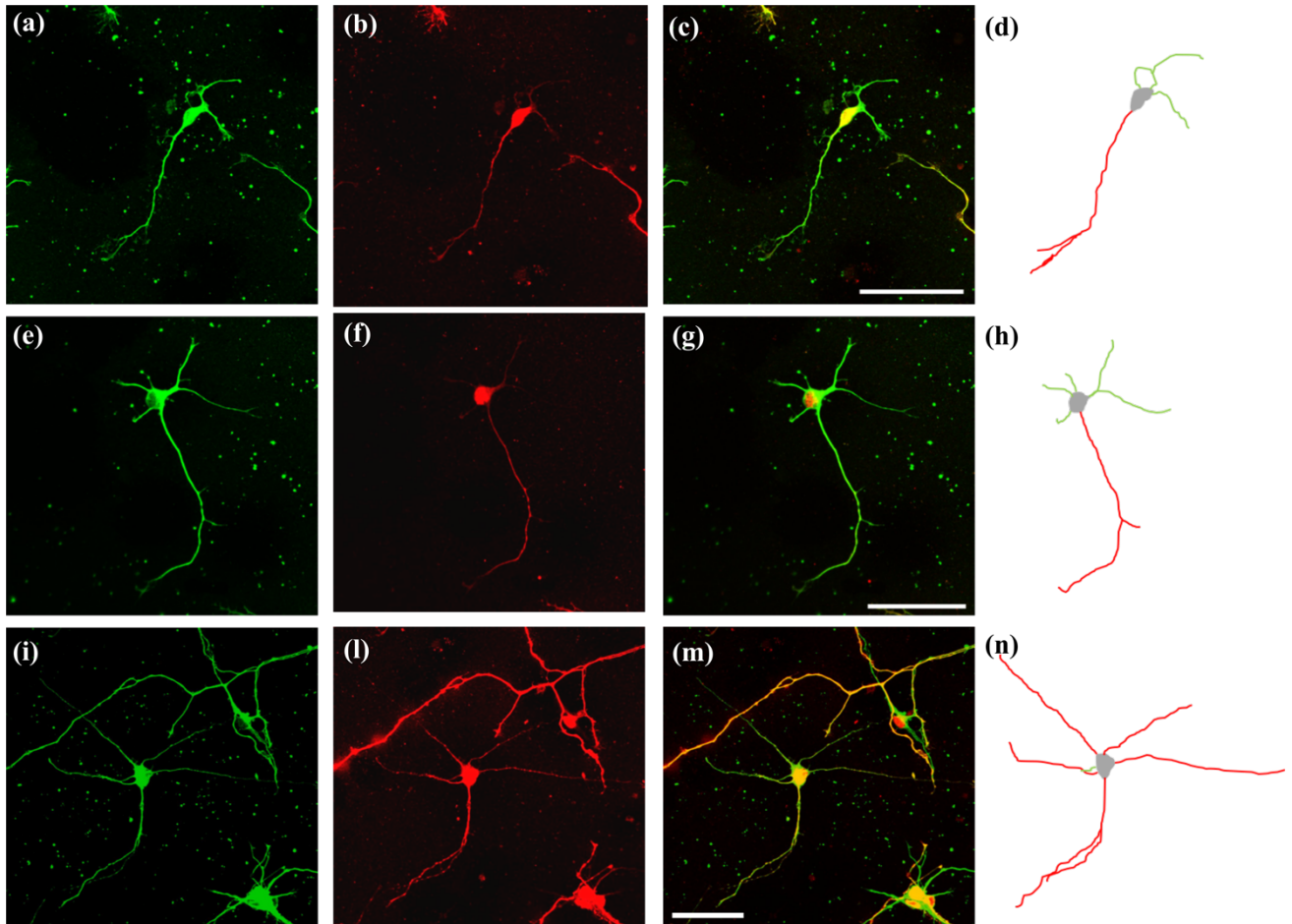


Figure 5.13 Confocal images of primary hippocampal neurons treated for 72 hours with Cy5.5-HGC NPs (a-c) or with Cy5.5-HGC-LKB1 NPs (e-g and i-m). The green channel depicts the Tuj staining (general neuronal marker) while the red channel shows the Smi-312 staining (specific for the axon). Overlaid images are reported in (c), (g) and (m) with scale bar of 50 μm . In (d), (h) and (n) the corresponding neuronal tracing are reported, showing in green the dendritic processes and in red the axons.

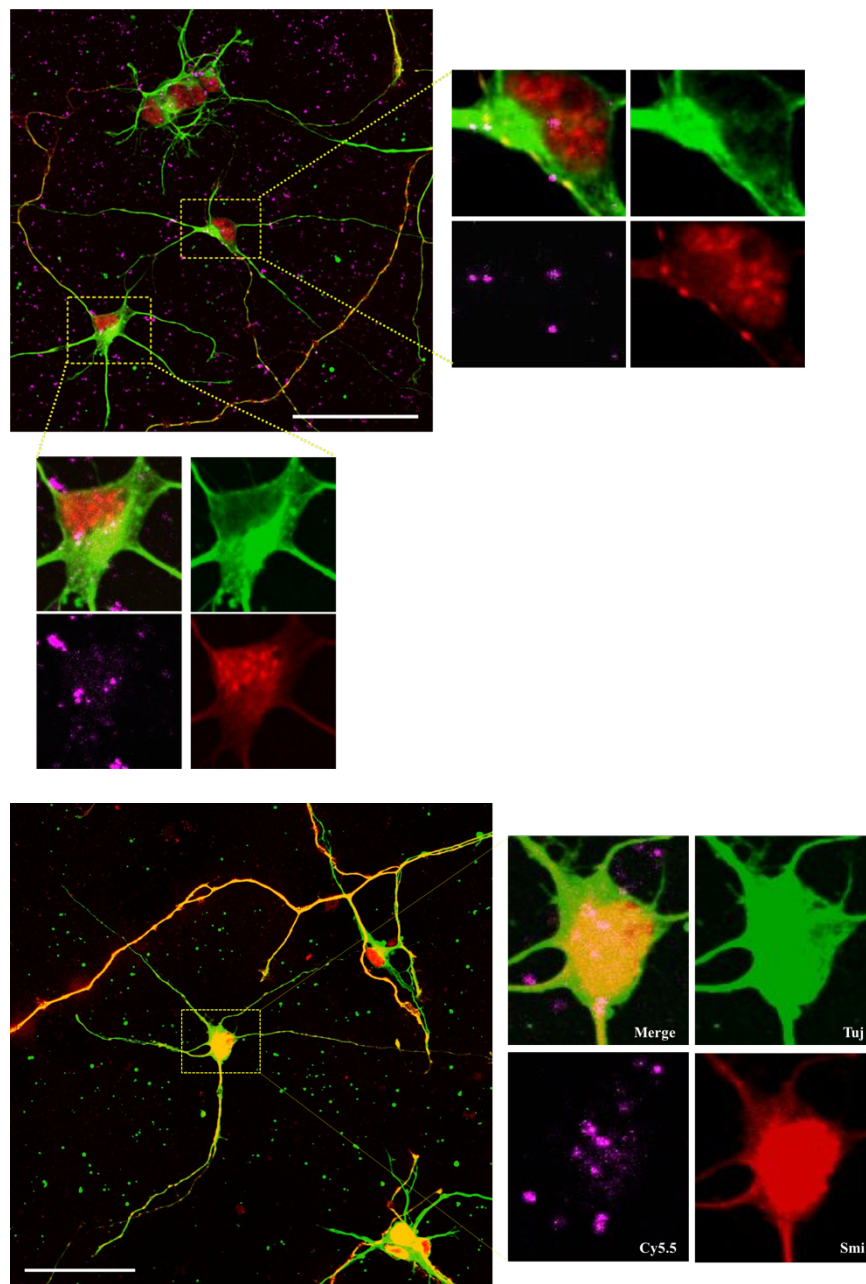


Figure 5.14 Confocal images of primary hippocampal neurons treated for 72 hours with Cy5.5-HGC-LKB1 NPs. The image is the overlay of green channel (Tuj), red channel (Smi) and magenta channel (Cy5.5) with a scale bar of 50 μm . The inserts are reporting the overlay and the separate channels of the cropped soma of the multiple axon neurons, to better visualize the localization of the HGC-LKB1 NPs within them.

In utero electroporation delivery of Cy5.5-HGC NPs confirmed the in vivo uptake

Upon completion of mitosis, cortical progenitors start to migrate radially to populate the different layers of the developing cortex.³¹²⁻³¹⁴ During migration, cortical pyramidal neurons undergo stereotypical morphological changes leading to polarized development of axon and dendrite.³¹⁴ The newborn neuron acquires a bipolar morphology in the ventricular zone (VZ), with apical-leading and basal-trailing processes. The trailing process will then become the axon. Previous studies have identified LKB1 as key regulator of axon formation in cortical neurons *in vivo*. Selective deletion of *lkb1* in mouse cortical pyramidal neurons,^{270, 276} or down-regulation of LKB1 in rat cortical progenitors with specific small hairpin RNAs using *in utero* electroporation²⁶⁹ resulted in striking absence of axon formation in all cortical layers. Furthermore, over-expressing of LKB1 resulted in ectopic axon formation and branching,²⁶⁹ while its deletion led to specific effects on axon formation from the basal pole, without affecting other aspects of development or cell migration.^{269, 285} Based on these experimental evidences, the level and localization of LKB1-activity should be precisely regulated in the trailing process at the basal pole to ensure proper formation of the axon *in vivo* (Figure 5.1).

With the aim of assessing to applicability of our engineered nano-micelles as protein delivery agents *in vivo*, *in utero* electroporation was performed. This survival procedure allows direct and precise embryonic manipulation and it is usually performed to carry out developmental studies. First, lateral ventricles are injected with plasmid DNA and, subsequently, electric pulses are applied to transiently disrupt and permeabilize the cell membrane, in order to drive charged molecules through temporary pores inside the neurons (Figure 5.3)³¹⁵ As a result, the wall lining the ventricles is transfected with the plasmids of interest, which may assist the tracking of neuronal progenitor cells originated in the VZ. In addition, the technique can be applied to overexpress or inhibit genes involved in neuronal development, by injection and further electroporation of small interfering RNA or small hairpin RNA,^{269, 316, 317} to observe migration of neurons towards the cortex and to monitor differentiation of progenitors into neurons or astrocytes.³¹⁵

To the best of our knowledge, in this study, the *in utero* electroporation of Cy5.5-HGC nano-micelles, in suspension with PBS was successfully performed for the first time. The nano-micelles were injected into lateral ventricles at E16.5 and embryos were sacrificed two days post-injection (at E18). Due to the type of surgery performed, no perfusion was carried out in the embryos.

Confocal imaging analysis, performed on brain slices counterstained with DAPI, revealed the presence of Cy5.5 signal in several areas, with patterns either diffused or localized, indicating the success of the injection method. More interestingly, uptake of chitosan micelles in cortical progenitors migrating towards the cortical plate (Figure 5.15 inserts d-f and Figure 5.16 insert d) and migrating radially from the ventricle (Figure 5.17) was observed. The zoomed image in Figure 5.15f distinctly displays Cy5.5-HGC nano-micelles internalized in the cytoplasm of cortical progenitors at 2-day post-injection. Our system's ability of permeating through the blood brain barrier (the layer of endothelial cells lining cerebral micro vessels) can be associated to the use of chitosan-derivative molecules as basic material.^{290, 318} Moreover, the presence of primary and secondary amine groups on the main polymeric chains constituting the self-assembled nano-vehicles are accountable for the resulting net positive charge: this characteristic might have played a critical role during the *in utero* electroporation delivery, favoring the transport of the charged micelles across the ventricle wall. These preliminary findings constitute direct confirmation of the suitability of our bio-polymeric construct as *in vivo* nano-vehicle for functional molecule delivery to the brain, to assist long-term developmental processes, such as axon specification.

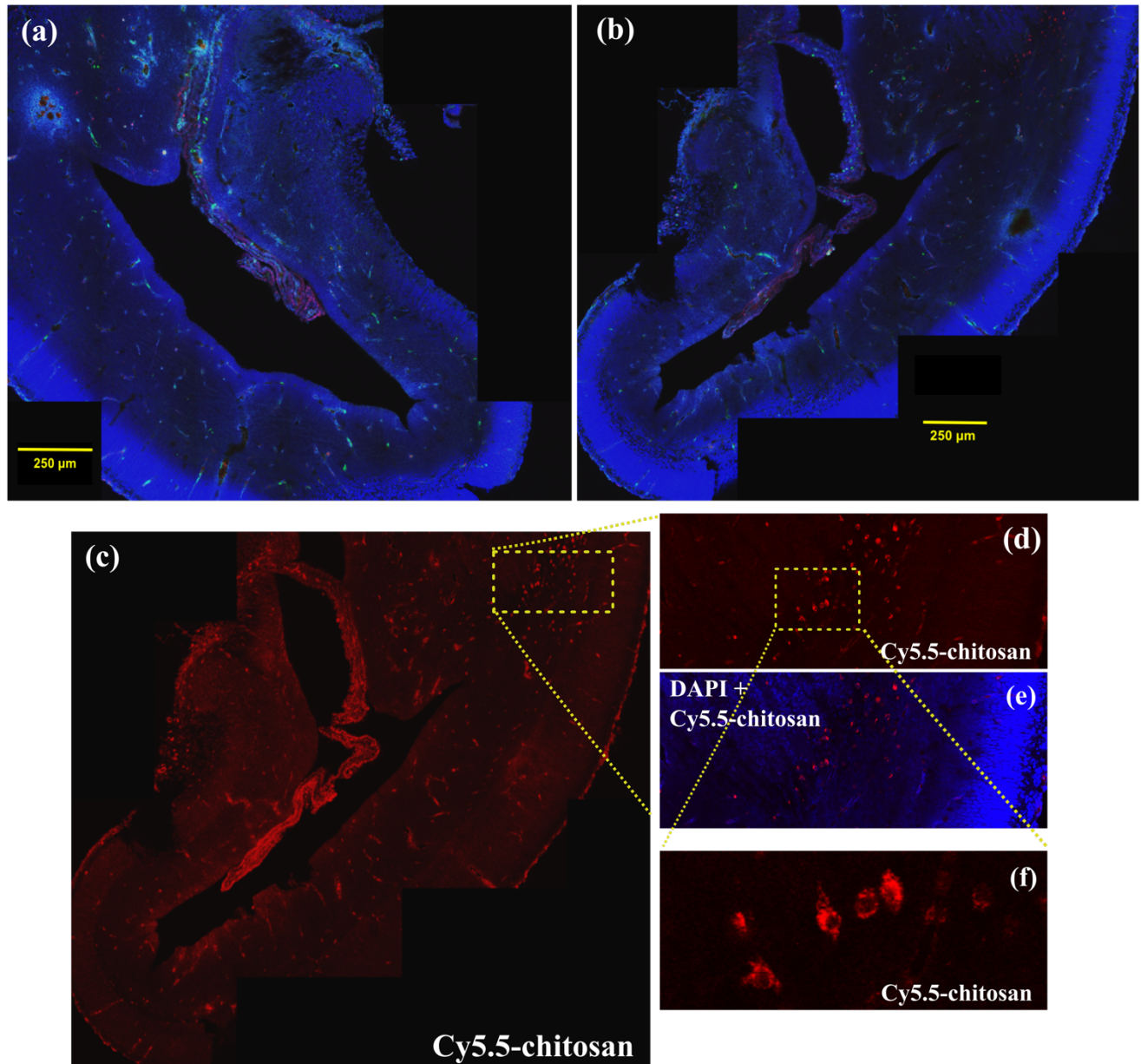


Figure 5.15 (a, b) Confocal microscopy overlay tiling of a E18 rat embryo brain slice, depicting left and right ventricles and cortical plate (scale bar 250 μm). (c) depicts the Cy5.5 signal pertaining to the chitosan nanomicelles, injected *via in utero* electroporation at E16.5. The inserts (d-f) show neurons migrating towards the cortical plate, presenting Cy5.5-chitosan nanomicelles internalized in the cell cytoplasm.

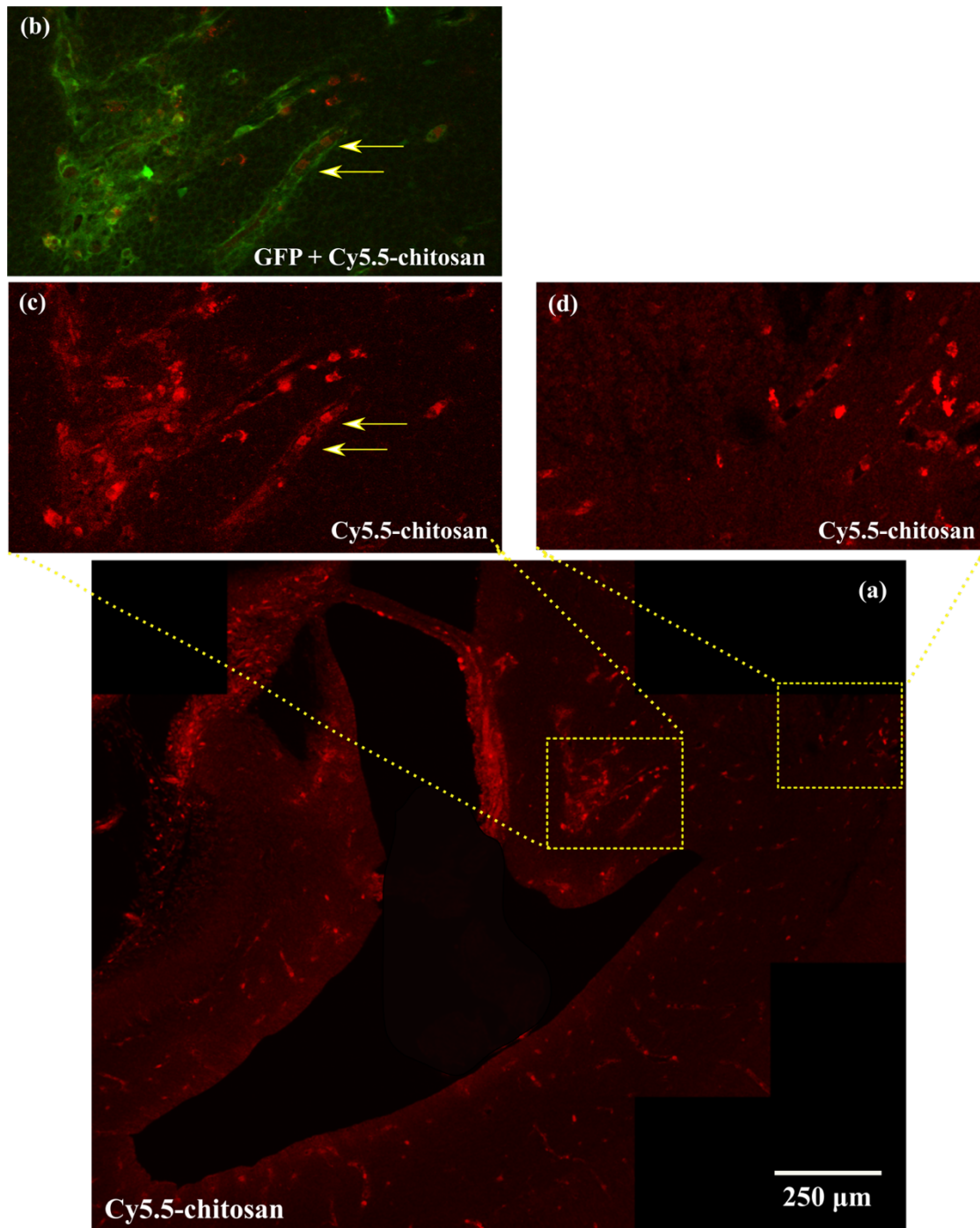


Figure 5.16 (a) Confocal microscopy tiling of a E18 rat embryo brain slice, depicting the ventricle, where the Cy5.5-chitosan micelles have been injected at E16.5 *via in utero* electroporation. Inserts (b) and (c) highlights the presence of some nanocomplexes in the blood vessels of the brain (yellow arrows), while insert (d) show the presence of Cy5.5-chitosan nanocomplexes internalized by neurons migrating toward the cortical plate.

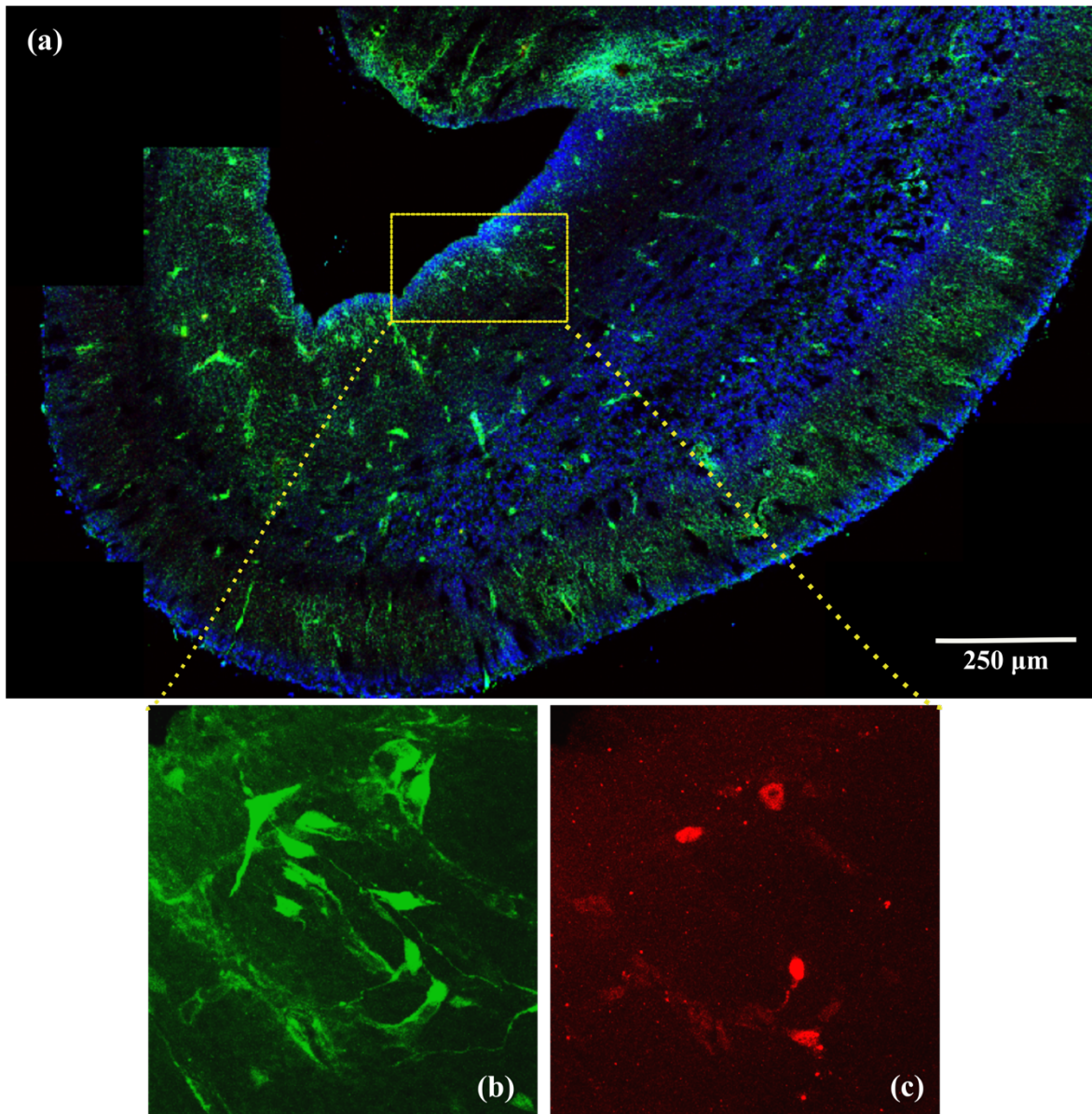


Figure 5.17 Confocal images of E18 cortical progenitors injected *in utero* at E16.5 with Cy5.5-HGC nanomicelles at a concentration of 0.025 mg/ml (c). The blue signal in (a) represents the counterstain with DAPI. In (b) and (c) inserts radially migrating neurons are visualized.

5.4 Conclusions and Future Perspectives

Axon formation is a spatio-temporally restricted developmental process, requiring subcellular localization of intracellular proteins. In this research project, we have developed a novel, biopolymeric-based nanotechnology able to deliver into the cytoplasm LKB1, a critical kinase involved in neuronal cell polarization, to regulate axon development.

LKB1 was successfully linked to amphiphilic, chitosan-derivative nano-micelles via biotin-avidin interactions: the engineered system preserved kinase functionality and presented prolonged structural stability. Our preliminary findings showed that chitosan micelles were rapidly internalized in different cellular compartments and cytoplasmic areas of primary E18/E19 hippocampal neurons *in vitro*, without affecting neuronal viability or development. Not only the nanoparticles appear to be distributed within the cell soma, but are also present at the tip and throughout the length of the growing processes, indicating the suitability of this system as protein delivery platform for neuronal cells. Furthermore, cells were able to develop long and branched projections and no visible cytotoxicity was observed for up to 48 hour-delivery, as confirmed by the neurite tracing analysis. The core-shell architecture of the glycol chitosan self-assembled micelles allows the encapsulation of active compounds or other specific components. In our design, multifunctional nanoparticles were obtained by functionalizing the polymer chains with biotinylated fluorescein and by complexing glucuronic acid-SPIONs onto the chitosan matrix, *via* dispersion with Pluronic P127 and subsequent probe-type sonication were prepared. Once again, the resulting systems showed facile cell internalization. Co-localization of the fluorescent signals pertaining to the different functional moieties confirmed the micelle stability in the cytoplasmic milieu and contributed to validate the concept of our engineered construct as platform for localized neuronal protein delivery.

More interestingly, when treated with HGC-LKB1 nanocomplexes *in vitro*, primary hippocampal neurons presented a multi-axon phenotype: this striking result constitutes the ultimate confirmation of the preserved functionality of the conjugated kinase and validates the potential of our multifunctional system as local protein delivery agent. In addition, for the first time *in utero* electroporation delivery of chitosan nano-micelles was successfully performed, and the results demonstrated *in vivo* uptake and internalization into cortical progenitors, radially migrating and at the cortical plate.

Our preliminary study opens the door to a prototypical conceptual model that will expand fundamental insight into mechanisms that regulate early neuronal development, both *in vitro* and *in vivo*. Moreover, this study constitutes a paradigm, applicable to many intracellular proteins, for assessing proper delivery and regulation of protein activity in a wide variety of central and peripheral neuronal tissues, leading to the design of new methodologies for the repair of underlying pathologies that arise from cell polarity break-down.

Chapter 6:

Conclusions and Future Outlook

Targeted drug delivery constitutes a promising strategy to overcome limitations and complications associated with the classical chemotherapy approaches. In the past years, the critical role of the tumor microenvironment in the disease progression has been recognized, highlighting lack of oxygen, unorganized vasculature and milieu acidification as key cancer hallmarks. Therefore, smart materials capable of actively triggering a response when in the proximity of cancer cells have been extensively researched. Polymeric micelles offer versatile chemistry and scalable technology, valuable characteristics for the design and development of anti-cancer nano therapeutics. More specifically, due to their biocompatibility and the presence of pH-sensitive functional groups, polysaccharides, such as chitosan and its derivatives, have been extensively explored for their biomedical potential. The rapidly growing field of cancer nano therapeutics have pointed out the importance of integrated multifunctional drug delivery systems, able to perform both diagnostic and therapeutic tasks. As a result, a strategic design of nano carrier materials, coupled with cancer cell target selectivity, tumor microenvironment stimuli-responsiveness and multimodal imaging capability, is necessary to support a safe and effective antitumor compound delivery.

Focus of this thesis work and main denominator of the various research projects presented throughout the different chapters, was the design and characterization of chitosan-derivative self-assembled micelles, properly engineered to exert a specific biological goal. The leading aim was to fabricate efficient nano therapeutics, by tailoring the chemistry of the basic material during the synthesis process, in order to fabricate nano constructs able to be internalized in a plethora of cell lines, and to deliver cytotoxic agents while allowing visualization and tracking. More specifically, fluorescent nano micelles were optimized to deliver an anti-cancer compound to osteosarcoma cells in monolayers (Chapter 2) and in 3D spheroidal assemblies (Chapter 4); to target the membrane-bound MMP-14 on aggressive breast cancer cells and limit the associated migratory functions (Chapter 3); and to promote axon formation in cultures of hippocampal primary neurons via the delivery of a protein kinase (Chapter 5).

In the first part of the work, hydrophobic modifications of glycol chitosan, by means of 5 β -cholanic acid moieties, were performed, with the aim of synthesizing amphiphilic molecules (HGC) able to self-organize in aqueous environment. The obtained polymeric self-assembled nanoparticles were characterized in terms of size, morphology and pH responsiveness. Moreover, the nanomicelle's ability to encapsulate and subsequently release a hydrophobic model drug (doxorubicin) was evaluated, to assess the role of the hydrophobic content on the physicochemical properties of the resulting systems. A higher degree of substitution of the steroid-like pendants correlated with the formation of stable nano micelles of about 288.6 nm in diameter, with a spheroid-like morphology and a positive surface charge of about +13.2 mV, able to encapsulate doxorubicin with a loading content of 7.15%. With the aim of testing the potential applications of the engineered nano micelles, a human osteosarcoma cell line in monolayer was first considered. Confocal microscopy aided the visualization of the Cy5.5-HGC NPs, efficiently internalized into the cells in monolayer with a time- and concentration- dependent uptake pattern. In the future, in order to elucidate which mechanisms of endocytosis are predominantly involved in the HGC micelle internalization, a more systematic study, with multiple vesicle staining and higher resolution image acquisition, should be carried out. This would constitute a crucial piece of information to establish effective nano therapeutics with a controlled cellular pharmacokinetics. Administration of empty, non-functionalized HGC NPs showed null or minimal cytotoxicity, over a broad range of nanoparticle concentrations tested, up to 72 hr post-treatment. In addition, no significant changes in the cell morphology, motility and their ability to produce the extracellular matrix protein fibronectin were observed to be associated with the HGC nano-micelle administration, suggesting the potential use of our construct as anti-cancer compound delivery systems in living systems. More interestingly, doxorubicin-loaded nanocomplexes, successfully internalized by the cells in monolayers, showed comparable cytotoxicity with the free model drug, indicating the preservation of the molecule functionality and activity.

To explore a different cellular approach, three-dimensional spheroids were used to study the chitosan-derivative micelles penetration into a solid, complex cell network. In fact, cells in monolayer poorly reflect the *in vivo* cellular assembly conditions. On the other hand, by mimicking the three-dimensional architecture of the cell-matrix network, microtissues *in vitro* can exhibit actual tumor microenvironment features, such as gradients in the oxygen content and in the pH, differential nutrient penetration, cell-to-cell signaling and matrix deposition.²²⁹ These cellular tools

might help to gain a deeper understanding of the nano-vehicle interactions with the heterogeneous milieu and their actual application for a successful tumor penetration and therapy. In this study, MG-63 three-dimensional cellular assemblies were established to model and characterize avascular tumor osteosarcoma clusters in terms of morphology, size, cell population and response to different nano therapeutic treatments. Reproducible spheroids, with diameters of 500 – 700 μm , were obtained via liquid overlay technique, and the live-dead staining revealed the presence of a core-shell structure, with an inner region composed of dead cells, and an outer layer of live, active cells. While free doxorubicin was predominantly observed in the outer layers of the spheroids, Cy5.5-HGC_(0.185) micelle penetration was confirmed to interest most of the mass volume homogeneously, with a time- and concentration-dependence. High magnification confocal imaging revealed the presence of nano micelle clusters within the cytosol of cells located in the spheroids' inner regions. The successful penetration of the chitosan-based micelles, compared to the free drug molecules, can be associated to the physicochemical characteristics of the nano vehicles (size, positive charge, surface stability, pH-responsiveness), which favor the cellular internalization and, therefore, the further drug transport within the network. Despite the successful internalization of the drug-loaded micelles, reduction of spheroids volume appeared to be not dependent on the treatment concentration. Possible interpretations of this outcome might be associated to: (1) an increased drug resistance imputable to the 3D network environment, in which the cellular response is differently modulated, or (2) the tumor volume does not allow the complete assessment of the spheroid sensitivity to the drug treatment, mostly considering the shedding off of the cells in the outer layer while not taking into account cytotoxic effects on the inner regions. Further assessment of spheroid viability via MTS or staining for apoptosis, necrosis and hypoxia markers should help gain more insight into the composition of multicellular assemblies, as well as the effect of the different treatments on the overall survival of the treated tumor masses. In addition, the employment of more sensitive techniques, such as fluorescence lifetime microscopy, would allow a deeper understanding of the intracellular processes which occur after the drug-loaded nano-vehicles are internalized in the solid mass. As a future objective, the physio-pathological features of the cancer masses *in vivo* can be further replicated by developing co-culture 3D systems (for example with stromal cells or endothelial cells), to observe how this affects nutrients and oxygen's exchange and, as a result, the size of the necrotic core. These engineered cellular systems might also provide information on cellular segregation and assembly into substructures and sub-regions

of the tumor mass, and to track collective cell motility within the solid tumor mass. Ultimately, by offering insights into cell-to-cell and cell-to-matrix communications, this bioengineered three-dimensional cellular model can bridge the gap between the limitations of the over-simplified *in vitro* studies and the complexity associated with *in vivo* pre-clinical models.

In a parallel research project, with the aim of improving uptake specificity to favor an active, preferential internalization in tumor cells, chitosan-derivative micelles were functionalized via avidin-biotin interactions with an inhibitory peptide (IVS4), known to limit MMP-14 associated migratory functions. Cell migration and invasion involve the travelling of cells through the ECM substratum, achieved by extension of the leading edges, and subsequent degradation of the surrounding matrix by specific proteases, preferentially located at the cell invadopodia. Membrane bound matrix metalloproteinase-14 (MMP-14) has shown to play a critical role in sparking the migratory cascade, by activation of pro-MMP2 at the surface of tumor cells. Our collaborator from Prof. Cao's group from the Department of Pharmacological Sciences recently unraveled the role of an inhibitory peptide (IVS4), able to mimic the binding motif of the hemopexin domain (PEX) of the MMP-14 protease and to interfere with the homodimerization of MMP-14 and the consequent migratory cascade. In this thesis study, IVS4-decorated HGC_(0.185) micelles have been synthesized, characterized and delivered to four model cell lines. The IVS4-HGC micelles presented preferential uptake into MMP-14 expressing cells, such as African green monkey epithelial COS-MM14 and human triple-negative breast cancer MDA-MB-231 cells. Imaging analysis via super resolution microscopy allowed the visualization of the coupling between the peptide-tagged fluorescence micelles and the MMP-14 expressed at the cell surface, validating the use of our engineered construct for targeting delivery. The intracellular fate experiment showed internalization of the Cy3-HGC_(0.185)-IVS4 NPs within early endosome after 8 hours of delivery, and association with the Golgi complex at longer time points (18 and 24 hours). In the future, the sorting and degradation role of the Golgi apparatus should be investigated. Moreover, the initial complexation with the membrane protease might lead to the internalization via clathrin-mediated endocytosis; thus, the staining for this intracellular vesicle protein might help to gain more insight into the IVS4-NPs uptake mechanism in triple negative breast cancer cells. A microtubule depolymerizing agent, the ansamitocin P3, was successfully encapsulated into our nano-vehicles, revealing the micelle cytotoxic potential comparable or higher than the free drug, especially after 6 days of delivery to MDA-MB-231 cells, at low concentrations such as 0.5 nM, 0.75 nM, and 1

nM. Release kinetics data should be collected, to confirm the presence of a sustained release of the active compound from the bio-polymer micellar system. Further development of this research study should include cytotoxicity of the AP3-IVS4-HGC_(0.185) micelles on breast cancer stem cells *in vitro* and the *in vivo* delivery to an animal model involving chicken embryos. More specifically, a chorioallantoic membrane (CAM) angiogenesis assay would allow to gain insight into possible cancer cell invasion ability across the membrane and formation of blood vessels associated with tumor growth. This experiment would provide critical information on the efficacy of our bio-polymer micellar system for the targeting of breast cancer invasiveness *in vivo*, and perhaps open the route for the implementation of a new strategy to prevent metastases formation.

A separate research project was conducted in Prof. Shelly's Laboratory of Developmental Biology, in the Department of Neurobiology and Behavior. Focus of this was the cytosolic delivery of a protein kinase, LKB1, to primary hippocampal neurons *in vitro*, to assess the chitosan-micelle potentials as protein delivery agents to assist axon development. Axon formation is a spatio-temporally restricted developmental process, requiring subcellular localization of intracellular proteins. Failure in regulating protein compartmentalization may lead to aberrant polarization and, ultimately, to lethal neurobiological disorders. Cy5.5-HGC_(0.185) was decorated with LKB1 via biotin-avidin interactions and the engineered system preserved kinase functionality and presented prolonged structural stability. Our preliminary findings showed that chitosan micelles were rapidly internalized in different cellular compartments and cytoplasmic areas of primary hippocampal neurons *in vitro*, without affecting neuronal viability or development (in terms of number and length of neuritic processes). More interestingly, when treated with HGC-LKB1 nanocomplexes *in vitro*, primary hippocampal neurons presented a multi-axon phenotype: this striking result constitutes the ultimate confirmation of the preserved functionality of the conjugated kinase and validates the potential of our multifunctional system as local protein delivery agent. In addition, for the first time *in utero* electroporation delivery of chitosan nano-micelles was successfully performed, and the results demonstrated *in vivo* uptake and internalization into cortical progenitors, radially migrating and at the cortical plate. This preliminary study opens the door to a prototypical conceptual model that will expand fundamental insight into mechanisms that regulate early neuronal development, both *in vitro* and *in vivo*. More importantly, this engineered system constitutes a paradigm applicable to many intracellular proteins, to properly deliver, localize and regulate protein activity in a wide variety of central and peripheral neuronal

tissues, leading to the design of new methodologies for the repair of underlying pathologies that arise from aberrant protein compartmentalization and cell polarity break-down.

In conclusion, taken together, the findings of the research projects carried out with this thesis work have shown the great potential of chitosan-derivative micelles as efficient drug and protein delivery nano vehicles. Thanks to the versatile chemistry and the physicochemical properties of the polymer matrix, engineered self-assembled nanocomplexes were successfully fabricated, characterized and delivered to various cellular systems, both in monolayers and in three-dimensional aggregates, where they were able to exert specific biological functions. The interdisciplinary, experimental strategies employed in this work may provide powerful chemical and biological tools for the targeting of cancer invasiveness at the tumor microenvironment. Ultimately, these approaches can assist the establishment of a valuable nanomedicine platform towards the effective eradication of neoplastic diseases.

References

- ¹ D. Hanahan, R.A. Weinberg, The hallmarks of cancer, *Cell*, 100 (2000) 57-70.
- ² D. Hanahan, R.A. Weinberg, Hallmark of Cancer: The Next Generation, *Cell*, 144 (2011) 646-674.
- ³ A.C. Society, *Cancer Facts & Figures*, Atlanta: American Cancer Society, (2014).
- ⁴ A.H. Stegh, Toward personalized cancer nanomedicine - past, present, and future, *Integrative Biology*, 5 (2013) 48-65.
- ⁵ K.Y. Choi, G. Liu, S. Lee, X.S. Chen, Theranostic nanoplateforms for simultaneous cancer imaging and therapy: current approaches and future perspectives, *Nanoscale*, 4 (2012) 330-342.
- ⁶ P.G. Corrie, Cytotoxic chemotherapy: clinical aspects, *Medicine*, 36 (2007) 24-28.
- ⁷ C. Holohan, S. Van Schaeybroeck, D.B. Longley, P.G. Johnston, Cancer drug resistance: an evolving paradigm, *Nature Reviews Cancer*, 13 (2013) 714-726.
- ⁸ I. Brigger, C. Dubernet, P. Couvreur, Nanoparticles in cancer therapy and diagnosis, *Advanced Drug Delivery Reviews*, 54 (2002) 631-651.
- ⁹ A. Vollrath, S. Schubert, U.S. Schubert, Fluorescence imaging of cancer tissue based on metal-free polymeric nanoparticles - a review, *Journal of Materials Chemistry B*, 1 (2013) 1994-2007.
- ¹⁰ R. Duncan, Polymer conjugates as anticancer nanomedicines, *Nature Reviews Cancer*, 6 (2006) 688-701.
- ¹¹ R. Trivedi, U.B. Kompella, Nanomicellar formulations for sustained drug delivery: strategies and underlying principles, *Nanomedicine*, 5 (2010) 485-505.
- ¹² Y. Nagasaki, M. Oishi, Stimuli-responsive smart nanogels for cancer diagnostics and therapy, *Nanomedicine*, 5 (2010) 451.
- ¹³ Y.M. Rane, E.B. Souto, Perspectives in Nanomedicine-Based Research Towards Cancer Therapies, *Current Nanoscience*, 7 (2011) 142-152.
- ¹⁴ H.M. Mansour, Y.S. Rhee, X. Wu, Nanomedicine in pulmonary delivery, *International Journal of Nanomedicine*, 4 (2009) 299-319.
- ¹⁵ ESF, *Nanomedicine: An ESF – European Medical Research Councils (EMRC) Forward Look report*, European Science Foundation Strasbourg cedex, France, 2004.
- ¹⁶ T.J. Webster, National Institute of Health, Roadmap for Medical Research: Nanomedicine, *International Journal of Medicine*, 1 (2006) 115-116.
- ¹⁷ C.L. Walsh, B.M. Babin, R.W. Kasinskas, J.A. Foster, M.J. McGarry, N.S. Forbes, A multipurpose microfluidic device designed to mimic microenvironment gradients and develop targeted cancer therapeutics, *Lab on a Chip*, 9 (2009) 545-554.
- ¹⁸ Y.H. Li, J. Wang, M.G. Wientjes, J.L.S. Au, Delivery of nanomedicines to extracellular and intracellular compartments of a solid tumor, *Advanced Drug Delivery Reviews*, 64 (2012) 29-39.
- ¹⁹ H. Hillaireau, P. Couvreur, Nanocarriers' entry into the cell: relevance to drug delivery, *Cellular and Molecular Life Sciences*, 66 (2009) 2873-2896.
- ²⁰ H. Maeda, J. Wu, T. Sawa, Y. Matsumura, K. Hori, Tumor vascular permeability and the EPR effect in macromolecular therapeutics: a review, *Journal of Controlled Release*, 65 (2000) 271-284.
- ²¹ Y. Matsumura, H. Maeda, A new concept of macromolecular therapeutics in cancer chemotherapy: mechanisms of tumor topic accumulation of proteins and antitumor agent SMANCS., *Cancer Research*, 46 (1986) 6387-6392.
- ²² K. Greish, Enhanced permeability and retention of macromolecular drugs in solid tumors: A royal gate for targeted anticancer nanomedicines, *Journal of Drug Targeting*, 15 (2007) 457-464.

- ²³ S.M. Moghimi, A.C. Hunter, J.C. Murray, Long-circulating and target-specific nanoparticles: Theory to practice, *Pharmacological Reviews*, 53 (2001) 283-318.
- ²⁴ Y. Aktas, M. Yemisci, K. Andrieux, R.N. Gursoy, M.J. Alonso, E. Fernandez-Megia, R. Novoa-Carballal, E. Quinoa, R. Riguera, M.F. Sargon, H.H. Celik, A.S. Demir, A.A. Hincal, T. Dalkara, Y. Capan, P. Couvreur, Development and brain delivery of chitosan-PEG nanoparticles functionalized with the monoclonal antibody OX26, *Bioconjugate Chemistry*, 16 (2005) 1503-1511.
- ²⁵ Y.G. Wang, K.J. Zhou, G. Huang, C. Hensley, X.N. Huang, X.P. Ma, T. Zhao, B.D. Sumer, R.J. DeBerardinis, J.M. Gao, A nanoparticle-based strategy for the imaging of a broad range of tumours by nonlinear amplification of microenvironment signals, *Nature Materials*, 13 (2014) 204-212.
- ²⁶ L. Brannon-Peppas, J.O. Blanchette, Nanoparticle and targeted systems for cancer therapy, *Advanced Drug Delivery Reviews*, 56 (2004) 1649-1659.
- ²⁷ M. Morille, C. Passirani, A. Vonarbourg, A. Clavreul, J.P. Benoit, Progress in developing cationic vectors for non-viral systemic gene therapy against cancer, *Biomaterials*, 29 (2008) 3477-3496.
- ²⁸ K.J. Cho, X. Wang, S.M. Nie, Z. Chen, D.M. Shin, Therapeutic nanoparticles for drug delivery in cancer, *Clinical Cancer Research*, 14 (2008) 1310-1316.
- ²⁹ S.D. Conner, S.L. Schmid, Regulated portals of entry into the cell, *Nature*, 422 (2003) 37-44.
- ³⁰ J.A. Swanson, C. Watts, Macropinocytosis, *Trends in Cell Biology*, 5 (1995) 424-428.
- ³¹ G.J. Doherty, H.T. McMahon, Mechanisms of Endocytosis, *Annual Reviews of Biochemistry*, 78 (2009) 857-902.
- ³² S. Mayor, R.E. Pagano, Pathways of clathrin-independent endocytosis, *Nature Reviews Molecular Cell Biology*, 8 (2007) 603-612.
- ³³ R. Duncan, S.C.W. Richardson, Endocytosis and Intracellular Trafficking as Gateways for Nanomedicine Delivery: Opportunities and Challenges, *Molecular Pharmaceutics*, 9 (2012) 2380-2402.
- ³⁴ K.A. Howard, Delivery of RNA interference therapeutics using polycation-based nanoparticles, *Advanced Drug Delivery Reviews*, 61 (2009) 710-720.
- ³⁵ C.W. Evans, M. Fitzgerald, T.D. Clemons, M.J. House, B.S. Padman, J.A. Shaw, M. Saunders, A.R. Harvey, B. Zdyrko, I. Luzinov, G.A. Silva, S.A. Dunlop, K.S. Iyer, Multimodal Analysis of PEI-Mediated Endocytosis of Nanoparticles in Neural Cells, *ACS Nano*, 5 (2011) 8640-8648.
- ³⁶ I.K. Ko, A. Ziady, S. Lu, Y.J. Kwon, Acid-degradable cationic methacrylamide polymerized in the presence of plasmid DNA as tunable non-viral gene carrier, *Biomaterials*, 29 (2008) 3872-3881.
- ³⁷ A. Shapira, Y.D. Livney, H.J. Broxterman, Y.G. Assaraf, Nanomedicine for targeted cancer therapy: Towards the overcoming of drug resistance, *Drug Resistance Updates*, 14 (2011) 150-163.
- ³⁸ S. Kunjachan, A. Blauz, D. Mockel, B. Theek, F. Kiessling, T. Etrych, K. Ulbrich, L. van Bloois, G. Storm, G. Bartosz, B. Rychlik, T. Lammers, Overcoming cellular multidrug resistance using classical nanomedicine formulations, *European Journal of Pharmaceutical Sciences*, 45 (2012) 421-428.
- ³⁹ P. Ma, R.J. Mumper, Anthracycline nano-delivery systems to overcome multiple drug resistance: A comprehensive review, *Nano Today*, 8 (2013) 313-331.

- ⁴⁰ E. Kobayashi, A.K. Iyer, F.J. Hornicek, M.M. Amiji, Z.F. Duan, Lipid-functionalized Dextran Nanosystems to Overcome Multidrug Resistance in Cancer: A Pilot Study, *Clinical Orthopaedics and Related Research*, 471 (2013) 915-925.
- ⁴¹ C. Riganti, C. Voena, J. Kopecka, P.A. Corsetto, G. Montorfano, E. Enrico, C. Costamagna, A.M. Rizzo, D. Ghigo, A. Bosia, Liposome-Encapsulated Doxorubicin Reverses Drug Resistance by Inhibiting P-Glycoprotein in Human Cancer Cells, *Molecular Pharmaceutics*, 8 (2011) 683-700.
- ⁴² M. Susa, A.K. Iyer, K. Ryu, F.J. Hornicek, H. Mankin, M.M. Amiji, Z.F. Duan, Doxorubicin loaded Polymeric Nanoparticulate Delivery System to overcome drug resistance in osteosarcoma, *Bmc Cancer*, 9 (2009) 12.
- ⁴³ X. Wang, Y. Cheng, F.Z. Dahmani, L.C. Yin, J.P. Zhou, J. Yao, Amphiphilic carboxymethyl chitosan-quercetin conjugate with P-gp inhibitory properties for oral delivery of paclitaxel, *Biomaterials*, 35 (2014) 7654-7665.
- ⁴⁴ H.Y. Yoon, S. Son, S.J. Lee, D.G. You, J.Y. Yhee, J.H. Park, M. Swierczewska, S. Lee, I.C. Kwon, S.H. Kim, K. Kim, M.G. Pomper, Glycol chitosan nanoparticles as specialized cancer therapeutic vehicles: Sequential delivery of doxorubicin and Bcl-2 siRNA, *Scientific Reports*, 4 (2014) 12.
- ⁴⁵ J.I. Fletcher, M. Haber, M.J. Henderson, M.D. Norris, ABC transporters in cancer: more than just drug efflux pumps, *Nature Reviews Cancer*, 10 (2010) 147-156.
- ⁴⁶ S. Tang, Q. Yin, Z.W. Zhang, W.W. Gu, L.L.L. Chen, H.J. Yu, Y.Z. Huang, X.Z. Chen, M.H. Xu, Y.P. Li, Co-delivery of doxorubicin and RNA using pH-sensitive poly (beta-amino ester) nanoparticles for reversal of multidrug resistance of breast cancer, *Biomaterials*, 35 (2014) 6047-6059.
- ⁴⁷ A.M. Chen, M. Zhang, D.G. Wei, D. Stueber, O. Taratula, T. Minko, H.X. He, Co-delivery of Doxorubicin and Bcl-2 siRNA by Mesoporous Silica Nanoparticles Enhances the Efficacy of Chemotherapy in Multidrug-Resistant Cancer Cells, *Small*, 5 (2009) 2673-2677.
- ⁴⁸ N.R. Patel, B.S. Pattni, A.H. Abouzeid, V.P. Torchilin, Nanopreparations to overcome multidrug resistance in cancer, *Advanced Drug Delivery Reviews*, 65 (2013) 1748-1762.
- ⁴⁹ A.K. Iyer, A. Singh, S. Ganta, M.M. Amiji, Role of integrated cancer nanomedicine in overcoming drug resistance, *Advanced Drug Delivery Reviews*, 65 (2013) 1784-1802.
- ⁵⁰ C. Daniel, C. Bell, C. Burton, S. Harguindey, S.J. Reshkin, C. Rauch, The role of proton dynamics in the development and maintenance of multidrug resistance in cancer, *Biochimica Et Biophysica Acta-Molecular Basis of Disease*, 1832 (2013) 606-617.
- ⁵¹ R. Liu, Y. Zhang, X. Zhao, A. Agarwal, L.J. Mueller, P. Feng, pH-Responsive Nanogated Ensemble Based on Gold-Capped Mesoporous Silica through an Acid-Labile Acetal Linker, *Journal of American Chemical Society Communication*, 132 (2010) 1500-1501.
- ⁵² L. Song, V.H. Ho, C. Chen, Z. Yang, D.M. Liu, R. Chen, Efficient, pH-triggered drug delivery using a pH-responsive DNA-conjugated gold nanoparticle. , *Advanced Healthcare Materials*, 2 (2013).
- ⁵³ L. Han, J.G. Zhao, X. Zhang, W. Cao, X. Hu, X. Duan, Enhanced siRNA delivery and silencing gold-chitosan nanosystem with surface charge-reversal polymer assembly and good biocompatibility. , *ACS Nano*, 6 (2012) 7340-7351.
- ⁵⁴ A. Ito, M. Shinkai, H. Honda, T. Kabayashi, Medical Application of Functionalized Magnetic Nanoparticles, *Journal of Bioscience and Bioengineering*, 100 (2005) 1-11.

- ⁵⁵ X. Hu, X. Hao, Y.P. Wu, J. Zhang, X.G. Zhang, P.C. Wang, G. Zou, X.J. Liang, Multifunctional hybrid silica nanoparticles for controlled doxorubicin loading and release with thermal and pH dual response, *Journal of Materials Chemistry B*, 1 (2013) 1109-1118.
- ⁵⁶ A.K. Gupta, M. Gupta, Synthesis and surface engineering of iron oxide nanoparticles for biomedical applications, *Biomaterials*, 26 (2005) 3995-4021.
- ⁵⁷ R. Banerjee, Y. Katsenovich, L. Lagos, M. McIntosh, X. SZhang, C.Z. Li, *Nanomedicine: Magnetic Nanoparticles and their Biomedical Applications*, *Current Medicinal Chemistry*, 17 (2010) 3120-3141.
- ⁵⁸ M.H. Hsiao, K.H. Lin, D.M. Liu, Improved pH-responsive amphiphilic carboxymethyl-hexanoyl chitosan-poly(acrylic acid) macromolecules for biomedical applications, *Soft Matter*, 9 (2013) 2458-2466.
- ⁵⁹ H.Y. Hwang, I.S. Kim, I.C. Kwon, Y.H. Kim, Tumor targetability and antitumor effect of docetaxel-loaded hydrophobically modified glycol chitosan nanoparticles, *Journal of Controlled Release*, 128 (2008) 23-31.
- ⁶⁰ J. Key, C. Cooper, A.Y. Kim, D. Dhawan, D.W. Knapp, K. Kim, J.H. Park, K. Choi, I.C. Kwon, K. Park, J.F. Leary, In vivo NIRF and MR dual-modality imaging using glycol chitosan nanoparticles, *Journal of Controlled Release*, 163 (2012) 249-255.
- ⁶¹ Z. Pan, Y.L. Gao, L.S. Heng, Y. Liu, G. Yao, Y. Wang, Y.P. Liu, Amphiphilic N-(2,3-dihydroxypropyl)-chitosan-cholic acid micelles for paclitaxel delivery, *Carbohydrate Polymers*, 94 (2013) 394-399.
- ⁶² X. Zhao, P. Liu, Q. Song, N. Gong, L. Yang, W.D. Wu, Surface charge-reversible polyelectrolyte complex nanoparticles for hepatoma-targeting delivery of doxorubicin, *Journal of Materials Chemistry B*, 3 (2015) 6185.
- ⁶³ Z.Q. Yuan, J.Z. Li, Y. Liu, W. Chen, S. Yang, C. Zhang, W. Zhu, X. Zhou, C. Liu, X. Zhang, Systemic delivery of micelles loading with paclitaxel using N-succinyl-palmitoyl-chitosan decorated with cRGDyK peptide to inhibit non-small-cell lung cancer, *International Journal of Pharmaceutics*, 492 (2015) 141-151.
- ⁶⁴ L. Fan, H. Wu, H. Zhang, L. F., T. WYang, T. Gu, Q. Yang, Novel super pH-sensitive nanoparticles responsive to tumor extracellular pH, *Carbohydrate Polymers*, 73 (2008).
- ⁶⁵ A. Di Martino, V. Sedlarik, Amphiphilic chitosan-grafted-functionalized polylactic acid based nanoparticles as a delivery system for doxorubicin and temozolomide co-therapy, *International Journal of Pharmaceutics*, 474 (2014) 134-145.
- ⁶⁶ M.R. Saboktakin, T. .M., A. Maharramov, M.A. Ramazanov, Design and characterization of chitosan nanoparticles as delivery systems for paclitaxel, *Carbohydrate Polymers*, 82 (2010) 466-471.
- ⁶⁷ H. Li, J. Liu, S. Ding, C. Zhang, W. Shen, Q. You, Synthesis of novel pH-sensitive chitosan graft copolymers and micellar solubilization of paclitaxel, *International Journal of Biological Macromolecules*, 44 (2009) 249-256.
- ⁶⁸ X. Xiangyang, L. Ling, Z. Jianping, L. Shiyue, Y. Jie, Y. Xiaojin, R. Jinsheng, Preparation and characterization of N-succinyl-N'-octyl chitosan micelles as doxorubicin carriers for effective anti-tumor activity, *Colloids and Surfaces B: Biointerfaces*, 55 (2007) 222-228.
- ⁶⁹ N. Rapoport, Stabilization and activation of pluronic micelles for tumor-targeted drug delivery, *Colloids and Surfaces B: Biointerfaces*, 16 (1999) 93-111.
- ⁷⁰ J. Liu, Y.R. Huang, A. Kumar, A. Tan, S.B. Jin, A. Mozhi, X.J. Liang, pH-Sensitive nano-systems for drug delivery in cancer therapy, *Biotechnology Advances*, 32 (2014) 693-710.

- ⁷¹ K. Engin, D.B. Leeper, J.R. Cater, A.J. Thistlethwaite, L. Tupchong, J.D. McFarlane, Extracellular pH distribution in human tumors, *International Journal of Hyperthermia*, 11 (1995) 211-216.
- ⁷² Y. Ma, X. Fan, L. Li, pH-sensitive polymeric micelles formed by doxorubicin conjugated prodrugs for co-delivery of doxorubicin and paclitaxel, *Carbohydrate Polymers*, 137 (2016) 19-29.
- ⁷³ R. Riva, H. Ragelle, A. Des Rieux, N. Duhem, C. Jerome, V. Preat, Chitosan and chitosan derivatives in drug delivery and tissue engineering, *Advances in Polymer Science*, 244 (2011) 19-44.
- ⁷⁴ H. Kamada, Y. Tsutsumi, Y. Yoshioka, Y. Yamamoto, H. Kodaira, S. Tsunoda, T. Okamoto, Y. Mukai, H. Shibata, S. Nakagawa, T. Mayumi, Design of a pH-sensitive polymeric carrier for drug release and its application in cancer therapy, *Clinical Cancer Research*, 10 (2004) 2545-2550.
- ⁷⁵ K. Ulbrich, T. Etrych, P. Chytil, M. Jelinkova, B. Rihova, Antibody-targeted polymer-doxorubicin conjugates with pH-controlled activation, *Journal of Drug Targeting*, 12 (2004) 477-489.
- ⁷⁶ F. Kratz, K. Abu Ajaj, A. Warnecke, Anticancer carrier-linked prodrugs in clinical trials, *Expert Opinion on Investigational Drugs*, 16 (2007) 1037-1058.
- ⁷⁷ A. Kakinoki, Y. Kaneo, T. Tanaka, Y. Hosokawa, Synthesis and evaluation of water-soluble Poly(vinyl alcohol)-paclitaxel conjugate as a macromolecular prodrug, *Biological & Pharmaceutical Bulletin*, 31 (2008) 963-969.
- ⁷⁸ M. Wang, T. Liu, L. Han, W. Gao, S. Yang, N. Zhang, Functionalized O-carboxymethyl-chitosan-polyethylenimine based novel dual pH-responsive nanocarriers for controlled co-delivery of DOX and genes, *Polymer Chemistry*, 6 (2015) 3324.
- ⁷⁹ E. Cabane, X.Y. Zhang, K. Langowska, C.G. Palivan, W. Meier, Stimuli-Responsive Polymers and Their Applications in Nanomedicine, *Biointerphases*, 7 (2012) 27.
- ⁸⁰ C.Y. Chuang, T.M. Don, W.Y. Chiu, Synthesis of Chitosan-Based Thermo- and pH-Responsive Porous Nanoparticles by Temperature-Dependent Self-Assembly Method and Their Application in Drug Release, *Journal of Polymer Science Part a-Polymer Chemistry*, 47 (2009) 5126-5136.
- ⁸¹ F. Wang, D. Zhang, C. Duan, L. Jia, F. Feng, Y. Liu, Y. Wang, L. Hao, Q. Zhang, Preparation and characterization of novel deoxycholic acid-O-carboxymethylated chitosan-folic acid conjugates and self-aggregates, *Carbohydrate Polymers*, 84 (2011) 1192-1200.
- ⁸² F. Wang, Y.A. Chen, D. Zhang, Q. Zhang, D. Zheng, L. Hao, Y. Liu, D. C., L. Jia, G. Liu, Folate-mediated targeted and intracellular delivery of paclitaxel using a novel deoxycholic acid-O-carboxymethylated chitosan-folic acid micelles, *International Journal of Nanomedicine*, 7 (2012) 325-337.
- ⁸³ M. Wang, Hu.H., Y. Sun, L. Qiu, J. Zhang, G. Guan, X. Zhao, Q. M., L. Cheng, L. Cheng, D. Chen, A pH-sensitive gene delivery system based on folic acid-PEG-chitosan_PAMAM-plasmid DNA complexes for cancer cell targeting, *Biomaterials*, 34 (2013) 10120-10132.
- ⁸⁴ M. Chopra, P. Kaur, M. Barnela, R. Thakur, Synthesis And Optimization of Streptomycin Loaded Chitosan-Alginate Nanoparticles, *International Journal of Scientific Research & Technology*, 1 (2012) 31-34.
- ⁸⁵ J. Liu, J. Jo, Y. Kawai, I. Aoki, C. Tanaka, M. Yamamoto, Y. Tabata, Preparation of polymer-based multimodal imaging agent to visualize the process of bone regeneration, *Journal of Controlled Release*, 157 (2012) 398-405.

- ⁸⁶ J.J. Wang, Z.W. Zeng, R.Z. Xiao, T.A. Xie, G.L. Zhou, X.R. Zhan, S.L. Wang, Recent advances of chitosan nanoparticles as drug carriers, *International Journal of Nanomedicine*, 6 (2011) 765-774.
- ⁸⁷ K. Nagpal, S.K. Singh, D.N. Mishra, Chitosan Nanoparticles: A Promising System in Novel Drug Delivery, *Chemical & Pharmaceutical Bulletin*, 58 (2010) 1423-1430.
- ⁸⁸ N. Duceppe, M. Tabrizian, Advances in using chitosan-based nanoparticles for in vitro and in vivo drug and gene delivery, *Expert Opinion on Drug Delivery*, 7 (2010) 1191-1207.
- ⁸⁹ B.R. Lee, K.T. Oh, H.J. Baik, Y.S. Youn, E.S. Lee, A charge-switched nano-sized polymeric carrier for protein delivery, *International Journal of Pharmaceutics*, 392 (2010) 78-82.
- ⁹⁰ H. Peniche, C. Peniche, Chitosan nanoparticles: a contribution to nanomedicine, *Polymer International*, 60 (2011) 883-889.
- ⁹¹ S.J. Shu, X.G. Zhang, D.Y. Teng, Z. Wang, C.X. Li, Polyelectrolyte nanoparticles based on water-soluble chitosan-poly (L-aspartic acid)-polyethylene glycol for controlled protein release, *Carbohydrate Research*, 344 (2009) 1197-1204.
- ⁹² A. Anitha, S. Maya, N. Deepa, K.P. Chennazhi, S.V. Nair, H. Tamura, R. Jayakumar, Efficient water soluble O-carboxymethyl chitosan nanocarrier for the delivery of curcumin to cancer cells, *Carbohydrate Polymers*, 83 (2011) 452-461.
- ⁹³ D. Hua, J. Jiang, L. Kuang, J. Jiang, W. Zheng, H. Liang, Smart chitosan-based stimuli-responsive nanocarriers for the controlled delivery of hydrophobic pharmaceuticals, *Macromolecules*, 44 (2011) 1298-1302.
- ⁹⁴ L. Jia, W. Zhong, T. Wen, G. Bian, Thermo and pH dual-responsive micelles of N-phtaloylchitosan-g-poly(N-isopropylacrylamide) and poly(acrylic acid-co-tert-butyl acrylate) for drug delivery, *Journal of Macromolecular Science, Part A*, 47 909-917.
- ⁹⁵ H.L. Chen, Z. Yinan, S. Cui, D. Zhi, S. Zhang, X. Peng, 6-O-dodecyl-chitosan carbamate-based pH-responsive polymeric micelles for gene delivery, *Journal of Applied Polymer Science*, (2015).
- ⁹⁶ J. Liu, H. Li, X. Jiang, C. Zhang, Q. Ping, Novel pH-sensitive chitosan-derived micelles loaded with paclitaxel, *Carbohydrate Polymers*, 82 (2010) 432-439.
- ⁹⁷ Z. Pan, Y. Gao, L.S. Heng, Y. Liu, G. TYao, Y. Wang, Y. Liu, Amphiphilic N-(2,3-dihydroxypropyl)-chitosan-cholic acid micelles for paclitaxel delivery, *Carbohydrate Polymers*, 94 (2013) 394-399.
- ⁹⁸ D. Qu, H. Lin, N. Zhang, J. Xue, C. Zhang, *In vitro* evaluation on novel modified chitosan for targeted antitumor drug delivery, *Carbohydrate Polymers*, 92 (2013) 545-554.
- ⁹⁹ X. Qu, V.V. Khutoryanskiy, A. Stewart, S. Rahman, B. Papahadjopoulos-Sternberg, C. Dufes, D. McCarhty, C.G. Wilson, R. Lyons, K.C. Carter, A. Schatzlein, I.F. Uchegbu, Carbohydrate-based micelle clusters which enhance hydrophobic drug bioavailability by up to 1 order of magnitude, *Biomacromolecules*, 7 (2006) 3452-3459.
- ¹⁰⁰ D.W. Chen, P. Song, F. Jiang, X. Meng, W. Sui, C. Shu, L.J. Wan, pH-responsive mechanism of a deoxycholic acid and folate comodified chitosan micelle under cancerous environment, *The Journal of Physical Chemistry B*, 117 (2013) 1261-1268.
- ¹⁰¹ F.Q. Hu, L.N. Liu, Y.Z. Du, H. Yuan, Synthesis and antitumor activity of doxorubicin conjugated stearic acid-g-chitosan oligosaccharide polymeric micelles, *Biomaterials*, 30 (2009) 6955-6963.
- ¹⁰² H. Du, X. Yang, X. Pang, G. Zhai, The synthesis, self-assembling and biocompatibility of a novel O-carboxymethyl chitosan cholate decorated with glycyrrhetic acid, *Carbohydrate Polymers*, 111 753-761.

- ¹⁰³ U. Termsarasab, I.S. Yoon, J.H. Park, H.T. Moon, H.J. Cho, D.D. Kim, Polyethylene glycol-modified arachidyl chitosan-based nanoparticles for prolonged blood circulation of doxorubicin, *International Journal of Pharmaceutics*, 464 (2014) 127-134.
- ¹⁰⁴ Y.S. Wang, L.R. Liu, Q. Jiang, Q.Q. Zhang, Self-aggregated nanoparticles of cholesterol-modified chitosan conjugate as a novel carrier of epirubicin, *European Polymer Journal*, 43 (2007) 43-51.
- ¹⁰⁵ J.M. Yu, X. Xie, M.R. Zheng, L. Yu, L. Zhang, J.G. Zhao, D.Z. Jiang, X.X. Che, Fabrication and characterization of nuclear localization signal-conjugated glycol chitosan micelles for improving the nuclear delivery of doxorubicin, *International Journal of Nanomedicine*, 7 (2012) 5079-5090.
- ¹⁰⁶ Y.H. Jin, H.Y. Hu, M.X. Qiao, J. Zhu, J.W. Qi, C.J. Hu, Q. Zhang, D.W. Chen, pH-sensitive chitosan-derived nanoparticles as doxorubicin carriers for effective anti-tumor activity: preparation and in vitro evaluation, *Colloids and Surfaces B-Biointerfaces*, 94 (2012) 184-191.
- ¹⁰⁷ T. Woraphatphadung, W. Sajomsang, P. Gonil, S. S., P. Opanasopit, Synthesis and characterization of pH-responsive N-naphthyl-N,O-succinyl chitosan micelles for oral meloxicam delivery, *Carbohydrate Polymers*, 121 (2015) 99-106.
- ¹⁰⁸ J.X. Niu, Z.G. Su, Y.Y. Xiao, A.W. Huang, H.Y. Li, X. Bao, S. Li, Y.A. Chen, M.J. Sun, Q.N. Ping, Octreotide-modified and pH-triggering polymeric micelles loaded with doxorubicin for tumor targeting delivery, *European Journal of Pharmaceutical Sciences*, 45 (2012) 216-226.
- ¹⁰⁹ J.J. Yan, Y.Z. Du, F.Y. Chen, Y. Jian, H. Yuan, F.Q. Hu, Effect of proteins with different isoelectric points on the gene transfection efficiency mediated by stearic acid grafted chitosan oligosaccharide micelles, *Molecular Pharmaceutics*, 10 (2013) 2568-2577.
- ¹¹⁰ Y.Z. Du, P. Lu, J.P. Zhou, H. Yuan, F.Q. Hu, Stearic acid grafted chitosan oligosaccharide micelle as a promising vector for gene delivery system: Factors affecting the complexation, *International Journal of Pharmaceutics*, 391 (2010) 260-266.
- ¹¹¹ J.H. Na, S.Y. Lee, S. Lee, H. Koo, K.H. Min, S.Y. Jeong, S.H. Yuk, K. Kim, I.C. Kwon, Effect of the stability and deformability of self-assembled glycol chitosan nanoparticles on tumor-targeting efficiency, *Journal of Controlled Release*, 163 (2012) 2-9.
- ¹¹² K. Kim, J.H. Kim, S. Kim, H. Chung, K. Choi, I.C. Kwon, J.H. Park, Y.S. Kim, R.W. Park, I.S. Kim, S.Y. Jeong, Self-assembled nanoparticles of bile acid-modified glycol chitosans and their applications for cancer therapy, *Macromolecular Research*, 13 (2005) 167-175.
- ¹¹³ C. Dufes, J.M. Muller, W. Couet, J.C. Olivier, I.F. Uchegbu, A.G. Schatzlein, Anticancer drug delivery with transferrin targeted polymeric chitosan vesicles, *Pharmaceutical Research*, 21 (2004) 101-107.
- ¹¹⁴ Y.I. Jeong, S.G. Jin, I.Y. Kim, J. Pei, M. Wen, T.Y. Jung, K.S. Moon, S. Jung, Doxorubicin-incorporated nanoparticles composed of poly(ethylene glycol)-grafted carboxymethyl chitosan and antitumor activity against glioma cells *in vitro*, *Colloids and Surfaces B-Biointerfaces*, 79 (2010) 149-155.
- ¹¹⁵ T.H. Kim, H. Jin, H.W. Kim, M.H. Cho, C.S. Cho, Mannosylated chitosan nanoparticle-based cytokine gene therapy suppressed cancer growth in BALB/c mice bearing CT-26 carcinoma cells, *Molecular Cancer Therapeutics*, 5 (2006) 1723-1732.
- ¹¹⁶ C.B. He, Y.P. Hu, L.C. Yin, C. Tang, C.H. Yin, Effects of particle size and surface charge on cellular uptake and biodistribution of polymeric nanoparticles, *Biomaterials*, 31 (2010) 3657-3666.

- ¹¹⁷ S.F. Peng, M.J. Yang, C.J. Su, H.L. Chen, P.W. Lee, M.C. Wei, H.W. Sung, Effects of incorporation of poly(γ -glutamic acid) in chitosan/DNA complex nanoparticles on cellular uptake and transfection efficiency, *Biomaterials*, 30 (2009) 1797-1808.
- ¹¹⁸ S.F. Peng, M.T. Tseng, Y.C. Ho, M.C. Wei, Z.X. Liao, H.W. Sung, Mechanisms of cellular uptake and intracellular trafficking with chitosan/DNA/poly(γ -glutamic acid) complexes as a gene delivery vector, *Biomaterials*, 32 (2011) 239-248.
- ¹¹⁹ D.R. Nogueira, L. Tavano, M. Mitjans, L. Perez, M.R. Infante, M.P. Vinardell, In vitro antitumor activity of methotrexate via pH-sensitive chitosan nanoparticles, *Biomaterials*, 34 (2013) 2758-2772.
- ¹²⁰ S. Kwon, J.H. Park, H. Chung, I.C. Kwon, S.Y. Jeong, I.S. Kim, Physicochemical characteristics of self-assembled nanoparticles based on glycol chitosan bearing 5 beta-cholanic acid, *Langmuir*, 19 (2003) 10188-10193.
- ¹²¹ S.Y. Park, H.J. Baik, Y.T. Oh, K.T. Oh, Y.S. Youn, E.S. Lee, A Smart Polysaccharide/Drug Conjugate for Photodynamic Therapy, *Angewandte Chemie-International Edition*, 50 (2011) 1644-1647.
- ¹²² S.E. Kim, I.C. Kwon, H.R. Song, K. Park, Insight of key factors influencing tumor targeting characteristics of glycol chitosan-based nanoparticles and *in vivo* applications, *Macromolecular Research*, 20 (2012) 1109-1117.
- ¹²³ J.H. Kim, Y.S. Kim, K. Park, E. Kang, S. Lee, H.Y. Nam, K. Kim, J.H. Park, D.Y. Chi, R.W. Park, I.S. Kim, K. Choi, I.C. Kwon, Self-assembled glycol chitosan nanoparticles for the sustained and prolonged delivery of antiangiogenic small peptide drugs in cancer therapy, *Biomaterials*, 29 (2008) 1920-1930.
- ¹²⁴ T. Nam, S. Park, S.Y. Lee, K. Park, K. Choi, I.C. Song, M.H. Han, J.J. Leary, S.A. Yuk, I.C. Kwon, K. Kim, S.Y. Jeong, Tumor targeting chitosan nanoparticles for dual-modality optical/MR cancer imaging, *Bioconjugate Chemistry*, 21 (2010) 578-582.
- ¹²⁵ H.Y. Nam, S.M. Kwon, H. Chung, S.Y. Lee, S.H. Kwon, H. Jeon, Y. Kim, J.H. Park, J. Kim, S. Her, Y.K. Oh, I.C. Kwon, K. Kim, S.Y. Jeong, Cellular uptake mechanism and intracellular fate of hydrophobically modified glycol chitosan nanoparticles, *Journal of Controlled Release*, 135 (2009) 259-267.
- ¹²⁶ S.J. Lee, H. Koo, D.E. Lee, S. Min, S. Lee, X.Y. Chen, Y. Choi, J.F. Leary, K. Park, S.Y. Jeong, I.C. Kwon, K. Kim, K. Choi, Tumor-homing photosensitizer-conjugated glycol chitosan nanoparticles for synchronous photodynamic imaging and therapy based on cellular on/off system, *Biomaterials*, 32 (2011) 4021-4029.
- ¹²⁷ A.L. Oliveira, A.J. Pedro, C.S. Arroyo, J.F. Mano, G. Rodriguez, J. San Roman, R.L. Reis, Biomimetic Ca-P Coatings Incorporating Bisphosphonates Produced on Starch-Based Degradable Biomaterials, *J. Biomed. Mater. Res. Part B*, 92B (2010) 55-67.
- ¹²⁸ J.H. Kim, Y.S. Kim, S. Kim, J.H. Park, K. Kim, K. Choi, H. Chung, S.Y. Jeong, R.W. Park, I.S. Kim, I.C. Kwon, Hydrophobically modified glycol chitosan nanoparticles as carriers for paclitaxel (Reprinted from *Journal of Controlled Release*, vol 109, pg 1, 2005), *Journal of Controlled Release*, 111 (2006) 228-234.
- ¹²⁹ Y.J. Son, J.S. Jang, Y.W. Cho, H. Chung, R.W. Park, I.C. Kwon, I.S. Kim, J.Y. Park, S.B. Seo, C.R. Park, S.Y. Jeong, Biodistribution and anti-tumor efficacy of doxorubicin loaded glycol-chitosan nanoaggregates by EPR effect, *Journal of Controlled Release*, 91 (2003) 135-145.

- ¹³⁰ S. Park, S.J. Lee, H. Chung, S. Her, Y. Choi, K. Kim, K. Choi, I.C. Kwon, Cellular uptake pathway and drug release characteristics of drug-encapsulated glycol chitosan nanoparticles in live cells, *Microscopy Research and Technique*, 73 (2010) 857-865.
- ¹³¹ K. Kim, J.H. Kim, H. Park, Y.S. Kim, K. Park, H. Nam, S. Lee, J.H. Park, R.W. Park, I.S. Kim, K. Choi, S.Y. Kim, K. Park, I.C. Kwon, Tumor-homing multifunctional nanoparticles for cancer theragnosis: Simultaneous diagnosis, drug delivery, and therapeutic monitoring, *Journal of Controlled Release*, 146 (2010) 219-227.
- ¹³² S.J. Lee, K. Park, Y.K. Oh, S.H. Kwon, S. Her, I.S. Kim, K. Choi, S.J. Lee, H. Kim, S.G. Lee, K. Kim, I.C. Kwon, Tumor specificity and therapeutic efficacy of photosensitizer-encapsulated glycol chitosan-based nanoparticles in tumor-bearing mice, *Biomaterials*, 30 (2009) 2929-2939.
- ¹³³ M.R. Huo, Y. Zhang, J.P. Zhou, A.F. Zou, D. Yu, Y.P. Wu, J. Li, H. Li, Synthesis and characterization of low-toxic amphiphilic chitosan derivatives and their application as micelle carrier for antitumor drug, *International Journal of Pharmaceutics*, 394 (2010) 162-173.
- ¹³⁴ K.T. Oh, D. Kim, H.H. You, Y.S. Ahn, E.S. Lee, pH-sensitive properties of surface charge-switched multifunctional polymeric micelle, *International Journal of Pharmaceutics*, 376 (2009) 134-140.
- ¹³⁵ X.W. Guan, Y.H. Li, Z.X. Jiao, J. Chen, Z.P. Guo, H.Y. Tian, X.S. Chen, A pH-sensitive charge-conversion system for doxorubicin delivery, *Acta Biomaterialia*, 9 (2013) 7672-7678.
- ¹³⁶ C.Y. Chen, T.H. Kim, W.C. Wu, C.M. Huang, H. Wei, C.W. Mount, Y.Q. Tian, S.H. Jang, S.H. Pun, A.K.Y. Jen, pH-dependent, thermosensitive polymeric nanocarriers for drug delivery to solid tumors, *Biomaterials*, 34 (2013) 4501-4509.
- ¹³⁷ Y. Lee, S. Fukushima, Y. Bae, S. Hiki, T. Ishii, K. Kataoka, A protein nanocarrier from charge-conversion polymer in response to endosomal pH, *Journal of the American Chemical Society*, 129 (2007) 5362-5363.
- ¹³⁸ J. Key, F.J. Leary, Nanoparticles for multimodal in vivo imaging in nanomedicine, *International Journal of Nanomedicine*, 9 (2014) 711-726.
- ¹³⁹ I.C. Sun, J.H. Na, S.Y. Jeong, D.E. Kim, I.C. Kwon, K. Choi, C.H. Ahn, K. Kim, Biocompatible glycol chitosan-coated gold nanoparticles for tumor-targeting CT imaging, *Pharmaceutical Research*, 31 (2014) 1418-1425.
- ¹⁴⁰ W. Yang, T. Mou, W. Guo, H. Jing, C. Peng, X. Zhang, Y. Ma, B. Liu, Fluorine-18 labeled galactosylated chitosan for asialoglycoprotein-receptor-mediated hepatocyte imaging, *Bioorganic & Medicinal Chemistry Letters*, 20 (2010) 4840-4844.
- ¹⁴¹ Y. Urano, D. Asanuma, Y. Hama, Y. Koyama, T. Barrett, M. Kamiya, T. Nagano, T. Watanabe, A. Hasegawa, P.L. Choyke, H. Kobayashi, Selective molecular imaging of viable cancer cells with pH-activatable fluorescence probes, *Nature Medicine*, 15 (2009) 104-109.
- ¹⁴² G.M. van Dam, G. Themelis, L.M.A. Crane, N.J. Harlaar, R.G. Pleijhuis, W. Kelder, A. Sarantopoulos, J.S. de Jong, H.J.G. Arts, A.G.J. van der Zee, J. Bart, P.S. Low, V. Ntziachristos, Intraoperative tumor-specific fluorescence imaging in ovarian cancer by folate receptor-alpha targeting: first in-human results, *Nature Medicine*, 17 (2011) 1315-1319.
- ¹⁴³ K. Nwe, C.H. Huang, A. Tsourkas, Gd-labeled glycol chitosan as a pH-responsive magnetic resonance imaging agent for detecting acidic tumor microenvironments, *Journal of Medicinal Chemistry*, 56 (2013) 7862-7869.
- ¹⁴⁴ I. Hajdu, G. Trencsenyi, M. Bodnar, M. Emri, G. Banfalvi, J. Sikula, T. Marian, J. Kollar, G. Vamosi, J. Borbely, Tumor-specific localization of self-assembled nanoparticle PET/MR modalities, *Anticancer Research*, (2014).

- ¹⁴⁵ J.Y. Yhee, S. Son, S.H. Kim, K. Park, K. Choi, I.C. Kwon, Self-assembled glycol chitosan nanoparticles for disease-specific theranostics, *Journal of Controlled Release*, 193 (2014) 202-213.
- ¹⁴⁶ A. Polyak, I. Hajdu, M. Bodnar, G. Trencsenyi, Z. Postenyi, V. Haasz, G. Janoki, G.A. KJanoki, L. Balogh, J. Borbely, ⁹⁹Tc-labelled nanosystem as tumor imaging agent for SPECT and SPECT/CT modalities, *International Journal of Pharmaceutics*, 449 (2013) 10-17.
- ¹⁴⁷ A. Polyak, I. Hajdu, M. Bodnar, G. Dabasi, R.P. Joba, J. Borbely, L. Balogh, Folate receptor targeted self-assembled chitosan-based nanoparticles for SPECT/CT imaging: demonstrating a preclinical proof of concept, *International Journal of Pharmaceutics*, 474 (2014) 91-94.
- ¹⁴⁸ N. Tsao, C.H. Wang, L.J. Her, K.Y. Tzen, J.Y. Chen, D.F. Yu, D.J. Yang, Development of ⁶⁸Ga-glycopeptide as an imaging probe for tumor angiogenesis, *Journal of Biomedicine and Biotechnology*, (2911).
- ¹⁴⁹ S. Lee, S. Kang, W., J.H. Ryu, J.H. Na, D.E. Lee, S.J. Han, C.M. Kang, Y.S. Choe, K.C. Lee, F.J. Leary, K. Choi, K.H. Lee, K. Kim, Tumor-homing glycol chitosan-based optical/PET dual imaging nanoprobe for cancer diagnosis, *Bioconjugate Chemistry*, 25 (2014) 601-610.
- ¹⁵⁰ W.I. Goldberg, Dynamic light scattering, *American Journal of Physics*, 67 (1999) 1152-1160.
- ¹⁵¹ M.I. Worldwide, *A basic guide to particle characterization*, 2012.
- ¹⁵² A. Sosnik, M.M. Raskin, Polymeric micelles in mucosal drug delivery: challenges towards clinical translation, *Biotechnology Advances*, 33 (2015) 1380-1392.
- ¹⁵³ Y. Matsumura, K. Kataoka, Preclinical and clinical studies of anticancer agent-incorporating polymer micelles, *Cancer Science*, 100 (2009) 572-579.
- ¹⁵⁴ K. Park, J.H. Kim, Y.S. Nam, S. Lee, H.Y. Nam, K. Kim, J.H. Park, I.S. Kim, K. Choi, S.Y. Kim, I.C. Kwon, Effect of polymer molecular weight on the tumor targeting characteristics of self-assembled glycol chitosan nanoparticles, *Journal of Controlled Release*, 122 (2007) 305-314.
- ¹⁵⁵ R. Gorlick, K. Janeway, S. Lessnick, R.L. Randall, N. Marina, Children's oncology group's 2013 blueprint for research: bone tumors, *Pediatric Blood & Cancer*, 60 (2013) 1009-1015.
- ¹⁵⁶ N.C. Daw, C.A. Billups, C. Rodriguez-Galindo, M.B. McCarville, B.N. Rao, A.M. Cain, J.J. Jenkins, M.D. Neel, W.H. Meyer, Metastatic Osteosarcoma. Results of two consecutive therapeutic trials at St. Jude Children's Research Hospital, *Cancer Immunology and Immunotherapy*, 106 (2006) 403-412.
- ¹⁵⁷ T. Kashima, K. Nakamura, J. Kawaguchi, M. Takanashi, T. Ishida, H. Aburatani, A. Kudo, M. Fukayama, A.E. Grigoriadis, Overexpression of cadherins suppresses pulmonary metastasis of osteosarcoma *in vivo*, *International Journal of Cancer*, 104 (2003) 147-154.
- ¹⁵⁸ A. Shen, Y. Zhang, H. Yang, R. Xu, G. Huang, Overexpression of ZEB1 relates to metastasis and invasion in osteosarcoma, *Journal of Surgical Oncology*, 105 (2012) 830-834.
- ¹⁵⁹ H.T. Ta, C.R. Dass, I. Larson, P.F.M. Choong, D.E. Dunstan, A chitosan hydrogel delivery system for osteosarcoma gene therapy with pigment epithelium-derived factor combined with chemotherapy, *Biomaterials*, 30 (2009) 4815-1823.
- ¹⁶⁰ M. Rebucci, C. Michiels, Molecular aspects of cancer cell resistance to chemotherapy, *Biochemical Pharmacology*, 85 (2013) 1219-1226.
- ¹⁶¹ Y. Niinaka, K. Harada, M. Fujimuro, M. Oda, A. Haga, M. Hosoki, N. Uzawa, N. Arai, S. Yamaguchi, M. Yamashiro, A. Raz, Silencing of autocrine motility factor induces mesenchymal-to-epithelial transition and suppression of osteosarcoma pulmonary metastasis, *Cancer Research*, 70 9483-9493.

- ¹⁶² E.P. Buddingh, M.W. Schilham, S.E.N. Ruslan, D. Berghuis, R.M. Egeler, M. Serra, P.C.W. Hogendoorn, A.C. Lankester, Chemotherapy-resistant osteosarcoma is highly susceptible to IL-15-activated allogeneic and autologous NK cells, *Cancer Immunology and Immunotherapy*, 60 (2011) 575-586.
- ¹⁶³ A.S. Hönicke, S.A. Ender, J. Radons, Combined administration of EGCG and IL-1 receptor antagonist efficiently downregulates IL-1-induced tumorigenic factors in U-2 OS human osteosarcoma cells, *International Journal of Oncology*, 41 (2012) 753-758.
- ¹⁶⁴ K. Ando, D. Heymann, K. Mori, Liposomal muramyl tripeptide phosphatidyl ethanolamine: a safe and effective agent against osteosarcoma pulmonary metastases, *Expert Review of Anticancer Therapy*, 8 (2008) 151-163.
- ¹⁶⁵ C.L. Schwartz, R. Gorlick, L. Teot, M. Krailo, Z. Chen, A. Goorin, H.E. Grier, M.L. Bernstien, P. Meyers, Multiple drug resistance in osteogenic sarcoma: INT0133 from the children's oncology group, *Journal of Clinical Oncology*, 25 (2007) 2057-2062.
- ¹⁶⁶ W. Yin, W. Li, D.A. Rubenstein, Y. Meng, Biocompatible and target specific hydrophobically modified glycol chitosan nanoparticles, *Biointerphases*, 11 (2016).
- ¹⁶⁷ G. Socrates, *Infrared and Raman Characteristic Group Frequencies: Tables and Charts*, Third Edition ed., New York, NY, USA, 2004.
- ¹⁶⁸ M.Z. Elsabee, R.E. Morsi, A.M. Al-Sabagh, Surface active properties of chitosan and its derivatives, *Colloids and Surfaces B: Biointerfaces*, 74 (2009) 1-16.
- ¹⁶⁹ S.J. Lee, H.S. Min, S.H. Ku, S. Son, I.C. Kwon, S.H. Kim, K. Kim, Tumor targeting glycol chitosan nanoparticles as a platform delivery carrier in cancer diagnosis and therapy, *Nanomedicine*, 9 (2014) 1697-1713.
- ¹⁷⁰ P. Perego, E. Corna, M. De Cesare, L. Gatti, D. Polizzi, G. Pratesi, R. Supino, F. Zunino, Role of apoptosis and apoptosis-related genes in cellular response and antitumor efficacy of anthracyclines, *Current Medicinal Chemistry*, 8 (2001) 31-37.
- ¹⁷¹ F. Kratz, A. Warnecke, B. Schmid, D.E. Chung, M. Gitzel, Prodrugs of anthracyclines in cancer chemotherapy, *Current Medicinal Chemistry*, 13 (2006) 477-523.
- ¹⁷² M.S. Horenstein, R.S. Heide, T.J. L'Ecuyer, Molecular basis of anthracycline-induced cardiotoxicity and its prevention, *Molecular Genetics and Metabolism*, 71 (2000) 436-444.
- ¹⁷³ B. Barbieri, F.C. Giuliani, T. Bordoni, A.M. Casazza, C. Geroni, O. Bellini, A. Suarato, B. Gioia, S. Penco, F. Arcamone, Chemical and biological characterization of 4'-Iodo-4'-deoxydoxorubicin, *Cancer Research*, 47 (1987) 4001-4006.
- ¹⁷⁴ M. Ripamonti, G. Pezzoni, E. Pesenti, A. Pastori, M. Farao, A. Bargiotti, A. Suarato, F. Spreafico, M. Grandi, *In vivo* anti-tumor activity of FCE 23762, a methoxymorpholinyl derivative of doxorubicin active on doxorubicin-resistant tumor cells, *British Journal of Cancer*, 65 (1992) 703-707.
- ¹⁷⁵ A. Suarato, Antitumor anthracyclines, in: C. Hall (Ed.) *Chemistry of Antitumor Agents*, Blackie, New York, pp. 30-59.
- ¹⁷⁶ A. Suarato, F. Angelucci, A. Bargiotti, Antitumor anthracyclines, *Chimicaoggi*, (1990) 9-19.
- ¹⁷⁷ W. Ye, A.H. Teng, D.Z. Liu, H. Cui, M. Liu, Y. Cheng, T.H. Yang, Q.B. Mei, S.Y. Zhou, Synthesis of a new pH-sensitive folate-doxorubicin conjugate and its antitumor activity *in vitro*, *Journal of Pharmaceutical Sciences*, 102 (2013) 530-540.
- ¹⁷⁸ D. Missirlis, R. Kawamura, N. Tirelli, J.A. Hubbell, Doxorubicin encapsulation and diffusional release from stable, polymeric, hydrogel nanoparticles, *European Journal of Pharmaceutical Sciences*, 29 (2006) 120-129.

- ¹⁷⁹ K. Kataoka, T. Matsumoto, M. Yokoyama, T. Okano, Y. Sakurai, S. Fukushima, K. Okamoto, G.S. Kwon, Doxorubicin-loaded poly(ethylene glycol)-poly(beta-benzyl-L-aspartate) copolymer micelles: their pharmaceutical characteristics and biological significance, *Journal of Controlled Release*, 64 (2000) 143-153.
- ¹⁸⁰ C. Wang, L. Cheng, Z. Liu, Drug delivery with upconversion nanoparticles for multi-functional targeted cancer cell imaging and therapy, *Biomaterials*, 32 (2011) 1110-1120.
- ¹⁸¹ F.J. Pavinatto, A. Pavinatto, L. Caseli, D.S. dos Santos, T.M. Nobre, M.E.D. Zaniquelli, O.N. Oliveira, Interaction of chitosan with cell membrane models at the air-water interface *Biomacromolecules*, 8 (2007) 1633-1640.
- ¹⁸² D.R. Hristov, L. Rocks, P.M. Kelly, S.S. Thomas, A.S. Pitek, P. Verderio, E. Mahon, K.A. Dawson, Tuning of nanoparticle biological functionality through controlled surface chemistry and characterization at the bioconjugated nanoparticle surface, *Scientific Reports*, 5 (2015).
- ¹⁸³ S.M. Alex, C.P. Sharma, Enhanced intracellular uptake and endocytic pathway selection mediated by hemocompatible ornithine grafted chitosan polycation, *Colloids and Surfaces B: Biointerfaces*, 122 (2014) 792-800.
- ¹⁸⁴ M. Huang, E. Khor, L.Y. Lim, Uptake and cytotoxicity of chitosan molecules and nanoparticles: effects of molecular weight and degree of deacetylation, *Pharmaceutical Research*, 21 (2004) 344-353.
- ¹⁸⁵ B. Alberts, A. Johnson, J. Lewis, M. Raff, K. Roberts, P. Walter, *Molecular Biology of the Cell*, Fifth Edition ed.2008.
- ¹⁸⁶ X. Dai, Z. Yue, M.E. Eccleston, J. Swartling, N.K.H. Slater, C.F. Kaminski, Fluorescence intensity and lifetime imaging of free and micellar-encapsulated doxorubicin in living cells, *Nanomedicine*, 4 (2008) 49-56.
- ¹⁸⁷ S.M. Sagnella, H. Duong, A. MacMillan, C. Boyer, R. Whan, J.A. McCarroll, T.P. Davis, M. Kavallaris, Dextran-based doxorubicin nanocarriers with improved tumor penetration, *Biomacromolecules*, 15 (2014) 262-275.
- ¹⁸⁸ J. Yu, X. Xie, M. Zheng, L. Yu, L. Zhang, J. Zhao, D. Jiang, X. Che, Fabrication and characterization of nuclear localization signal-conjugation glycol chitosan micelles for improving the nuclear delivery of doxorubicin, *International Journal of Nanomedicine*, 7 (2012) 5079-5090.
- ¹⁸⁹ T. Thambi, D.G. You, H.S. Han, V.G. Deepagan, S.M. Jeon, Y.D. Suh, K.Y. Choi, K. Kim, I.C. Kwon, G.R. Yi, J.Y. Lee, D.S. Lee, J.H. Park, Bioreducible carboxymethyl dextran nanoparticles for tumor-targeted drug delivery, *Advance Healthcare Materials*, (2014).
- ¹⁹⁰ L. Sitia, R. Ferrari, M.B. Violatto, L. Talamini, L. Dragoni, C. Colombo, L. Colombo, M. Lupi, P. Ubezio, M. D'Incalci, M. Morbidelli, M. Salmona, D. Moscatelli, P. Bigini, Fate of PLA and PCL-based polymeric nanocarriers in cellular and animal models of triple-negative breast cancer, *Biomacromolecules*, 17 (2016) 744-755.
- ¹⁹¹ H.L. Ma, Q. Jiang, S. Han, Y. Wu, J.C. Tomshine, D. Wang, Y. Guan, G. Zou, X.J. Liang, Multicellular tumor spheroids as an *in vivo*-like tumor model for three dimensional imaging of chemotherapeutic and nano material cellular penetration, *Molecular Imaging*, 11 (2012) 487-498.
- ¹⁹² W.M. Guo, X.J. Loh, E.Y. Tan, J.S.C. Loo, V.H.B. Ho, Development of a magnetic 3D spheroid platform with potential application for high-throughput drug screening, *Molecular Pharmaceutics*, 11 (2014) 2182-2189.
- ¹⁹³ T.H. Kim, C.W. Mount, W.R. Gombotz, S.H. Pun, The delivery of doxorubicin to 3-D multicellular spheroids and tumors in a murine xenograft model using tumor-penetrating triblock polymeric micelles, *Biomaterials*, 31 (2010) 7385-7397.

- ¹⁹⁴ X. Wang, X. Zhen, J. Wang, J. Zhang, W. Wu, X. Jiang, Doxorubicin delivery to 3D multicellular spheroids and tumors based on boronic acid-rich chitosan nanoparticles, *Biomaterials*, 34 (2013) 4667-4679.
- ¹⁹⁵ T.R. Cawthorn, J.C. Moreno, M. Dharsee, D. Tran-Thanh, S. Ackloo, P.H. Zhu, G. Sardana, J. Chen, P. Kupchak, L.M. Jacks, N.A. Miller, B.J. Youngson, V. Iakovlev, C.J. Guidos, K.A. Vallis, K.R. Evans, D. McCready, W.L. Leong, S.J. Done, Proteomic analyses reveal high expression of decorin and endoplasmic chaperone (HSP90B1) are associated with breast cancer metastasis and decreased survival, *PLOS ONE*, 7 (2012).
- ¹⁹⁶ M.H. Forouzanfar, K.J. HForeman, A.M. Delossantos, R. Lozano, A.D. Lopez, Breast and cervical cancer in 187 countries between 1980 and 2010: a systematic analysis, *The Lancet*, 387 (2011) 1461-1484.
- ¹⁹⁷ R. Poincloux, F. Lizárraga, P. Chavrier, Matrix invasion by tumor cells: a focus on MT1-MMP trafficking to invadopodia, *Journal of Cell Science*, 122 (2009) 3015-3024.
- ¹⁹⁸ C. Schmidt, When tumor cells travel, *CR Magazine*, 2007.
- ¹⁹⁹ J. Cathcart, A. Pulkoski-Gross, J. Cao, Targeting matrix metalloproteinases in cancer: bringing new life to old ideas, *Genes & Diseases*, 2 (2015) 26-34.
- ²⁰⁰ R. Bhat, M.J. Bissell, Of plasticity and specificity: dialectics of the microenvironment and macroenvironment and the organ phenotype, *WIREs Dev Biol*, 3 (2014) 147-163.
- ²⁰¹ M.J. Bissell, W.C. Hines, Why don't we get more cancer? A proposed role of the microenvironment in restraining cancer progression, *Nature Medicine*, 17 (2011) 320-329.
- ²⁰² A.L. Correia, M.J. Bissell, The tumor microenvironment is a dominant force in multidrug resistance, *Drug Resistance Updates*, 15 (2012) 39-49.
- ²⁰³ R. Xu, A. Boudreau, M.J. Bissell, Tissue architecture and function: dynamic reciprocity via extra- and intra-cellular matrices, *Cancer Metastasis Review*, 28 (2009) 167-176.
- ²⁰⁴ J. Cao, C. Chiarelli, O. Richman, K. Zarrabi, P. Kozarekar, S. Zucker, Membrane type 1 matrix metalloproteinase induces epithelial-to-mesenchymal transition in prostate cancer, *Journal of Biological Chemistry*, 283 (2008) 6232-6240.
- ²⁰⁵ S. Pahwa, M.J. Stawikowski, G.B. Fields, Monitoring and inhibiting MT1-MMP during cancer initiation and progression, *Cancers*, 6 (2014) 416-435.
- ²⁰⁶ A. Jacob, R. Prekeris, The regulation of MMP targeting to invadopodia during cancer metastasis, *Frontiers in Cell and Developmental Biology*, 3 (2015).
- ²⁰⁷ U.B. Hofmann, R. Houben, E.B. Bröcker, J.C. Becker, Role of matrix metalloproteinases in melanoma cell invasion, *Biochimie*, 87 (2005) 307-314.
- ²⁰⁸ J. Cao, C. Chiarelli, P. Kozarekar, H.L. Adler, Membrane type 1-matrix metalloproteinase promotes human prostate cancer invasion and metastasis, *Thrombosis and Haemostasis*, 93 (2005) 770-778.
- ²⁰⁹ K. Zarrabi, A. Dufour, J. Li, C. Kuscu, A. Pulkoski-Gross, J. Zhi, Y. Hu, N.S. Sampson, S. Zucker, J. Cao, Inhibition of matrix metalloproteinase 14 (MMP-14)-mediated cancer cell migration, *Journal of Biological Chemistry*, 286 (2011) 33167-33177.
- ²¹⁰ J. Cao, P. Kozarekar, M. Pavlaki, C. Chiarelli, W.F. Bahou, S. Zucker, Distinct roles for the catalytic and hemopexin domains of membrane type 1-matrix metalloproteinase in substrate degradation and cell migration, *The Journal of Biological Chemistry*, 279 (2004) 14129-14139.
- ²¹¹ S.R. Grobmyer, G. Zhou, L.G. Gutwein, N. Iwakuma, P. Sharma, S.N. Hochwald, Nanoparticle delivery for metastatic breast cancer, *Nanomedicine: Nanotechnology, Biology and Medicine*, 8 (2012) S21-S30.

- ²¹² J. Choi, H. Kim, Y. Choi, Theranostic nanoparticles for enzyme-activable fluorescence imaging and photodynamic/chemo dual therapy of triple-negative breast cancer, *Quantitative Imaging in Medicine and Surgery*, 5 (2015) 656-664.
- ²¹³ A. Chin, G. Suarato, Y. Meng, Evaluation of physicochemical characteristics of hydrophobically modified glycol chitosan nanoparticles and their biocompatibility in murine osteosarcoma and osteoblast-like cells, *Journal of Nanotechnology and Smart Materials*, 1 (2014).
- ²¹⁴ Z. Liu, H.G. Floss, J.M. Cassady, K.K. Chan, Metabolism studies of the anti-tumor agent maytansine and its analog ansamitocin P-3 using liquid chromatography/tandem mass spectroscopy, *Journal of Mass Spectrometry*, 40 (2005) 389-399.
- ²¹⁵ Z. Liu, H.G. Floss, J.M. Cassady, J. Xiao, K.K. Chan, An API LC/MS/MS quantification method for ansamitocin P-3 (AP3) and its preclinical pharmacokinetics, *Journal of Pharmaceutical and Biomedical Analysis*, 35 (2004) 815-821.
- ²¹⁶ G.Z. Wei, L.Q. Bai, T. Yang, J. Ma, Y. Zeng, Y.M. Shen, P.J. Zhao, A new antitumor ansamitocin from *Actinosynnema pretiosum*, *Natural Product Research*, 24 (2010) 1146-1150.
- ²¹⁷ P. Tassone, A. Gozzini, V. Goldmacher, M.A. Shammash, K.R. Whiteman, D.R. Carrasco, C. Li, C.K. Allam, S. Venuta, K.C. Anderson, N.C. Munchi, *In vitro* and *in vivo* activity of the Maytansinoid Immunoconjugate huN901-N²-Deacetyl-N²-(3-mercapto-1-oxopropyl)-Maytansine against CD56⁺ multiple myeloma cells, *Cancer Research*, 64 (2004) 4629 - 4636.
- ²¹⁸ H. Ikeda, T. Hideshima, M. Fulciniti, R.J. Lutz, H. Yasui, Y. Okawa, T. Kiziltepe, S. Vallet, S. Pozzi, L. Santo, B. Dalken, S. Aigner, F. Osterroth, N. Munshi, P. Richardson, K.C. Anderson, The monoclonal antibody nBT062 conjugated to cytotoxic maytansinoids has selective cytotoxicity against CD138-positive multiple myeloma cells *in vitro* and *in vivo*, *Cancer Therapy: Preclinical*, 15 (2009) 4028-4037.
- ²¹⁹ J.B. Venghateri, T.K. Gupta, P.J. Verma, A. Kunwar, D. Panda, Ansamitocin P3 depolymerizes microtubules and induces apoptosis by binding to tubulin at the vinblastine site, *PLOS ONE*, 8 (2013).
- ²²⁰ k. Okamoto, K. Harada, S. Ikeyama, S. Iwasa, Therapeutic effect of ansamitocin targeted of tumor by a bispecific monoclonal antibody, *Japanese Journal of Cancer Research*, 83 (1992) 761-768.
- ²²¹ J.A. Reddy, E. Westrick, H.K.R. Santhapuram, S.J. Howard, M.L. Miller, M. Vetzal, I. Vlahov, R.V.J. Chari, V. Goldmacher, C.P. Leamon, Folate receptor-specific antitumor activity of EC131 a folate-maytansinoid conjugate, *Cancer Research*, 67 (2007) 6376-6382.
- ²²² Y. Yao, Z. Cheng, H. Ye, Y. Xie, J. He, M. Tang, T. Shen, J. Wang, Y. Zhou, Z. Lu, F. Luo, C. L., L. Yu, J. Yang, Y. Wei, Preparative isolation and purification of anti-tumor agent ansamitocin P-3 from fermentation broth of *Actinosynnema pretiosum* using high-performance counter-current chromatography, *Journal of Separation Science*, 33 (2010) 1331-1337.
- ²²³ F.R. Maxfield, T.E. McGraw, Endocytic Recycling, *Nature Molecular Cell Biology*, 5 (2004) 121-132.
- ²²⁴ E. Seydoux, B. Rothen-Rutishauser, S.M. Nita, S. Balog, A. Gazdhar, P.A. Stumbles, A. Petri-Fink, F. Blank, C. von Garnier, Size-dependent accumulation of particles in lysosomes modulates dendritic cell function through impaired antigen degradation, *International Journal of Nanomedicine*, 9 (2014) 3885-3902.
- ²²⁵ J. Li, S. Zucker, A. Pulkoski-Gross, C. Kuscus, M. Karaayvaz, J. Ju, H. Yao, E. Song, J. Cao, Conversion of stationary to invasive tumor initiating cells (TICs): role of hypoxia in membrane type 1-matrix metalloproteinase (MT1-MMP) trafficking, *PLOS ONE*, 7 (2012).

- ²²⁶ S. Breslin, L. O'Driscoll, Three-dimensional cell culture: the missing link in drug discovery, *Drug Discovery Today*, 18 (2013) 240-249.
- ²²⁷ F. Pampaloni, E.G. Reynaud, E.H. Stelzer, The third dimension bridges the gap between cell culture and live tissue, *Nature Review Molecular Cell Biology*, 8 (2007) 839-845.
- ²²⁸ C. Heylman, A. Sobrino, V.S. Shirure, C.C.W. Hughes, S.C. George, A strategy for integrating essential three-dimensional microphysiological systems of human organs for realistic anticancer drug screening, *Experimental Biology and Medicine*, 239 (2014) 1240-1254.
- ²²⁹ G. Mehta, A.Y. Hsiao, M. Ingram, G.D. Luker, S. YTakayama, Opportunities and challenges for use of tumor spheroids as models to test drug delivery and efficacy, *Journal of Controlled Release*, 164 (2012) 192-204.
- ²³⁰ K.S.M. Smalley, M. Lioni, M. Herlyn, Life isn't flat: taking cancer biology to the next dimension, *In vitro Cellular & Developmental Biology*, 42 (2006) 242-247.
- ²³¹ X. Jiang, H. Xian, J. Gu, F. Du, C. Feng, Y. Xie, X. Fang, Enhanced antitumor efficacy by D-glucosamine-functionalized and paclitaxel-loaded poly(ethylene glycol)-co-poly(trimethylene carbonate) polymer nanoparticles, *Pharmaceutics, Drug Delivery and Pharmaceutical Technology*, 103 (2014) 1487-1496.
- ²³² A.I. Minchinton, I.F. Tannock, Drug penetration in solid tumors, *Nature Reviews*, 6 (2006) 583-592.
- ²³³ E. Urich, C. Patsch, S. Aigner, M. Graf, R. Iacone, P.O. Freskgard, Multicellular self-assemble spheroidal model of the blood brain barrier, *Scientific Reports*, 3 (2013).
- ²³⁴ S. Sart, A.C. Tsai, Y. Li, T. Ma, Three-dimensional aggregates of mesenchymal stem cells: cellular mechanisms, biological properties, and applications, *Tissue Engineering: Part B*, 20 (2014) 365-380.
- ²³⁵ M. Rimann, U. Graf-Hausner, Synthetic 3D multicellular systems for drug development, *Current Opinion in Biotechnology*, 23 (2012) 803-809.
- ²³⁶ M. Rimann, S. Laternser, A. Gvozdenovic, R. Muff, B. Fuchs, J.M. Kelm, U. Graf-Hausner, An *in vitro* osteosarcoma 3D microtissue model for drug development, *Journal of Biotechnology*, 189 (2014) 129-135.
- ²³⁷ A.S. Mikhail, S. Etezadi, C. Allen, Multicellular tumor spheroids for evaluation of cytotoxicity and tumor growth inhibitory effects of nanomedicines *in vitro*: a comparison of docetaxel-loaded block copolymer micelles and taxotere, *PLOS ONE*, 8 (2013).
- ²³⁸ Y.J. Huang, S.H. Hsu, Acquisition of epithelial-mesenchymal transition and cancer stem-like phenotypes within chitosan-hyaluronan membrane-derived 3D tumor spheroids, *Biomaterials*, 35 (2014) 10070-10079.
- ²³⁹ Y. Gao, M. Li, B. Chen, Z. Shen, P. Guo, M.G. Wuentjes, J.L.S. Au, Predictive models of diffusive nanoparticle transport in 3-dimensional tumor cell spheroids, *The AAPS Journal*, 15 (2013) 816-831.
- ²⁴⁰ J. Friedrich, C. Seidel, R. Ebner, L.A. SKunz-Schughart, Spheroid-based drug screen: considerations and practical approach, *Nature Protocols*, 3 (2009) 309-324.
- ²⁴¹ E.C. Costa, V.M. Gaspar, P. Coutinho, I.J. Correia, Optimization of liquid overlay technique to formulate heterogenic 3D co-culture models, *Biotechnology and Bioengineering*, 111 (2014) 1672-1685.
- ²⁴² J.S. Basuki, H.T.T. Duong, A. Macmillan, R.B. Erlich, L. Lesser, M.C. Akerfeldt, R.M. Whan, M. Kavallaris, C. Boyer, T.P. Davis, Using fluorescence lifetime imaging microscopy to monitor thernostic nanoparticle uptake and intracellular doxorubicin release, *ACS NANO*, 11 (2013) 10175-10189.

- ²⁴³ Y.C. Tung, A.Y. Hsiao, S.G. Allen, Y. Torisawa, M. Ho, S. Takayama, High-throughput 3D spheroid culture and drug testing using a 384 hanging drop array, *Analyst*, 136 (2011) 473-478.
- ²⁴⁴ X. Xu, M.C. Farach-Carson, X. Jia, Three-dimensional *in vitro* tumor models for cancer research and drug evaluation, *Biotechnology Advances*, 32 (2014) 1256-1268.
- ²⁴⁵ A.P. Napolitano, D.M. Dean, A.J. Man, J. Youssef, D.N. Ho, A.P. Rago, M.P. Lech, J.R. Morgan, Scaffold-free three-dimensional cell culture utilizing micromolded nonadhesive hydrogels, *BioTechniques*, 43 494-500.
- ²⁴⁶ E. Fennema, N. Rivron, J. Rouwkema, C. van Blitterswijk, J. de Boer, Spheroid culture as a tool for creating 3D complex tissues, *Trends in Biotechnology*, 31 (2013) 106-115.
- ²⁴⁷ P. Indovina, G. Rainaldi, M.T. Santini, Hypoxia increases adhesion and spreading of MG-63 three-dimensional tumor spheroids, *Anticancer Research*, 28 (2008) 1013-1022.
- ²⁴⁸ P. Indovina, M. Collini, G. Chirico, M.T. Santini, Three-dimensional cell organization leads to almost immediate HRE activity as demonstrated by molecular imaging of MG-63 spheroids using two-photon excitation microscopy, *FEBS Letters*, 581 (2007) 719-726.
- ²⁴⁹ W. Chen, C. Ong, E. Vosburgh, A.J. Levine, D.J. Foran, E.Y. Xu, High-throughput image analysis of tumor spheroids: a user-friendly software application to measure the size of spheroids automatically and accurately, *Journal of Visualized Experiments*, 89 (2014).
- ²⁵⁰ H. Gao, Q. Zhang, Y. Yang, X. Jiang, Q. He, Tumor homing cell penetrating peptide decorated nanoparticles used for enhancing tumor targeting delivery and therapy, *International Journal of Pharmaceutics*, 478 (2015) 240-250.
- ²⁵¹ A.S. Mikhail, S. Eteziadi, S.N. Ekdawi, J. Stewart, Image-based analysis of the size- and time-dependent penetration of polymeric micelles in multicellular tumor spheroids and tumor xenografts, *International Journal of Pharmaceutics*, 464 (2014) 168-177.
- ²⁵² Q. Zhang, J. Tang, L. Fu, R. Ran, Y. Liu, M. Yuan, Q. He, A pH-responsive alpha-helical cell penetrating peptide-mediated liposomal delivery system, *Biomaterials*, 34 (2013) 7980-7993.
- ²⁵³ J. Li, Y. Han, Q. Chen, H. Shi, S. Rehman, M. Siddiq, Z. Ge, S. Liu, Dual endogenous stimuli-responsive polyplex micelles as smart two-step delivery nanocarriers for deep tumor tissue penetration and combating drug resistance of cisplatin, *Journal of Material Chemistry B*, 2 (2014) 1813-1824.
- ²⁵⁴ M. Zanoni, F. Piccinini, C. Arienti, A. Zamagni, S. Santi, R. Polico, A. Bevilaqua, A. Tesei, 3D tumor spheroid models for *in vitro* therapeutic screening: a systematic approach to enhance the biological relevance of data obtained, *Scientific Reports*, 6 (2016).
- ²⁵⁵ B.W. Graf, S.A. Boppart, *Imaging and analysis of three-dimensional cell culture models*, *Methods in Molecular Biology*, Humana Press 2010.
- ²⁵⁶ C. Sarisozen, A.H. Abouzeid, V.P. Torchilin, The effect of co-delivery of paclitaxel and curcumin by transferrin-targeted PEG-PE-based mixed micelles on resistant ovarian cancer in 3-D spheroids and *in vivo* tumors, *European Journal of Pharmaceutics and Biopharmaceutics*, 88 (2014) 539-550.
- ²⁵⁷ M. Han, Y. Bae, N. Nishiyama, K. Miyata, M. Oba, K. Kataoka, Transfection study using multicellular tumor spheroids for screening non-viral polymeric gene vectors with low cytotoxicity and high transfection efficiencies, *Journal of Controlled Release*, 121 (2007) 38-48.
- ²⁵⁸ H. Liang, X. Ren, J. Quian, X. Zhang, L. Meng, X. Wang, L. Li, X. Fang, X. Sha, Size-shifting micelle nanoclusters based on a cross-linked and pH-sensitive framework for enhanced tumor targeting and deep penetration features, *Applied Materials & Interfaces*.

- ²⁵⁹ W.Y. Ho, S.K. Yeap, C.L. Ho, R.A. Rahim, N.B. Alitheen, Development of multicellular tumor spheroid (MCTS) culture from breast cancer cell and high throughput screening method using the MTT assay, *PLOS ONE*, 7 (2012).
- ²⁶⁰ M. Upreti, A. Jamshidi-Parsian, N.A. Koonce, J.S. Webber, S.K. Sharma, A.A.A. Asea, M.J. Mader, R.J. Griffin, Tumor-endothelial cell three-dimensional spheroids: new aspects to enhance radiation and drug therapeutics, *Translational Oncology*, 4 (2011) 365-376.
- ²⁶¹ A.I. Marcus, W. Zhou, LKB1 regulated pathways in lung cancer invasion and metastasis, *Journal of Thoracic Oncology*, 5 (2010) 1883-1886.
- ²⁶² S.N. Wingo, T.D. Gallardo, E.A. Akbay, M.C. Liang, C.M. Contreas, T. Boren, T. Shimamura, D.S. Miller, N.E. Sharpless, N. Bardeesy, D.J. Kwiatkowski, J.O. Schorge, K.K. Wong, D.H. Castrillon, Somatic LKB1 mutations promote cervical cancer progression, *PLOS ONE*, 4 (2009).
- ²⁶³ N. Arimura, K. Kaibuchi, Neuronal polarity: from extracellular signals to intracellular mechanisms, *Nature Reviews Neuroscience*, 8 (2007) 194-205.
- ²⁶⁴ A.P. Barnes, F. Polleux, Establishment of axon-dendrite polarity in developing neurons, *Annual Reviews in Neuroscience*, 32 (2009) 347-381.
- ²⁶⁵ C.G. Dotti, C.A. Sullivan, G.A. Banker, The establishment of polarity by hippocampal neurons in culture, *The Journal of Neuroscience*, 8 (1988) 1454-1468.
- ²⁶⁶ C.G. Dotti, G.A. Banker, Experimentally induced alteration in the polarity of developing neurons, *Nature*, 330 (1987) 254-256.
- ²⁶⁷ K.A. Orlova, W.E. Parker, G.G. Heuer, V. Tsai, J. Yoon, M. Baybis, R.S. Fenning, K. Strauss, P.S. Crino, STRADa deficiency results in aberrant mTORC1 signaling during corticogenesis in humans and mice, *The Journal of Clinical Investigation*, 120 (2010) 1591-1602.
- ²⁶⁸ E.G. Puffenberger, K. Strauss, K.E. Ramsey, D.W. Craig, D.A. Stephen, D.L. Robinson, C.L. Hendrickson, S. Gottlieb, D.A. Ramsay, V.M. Siu, G.G. Heuer, P.S. Crino, D.H. Morton, Polyhydramnios, megalencephaly and symptomatic epilepsy caused by a homozygous 7-kilobase deletion in LYK5, *Brain*, 130 (2007) 1929-1941.
- ²⁶⁹ M. Shelly, C. L., S. Heilshorn, G. Sumbre, M. Poo, LKB1/STRAD promotes axon initiation during neuronal polarization, *Cell*, 129 (2007) 565-577.
- ²⁷⁰ A.P. Barnes, B.N. Lilley, Y.A. Pan, L.J. Plummer, A.W. Powell, A.N. Raines, J.R. Sanes, F. Polleux, LKB1 and SAD kinases define a pathway required for the polarization of cortical neurons, *Cell*, 129 (2007) 549-563.
- ²⁷¹ M. Shelly, B.K. Lim, L. Cancedda, S. Heilshorn, H. Gao, M. Poo, Local and long-range reciprocal regulation of cAMP and cGMP in axon/dendrite formation, *Science*, 327 (2010) 547-552.
- ²⁷² C. Jacobson, B. Schnapp, G.A. Banker, A change in the selective translocation of the kinesin-1 motor domain marks the initial specification of the axon, *Neuron*, 49 (2006) 797-804.
- ²⁷³ P. Cheng, H. Lu, M. Shelly, H. Gao, M. Poo, Phosphorylation of E3 Ligase Smurf1 switches its substrate preference in support of axon development, *Neuron*, 69 (2011) 231-243.
- ²⁷⁴ S.H. Shi, L.Y. Jan, Y.N. Jan, Hippocampal neuronal polarity specified by spatially localized mPar3/mPar6 and PI 3-Kinase activity, *Cell*, 112 (2003) 63-75.
- ²⁷⁵ W. Huang, L. She, X. Chang, R. Yang, L. Wang, L. Ji, J. Jaio, M. Poo, Protein kinase LKB1 regulates polarized dendrite formation in adult hippocampal newborn neurons, *PNAS*, 111 (2014) 469-474.
- ²⁷⁶ M. Kishi, Y.A. Pan, J.G. Crump, J.R. Sanes, Mammalian SAD kinases are required for neuronal polarization, *Science*, 307 (2005) 929-932.

- ²⁷⁷ B.O. Valeva-Rotse, J.L. Smart, A.F. Baas, B. Edmonds, Z. Zhao, A. Brown, L.R. Klug, K. Hansen, G. Reilly, A.P. Gardner, K. Subbiah, E.A. Gaucher, H.C. Clevers, A.F. Baas, STRAD pseudokinases regulate axogenesis and LKB1 stability, *Neural Development*, 9 (2014).
- ²⁷⁸ D. St Johnston, J. Ahringer, Cell polarity in eggs and epithelia: parallels and diversity, *Cell*, 141 (2010) 757-774.
- ²⁷⁹ A.P. Barnes, D. Solecki, F. Polleux, New insights into the molecular mechanisms specifying neuronal polarity in vivo, *Current Opinion in Neurobiology*, 18 (2008) 44-52.
- ²⁸⁰ M. Shelly, L. Cancedda, B.K. Lim, A.T. Popescu, P. Cheng, H. Gao, M. Poo, Semaphorin3A regulates neuronal polarization by suppressing axon formation and promoting dendrite growth, *Neuron*, 71 (2011) 433-446.
- ²⁸¹ M. Shelly, L. Cancedda, S. Heilshorn, G. Sumbre, M.-m. Poo, LKB1/STRAD promotes axon initiation during neuronal polarization, *Cell*, 129 (2007) 565-577.
- ²⁸² M. Shelly, M. Poo, Role of LKB1-SAD/MARK pathway in neuronal polarization, *Developmental Neurobiology*, 71 (2011) 508-527.
- ²⁸³ A.F. Baas, J. Kulpers, N.N. van der Wel, E. Battle, H.K. Koerten, P.J. Peters, H.C. Clevers, Complete polarization of single intestinal epithelial cells upon activation of LKB1 by STRAD, *Cell*, 116 (2004) 457-466.
- ²⁸⁴ A.F. Baas, J. Boudeau, G.P. Sapkota, L. Smit, R. Medema, N.A. Morrice, D.R. Alessi, H.C. Clevers, Activation of the tumor suppressor kinase LKB1 by the STE20-like pseudokinase STRAD, *The EMBO Journal*, 22 (2009) 3062-3072.
- ²⁸⁵ A.P. Barnes, B.N. Lilley, A. Pan, L.J. Plummer, A.W. Powell, A.N. Raines, J.R. Sanes, F. Polleux, LKB1 and SAD kinase define a pathway required for the polarization of cortical neurons, *Cell*, 129 (2007) 549-563.
- ²⁸⁶ E. Zehiraj, B.M. Filippi, M. Deak, D.R. Alessi, D.M.F. van Aalten, Structure of the LKB1-STRAD-MO25 complex reveals an allosteric mechanism of kinase activation, *Science*, 326 (2009) 1707-1711.
- ²⁸⁷ H. Oliveira, L.R. Pires, R. Fernandez, M.C.L. Martins, S. Simoes, A.P. Pego, Chitosan-based gene delivery vectors targeted to the peripheral nervous system, *Journal of Biomedical Materials Research A*, 85A (2010) 801-810.
- ²⁸⁸ J.H. Park, S. Kwon, J.O. Nam, R.W. Parl, H. Chung, S.B. Seo, I.S. Kim, I.C. Kwon, S.Y. Jeong, Self-assembled nanoparticles based on glycol chitosan bearing 5-beta-cholanic acid for RGD peptide delivery, *Journal of Controlled Release*, 95 (2004) 579-588.
- ²⁸⁹ J.H. Kim, K. Y.S., K. Park, E. Kang, S. Lee, H.Y. Nam, K. Kim, J.H. Park, D.Y. Chi, R.W. Park, I.S. Kim, K. Choi, I.C. Kwon, Self-assembled glycol chitosan nanoparticles for the sustained and prolonged delivery of antiangiogenic small peptide drugs in cancer therapy, *Biomaterials*, 29 (2008) 1920-1930.
- ²⁹⁰ M. Malatesta, V. Galimberti, B. Cisterna, M. Costanzo, M. Biggiogera, C. Zancanaro, Chitosan nanoparticles are efficient carriers for delivering biodegradable drugs to neuronal cells, *Histochem Cell Biol*, 141 (2014) 551-558.
- ²⁹¹ W.W. Hu, W.J. Syu, W.Y. Chem, R.C. Ruaan, Y.C. Cheng, C.C. Chien, C. Li, C.A. Chung, C.W. Tsao, Use of biotinylated chitosan for substrate gene delivery, *Bioconjugate Chemistry*, 23 (2012) 1587-1599.
- ²⁹² K.Y. Lee, Chitosan and its derivatives for gene delivery, *Macromolecular Research*, 15 (2007) 195-201.

- ²⁹³ M. Morille, C. Passirani, A. Vonarbourg, A. Clavreul, J.P. Benoit, Progress in developing cationic vectors for non-viral systemic gene therapy against cancer, *Biomaterials*, 29 (2008) 3477-3496.
- ²⁹⁴ M. Yemisci, S. Caban, Y. Gursoy-Ozdemir, S. Lule, R. Novoa-Carballal, R. Rigueira, E. fernandez-Megia, K. Andrieux, P. Couvreur, Y. Capan, T. Dalkara, Systematically administrated brain-targeted nanoparticles transport peptides across the blood-brain barrier and provide neuroprotection, *Journal of Cerebral Blood Flow & Metabolism*, 35 (2015) 469-475.
- ²⁹⁵ N.K. Bari, M. Fazli, M.Q. Hassan, M.R. Haider, B. Gaba, J.K. Narang, S. Baboota, J. Ali, Brain delivery of buspirone hydrochloride chitosan nanoparticles for the treatment of general anxiety disorder, *International Journal of Biological Macromolecules*, 81 (2015) 49-59.
- ²⁹⁶ A. Lalatsa, A.G. Schatzlein, J.F. Uchegbu, Strategies to deliver peptide drugs to the brain, *Molecular Pharmaceutics*, 11 (2014) 1081-1093.
- ²⁹⁷ O. Gartzandia, E. Herran, J.L. Pedraz, E. Carro, M. Igartua, H. R.M., Chitosan coated nanostructured lipid carriers for brain delivery of proteins by intranasal administration, *Colloids and Surfaces B: Biointerfaces*, 134 (2015) 304-313.
- ²⁹⁸ R.Y. Hong, B. Feng, L.L. Chen, G.H. Liu, H.Z. Li, Y. Zheng, D.G. Wei, Synthesis, characterization and MRI application of dextran-coated Fe₃O₄ magnetic nanoparticles, *Biochemical Engineering Journal*, 42 (2008) 290-300.
- ²⁹⁹ B. Zheng, B. Vazin, P.W. Goodwill, A. Conway, A. Verma, S. E.U., D. Schaffer, S.M. Conolly, Magnetic particle imaging tracks the long-term fate of in vivo neural cell implants with high image contrast, *Scientific Reports*, 5 (2015).
- ³⁰⁰ R. Banarjee, Y. Katsenovich, L. Lagos, M. McIntosh, X. Zhang, C.Z. Li, Nanomedicine: magnetic nanoparticles and their biomedical applications, *Current Medicinal Chemistry*, 17 (2010) 3120-3141.
- ³⁰¹ Q.A. Pankhurst, J. Connolly, S.K. Jones, J. Dobson, Applications of magnetic nanoparticles in biomedicine, *Journal of Physics D: Applied Physics*, 36 (2003) R167-R181.
- ³⁰² S.J.H. Soenen, U. Himmelreich, N. Nuytten, M. De Cuyper, Cytotoxic effects of iron oxide nanoparticles and implications for safety in cell labeling, *Biomaterials*, 32 (2011) 195-205.
- ³⁰³ J.A. Kim, N. Lee, B.H. Kim, W.J. Rhee, S. Yoon, T. Hyeon, T.H. Park, Enhancement of neurite outgrowth in PC12 cells by iron oxide nanoparticles, *Biomaterials*, 32 (2011).
- ³⁰⁴ S. Ghosh, S. GhoshMitra, T. Cai, D.R. Diercks, N.C. Mills, D.L. Hynds, Alternating magnetic field controlled, multifunctional nano-reservoirs: intracellular uptake and improved biocompatibility, *Nanoscale Reserach Letters*, 5 (2010) 195-204.
- ³⁰⁵ M. Geppert, M.C. Hohnholt, K. Thiel, S. Nurnberg, I. Grunwald, K. Rezwani, R. Dringen, Uptake of dimercaptosuccinate-coated magnetic iron oxide nanoparticles by cultured brain astrocytes, *Nanotechnology*, 22 (2011).
- ³⁰⁶ C. Petters, R. Dringen, Accumulation of iron oxide nanoparticles by cultured primary neurons, *Neurochemistry International*, 81 (2015) 1-9.
- ³⁰⁷ M.P. Calatayud, C. Riggio, V. Raffa, B. Sanz, T.E. Torres, M.R. Ibarra, C. Hoskins, A. Cuschieri, L. Wang, J. Pinkernelle, G. Keilhoff, G.F. Goya, Neuronal cells loaded with PEI-coated Fe₃O₄ nanoparticles for magnetically guided nerve regeneration, *Journal of Materials Chemistry B*, 1 (2013) 3607-3616.
- ³⁰⁸ A.M. Grabrucker, C.C. Garner, T.M. Boeckers, L. Bondioli, B. Ruozi, F. Forni, M.A. Vandelli, G. Tosi, Development of novel Zn²⁺ loaded nanoparticles designed for cell-type targeted drug release in CNS neurons: in vitro evidences, *PLOS One*, 6 (2011).

- ³⁰⁹ J.S. Weinstein, C.G. Varallayay, E. Dosa, S. Gahramanov, B. Hamilton, W.D. Rooney, L.L. Muldoon, E.A. Neuwelt, Superparamagnetic iron oxide nanoparticles: diagnostic magnetic resonance imaging and potential therapeutic applications in neurooncology and central nervous system inflammatory pathologies, a review, *Journal of Cerebral Blood Flow & Metabolism*, 30 (2010) 15-35.
- ³¹⁰ S.H. Bakhru, E. Altiok, C. Highley, D. Delubac, J. Suhan, T.K. Hitchens, C. Ho, S. Zappe, Enhanced cellular uptake and long-term retention of chitosan-modified iron-oxide nanoparticles for MRI-based cell tracking, *International Journal of Nanomedicine*, 7 (2012) 4613-4623.
- ³¹¹ V. Balan, I.A. Petrache, M.I. Popa, M. Butnaru, E. Barbu, J. Tsibouklis, L. Verestiuc, Biotinylated chitosan-based SPIONs with potential in blood-contacting applications, *Journal of Nanoparticle Research*, 14 (2012).
- ³¹² P. Rakic, Neuron-glia relationship during granule cell migration in developing cerebellar cortex. A Golgi and electronmicroscopic study in Macacus Rhesus, *The Journal of Comparative Neurology*, 141 283-312.
- ³¹³ Y. Hatanaka, F. Murakami, In vitro analysis of the origin, migratory behavior, and maturation of cortical pyramidal cells, *The Journal of Comparative Neurology*, 454 (2002) 1-14.
- ³¹⁴ S. Noctor, C., M.-C. V., L. Ivic, A.R. Kriegstein, *Nature Neuroscience*, 7 (2004) 136-144.
- ³¹⁵ J. De Vry, P. Martinez-Martinez, M. Losen, Y. Temel, T. Steckler, H.W.M. Steinbusch, M.H. De Baets, J. Prickaerts, *In vivo* electroporation of the central nervous system: a non-viral approach for targeted gene delivery, *Progress in Neurobiology*, 92 (2010) 227-244.
- ³¹⁶ L. Cancedda, H. Fiumelli, K. Chen, M. Poo, Excitatory GABA action is essential for morphological maturation of cortical neurons in vivo, *The Journal of Neuroscience*, 27 (2007) 5224-5232.
- ³¹⁷ T.I. Young-Pearse, J. Bai, R. Chang, J.B. Zheng, J.J. LoTurco, D.J. Selkoe, A critical function for beta-amyloid precursor protein in neuronal migration revealed by *in utero* RNA interference, *The Journal of Neuroscience*, 27 (2007) 14459-14469.
- ³¹⁸ H. Karatas, Y. Aktas, Y. Gursoy-Ozdemir, E. Bodur, M. Yemisci, S. Caban, A. Vural, K. Pinarbasli, Y. Capan, E. Fernandez-Megia, R. Novoa-Carballal, R. Riguera, K. Andrieux, P. Couvreur, T. Dalkara, A nanomedicine transports a peptide caspase-3 inhibitor across the blood-brain barrier and provides neuroprotection, *The Journal of Neuroscience*, 29 (2009) 13761-13769.